University of Southampton

Faculty of Engineering, Science and Mathematics

School of Chemistry & Institute of Sound
and Vibration Research

# Acoustoelectrochemical characterisation of cavitation and its use in the study of surface processes

by

Douglas Graham Offin

A thesis submitted for degree of
Doctor of Philosophy

January 2006

UNIVERSITY OF SOUTHAMPTON

ABSTRACT

Faculty of Engineering, Science and Mathematics
School of Chemistry & Institute of Sound and Vibration Research

Doctor of Philosophy

# Acoustoelectrochemical characterisation of cavitation and its use in the study of surface processes

by Douglas Graham Offin

The environment in the vicinity of an operating ultrasonic horn is characterised through the use of electrochemical, acoustic and luminescent techniques, high-speed video and laser scattering.

The sound field produced by the horn is modelled and acoustic pressure measurements are made. The acoustic pressure is greatest at the tip of the horn and decreases as the axial distance is increased. In the presence of cavitation the pressure wave is complex, consisting of a sinusoidal driving wave superimposed with high amplitude pressure shocks every 3-4 cycles of the driving wave. The shocks are attributed to emissions from cavitation activity.

The spatial extent of inertial cavitation is investigated using multibubble sonoluminescence (MBSL) imaging and a novel electrochemical erosion technique. The electrochemical technique utilises a novel Pb/Pt dual microelectrode, which has the ability to detect both the mass transfer and erosive effects of sonication and cavitation. Inertial cavitation only exists close to the horn but is found to extend further than expected. This is because the introduction of an electrode can have a significant effect on the sound field, due to scattering of the incident pressure waves. It is found that the degree of scattering depends on the wavenumber, radius of the electrode, position on the electrode surface and the acoustic properties of the electrode and solution. It is shown that under the conditions used here the driving wave is not scattered significantly by the electrode. However, the high frequency shock waves are scattered effectively. The degree of scattering is shown to be greater for a soda glass-bodied electrode when compared to an Epofix epoxy-bodied electrode.

The dynamics of cavitation bubbles is studied. Close to the tip of the horn small bubbles can be seen to appear in high-speed video footage, which are associated with surface erosion and MBSL. These become visible following the periodic collapse of a large bubble cloud, which exists at the tip of the horn. They have maximum visible radii of 10's of microns and lifetimes of less than 10 μs. Two mechanisms are proposed which may explain the observed bubble dynamics: a shielding effect and bubble rebound. Large (100's of microns), electrode-surface bound bubbles, which exist at greater distances from the tip of the horn, are also investigated. Oscillation of the bubbles in the sound field leads to periodic mass transfer enhancement. Evidence of surface waves is also presented.

Inertial cavitation is applied to the study of repassivation of stainless steel. It is found that many repassivation transients can be collected in a short time. Kinetic analysis shows that both ion migration and place exchange mechanisms for film growth are in evidence. This is the result of the removal of varying amounts of material by each inertial cavitation event. The stability of a generic corrosion inhibitor in a cavitation environment is also studied. The importance of a thorough understanding of the local environment generated by sonication is emphasised if acoustic cavitation is to be used as an effective tool.

# Contents

# Acknowledgements

Firstly, I would like to sincerley thank my supervisor Dr Peter Birkin for his continual help, support, advice and guidance throughout the course of the research undertaken and presented in this thesis. He was always interested in the work and was invaluable both in the lab and while this thesis was being written.

I would like to extend my gratitude to Prof. Timothy Leighton for useful discussions, insights and valuable advice for the completion of this thesis.

Also, I would like to thank Dr Phillip Joseph.

Finally, for their friendship, support and love I would like to thank,

▫ Russell ▫ Hamid ▫ Eleanor ▫ Paul ▫ Gareth ▫
▫ Steve ▫ Suz ▫ Ken ▫ Tim ▫ Matt ▫ Jason ▫
▫ John ▫ Yvonne ▫ Chris ▫ Hanne ▫ Jyo ▫
▫ Mum & Dad ▫
▫ Laura ▫

I also acknowledge the funding given by EPSRC.

# Symbols and Abbreviations

## Symbols

| | |
|---|---|
| $a$ | Function defined by Equation 1.22 |
| $a_E$ | Radius of the tip of the electrode body |
| $a_T$ | Radius of the tip of the ultrasonic horn |
| $A$ | Parameter related to the properties of a thin oxide film |
| $A_{sine}$ | Amplitude of generated sine wave |
| $b$ | Number of moles |
| $B$ | Parameter related to the properties of a thin oxide film |
| $c$ | Velocity of sound |
| $c_E$ | Velocity of sound in the material used in the main body of an electrode |
| $c_S$ | Velocity of sound in the electrolyte |
| $C_p$ | Specific heat capacity of a liquid sample |
| $C_{p(g)}$ | Specific heat capacity of gas within a bubble |
| $C_t$ | Threshold bubble wall displacement amplitude required for the onset of surface waves |
| $d$ | Thickness of the disc used to determine the speed of sound in solids |
| $d_{rad}$ | Radiation damping coefficient |
| $d_{th}$ | Thermal damping coefficient |
| $d_{tot}$ | Total damping coefficient |
| $d_\eta$ | Viscous damping coefficient |
| $E$ | Electrode potential |
| $E_{corr}$ | Corrosion potential |
| $E_1$ | Uninhibited corrosion potential |
| $E_2$ | Inhibited corrosion potential |
| $E_3$ | Inhibited corrosion potential under ultrasound at 5 mm electrode-to-horn separation |
| $E_4$ | Inhibited corrosion potential under ultrasound at 0.5 mm electrode-to-horn separation |
| $f$ | Frequency |
| $F$ | Faraday's constant |

| | |
|---|---|
| $F_E$ | Electric field strength across a thin oxide film |
| $g$ | Function defined by Equation 1.23 |
| $h$ | Distance propagated by a plane wave |
| $H$ | Scattering function |
| $i$ | Current |
| $i_{N(silent)}$ | Current normalised to the value recorded under silent conditions |
| $i_{Pb}$ | Current recorded at a lead electrode |
| $i_{Pt}$ | Current recorded at a platinum electrode |
| $I_h$ | Intensity of a sound wave after a distance, $h$ |
| $I_0$ | Initial intensity of a sound wave |
| $j$ | $\sqrt{-1}$ |
| $J_1$ | Bessel function of the first kind |
| $k$ | Wavenumber |
| $K_g$ | Thermal conductivity |
| $K_{SP}$ | Solubility product |
| $K_1$ | Struve function of the first kind |
| $m$ | Integer value defining maxima and minima in the near field |
| $M$ | Mass |
| $M_{FFT}$ | Magnitude of FFT |
| $n$ | Mode number of a surface wave |
| $N_{events}$ | Number of erosion transients recorded by a passivated Pb electrode |
| $p$ | Pressure |
| $P$ | Acoustic pressure |
| $\langle P \rangle$ | Average acoustic pressure over the surface of the electrode |
| $P_A$ | Acoustic pressure amplitude |
| $P_A(2^{nd})$ | Second harmonic acoustic pressure amplitude |
| $P_{A(N)}$ | Normalised acoustic pressure amplitude |
| $P_{A(drive)}$ | Acoustic pressure amplitude at the driving frequency |
| $P_B$ | Blake pressure |
| $P_g$ | Gas pressure in a bubble |
| $P_{g,E}$ | Gas pressure in a bubble under equilibrium conditions |
| $P_l$ | Internal pressure of a bubble |
| $P_{l,E}$ | Internal pressure of a bubble under equilibrium conditions |
| $P_i$ | Incident acoustic pressure |

| | |
|---|---|
| $P_L$ | Pressure in the liquid at a bubble wall |
| $P_{L(crit)}$ | Critical pressure in the liquid at a bubble wall for explosive growth as defined by the Blake threshold |
| $P_s$ | Scattered acoustic pressure |
| $P_T$ | Peak negative pressure required to generate inertial cavitation |
| $P_{T(surface)}$ | Threshold acoustic pressure required to generate surface waves |
| $P_t$ | Total acoustic pressure |
| $P_V$ | Vapour pressure |
| $P_\sigma$ | Surface tension (or Laplace) pressure |
| $P_0$ | Hydrostatic pressure |
| $P_\infty$ | Pressure an infinite distance from a bubble |
| $\Delta P$ | Time averaged pressure difference across a bubble wall |
| $q$ | Function defined by Equation 1.24 |
| $Q_T$ | Charge passed |
| $r$ | Distance between a point source and an observer |
| $r_{ax}$ | Distance from the centre of the tip of the horn along the axis of symmetry |
| $r_{ax(m)}$ | Distance of pressure maxima and minima from the centre of the tip of the horn along the axis of symmetry, $m$ is an integer value |
| $r_{electrode\text{-}to\text{-}horn}$ | Distance from the tip of the horn to the electrode |
| $r'$ | Radial distance from the centre of the electrode |
| $R$ | Radius of a bubble |
| $R_0$ | Equilibrium radius of a bubble |
| $R_B$ | Blake radius of a bubble |
| $R_C$ | Radius of a bubble cluster |
| $R_{crit}$ | Critical radius for bubble stability with respect to hydrostatic pressure changes |
| $R_{max}$ | Maximum radius of a bubble |
| $R'$ | Distance between a point on the surface of the electrode and a surface element |
| $R'_{lim}$ | Maximum distance between a point on the surface of the electrode and the edge of the electrode |
| $R1_{gain}$ | Value of the measuring resistor on channel 1 of a bipotentiostat |
| $R2_{gain}$ | Value of the measuring resistor on channel 2 of a bipotentiostat |
| $(R_{max}/R_0)_c$ | Critical expansion ratio |

| | |
|---|---|
| $(R_{max}/R_0)_d$ | Dynamic expansion ratio |
| $(R_{max}/R_0)_t$ | Threshold expansion ratio |
| $t$ | Time |
| $t_{delay}$ | Time after the pressure exceeds $P_B$ before growth begins |
| $t_{grow}$ | Net time for bubble growth in prompt response to negative sinusoidal pressure pulse |
| $t_{trig\text{-}peak1}$ | Time from trigger to the first peak in speed of sound measurements |
| $t_{1st}$ | Time of the first frame in a video sequence |
| $t_1$ | Time taken, after start of negative-halfcycle of a sinusoidal pulse, for the negative acoustic pressure to exceed $P_B$ |
| $t_2$ | Time until the liquid ceases to be in tension after start of negative-halfcycle of a sinusoidal pulse |
| $\Delta t$ | Time between spike in $V_{PD}$ and pressure shock in laser scattering experiments |
| $\Delta t_I$ | Delay (after pressure exceeds $P_B$) before bubble grows, caused by inertia |
| $\Delta t_\sigma$ | Delay (after pressure exceeds $P_B$) before bubble grows, caused by surface tension |
| $\Delta t_\eta$ | Delay (after pressure exceeds $P_B$) before bubble grows, caused by viscosity |
| $T$ | Temperature |
| $T_{max}$ | Maximum temperature attained during the collapse of a bubble |
| $u_i$ | Incident particle velocity |
| $u_s$ | Scattered particle velocity |
| $U$ | Amplitude of the velocity of the tip of the ultrasonic horn |
| $V$ | Volume |
| $V_H$ | Hydrophone output voltage in speed of sound experiments |
| $V_{PD}$ | Photodiode output voltage |
| $V_{PMT}$ | Photomultiplier tube output voltage |
| $V1_{app}$ | Voltage applied to channel 1 of a bipotentiostat |
| $V2_{app}$ | Voltage applied to channel 2 of a bipotentiostat |
| $V1_{out}$ | Voltage output from channel 1 of a bipotentiostat |
| $V2_{out}$ | Voltage output from channel 2 of a bipotentiostat |
| $W$ | Work done on a bubble by the liquid during the collapse phase |

| | |
|---|---|
| $W_c$ | Calorific power |
| $\Delta W$ | Work done on or by a bubble during a complete growth and collapse cycle |
| x | Distance coordinate in the Cartesian frame |
| $x_A$ | Distance in the x direction to a point, A |
| y | Distance coordinate in the Cartesian frame |
| z | Distance coordinate in the Cartesian frame |
| $z_A$ | Distance in the z direction to a point, A |

| | |
|---|---|
| $\alpha$ | Attenuation coefficient |
| $\beta$ | Volume fraction of cavities in a cluster at the maximum cluster radius |
| $\Gamma$ | Function defined by Equation 1.27 |
| $\kappa$ | Polytropic index |
| $\Lambda$ | Reflection coefficient |
| $\lambda$ | Wavelength |
| $\eta$ | Dynamic viscosity |
| $\rho$ | Density |
| $\rho_E$ | Density of the material used in the main body of an electrode |
| $\rho_g$ | Density of gas |
| $\rho_S$ | Density of the electrolyte |
| $\sigma$ | Surface tension |
| $\tau$ | Collapse time for a bubble cluster |
| $\omega$ | Circular frequency |
| $\omega_0$ | Resonance frequency of a bubble |
| $\psi$ | Function defined by Equation 4.14 |

## Abbreviations

| | |
|---|---|
| ADC | Analogue-to-digital conversion |
| CV | Cyclic voltammetry |
| EDTA | Ethylenediaminetetraacetic acid |
| EDX | Energy dispersive x-ray |
| FFT | Fast Fourier transform |

| | |
|---|---|
| IF | Inertial function |
| MBSCL | Multibubble sonochemiluminescence |
| MBSL | Multibubble sonoluminescence |
| MPO | 3-methyl-2-pyrazoline-5-one |
| MTL | Mass transfer limited |
| PF | Pressure function |
| PTFE | Polytetrafluoroethylene |
| SBSL | Single bubble sonoluminescence |
| SCE | Saturated calomel electrode |
| SECM | Scanning electrochemical microscopy |
| TOC | Total organic content |

# Chapter 1 Introduction

The collapse of a cavitation bubble can generate temperatures in excess of 5000 K [1, 2] and pressures greater than 500 bar [2]. While these extreme conditions are short-lived and localised, the effects (both beneficial and detrimental) can be seen in a global sense. The generation of such bubbles through the use of ultrasound ($f$ > 16 kHz) is relatively easy, and the advantageous effects associated with them are one of the main reasons for the use of sonication as a tool in research and industry [3, 4]. For example, in biology it is used for the destruction of cells [5, 6]. In the pharmaceutical industry its applications include the extraction of compounds from plant materials [7, 8]. In sonochemistry it is used for the destruction of organic pollutants [9-13], a variety of organic syntheses [14-17] and the formation of nanoparticles [18-21]. Ultrasound is also useful as a technique for emulsification, which can be vital in both industrial processes and analytical techniques [22-27]. Recently the application of ultrasound to 'green' chemistry has also been proposed [4, 28], owing to the accessibility of extreme conditions from a technique that results in a relatively mild environmental impact.

While the generation of acoustic cavitation is easy, control and reproducibility can be difficult. One of the primary aims of the work presented in this thesis was to monitor the effects of power ultrasound using electrochemical technology but importantly to interpret the results through consideration of the acoustics involved. Hence the work is considered to be "acoustoelectrochemical" [29] in nature as opposed to "sonoelectrochemical". This distinction is important as there is a need to link the extensive acoustic and sonochemical/ sonoelectrochemical literature. There follows an introduction to acoustic cavitation, its physical effects and the detection of the effects using electrochemical (and other) techniques.

## 1.1 Acoustic cavitation and bubble dynamics

When a sound wave is passed through a solution the liquid is subjected to compression and rarefaction cycles. The response of a cavity in such a solution

is dependent on the amplitude and frequency of the sonic irradiation, the size of the cavity and many other factors concerning the liquid properties, location of the cavity and the ambient experimental conditions. There follows a brief summary of the study of bubble dynamics. This is not intended to be an exhaustive review and interested readers are directed to an excellent text by Leighton [30] and several other review papers [31, 32], which are far more detailed.

The dynamics of bubbles have been widely studied under both static and dynamic conditions. In a pioneering paper in 1917, Rayleigh [33] refined the work of Besant [34] in considering the collapse of an empty, spherical cavity in an incompressible liquid. This work was extended to include surface tension effects and the pressure of liquid vapour in the bubble and in 1949 Plesset [35] developed an equation for the motion of a vapour filled bubble in a changing pressure field. This early work was concerned with hydrodynamic cavitation, where the pressure changes experienced by a bubble are the result of a distribution in the fluid velocity throughout the system in question. This makes it difficult to be sure of the instantaneous pressure at the point of interest because of complex spatial variations. With this in mind, Noltingk and Neppiras [36, 37] considered cavitation generated by ultrasonic sound waves, where the pressure changes are more accurately known and controllable. However, before considering the dynamic situation it is helpful to look at a bubble subjected to a static pressure change.

### 1.1.1 Response of a bubble to a static pressure change

Consider a bubble of radius, $R_0$. Under equilibrium conditions the internal pressure of a bubble, $P_I$ is equal to the sum of the pressure in the liquid at the bubble wall, $P_L$ and the surface tension (or Laplace) pressure, $P_\sigma$. That is to say,

$$P_I = P_L + P_\sigma \tag{1.1}$$

The internal pressure is the sum of the gas and vapour pressures within the bubble ($P_{I,E} = P_{g,E} + P_V$ where the subscript $E$ denotes equilibrium conditions) and the surface tension pressure is inversely proportional to the radius of the bubble ($P_\sigma = 2\sigma/R_0$ where $\sigma$ is the surface tension). Since the conditions are

considered to be static, the pressure at the bubble wall is equal to the hydrostatic pressure throughout the liquid, $P_0$ and hence,

$$P_{g,E} = P_0 + \frac{2\sigma}{R_0} - P_V \tag{1.2}$$

Now, if the pressure in the liquid is changed, the radius of the bubble will change such that the gas pressure within the bubble is given by

$$P_g = P_{g,E}\left(\frac{R_0}{R}\right)^{3\kappa} = \left(P_0 + \frac{2\sigma}{R_0} - P_V\right)\left(\frac{R_0}{R}\right)^{3\kappa} \tag{1.3}$$

assuming that the gas in the bubble behaves as a polytropic gas ($pV^{\kappa}$= constant, where $\kappa$ is the polytropic index [38]). Substitution of Equation 1.3 into the appropriate equations above and rearrangement results in an expression, which gives the pressure in the liquid at the bubble wall following such a change in bubble radius from $R_0$ to $R$.

$$P_L = \left(P_0 + \frac{2\sigma}{R_0} - P_V\right)\left(\frac{R_0}{R}\right)^{3\kappa} + P_V - \frac{2\sigma}{R} \tag{1.4}$$

This is an important equation and will be used in the following section, which considers a bubble in an oscillating pressure field and also later, in the context of the cavitation threshold (Section 1.3).

### 1.1.2 Response of a bubble to an oscillating pressure field

Consider a spherical bubble in a time-varying pressure field such that the instantaneous pressure an infinite distance from the bubble at any time, $t$ is given by

$$P_{\infty} = P_0 - P_A \sin(\omega t) \tag{1.5}$$

where $P_0$ is the hydrostatic pressure and $P_A$ is the amplitude of an applied (acoustic) pressure wave of frequency, $f = \omega/2\pi$. At time $t = 0$ let the bubble be of radius $R_0$ and contain gas such that the bubble is at equilibrium. At some time, $t > 0$, the bubble radius changes to a new value, $R$ in response to the change in pressure and the liquid will acquire kinetic energy, which is given by

$$\frac{1}{2}\left[\rho 4\pi R^3\left(\frac{dR}{dt}\right)^2\right] = 2\rho\pi R^3\left(\frac{dR}{dt}\right)^2 \quad (1.6)$$

assuming that the liquid is incompressible. This kinetic energy is equal to the difference in the work done by the pressure an infinite distance from the bubble and the work done by the pressure in the liquid at the bubble wall,

$$\int_{R_0}^{R}(P_L - P_\infty)4\pi R^2 dR = 2\rho\pi R^3\left(\frac{dR}{dt}\right)^2 \quad (1.7)$$

Differentiation of this equation with respect to $R$ gives

$$\frac{P_L - P_\infty}{\rho} = \frac{3}{2}\left(\frac{dR}{dt}\right)^2 + R\left(\frac{d^2R}{dt^2}\right) \quad (1.8)$$

Substitution of Equations 1.4 and 1.5 into 1.8 results in the equation of motion for a bubble in an oscillating pressure field, originally derived by Noltingk and Neppiras [37].

$$\frac{1}{\rho}\left[\left(P_0 + \frac{2\sigma}{R_0} - P_V\right)\left(\frac{R_0}{R}\right)^{3\kappa} + P_V - \frac{2\sigma}{R} - P_0 - P_A\sin(\omega t)\right] = \frac{3}{2}\left(\frac{dR}{dt}\right)^2 + R\left(\frac{d^2R}{dt^2}\right) \quad (1.9)$$

This equation was refined by Poritsky [39] to include the effects of viscosity ($\eta$), resulting in the R.P.N.N.P equation (after those who contributed to its formulation) or, as it is more commonly known, the Rayleigh-Plesset equation:

$$\frac{1}{\rho}\left[\left(P_0 + \frac{2\sigma}{R_0} - P_V\right)\left(\frac{R_0}{R}\right)^{3\kappa} + P_V - \frac{2\sigma}{R} - \frac{4\eta}{R}\left(\frac{dR}{dt}\right) - P_0 - P_A\sin(\omega t)\right] = \frac{3}{2}\left(\frac{dR}{dt}\right)^2 + R\left(\frac{d^2R}{dt^2}\right)$$

(1.10)

## 1.2 Examples of bubble behaviour

Numerical solutions of the Rayleigh-Plesset equation can be used to show bubble behaviour under various experimental conditions. In Figure 1.1 the effect of the initial bubble radius is examined and Figure 1.2 the effect of increasing the acoustic pressure is shown. These plots were constructed by solving the Rayleigh-Plesset equation (Equation 1.10) using a four-order Runge

Kutta method [40, 41]. A program written to achieve this, based on that given in reference [41], is shown in Section A.5.

### 1.2.1 Effect of initial bubble radius

Figure 1.1 shows radius-time plots for three bubbles of initial radii 2 mm (Figure 1.1b), 0.2 mm (Figure 1.1c) and 0.02 mm (Figure 1.1d) exposed to an oscillating pressure wave ($f$ = 23 kHz, $P_A$ = 200 kPa (Figure 1.1a)). The other parameters used are given in Table 1.1 and represent similar conditions to those employed throughout the work presented in this thesis. Clearly the initial bubble radius has a dramatic effect on the behaviour of the bubble. However, in order to understand this, it is necessary to consider the resonance of a bubble in an oscillating pressure field.

A bubble of a given radius, $R_0$ has a resonance frequency, $\omega_0$ which is given by Equation 1.11,

$$\omega_0 \approx \frac{1}{R_0\sqrt{\rho}}\sqrt{3\kappa\left(P_0+\frac{2\sigma}{R_0}-P_V\right)-\frac{2\sigma}{R_0}+P_V-\frac{4\eta^2}{\rho R_0^2}} \qquad (1.11)$$

This equation is produced by a small amplitude linear approximation of Equation 1.10. Of course, equally for a given driving frequency there is a resonant bubble radius. The largest bubble (Figure 1.1b) is much bigger than the resonant size (~120 μm) and responds slowly to the pressure changes, which are rapid, compared to the response time of the bubble. There are two main frequency components in the radius-time plot. A low frequency oscillation (~1400 Hz) associated with the resonance frequency of the bubble itself and a higher frequency component due to the applied pressure wave. For the intermediate bubble (Figure 1.1c), the radius is close to the resonant size and the response is quite different. The change in the bubble radius with time is of greater amplitude and is non-linear. Nonetheless the bubble oscillates over a long period of time and like the larger bubble can be termed stable. In contrast to these, the smallest bubble (Figure 1.1d) is much smaller than the resonance size and can respond quickly to the pressure changes. This results in an expansion (during the rarefraction cycle of the pressure wave) to more than 7 times the initial radius followed by a rapid, violent collapse. This bubble is unstable, and transient in terms of its temporal characteristics.

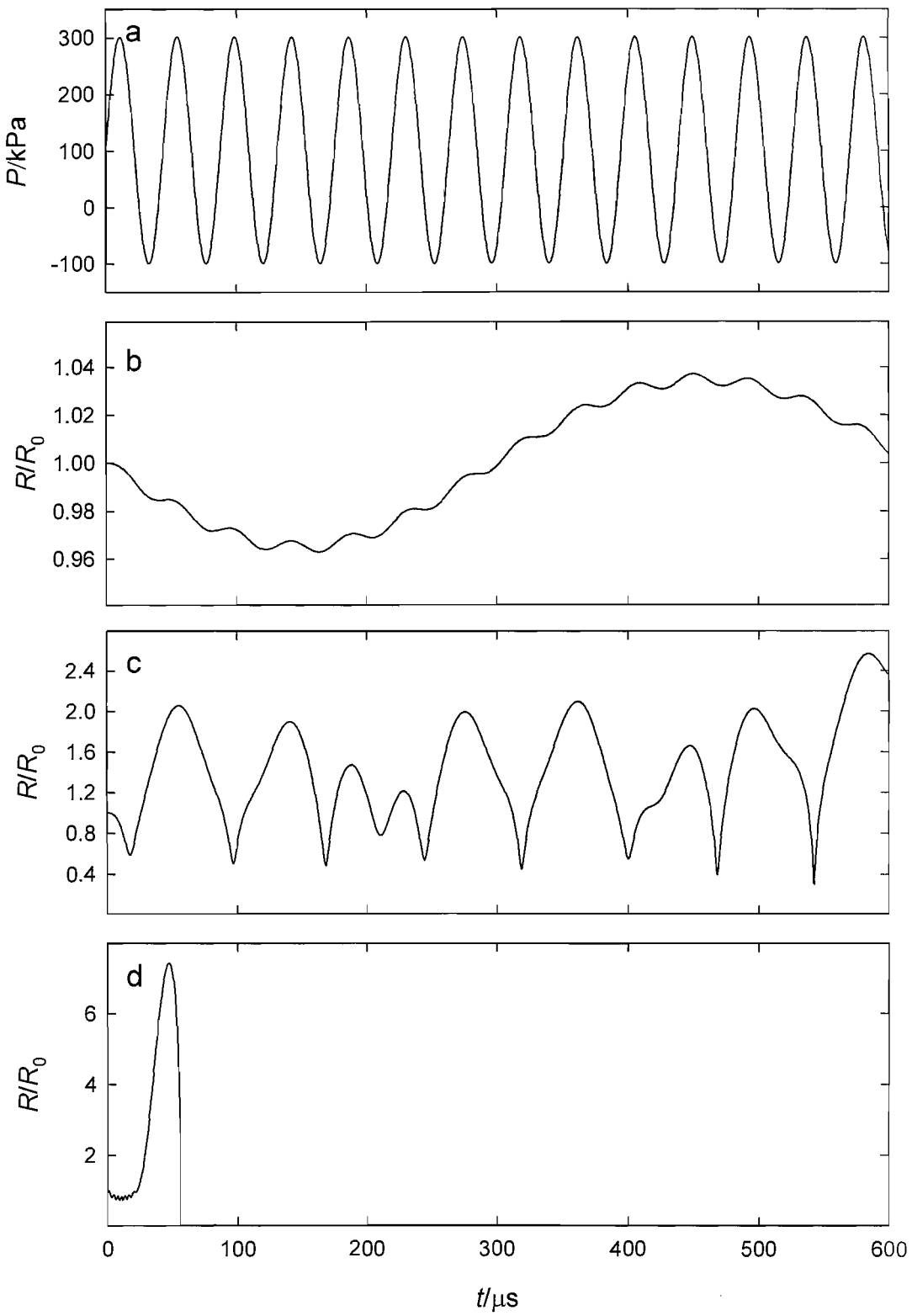


**Figure 1.1** Plots showing the response of three bubbles to an oscillating pressure field **(a)**. The bubbles are of initial radius **(b)** 2 mm, **(c)** 0.2 mm and **(d)** 0.02 mm. The other conditions are as shown in Table 1.1.

### 1.2.2 Effect of acoustic pressure amplitude

A similar change in bubble behaviour can be seen if, rather than changing the initial bubble radius, it is the amplitude of the sound field which is varied. Figure 1.2 shows the response of a bubble, initial radius 5 μm to an oscillating pressure field (23 kHz) of increasing amplitude (50 kPa (Figure 1.2b), 100 kPa (Figure 1.2c) and 200 kPa (Figure 1.2d)). Again there is a transition from stable oscillation (Figure 1.2b) to a short lived, unstable bubble, characterised by a rapid growth and violent collapse (Figure 1.2d). Figure 1.2c represents an interesting intermediate situation. The bubble expands to more than twice the initial radius, and then undergoes a rapid collapse. However, the collapse is arrested and the bubble rebounds. The bubble radius then oscillates rapidly (during the compression phase of the pressure cycle) before expanding again as the pressure drops. The bubble then collapses and rebounds again; however following the second rebound the bubble undergoes a collapse from which it does not rebound. The fact that this occurs after a period of time raises an important point. While there are a number of behavioural possibilities when a bubble is subjected to a high amplitude pressure field, ranging from low amplitude pulsation, to high amplitude stable oscillation, to high amplitude oscillation for several acoustic cycles followed by collapse, to growth and violent collapse in a single acoustic cycle, it is common for sonochemists to appeal to a bimodal distinction, whereby bubbles are termed as either 'transient' or 'stable'. This terminology is unfortunate as it implies a temporal connotation. It is perhaps more appropriate to classify bubbles depending on the physics of the collapse phase, as it is during this time that the phenomenological distinctions familiar to sonochemists are manifested. The generation of radical species [42-45], high internal bubble temperatures and pressures [1, 2], light output (MBSL) [46] and surface erosion [47] are all associated with a violent bubble collapse, which concentrates significant amounts of energy. This distinction is discussed further in the following section, which details the concept of a threshold that demarcates between these two forms of cavitation and also contains a discussion of the terminology associated with each.

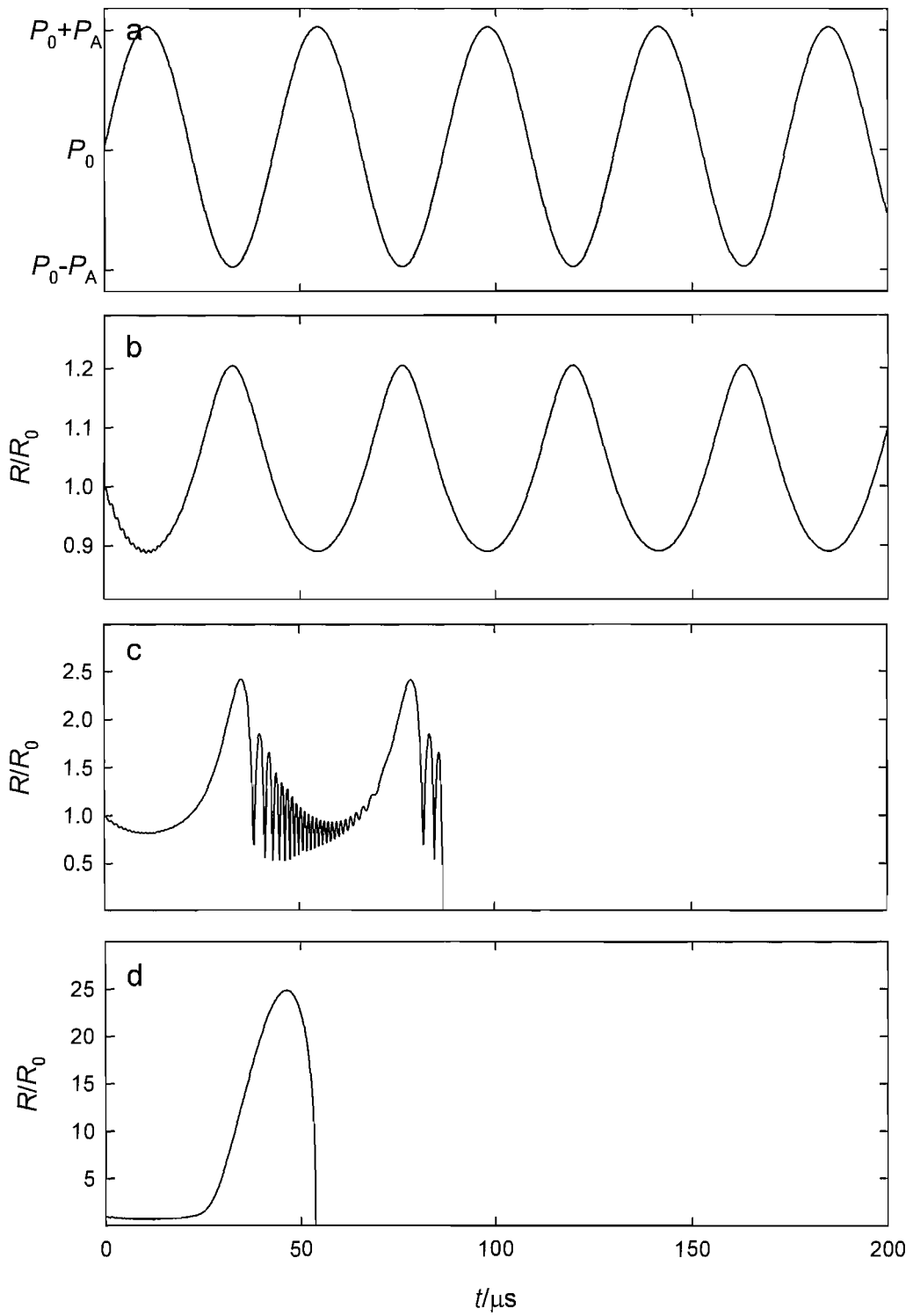


**Figure 1.2** Plots showing the response of three bubbles to an oscillating pressure field (23 kHz **(a)**). The bubbles are all of initial radius 5 μm and the amplitude of the pressure wave ($P_A$) is **(b)** 50 kPa, **(c)** 100 kPa and **(d)** 200 kPa. The other conditions are as shown in Table 1.1.

| Parameter | Value |
|---|---|
| Vapour pressure ($P_V$) | 3.5 kPa |
| Dynamic viscosity ($\eta$) | $8.91 \times 10^{-4}$ kg m$^{-1}$ s$^{-1}$ |
| Density ($\rho$) | 990 kg m$^{-3}$ |
| Surface tension ($\sigma$) | $7.30 \times 10^{-2}$ N m$^{-1}$ |
| Hydrostatic pressure ($P_0$) | 101 kPa |

**Table 1.1** Parameters used in the solution of Equation 1.10 shown in Figures 1.1 and 1.2.

## 1.3 Thresholds in bubble behaviour: Stable *vs.* transient, non-inertial *vs.* inertial

Flynn [48] first proposed the use of the terms 'stable' and 'transient' cavitation but importantly recognised the need to emphasise the high-energy, violent aspects of a 'transient' collapse. There are two important characteristics associated with 'transient' cavitation; an initial explosive growth and a rapid collapse, which is violent and concentrates significant amounts energy. A number of thresholds have been described and summarised in detail by Leighton [30].

### 1.3.1 The Blake threshold

The Blake threshold gives a threshold pressure for the explosive growth phase of a 'transient' cavitation event but can give no information about the subsequent collapse. Consider Equation 1.4, which describes the response of a bubble to a quasi-static pressure change from $P_0$ to $P_L$. If this new pressure is sufficiently negative then bubbles above a critical radius, $R_{crit}$ are unstable and will grow explosively, satisfying the first condition for violent cavitation. This critical radius can be found by differentiating Equation 1.4 with respect to $R$, and setting the result equal to 0,

$$R_{crit} = \sqrt{\frac{3R_0^3}{2\sigma}\left(P_0 + \frac{2\sigma}{R_0} - P_V\right)} \tag{1.12}$$

It should be noted that this result assumes isothermal conditions ($\kappa$ = 1). Substitution of this critical radius into Equation 1.4 yields the critical pressure required to generate explosive growth. The Blake threshold pressure, $P_B$ is

defined as the difference between this critical pressure and the original hydrostatic pressure ($P_B = P_0 - P_{L(crit)}$) and hence,

$$P_B = P_0 + \frac{8\sigma}{9}\sqrt{\frac{3\sigma}{2R_B^3(P_0 + (2\sigma/R_B))}} \tag{1.13}$$

There are several important points to be noted regarding this equation. First, the term $R_B$ has been used in place of $R_0$. This ($R_B$) is known as the Blake radius and represents the minimum bubble radius required for explosive growth as defined by the Blake threshold. Second, this equation neglects viscous and inertial effects and hence can only be applied when surface tension dominates and in quasi-static situations. In terms of acoustic cavitation this means that the frequency of the applied sound field must be much lower than the resonance frequency of the bubble. Of course the growth will not continue forever. Rather, the bubble will reach some maximum size and then collapse. The nature of the collapse in terms of the concentration of energy, temperatures generated and bubble wall velocities obtained can all be used to define a threshold for 'transient' cavitation and this is the subject of the following subsections.

### 1.3.2 Flynn's threshold

In a series of papers Flynn [49, 50] considered the collapse of a bubble in terms of energy concentration. It was shown that it is possible to express the acceleration of the bubble wall as the sum of two terms, an inertial function, IF and a pressure function, PF (see Figure 1.3). The IF represents the acceleration due to the force of the converging liquid and the PF is the acceleration due to the combined pressure forces acting on the bubble. During the collapse, PF is initially negative (acting inwards), reaches a minimum and then becomes positive (acting outwards, slowing the collapse). In contrast, IF is always negative and increases in magnitude as the bubble radius decreases. The nature of the collapse is determined by the relative magnitudes of IF and PF. Consider Figure 1.3a and b, which show how the acceleration, IF and PF vary during the collapse of two bubbles, generated by a negative pressure pulse of 5.03 bar and 41.20 bar respectively. In Figure 1.3a the maximum radius of the bubble, $R_{max}$ is 1.46 $R_0$. In this case the acceleration of the bubble wall is dominated by the PF. However, in Figure 1.3b $R_{max}$ is 2.01 $R_0$ and here the IF

is dominant in controlling the acceleration. Near its minimum value, PF is a slowly changing function and if the IF falls below the PF at or near this point the IF will control the collapse (PF cannot respond fast enough to slow the contraction of the bubble). Comparing Figure 1.3a and b, PF is independent of the ratio $R_{max}/R_0$ whereas the intersection of IF with PF depends on the value of this ratio. The value of $R_{max}/R_0$ for which IF intersects PF at its minimum can be termed the critical ratio, $(R_{max}/R_0)_c$. Bubbles, which grow to such a size that $R_{max}/R_0 > (R_{max}/R_0)_c$ will collapse under inertial control and ever increasing amounts of energy will be transferred to the bubble from the converging liquid. Additionally, Flynn considers the dissipation of energy by defining an energy dissipation modulus, $\Delta W/W$ where $\Delta W$ is the work done on or by a bubble during a complete growth and collapse cycle and $W$ is the work done on the bubble by the liquid during the collapse. The value of $\Delta W/W$, which is the fraction of available energy dissipated in a cycle, varies with the ratio $R_{max}/R_0$ but has a maximum value at the so called dynamical threshold, $(R_{max}/R_0)_d$.

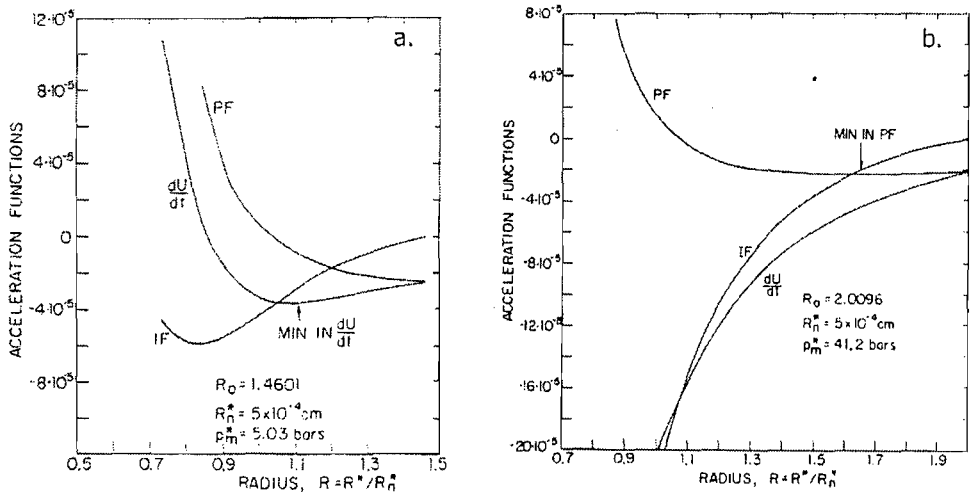


**Figure 1.3** Plots showing the acceleration of the bubble wall (dU/dt), the pressure function and the inertia function for two bubbles. After Flynn [50].

For values of $R_{max}/R_0 > (R_{max}/R_0)_d$ the amount of energy dissipated decreases with increasing $R_{max}/R_0$. If $R_{max}/R_0 > (R_{max}/R_0)_d$ and $R_{max}/R_0 > (R_{max}/R_0)_c$ then ever increasing amounts of kinetic energy is supplied to the bubble from the inertia of the liquid and ever decreasing amounts of energy are dissipated. Flynn suggests that this concentration of energy results in the effects commonly associated with unstable cavitation and that a threshold, $(R_{max}/R_0)_t$ is defined that satisfies these criteria. There are two important conclusions to be drawn

from Flynn's analysis. First, the minimum value of $R_{max}/R_0$ for which a bubble will undergo a violent collapse is approximately 2 and second, such a collapse will be dominated by inertial forces. It has been suggested [51] that events such as these be termed as 'inertial' cavitation rather than 'transient' cavitation in order to avoid any temporal connotations. This is the terminology adopted in this work. Likewise bubble collapses which are controlled by pressure forces are termed 'non-inertial' rather than 'stable'.

### 1.3.3 Holland and Apfel's threshold

Apfel and Holland's [52, 53] approach to estimating the inertial cavitation threshold was to consider a bubble exposed to a single acoustic cycle (see Figure 1.4).

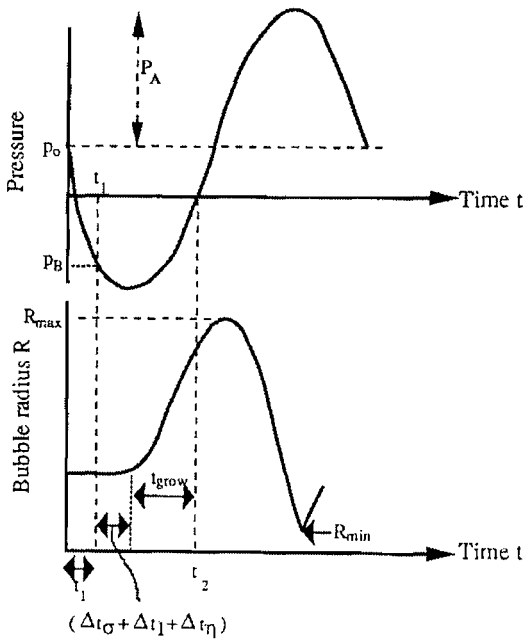


**Figure 1.4** Schematic of the growth and collapse of a bubble subjected to a single pressure cycle. See text for a detailed explanation. Taken from reference [30] (redrawn from reference [53]).

The pressure begins to drop at time, $t = 0$ and at $t = t_1$ the pressure exceeds the Blake threshold, $P_B$ where

$$t_1 = \left(\frac{1}{\omega}\right)\left(\frac{\pi}{2} - \sqrt{2\left(1 - \frac{P_B}{P_A}\right)}\right) \tag{1.14}$$

At $t = t_2$ the liquid ceases to be in tension, where

$$t_2 = \left(\frac{1}{\omega}\right)\left(\frac{\pi}{2} + \sqrt{2\left(1 - \frac{P_0}{P_A}\right)}\right) \tag{1.15}$$

For a time, $t_2 - t_1$ the bubble is subject to a force, which enables the bubble to grow. This force is given by the time averaged pressure difference, $\Delta P$ during this time,

$$\Delta P = \frac{1}{t_2 - t_1}\int_{t_1}^{t_2}(P_A \sin\omega t - P_0)dt \tag{1.16}$$

$$\Delta P \approx \frac{1}{3}(P_A + P_B - 2P_0 + \sqrt{(P_A - P_0)(P_A - P_B)}) \tag{1.17}$$

Although this force acts on the bubble for the duration $t_2 - t_1$ there is a delay, $t_{delay}$ before the bubble begins to grow. This delay, given by Equation 1.18, comprises surface tension ($\Delta t_\sigma$), inertia ($\Delta t_I$) and viscosity ($\Delta t_\eta$) components, which are indicated by the labels below Equation 1.18.

$$t_{delay} = \underbrace{\left(\frac{2\sigma}{P_A - P_B}\sqrt{\frac{3\rho}{2(P_A - P_B)}}\right)}_{\Delta t_\sigma} + \underbrace{\left(\frac{2R_0}{3}\sqrt{\frac{\rho}{\Delta P}}\right)}_{\Delta t_I} + \underbrace{\left(\frac{4\eta}{\Delta P}\right)}_{\Delta t_\eta} \tag{1.18}$$

The time for which the bubble actually grows is therefore given by

$$t_{grow} = t_2 - t_1 - t_{delay} \tag{1.19}$$

The maximum radius the bubble attains is then given by

$$R_{max} = \left(R_0 + \sqrt{\frac{2\Delta P}{3\rho}}t_{grow}\right)\left(\frac{\Delta P}{P_0} + 1\right)^{1/3} \tag{1.20}$$

Apfel [52] then used an expansion ratio of $R_{max}/R_0$ = 2.3 as a definition for inertial cavitation to construct plots, which predict bubble behaviour as a function of the expansion ratio and acoustic pressure. It is important to recognise that the value for the critical expansion ratio of 2.3 is somewhat artificial. It represents the expansive criterion required to generate supersonic bubble wall velocities during the collapse of a cavity in water. Under these conditions the assumption of incompressibility of the liquid becomes invalid and

hence the ratio, $R_{max}/R_o$ = 2.3 reflects the moment at which calculations based on this assumption (see Equation 1.6) break down, rather than being based on fundamental physics of inertial cavitation. Nevertheless it has come into common use and also, as shown above, Flynn has demonstrated that at the expansion criterion of around 2, energy concentration in a collapsing bubble is controlled by the inertial forces, which clearly does reflect the fundamental physics of the process.

Whilst this analysis is based on an expansive criterion, in a later paper Holland and Apfel [53] use temperature based arguments. Assuming an adiabatic collapse it is possible to calculate the maximum temperature, $T_{max}$ generated within the bubble and define an inertial event as one in which $T_{max}$ > 5000 K. This value was found experimentally by Suslick *et al.* [54] using comparative rate thermometry, although it should be noted that other temperatures have been used ranging from 990-5000 K [55]. As with the expansive criterion this is a somewhat artificial threshold, which depends on the value chosen for $T_{max}$.

A comparison of the peak negative pressure, $P_T$ required to meet the expansive and thermal criteria as a function of initial bubble radius is shown in Figure 1.5. This figure was constructed by numerically solving the equations described above. In the region above the curves inertial bubble behaviour is expected, while below non-inertial behaviour exists. For very small nuclei (< 1 μm) the pressure required to force inertial behaviour increases dramatically with decreasing bubble size, because surface tension forces hinder bubble expansion. It is apparent that both the thermal and the expansive criteria show a minimum, which gives the optimum radius for inertial cavitation under these physical conditions to be *ca.* 3-5 μm. For bubbles of this radius the peak negative pressure required to undergo inertial cavitation is of the order of 110-120 kPa. While surface tension effects dominate for smaller bubbles, above this size the pressure threshold gradually rises owing to viscosity and inertial effects associated with the bubble growth.

Included on Figure 1.5 is the Blake pressure (see Section 1.3.1), which demarcates the threshold pressure required for explosive bubble growth but which contains no information on the subsequent collapse. Hence, it can be

thought of as representing the minimum criterion for inertial cavitation (*i.e.* necessary but not always sufficient). It is apparent that the temperature criterion follows this closely until $R_0$ reaches *ca.* 3 μm while the expansive criteria deviates over a larger range of $R_0$.

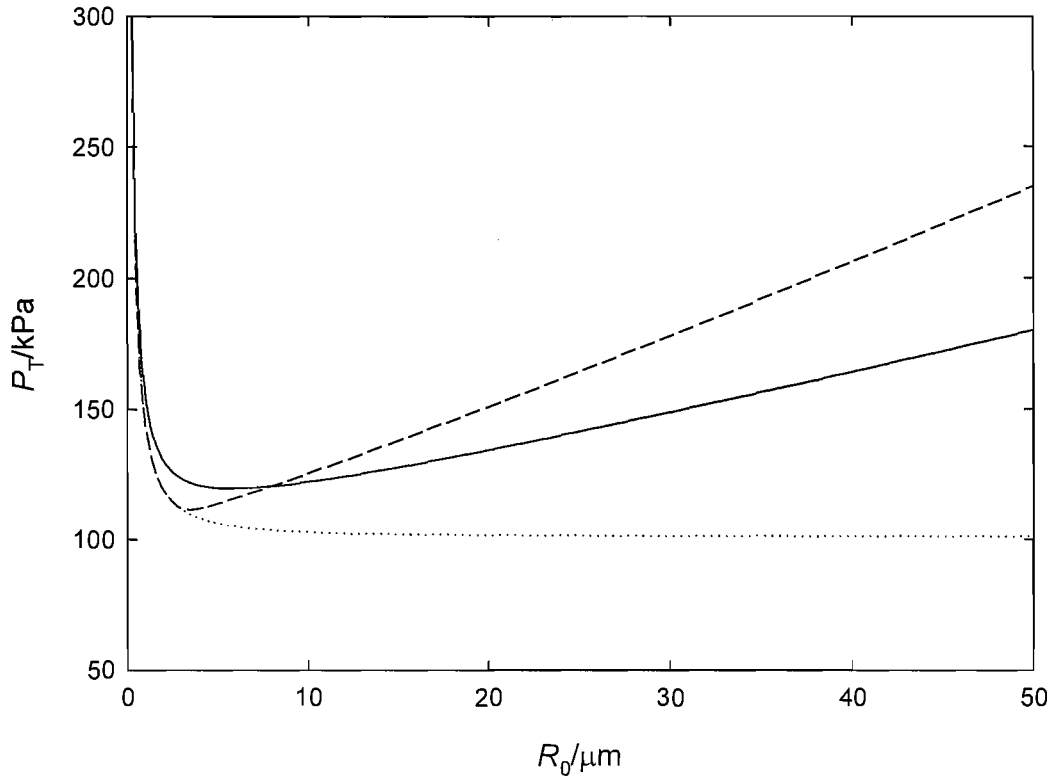


**Figure 1.5** Plot showing the peak negative threshold pressures, $P_T$, for inertial cavitation (or explosive growth in the case of the Blake threshold) as a function of the initial bubble radius, $R_0$. The dotted line (·····) indicates the Blake pressure, (—) the expansive criterion and (- - -) the thermal criterion. The plots were calculated using parameters for air bubbles in aqueous solution at 25 °C and an ultrasonic frequency of 22.8 kHz.

It must be noted that Figure 1.5 is somewhat illustrative when applied in the context of the work presented in this thesis. This is for a number of reasons. First, Holland and Apfel's threshold calculation applies to isolated bubbles, subjected to a single acoustic cycle. This is far removed from the multibubble, continuous wave work reported here. Second, both the expansive and thermal criteria represent relatively ill defined, artificial thresholds based on either the breaking down of theory or indirectly measured parameters respectively. While this highlights an important point: the inertial/non-inertial threshold is extremely blurred, the pressure threshold calculation is still worthwhile. Firstly, the prediction of a threshold of the order of 1 bar is consistent with previous work

[56]. Also, Figure 1.5 is informative in showing the range of bubble nuclei with the possibility of undergoing inertial cavitation. As the pressure increases then the range of possible nuclei increases. This implies that two phenomena, the increased violence of collapse and the increased number of possible events, are associated with increases of the driving pressure above the threshold required to generate inertial cavitation effects. Higher amplitude driving fields may therefore generate increased effects associated with inertial cavitation. These effects and their detection using electrochemical and luminescence techniques (a key part of the work described in this thesis) are discussed in Sections 1.5, 1.6 and 1.7. However, in the next section an important phenomenon associated with non-inertial bubble oscillation, namely surface waves, is introduced.

## 1.4 Departure from spherical symmetry: Surface waves

In the preceding sections the bubble was assumed to be isolated and retain spherical symmetry. Under small amplitude oscillation, these symmetric pulsations represent zero-order spherical harmonic motion, known as the breathing mode. However, an oscillating bubble can depart from spherical symmetry owing to the onset of higher order modes (>1) known as surface waves[1]. Surface waves on a plane interface were first reported by Faraday [57], who observed the oscillations formed on the free surface of vertically vibrated water. Subsequently, surface waves were observed on the surface of bubbles, which were acoustically driven [58]. These waves are a threshold phenomenon, which occurs when the amplitude of oscillation of the liquid/gas interface exceeds a certain value. For a spherical cavity the theoretical wall displacement amplitude, which is required, was first derived by Francescutto and Nabergoj [59] and is given by,

$$C_t = \sqrt{\frac{(a-1)^2 + 4g}{\left(2g - \frac{3a}{2} + 2n + 1\right)^2 + q^2}} \tag{1.21}$$

where $n$ is the integer value of the mode of interest and,

[1] The first order mode corresponds to translation of the entire bubble.

$$a = \frac{4(n-1)(n+1)(n+2)\sigma}{\rho\omega^2 R_0^3} \tag{1.22}$$

$$g = \left[\frac{(2(n+2)(2n+1))\eta}{\rho\omega R_0^2}\right]^2 \tag{1.23}$$

$$q = \frac{6(n+2)\eta}{\rho\omega R_0^2} \tag{1.24}$$

The threshold acoustic pressure amplitude required to generate surface waves is then given by [60],

$$P_{T(surface)} = R_0^2 \rho C_t \sqrt{\left(\omega_0^2 - \omega^2\right)^2 + \left(\omega^2 d_{tot}\right)^2} \tag{1.25}$$

Included in Equation 1.25 is a dimensionless damping coefficient, $d_{tot}$, which is the sum of radiation ($d_{rad}$), viscous ($d_\eta$) and thermal ($d_{th}$) damping constants [61], which are indicated by the labels below Equation 1.26.

$$d_{tot} = \underbrace{\frac{\rho(R_0\omega)^3}{3\kappa P_0 c}}_{d_{rad}} + \underbrace{\frac{4\eta\omega}{3\kappa P_0}}_{d_\eta} + \underbrace{\frac{1.2\{\Gamma[\sinh(\Gamma)+\sin(\Gamma)]-2[\cosh(\Gamma)-\cos(\Gamma)]\}}{\Gamma^2[\cosh(\Gamma)+\cos(\Gamma)]+1.2[\sinh(\Gamma)-\sin(\Gamma)]}}_{d_{th}} \tag{1.26}$$

where,

$$\Gamma = R_0\sqrt{\frac{2\omega C_{p(g)}\rho_g}{K_g}} \tag{1.27}$$

and $C_{p(g)}$ is the specific heat capacity of the gas in the bubble at constant pressure, $\rho_g$ is the density of the gas in the bubble and $K_g$ is the thermal conductivity of the gas in the bubble. The surface wave mode for which $P_{T(surface)}$ is a minimum is known as the Faraday wave, which oscillates at half the driving frequency. As the acoustic pressure amplitude is increased additional modes can be excited at other frequencies.

## 1.5 The physical effects of sonication

In this section some of the important mechanisms, which result from sonication and cavitation, and lead to observable physical effects are introduced. The detection of these effects through the use of electrochemical sensors and

luminescence techniques, which comprises a key component of the work presented in this thesis, is described in subsequent sections.

### 1.5.1 Acoustic streaming

Acoustic streaming is the macroscopic flow of liquid due to the attenuation of a sound wave travelling through a fluid. The attenuation results in a pressure gradient and consequently fluid motion in the same direction as the sound wave propagation. Assuming plane waves, the attenuation can be described by the following equation,

$$\left(\frac{I_h}{I_0}\right) = e^{-2\alpha h} \tag{1.28}$$

where $I_0$ is the initial intensity of the wave, $I_h$ is the intensity after a distance, $h$ and $\alpha$ is the attenuation coefficient. For bubble free water at 25 °C, $\alpha$ = 1.16 x $10^{-7}$ neper $cm^{-1}$ at 23 kHz, varying with approximately the square of the frequency up to 1 MHz. Sonoelectrochemical results have suggested streaming speeds of up to 10 cm $s^{-1}$ close to the tip of an ultrasonic horn [62].

### 1.5.2 Microstreaming

A second type of streaming process can occur near small obstacles (such as bubbles) placed in a sound field. Frictional forces at the boundary lead to circulation of fluid in a small (often microscopic) layer, which is termed microstreaming. Elder [63] studied the flow patterns near a bubble, which was on the upper surface of a 10 kHz transducer through the use of a suspension of aluminium dust. Four distinct patterns were observed, shown in Figure 1.6. The type of microstreaming observed depends on the viscosity, acoustic pressure amplitude as well as other factors and is summarised below:

Type a: Observed in low viscosity liquid at low pressure amplitude if the surface of the bubble is contaminated.

Type b: Observed over a wide range of viscosities and pressure amplitudes.

Type c: Observed coincident with the onset of the first surface mode (see Section 1.4). Usually seen in low viscosity liquids but can be observed in liquids of higher viscosity if the pressure amplitude is great enough.

Type d: Observed under conditions of high pressure amplitude and low viscosity, which allow more than one surface mode to be excited.

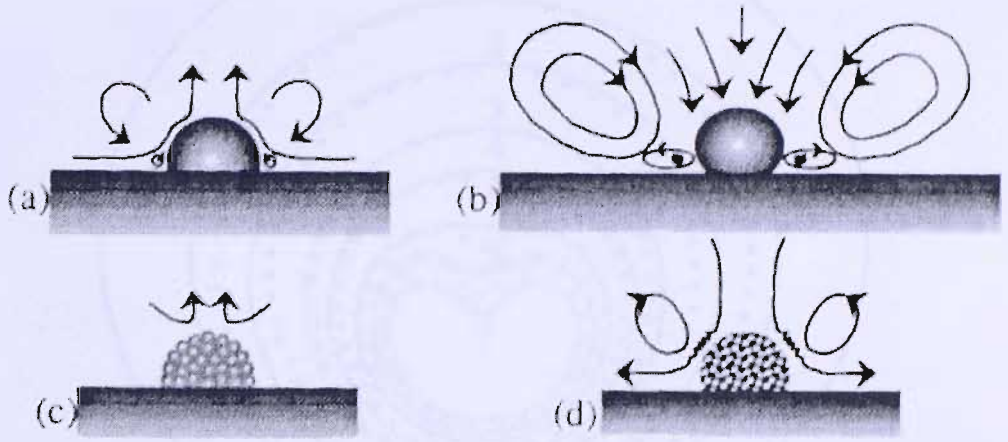


**Figure 1.6** Schematic representation of the four types of microstreaming identified by Elder [63]. Taken from a re-drawing by Leighton [30].

### 1.5.3 Microjetting

When a bubble collapse occurs near a solid boundary, inhibited fluid flow can lead to an asymmetric collapse and the formation of a microjet towards the surface. Microjets are one of the mechanisms for cavitation-induced erosion; the high-speed liquid jet impacts on a surface leaving characteristic 'pits' that are approximately one-tenth the radius of the original cavity [64-66]. Neppiras [31] studied the collapse of an initially spherical bubble in water generated by laser action in the vicinity of a solid boundary by employing high-speed photography (305,000 f.p.s). Under these conditions jetting first occurs towards the solid boundary and on the rebound a counter jet is formed. After that the bubble disintegrates. Lauterborn *et al.* [67, 68] also investigated liquid jets using high-speed photography following the generation of a single cavity by laser action. Jets with velocities of 120 m $s^{-1}$ were observed. This experimental work enabled numerical calculations of bubble collapse near a solid boundary to be confirmed experimentally. Figure 1.7 shows the agreement between the theory developed by Plesset and Chapman [69] and the experimental work by Lauterborn and Bolle [68]. The jet may traverse the bubble interior, to penetrate the remote bubble surface. A picture of this effect, taken by Crum is shown in Figure 1.8.

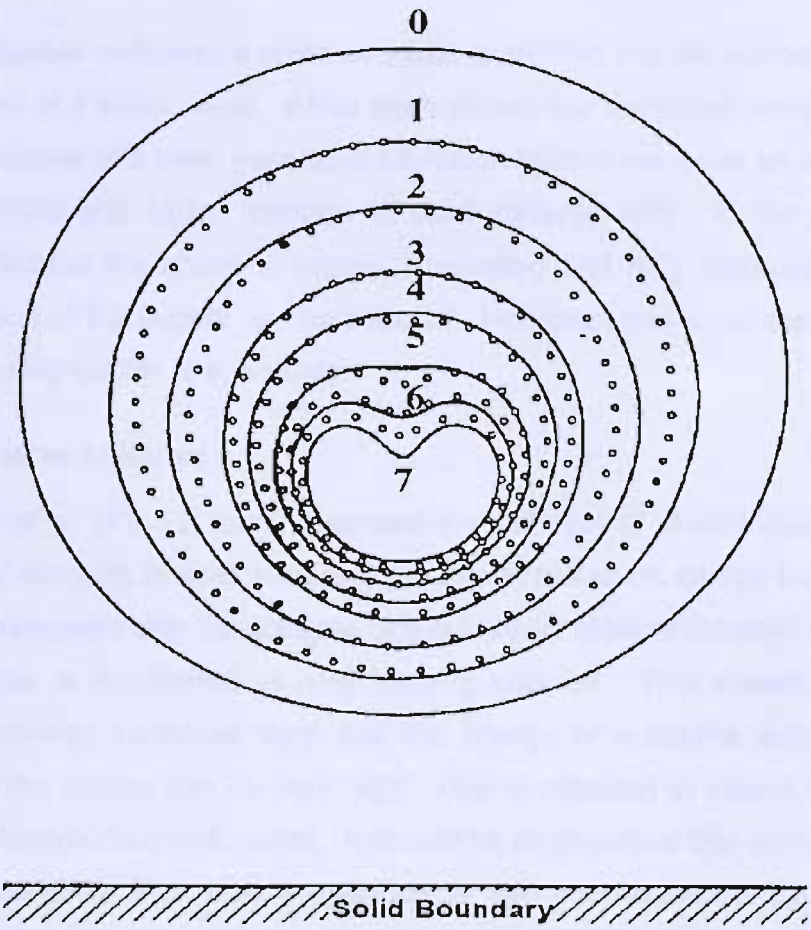


**Figure 1.7** Plot showing the comparison of experimentally determined bubble shapes on collapse (o) (After Lautherborn and Bolle [68]) of a spherical bubble near a plane solid wall with theoretical curves taken from Plesset and Chapman [69] (—). Lautherborn and Bolle's experimental analysis employed a framing rate of 305,000 f.p.s. The initial bubble radius was 2.6 mm and the distance of the bubble centre from the wall was 3.9 mm.

**Figure 1.8** Jet formation during the collapse of an oscillating gas-vapour bubble at low pressure (0.04-0.05 bar) in a 60 Hz sound field. The bubble size is approximately 0.2 cm (published in reference [70]).

### 1.5.4 Shock waves

When a bubble collapses a pressure pulse is emitted into the surrounding liquid in the form of a shock wave. It has been shown that the shock wave generated by the collapse of a laser generated cavitation bubble can have an amplitude of up to 1 GPa and cause damage to solid surfaces [67]. In the case of an isolated bubble the shock is rapidly attenuated and only surfaces within the initial radius of the bubble can be affected. However, this is not the case when the collapsing bubble is in a cluster.

### 1.5.5 Cluster collapse

Hansson *et al.* [71, 72] have described the concept of cluster collapse in the context of damage to solid surfaces in a model based on energy transfer. The energy associated with the collapse of a bubble (or shell of bubbles) at the edge of a cluster is transferred to neighbouring bubbles. This inward transfer of collapse energy continues such that the energy of a bubble collapse in the centre of the cluster can be very high. This is reflected in violent microjetting and high amplitude shock waves. It should be emphasised that damage to solid surface resulting from cluster collapse is still attributable to the effects of individual bubbles (microjets and shock waves) but the magnitude of the effects are amplified by the nature of the cluster collapse.

## 1.6 Detection of the effects using electrochemistry

In the previous section the physical effects of sonication and acoustic cavitation were discussed. The subject of this section is the detection of these processes through the use of electrochemical techniques. In terms of detection, the effects seen can be broadly categorised in two ways. First, those which affect the mass transfer of electroactive species to the electrode and second, those which lead to erosion of the electrode or other surface effects. It should be noted that detection of radical species generated from the extreme conditions prevalent during an inertial collapse is also possible using electrochemical techniques [42, 43, 73]. However, this work is concentrated on detection of the physical effects (fluid flow, surface erosion, *etc*).

### 1.6.1 Mass transfer

The enhancement of mass transfer is an important aspect associated with the use of ultrasound in electrochemical processes. Bard [74] investigated the

employment of ultrasound as a mass transfer enhancement tool as early as 1963. Also in the 1960s, Nyborg *et al.* [75, 76] employed electrochemical techniques to study acoustic streaming processes using oscillating electrodes and arrays of electrodes. More recently, there have been a number of noteworthy studies. Zhang and Coury [77] were one of the first to report the most common experimental arrangement employed for the investigation of sonoelectrochemical effects. In a subsequent pioneering paper which employed the same experimental geometry [78], the mass transfer effects of an operating ultrasonic horn placed above an electrode were investigated. Other investigators have adopted this experimental approach and developed important refinements on the operation and geometries employed. A review by Compton *et al.* [79] gives details of a number of studies investigating the effects of coupling ultrasound to electrochemistry and its effects on the mass transfer characteristics of the system. In all cases a horn-type transducer was used, operating at a fixed frequency (~20 kHz). A number of different electrochemical systems have been studied using various electrode geometries, which will now be discussed.

Klíma *et al.* [80, 81] studied the effect of ultrasound on the reduction of methylviologen in 9:1 acetonitrile and water with 0.1 M $Bu_4NPF_6$ as a supporting electrolyte. A 'face on' geometry was employed, in which the surface of the working electrode was parallel with the faceplate of the horn. Platinum working electrodes (0.5 mm diameter) were used and a working distance (electrode to tip of the ultrasonic horn) of 20 mm. An increase in the cathodic current was observed, which was characterised by large current spikes, superimposed on an increased background current. The individual peaks in current were attributed to the inertial collapse of a cavitation bubble. However, while the acoustic pressure was estimated from calorific measurements, no attempt was made to determine the acoustic pressure amplitude at the electrode surface and as a result it is hard to justify such a conclusion. Non-inertial cavitation and the motion of large gas bubbles were considered as mechanisms for the current enhancement but these are neglected for reasons, which are not made clear. Similar results have been obtained for various aqueous and non-aqueous systems, employing different electrode materials and working distances in the face on arrangement. For example, the oxidation of ferrocene in various

organic solvents [82, 83], the reduction of $Ru(NH_3)_6^{3+}$ in KCl [83, 84] and the reduction of nitrotoluene in liquid ammonia [83] have all been studied. In all cases the effect of sonication is to enhance mass transfer in a quasi-steady state fashion, resulting in elevated background currents superimposed with transient current spikes. The increased background current is attributed to acoustic streaming while the transient component is considered to be the result of microjetting. However, it should be noted that mass transfer is sensitive to any hydrodynamic process and hence microstreaming, stable bubble oscillation and the motion of gas bubbles will also contribute to the effects seen.

In an alternative geometry, Reisse and co-workers [85] employed the titanium horn itself as a working electrode. Compton *et al.* [86] introduced a modified version of this by altering the titanium tip of the horn to enable the insertion of a platinum disc (so called Pt sonotrode). The reduction of *p*-benzoquinone in KCl and the oxidation of ferrocene in acetonitrile were studied. The magnitude of the limiting currents obtained was substantially larger than experiments where the horn is positioned above the working electrode. However, it was found that the robustness of such a system was severely limited as a result of electrode erosion. Another alternative geometry is a side on approach, whereby the electrode is placed perpendicular to the horn [87, 88]. However, the face on geometry has become commonplace.

A major limitation of a number of these studies is the size of the working electrode employed. Macroelectrodes lack the spatial resolution to discriminate individual cavitation event and as result a spatially-averaged response is seen. The use of microelectrodes can help to alleviate this problem. The employment of microelectrodes in a fluid, which is undergoing cavitation, has several key advantages. First, microelectrodes can be fabricated down to the nm length scale and hence are small in comparison to cavitation events. Individual bubbles above the electrode may shield it from other events, which occur within the same cavitation bubble cloud at the same instant. Information may therefore be discerned on the basis of an individual event rather than in a spatially averaged sense. Second, microelectrodes have fast diffusion field relaxation enabling the measurement of individual mass transport events at high temporal resolution. Birkin and Silva-Martinez were the first to demonstrate the use of

microelectrodes for the study of mass transfer enhancement [41, 89, 90]. Using a combination of small (6-25 μm diameter) electrodes and fast data acquisition it was shown that individual current transients could be detected when the electrode was held at a mass transfer limiting (MTL) potential. Very small working distances were used (< 2 mm) and a high degree of control of this distance was advocated. The large current transients were attributed to forced convection caused by individual microjets. In a series of interesting papers [91-93], microelectrode arrays have been employed to study the dynamics of a non-inertial cavitation bubble on the surface of an electrode. In contrast to the single current transients reported previously, periodic enhancement was seen, which was interpreted as a hemispherical bubble blocking and unblocking the electrode. When a bubble blocks the electrode the current falls to nearly zero as the electroactive material in the layer of liquid between the bubble and the electrode is depleted. The bubble then moves away and the solution is refreshed leading to a large current spike, which decays back to zero when the bubble returns. Oscillation of the bubble leads to continuous blocking and unblocking of the electrode and a periodic signal.

### 1.6.2 Erosion

While mass transfer is sensitive to a myriad of hydrodynamic process, erosion of an electrode surface can only be caused by high energy events associated with inertial cavitation (microjets and shock waves). Although the effects of ultrasound on electrode surfaces have been relatively widely studied [77, 94-97], there has been little *in-situ* electrochemical work published. Perusich and Alkire [94, 95] used passivated iron electrodes to detect surface erosion due to exposure to ultrasound. While this work is noteworthy, the large size of the electrode (6 mm diameter) limited the spatial and temporal resolution of the technique and an averaged response was seen. The first spatially and temporally resolved study was made by Birkin *et. al.* [98] using passivated lead microelectrodes. It was shown that by employing fast data acquisition it is possible to detect the erosive effects, which were attributed to individual cavitation events. These were detected as current transients due to spontaneous repassivation of the electrode surface, which was held at +0.5 V *vs.* SCE in a solution of 1 M $H_2SO_4$.

## 1.7 Luminescence effects

There are other observable effects associated specifically with cavitation, which can be used in conjunction with the electrochemical techniques described above for studying the effects of sonication.

### 1.7.1 Multibubble sonochemiluminescence (MBSCL)

Chemiluminescence can be defined as the emission of light as a result of the generation of electronically excited states formed by a chemical reaction. It is well known that alkaline solutions of luminol emit light when submitted to ultrasound of sufficient intensity to produce inertial cavitation. This is an oxidative chemiluminescent process involving sonochemically generated $OH^{\bullet}$ and other radical species. It is in essence a trapping system for hydroxyl radicals, generated during the violent collapse. The proposed mechanism is illustrated in Figure 1.9.

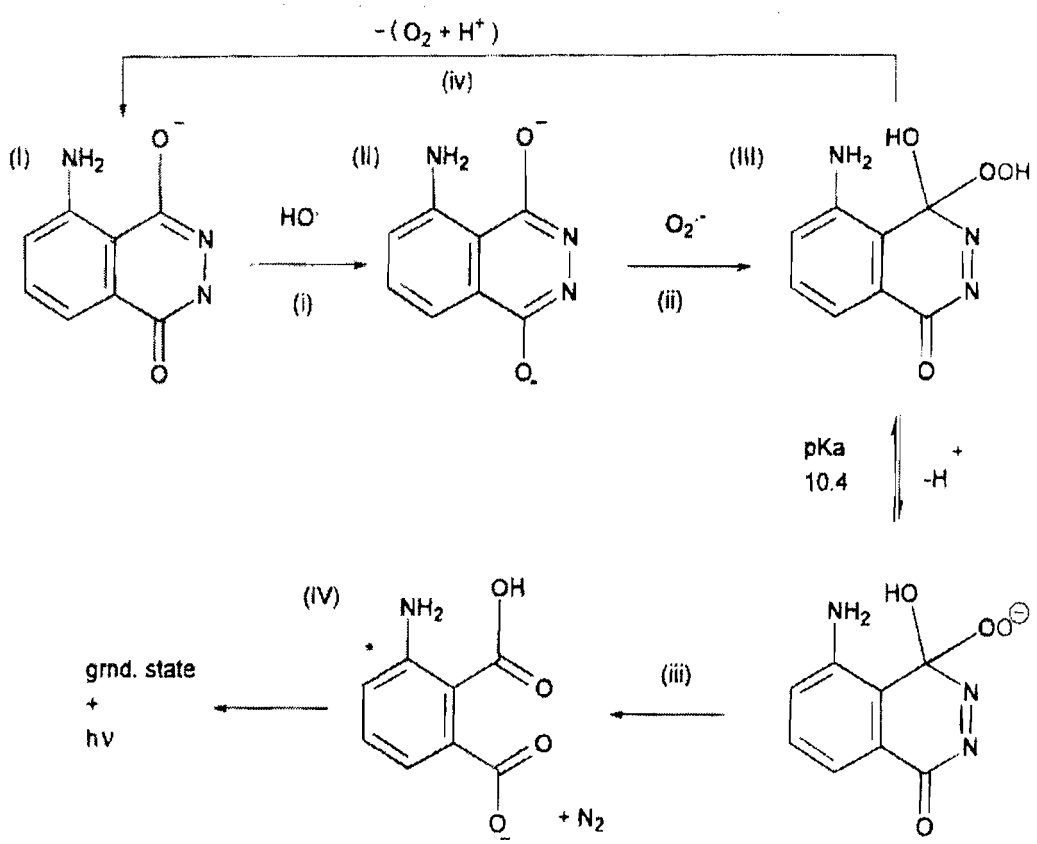


**Figure 1.9** Proposed mechanism for the chemiluminescence of luminol (After McMurray *et al.* [99]).

Previous studies [99, 100] have shown that the process is most efficient at high pH, and that the emission of light is strongly influenced by $H_2O_2$ concentration. The study of sonochemiluminescence of luminol in the presence of $H_2O_2$ is potentially complicated by a background non-sonochemical process of chemiluminescence catalysed by divalent metal cations. A chelating agent (EDTA) is used to bind the metal cations that may be introduced into the solution by leeching from equipment or from impurities in reagents and thus prevent this non-sonochemical background reaction. The addition of $H_2O_2$ to the solution generates the $O_2^{\bullet-}$ radical species required for reaction (ii) in Figure 1.9. The majority of sonochemiluminescence reported is related to multibubble cavitation systems [73, 99, 101, 102] and is termed multibubble sonochemiluminescence (MBSCL). Sonochemiluminescence has been observed for a single bubble [103]. However, all the work presented in this thesis was carried out under multibubble conditions. Whilst sonochemiluminescence produces light from cavitation, the origin of the light is chemical in nature. Light emission from cavitation itself is also possible and is discussed in the following section.

### 1.7.2 Multibubble sonoluminescence (MBSL)

Sonoluminescence is a process which has been studied for 70 years. The phenomenon was discovered in 1934 when Frenzel and Schultes [104] exposed a photographic plate to acoustic waves generated in a water bath. A darkening of the plate was observed, which was attributed to luminescence from the sound field. It is now known that rather than the sound field itself, it is the cavitation process that generates light. When the acoustic pressure amplitude exceeds the inertial cavitation threshold and the liquid cavitates, light is emitted. In multibubble system, many individual cavitation events occur, each emitting a discrete burst of light. This is termed multibubble sonoluminescence (MBSL). It is also possible to observe sonoluminescence from a single bubble [105], which is called single bubble sonoluminescence (SBSL). There is much debate over the actual mechanism for light emission in sonoluminescence. A number of theories have been proposed including thermal [106], mechanochemical [107-109] and electrical [110, 111]. However, detailed discussion of these is beyond the scope of this work and interested readers are directed to a number of review papers in the literature [112-114].

## 1.8 Inertial cavitation as a tool for the study of surface processes

Thus far the discussion has focused on the dynamics of cavitation, its physical effects and the detection of these effects through the use of electrochemical and luminescent techniques. Largely as a result of the extreme physical conditions generated during cavitation, ultrasound has become a useful tool in many applications. A number of examples were given at the start of this chapter. Part of the work presented in this thesis aimed to investigate the use of ultrasound in a novel function, namely to study industrially relevant surface processes. Two particular systems are of interest. First, the passivation of technologically important metals, such as stainless steel and second the performance of corrosion inhibitors in extreme environments, where cavitation may be present. The remainder of this chapter is dedicated to an introduction to these systems.

## 1.9 Passive films on metals and alloys

Passive oxide films on many metals and alloys are crucial in terms of corrosion protection. However, the formation of such films is inherently difficult to study owing to the formation of the passive film at very low potentials. This can make the deconvolution of the film formation from hydrogen evolution difficult. In order to study the formation of the passive film, it is necessary to expose the bare metal surface very rapidly under electrochemical control. One of the aims of the work presented in this thesis was to investigate the feasibility of using inertial cavitation as a tool for this purpose, as it may offer significant advantages over traditional techniques. The potential advantages are discussed in more detail in Chapter 6. However, the current mechanical techniques are considered in the following section.

### 1.9.1 Current experimental techniques

#### Scratched electrode

The scratched electrode technique involves the use of a stylus to remove the surface film from the electrode. Ford *et al.* [115] were the first to describe the most common system, in which a rotating electrode under potential control is impinged upon by a diamond stylus. The stylus is removed from the surface of the electrode by an electromagnet after approximately 1 ms resulting in a shallow arc of bare metal with an area of ~4 × $10^{-4}$ $cm^2$. This technique (and

other variations) have been widely used by a number of workers studying a variety of metal systems [116-121]. However, its application is limited for a number of reasons. The long contact time between the stylus and the electrode surface means that it is impossible to study the initial stages of film growth. Also, the sequential nature of the metal exposure complicates the analysis. The metal surface exposed at the start of the scratch undergoes passivation, while at the same time a fresh metal surface is produced at the end of the scratch. In addition to these temporal issues, that area exposed is relatively large, leading to high currents and consequently large losses due to iR drop.

**Guillotined/breaking electrode**

The guillotined electrode technique has been described in detail by Burstein and co-workers [122-126]. The experimental apparatus consists of a spring loaded, boron nitride tipped guillotine blade, which is used to cut an electrode to expose a disc of bare metal. The electrode is constructed by sealing a wire of the test metal in an insulating material (generally epoxy resin). It is estimated that the time taken to expose the electrode surface is of the order of 100 μs. Also, a system has recently been described, which allows a flow of electrolyte over the freshly guillotined electrode [127].

An alternative approach is to use a thin film breaking electrode technique, which has been described by Frankel *et. al.* [128, 129]. In summary, a strip of Al (6.35 mm wide) was sputtered onto an insulated Si wafer to form a thin (0.15 μm) layer, which was then coated with an insulating layer of $Si_3N_4$. This was clamped in an electrochemical cell and broken through tapping with a Plexiglas plunger. The use of Si wafers ensured that the break was reproducible and resulted in an area of exposed Al of approximately $1 \times 10^{-5}$ $cm^2$. By assuming that crack propagation in the Si wafer occurs at 3000 m $s^{-1}$ it is estimated that the bare metal is exposed in as little as 2 μs. The breaking electrode technique is perhaps the best method for studying the initial stages of metal passivation because of the rapid exposure of small areas of bare metal. However, there are a number of drawbacks. As with the other techniques described in this section, it is a relatively complex procedure, which limits the amount of data, which can be collected. Also, it is limited to systems in which the test material can be sputtered onto the Si wafer.

Following the exposure of a fresh surface (by whatever means) the metal (held at an appropriate potential) undergoes spontaneous repassivation. There are two major mechanisms for the growth of thin oxide films, which are discussed in the following section.

### 1.9.2 Models for passive film growth

If it is assumed that the surface film is thin and the potential drop at the solid/liquid interface occurs across the film then the growth of the passive film occurs under high electric field conditions. There are two major models for the growth of oxide films under high electric fields; ion migration and place exchange.

#### Ion migration

Under the ion migration model originally proposed by Cabrera and Mott [130], growth occurs *via* the migration of cations across the film. Although a number of refined theories exist [131, 132] all can be represented (or approximated) by:

$$i = A\exp(BF_E) \tag{1.29}$$

where $F_E$ is the electric field strength over the oxide film and $A$ and $B$ are constants related to the film properties. The electric field strength is inversely proportional to the film thickness, which assuming that there is no dissolution can be related to the charge consumed during the formation. Growth according to Equation 1.29 is self-limiting; $F_E$ is lowered as the film thickness increases (for a constant voltage across the film).

#### Place exchange

This mechanism is fundamentally different to ion migration. It proposes that the film growth process is limited by an increased activation energy associated with the growth process as the film thickens. Following Lanyon and Trapnell [133], Sato and Cohen [134] proposed a place exchange mechanism for the growth of passivating oxide films on iron in neutral solutions. This mechanism has also been suggested by a number of other authors [135-137]. Such a mechanism, illustrated schematically in Figure 1.10, involves the adsorption of oxygen onto the metal surface followed by a place exchange, possibly by rotation with the underlying metal. A second layer of oxygen then adsorbs and two M-O pairs exchange places simultaneously. This process then repeats to continue film

growth. However, this is only physically realistic for the first few atomic layers after which the activation energy required for further growth becomes excessive [121].

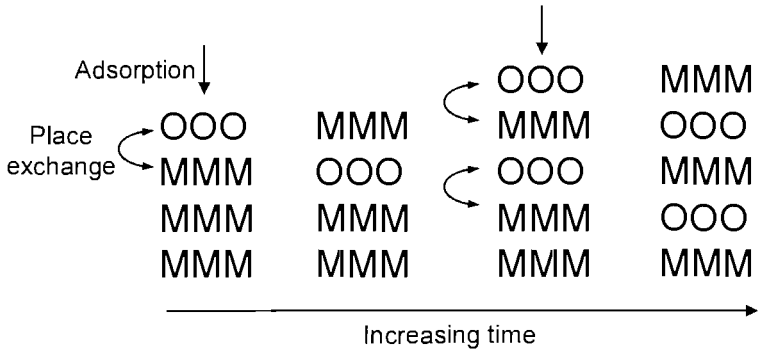


**Figure 1.10** Schematic showing the mechanism proposed under place exchange oxide growth.

## 1.10 Corrosion inhibitors

Although the passivity of metals and alloys is an attractive property in terms of corrosion protection, often metals which exhibit the phenomenon are not suitable for large scale applications owing to excessive cost. In cases in which metals are in contact with solution (particularly closed systems) the addition of chemicals designed to inhibit the corrosion process is an attractive alternative. Corrosion inhibitors can be organic or inorganic species and may inhibit the anodic, cathodic or both corrosion reactions. They can function through adsorption onto the surface or by promoting the formation of protective precipitates on the metal. Examples of the former include aromatic and aliphatic amines [138-144], various sulphur containing compounds [145-149] and carbonyl molecules [150, 151] while inorganic anions [152-156] ions act in the latter fashion. In many cases corrosion inhibitors are deployed in applications where they may be exposed to hydrodynamic cavitation. However, there has been little work published on the effect of cavitation on their performance. The most notable work has been carried out by Petersen *et al.* who have studied the sweet corrosion of carbon steel under various flow and/or cavitation conditions in the presence and absence of corrosion inhibitors [157, 158].

## 1.11 Summary of work presented

The primary aim of the work presented in this thesis was to study surface reformation under potential control in the presence of inertial cavitation. The

approach used may be termed as acoustoelectrochemical: a combination of electrochemical (and other) techniques with detailed consideration of the acoustic properties of the experimental set-up. In the first part of this thesis the sound field and cavitation generated by the ultrasonic horn is characterised. Following this, the well understood system is used to study industrially relevant processes.

Chapter 2 details the experimental techniques and procedures used throughout the work presented in the subsequent chapters.

Chapter 3 gives details of a novel lead/platinum dual microelectrode, which is an excellent sensor for studying the effects of sonication.

Chapter 4 discusses the sound field generated by a horn-type transducer, the extent of the effects of inertial cavitation and explores the effect of the electrode on the sound field.

Chapter 5 is dedicated to the correlation of the physical effects observed during sonication with bubble dynamics. Electrochemistry, acoustics, high-speed photography and laser scattering are used in conjunction with each other to give valuable insights into the behaviour of cavitation bubbles.

Chapter 6 uses conclusion drawn in Chapter 4 and 5 to put inertial acoustic cavitation into work as an effective tool for studying surface processes. Two commercially important processes, passivation of stainless steel and surface active corrosion inhibition are probed.

Chapter 7 draws together general conclusions about the four preceding chapters.

# Chapter 2 Experimental

The results and conclusions presented in this thesis were obtained from a combination of electrochemical, acoustic and luminescent techniques, high-speed video and laser scattering experiments. This chapter gives details of the experimental procedures, which were used in the work.

## 2.1 Generation of ultrasound

Ultrasound and cavitation were generated by means of a Grundig Digimess FG 100 function generator, Brüel & Kjær Type 2713 power amplifier and ultrasonic transducer fitted with a 3 mm diameter titanium tip (Adaptive Biosystems). The function generator was interfaced with a PC using software written in-house, allowing the frequency, power and duration of the ultrasound to be accurately controlled. The nominal frequency of the ultrasound was ~23 kHz. The exact details of the conditions employed are given in the appropriate figure legends.

## 2.2 Electrochemical experiments

### 2.2.1 General experimental set-up

The experimental set-up for all acoustoelectrochemical experiments is shown in Figure 2.1. The working electrode was inserted in the bottom of the electrochemical cell, which itself was placed on an XY stage (Photon Control). The stage allowed 25 mm of movement in each direction with 0.01 mm resolution, enabling the position of the working electrode to be accurately controlled in a plane below the tip of the ultrasonic horn. The position of the horn was fixed in the XY plane but controlled in the Z direction by means of a micrometer and stage (Newport), which allowed 25 mm of movement with 0.02 mm resolution. This allowed the separation between the surface of the working electrode and the tip of the ultrasonic horn to be controlled with a high degree of precision. This is key to obtaining reproducible results from acoustoelectrochemical studies.

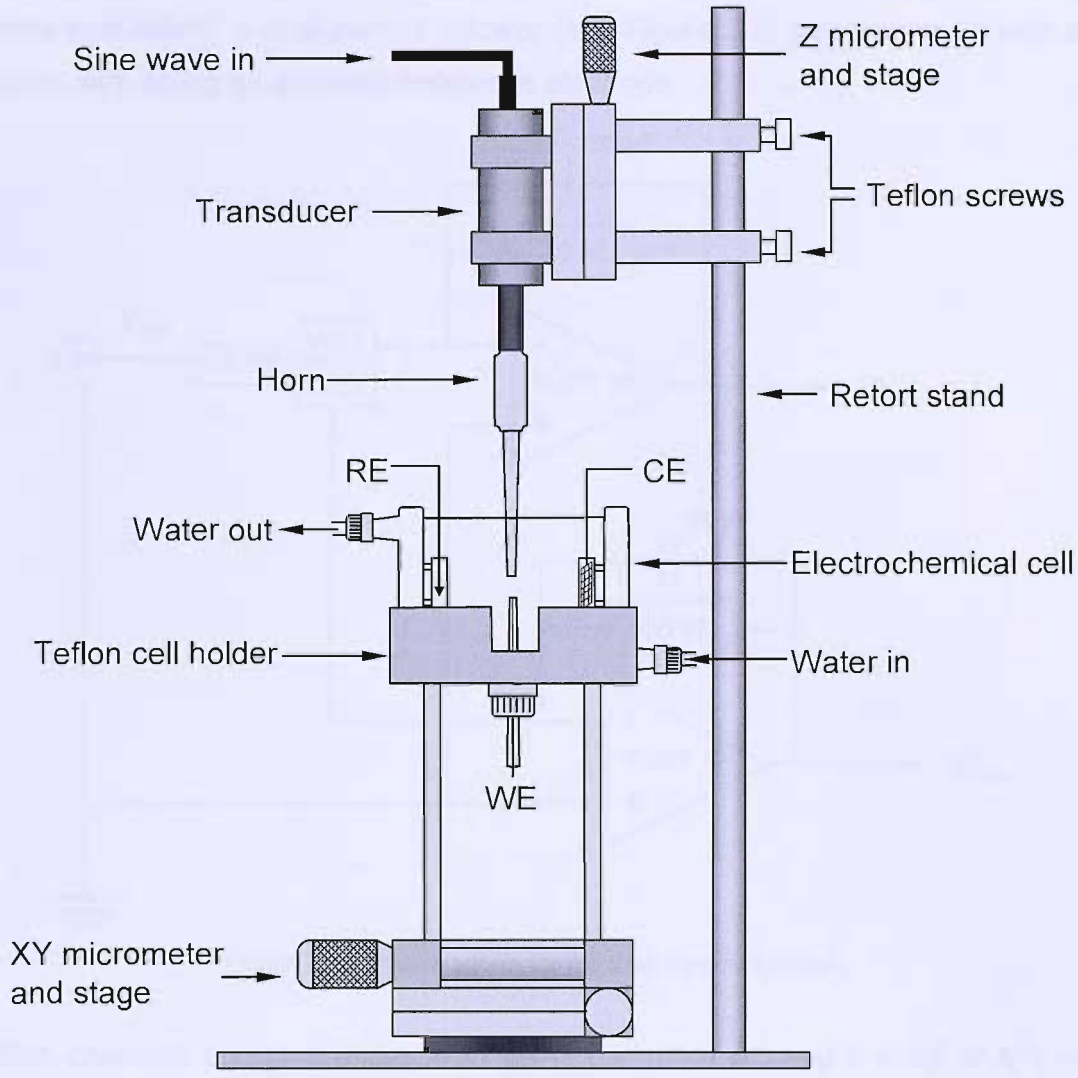


**Figure 2.1** Experimental set-up for acoustoelectrochemical experiments.

### 2.2.2 Electronics and data acquisition

Two types of acquisition electronics employed. For general electrochemical experiments, such as cyclic voltammetry, a potentiostat built in house was employed utilising a three electrode set-up. This was also used for acoustoelectrochemical experiments involving only one working electrode. In these cases the reference electrode was a home made saturated calomel electrode (SCE), prepared in the usual way [159] and the counter electrode was a platinum mesh. The potential of the reference electrodes were measured against a commercial SCE (Asea Brown Boveri) and used only if they were found to be within ± 2 mV.

For experiments involving dual electrodes (and hence the use of synchronous data acquisition) a dual current follower (see Figure 2.2) was employed with a silver wire acting as a counter/reference electrode.

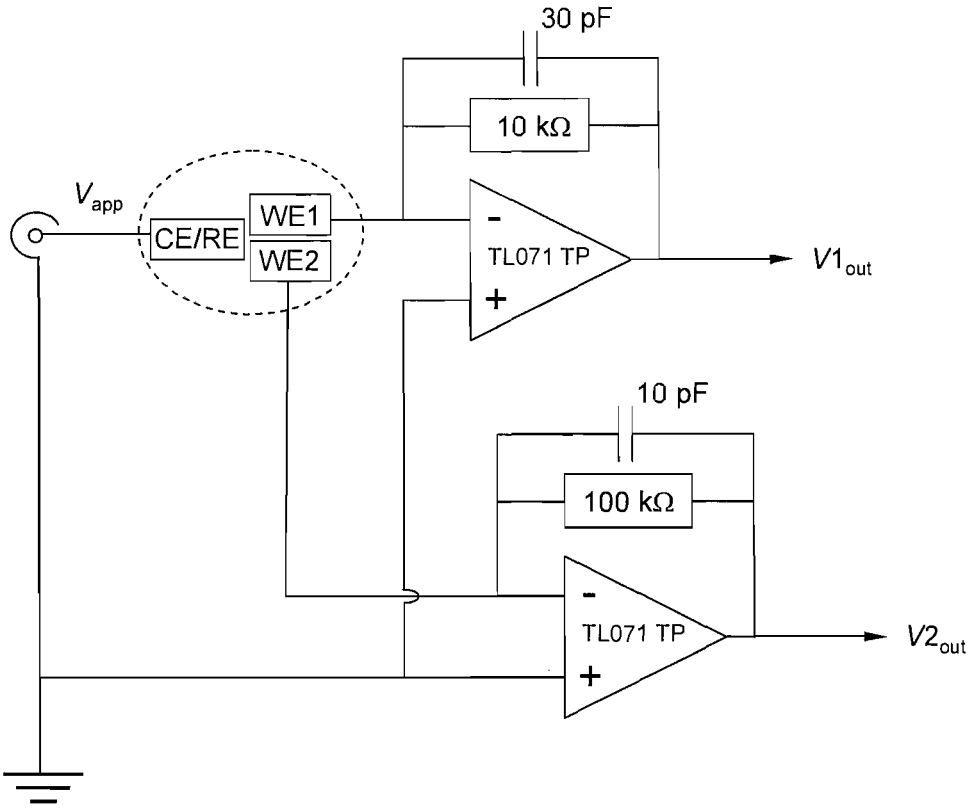


**Figure 2.2** Circuit diagram for the dual current follower.

Both channels operated under fixed gain ($1 \times 10^4$ V $A^{-1}$ and $1 \times 10^5$ V $A^{-1}$) in order to eliminate electronic coupling, which was found to be a major problem if any switches were used. In order to eliminate oscillations a small amount of capacitive damping was used (10 pF for the low gain channel and 30 pF for the high gain channel). The magnitudes of the gains were chosen such that peak currents could be resolved. Also, the use of relatively low gains ensured that the response time of the data acquisition electronics was not unduly limited. In order to confirm that the electronics could respond fast enough to record the transient electrochemical signals associated with cavitation events, the upper frequency limit of both channels were measured. This was achieved by applying an AC signal and measuring the output with an oscilloscope (Tektronix TDS 224). The upper frequency limit was defined as the input frequency for which the output is attenuated by 30%. For the lower gain channel (used to measure erosion transients) this was found to be 790 kHz and for the higher gain channel (used for mass transfer events) it was 240 kHz. Also, the

response to a large amplitude step through a resistor (10 kΩ for the lower gain channel and 100 kΩ for the higher gain channel) was recorded and compared with actual current transients to ensure that the data were not distorted by the response time of the electronics. The magnitude of the potential step was chosen such that the resultant current was of similar amplitude to actual current transients. The results of these potential step experiments are shown in Figures 2.3 and 2.4. They clearly illustrate that the electronics respond faster than is necessary to record the current transients of interest. From this data it is also possible to calculate the slew rates, which were found to be 13.7 A $s^{-1}$ and 374 A $s^{-1}$ for the 1 × $10^5$ V $A^{-1}$ and 1 × $10^4$ V $A^{-1}$ gain channels respectively.

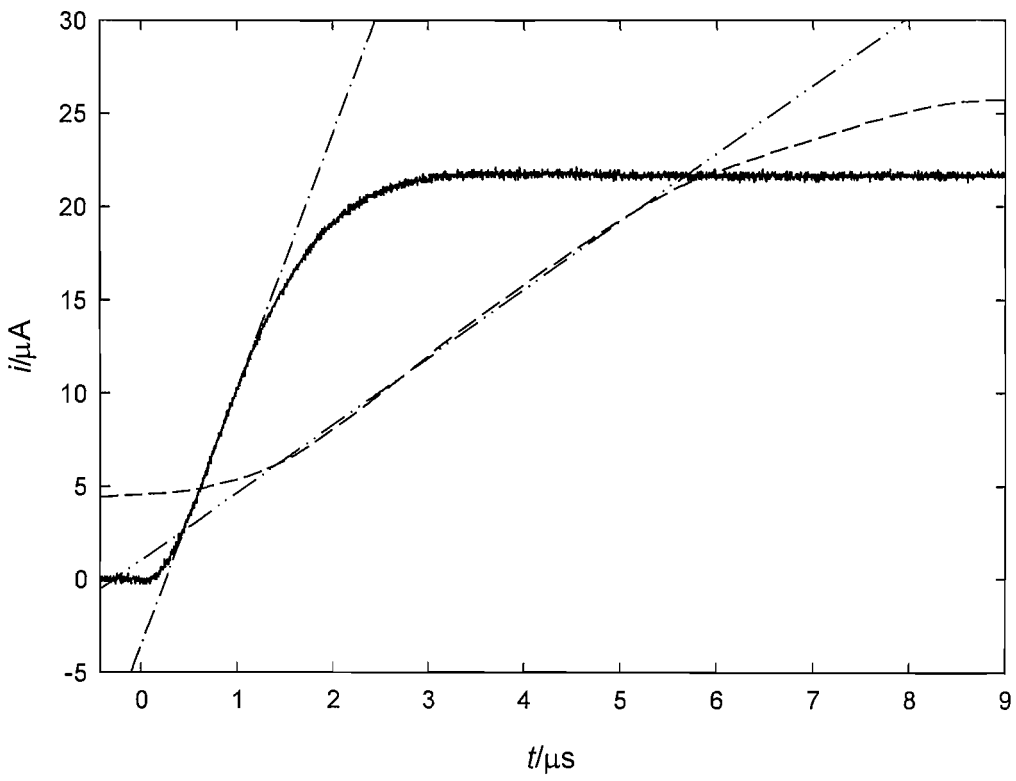


**Figure 2.3** Plot showing the response of the 1 × $10^5$ V $A^{-1}$ gain channel of the dual current follower to a potential step (—) compared with an actual mass transfer event (– –) generated by cavitation. Slew rates were calculated from the gradient of the rising portion of the graph and found to be 13.7 A $s^{-1}$ in response to the potential step (—·) compared with 4.0 A $s^{-1}$ for the mass transfer event (—··—).

Data from the acquisition electronics were recorded by either an ADC card (Measurement Computing PCI-DAS 4020/12) interfaced with a PC using software written in house or an oscilloscope (Tektronix TDS 220) and data transfer software (WaveStar). The oscilloscope has the ability to record at a rate of up to 100 MHz but it can only store 2,500 data points per channel. The

ADC card chosen offers a relatively high sample rate (up to 20 MHz) but importantly has the ability to capture a large amount of data, in terms of both the number of points in an individual dataset and the number of datasets. This, together with the software programmable trigger function, was an important feature for the results presented in Section 6.1.2.

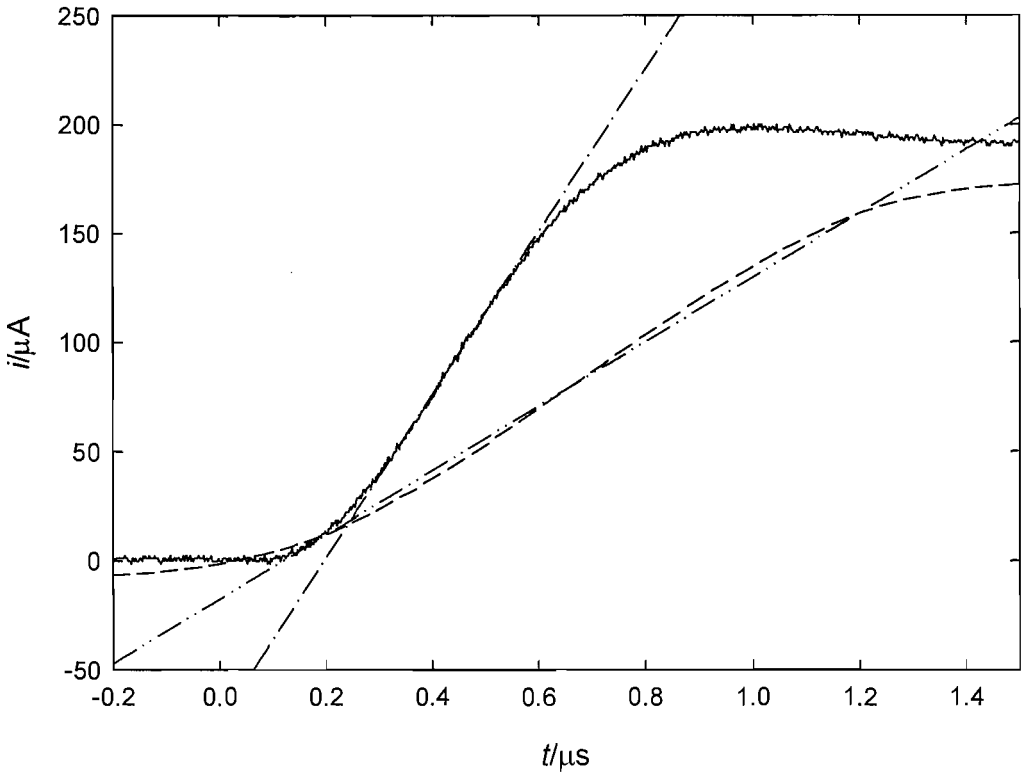


**Figure 2.4** Plot showing the response of the 1 × $10^4$ V $A^{-1}$ gain channel of the dual current follower to a step (—) compared with an actual erosion event (– –) generated by cavitation. Slew rates were calculated from the gradient of the rising portion of the graph and found to be 374 A $s^{-1}$ in response to the potential step (—·) compared with 147 A $s^{-1}$ for the erosion event (—··—).

One disadvantage of the ADC card was that it was unable to store pre-trigger data and hence in experiments where this was necessary (for example high-speed video imaging (see Section 2.6)) the oscilloscope was used. The potential input was supplied by either a waveform generator (PP R1, Hi-Tek Instruments) or home built potential step source. All the electrochemical experiments were conducted in a Faraday cage to reduce electrical noise.

### 2.2.3 Electrochemical cells

Two types of electrochemical cells were used for acoustoelectrochemical experiments. The first (type A) was a temperature controlled cell, fitted with a

water jacket. This cell was used in all experiments that did not require the use of imaging. Where imaging was used a second cell (type B), fitted with a flat window was employed. In both cases the cells were cylindrical and designed such that the working electrode could be inserted through the bottom of the cell and fixed with an SQ13 joint. Top and side views of both types of cell are shown in Figures 2.5 and 2.6.

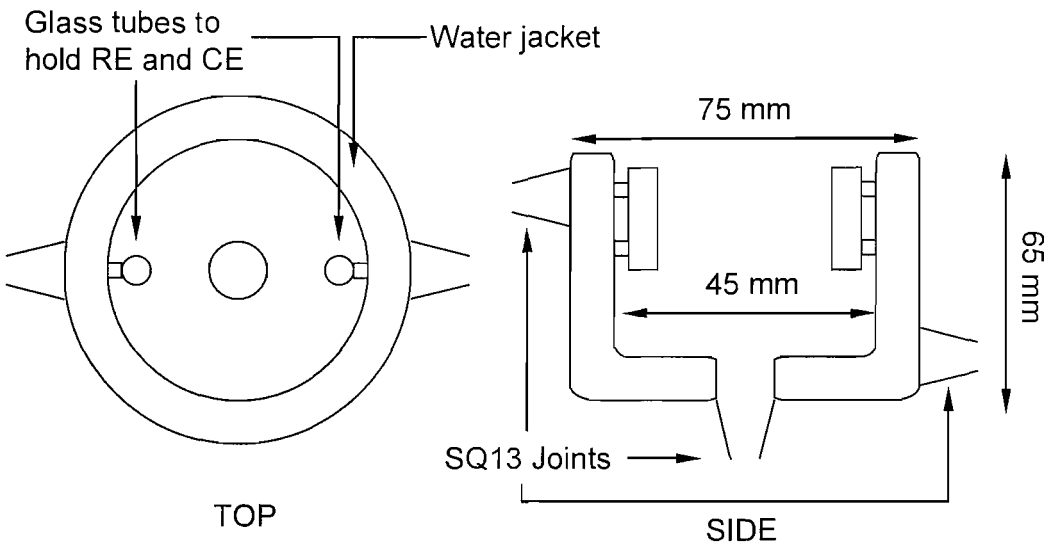


**Figure 2.5** Acoustoelectrochemical cell type A.

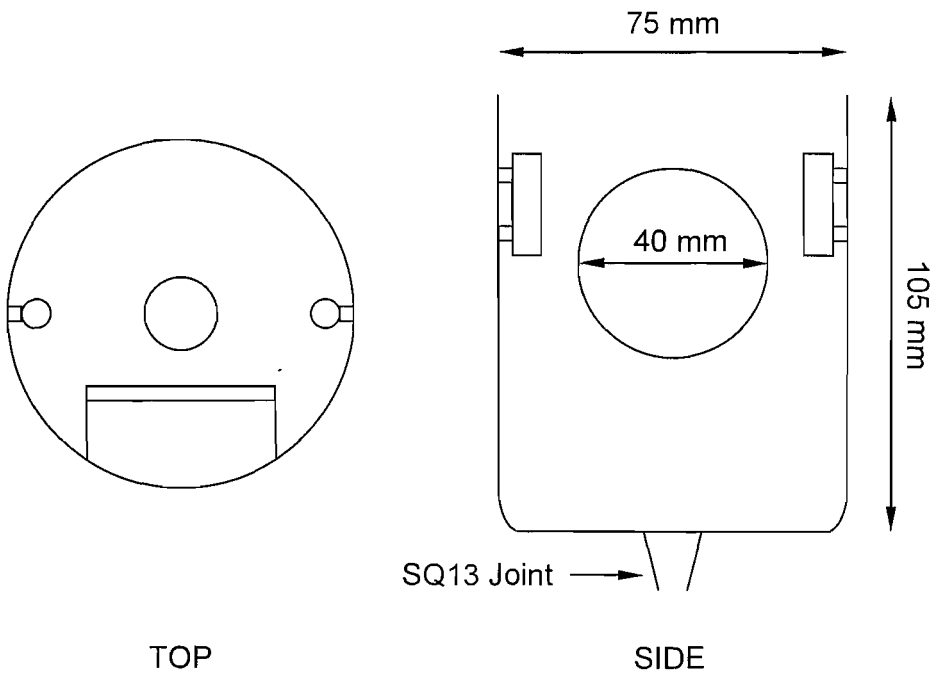


**Figure 2.6** Acoustoelectrochemical cell type B.

### 2.2.4 Electrodes

#### Lead/platinum dual electrode

The lead/platinum dual microelectrode was used in two versions. In the majority of cases the main body consisted of epoxy resin (Struers Epofix). However, a second electrode housing in which soda glass was used in the construction was also employed. The epoxy bodied electrodes were constructed as follows (see Figure 2.7).

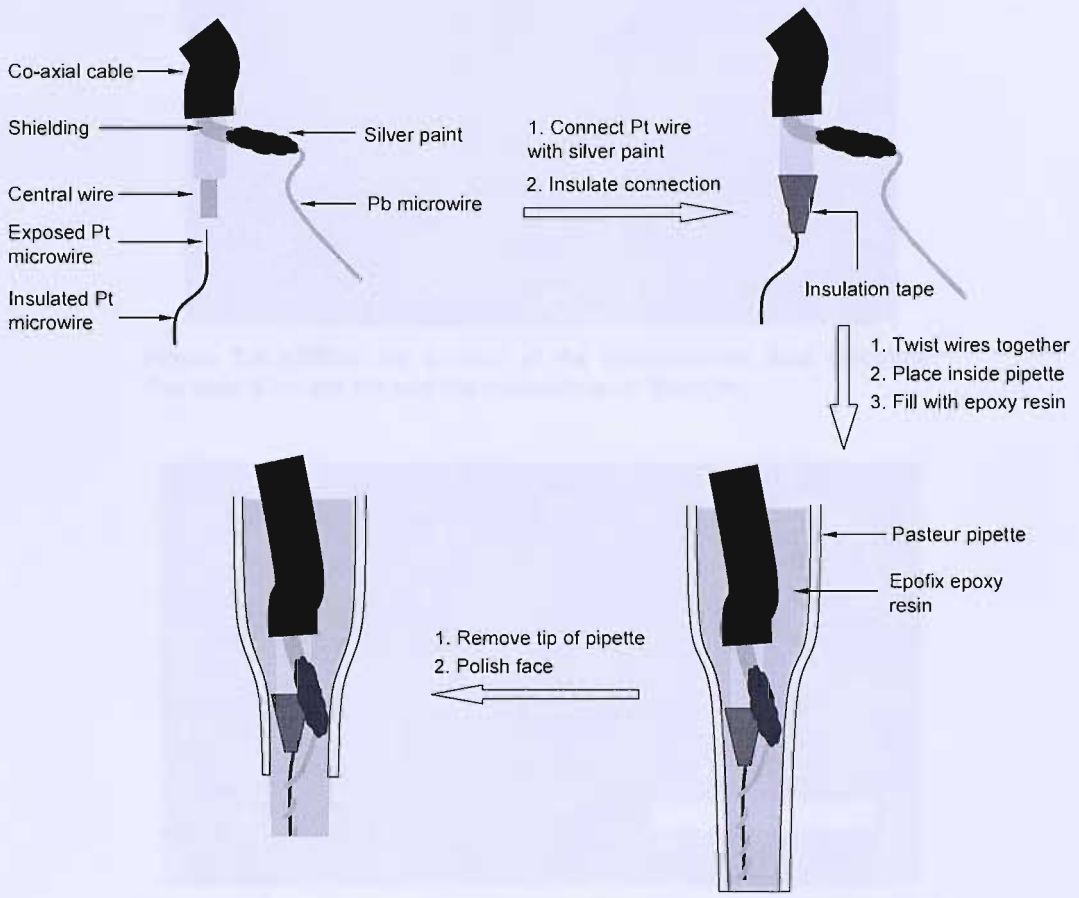


**Figure 2.7** Schematic showing the method used to construct the epoxy-bodied Pb/Pt dual electrode (not to scale).

First, lead wire (125 μm diameter, 99.5%, Goodfellow) was connected to the shielding of a 15 cm length of co-axial wire (2 mm diameter, RS) by means of conducting silver paint (RS). Approximately 1 cm of insulation was then removed from the end of a 4 cm length of polyester insulated platinum wire (50 μm diameter, 99.99%, Goodfellow) by immersion in concentrated $H_2SO_4$ for 30 minutes. This was connected to the central part of the co-axial wire with silver paint and the connection insulated with electrical tape. The microwires were

then twisted together and sealed in a glass Pasteur pipette with epoxy casting resin (Struers Epofix). After the resin had set the glass was removed from tip of the electrode and the face polished with increasing grades of silicon carbide paper and aqueous alumina slurries (1.0 μm and 0.3 μm) to a mirror finish. An SEM of the electrode after polishing is shown in Figure 2.8. This image (and all SEMs presented in this work) was taken using a Philips XL 30 ESEM.

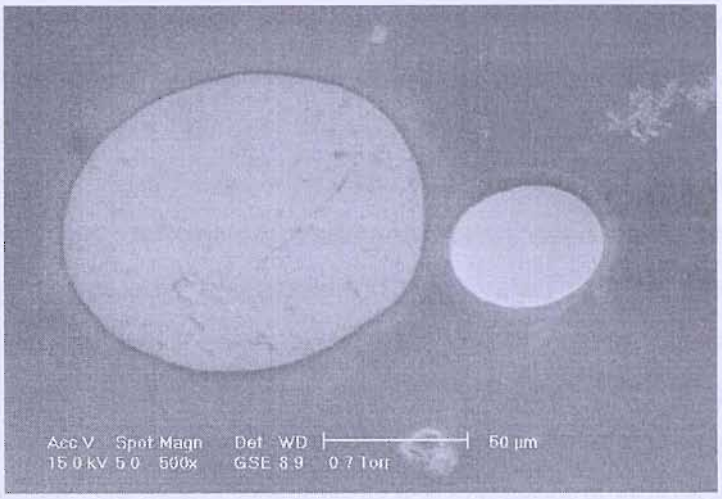


**Figure 2.8** SEM of the surface of the lead/platinum dual electrode. The lead is on the left and the platinum is on the right.

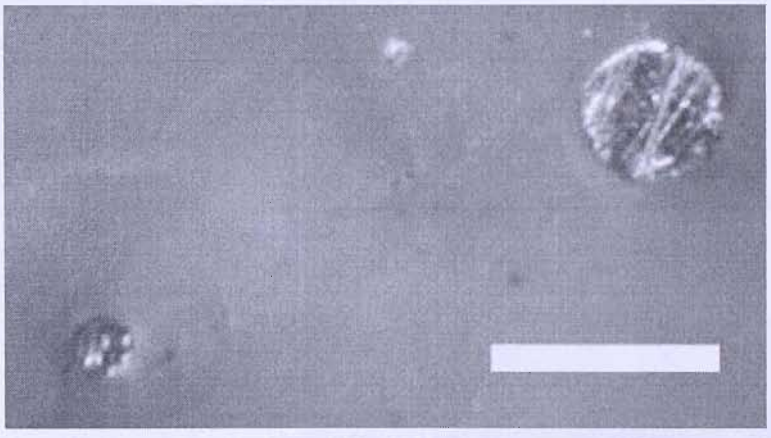

**Figure 2.9** Image of two Pt microwires (50 μm, left and 125 μm, right) sealed in soda glass. The scale bar represents 200 μm.

For the glass-bodied electrode two platinum wires (125 μm and 50 μm diameter) were sealed in glass by the scientific glass blowing service in the School of Chemistry at the University of Southampton in such a way that they remained electronically isolated from each other but within ~500 μm (see Figure 2.9). The 125 μm wire was etched in the type A acoustoelectrochemical cell using a two-electrode arrangement with a vitreous carbon rod acting as the counter electrode. The applied potential was switched between +6 V and –6 V

at a frequency of 25 Hz (0.02 second pulses). The etching solution consisted of 60% saturated $CaCl_2$, 36% $H_2O$ and 4% concentrated HCl (by volume). Prior to etching the electrode was polished with increasing grades of silicon carbide paper and aqueous alumina slurries (1.0 µm and 0.3 µm). During etching, the solution was cavitated at a distance of 5 mm in order to remove reaction products from the cavity, which can hinder the etching process. The progress of the etching was monitored using an optical stereomicroscope and it was stopped when the depth of the cavity was approximately 100 µm. Following the etching process the electrode was thoroughly rinsed and lead was deposited in the cavity potentiostatically from a solution consisting of 0.3 mol $dm^{-3}$ $PbCO_3$ in 2 mol $dm^{-3}$ $CH_3SO_3H$. A three electrode set-up was used with a ring of platinum mesh acting as the counter electrode and a saturated calomel electrode as the reference. The ring was positioned around the tip of the glass electrode to create a uniform current density profile. Figure 2.10 shows a cyclic voltammogram of the recessed 125 µm diameter platinum electrode in the lead deposition solution. An image of the tip of the electrode is shown as an insert in Figure 2.10.

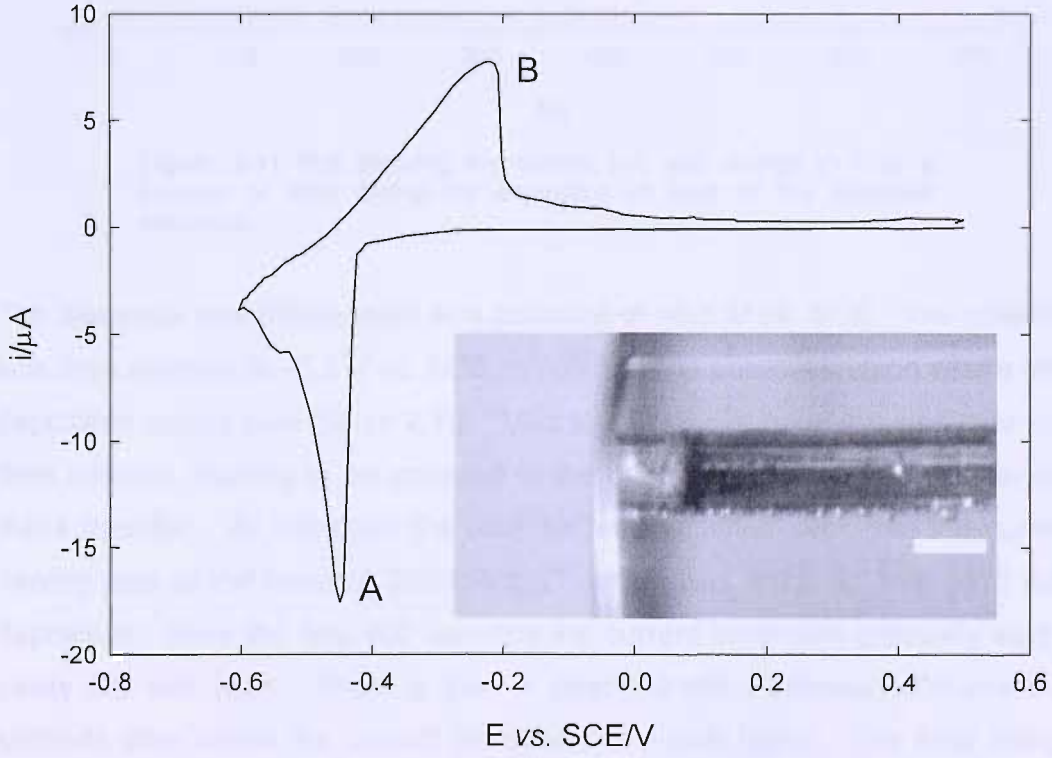


**Figure 2.10** Cyclic voltammogram of a recessed platinum electrode (125 µm diameter) in a solution of 0.3 mol $dm^{-3}$ $PbCO_3$ in 2 mol $dm^{-3}$ $CH_3SO_3H$. The sweep rate was 20 mV $s^{-1}$ and the temperature was 25 °C. **Insert** Image of the tip of the etched electrode. The scale bar represents 100 µm.

The potential was swept from +0.5 V *vs.* SCE at 20 mV $s^{-1}$. The onset of lead deposition is marked by the sharp increase in cathodic current at *ca.* –0.42 V *vs.* SCE (labelled A). On the positive scan a large peak due to stripping of the deposited lead can be seen (labelled B). A current-time trace for the deposition of lead is shown in Figure 2.11.

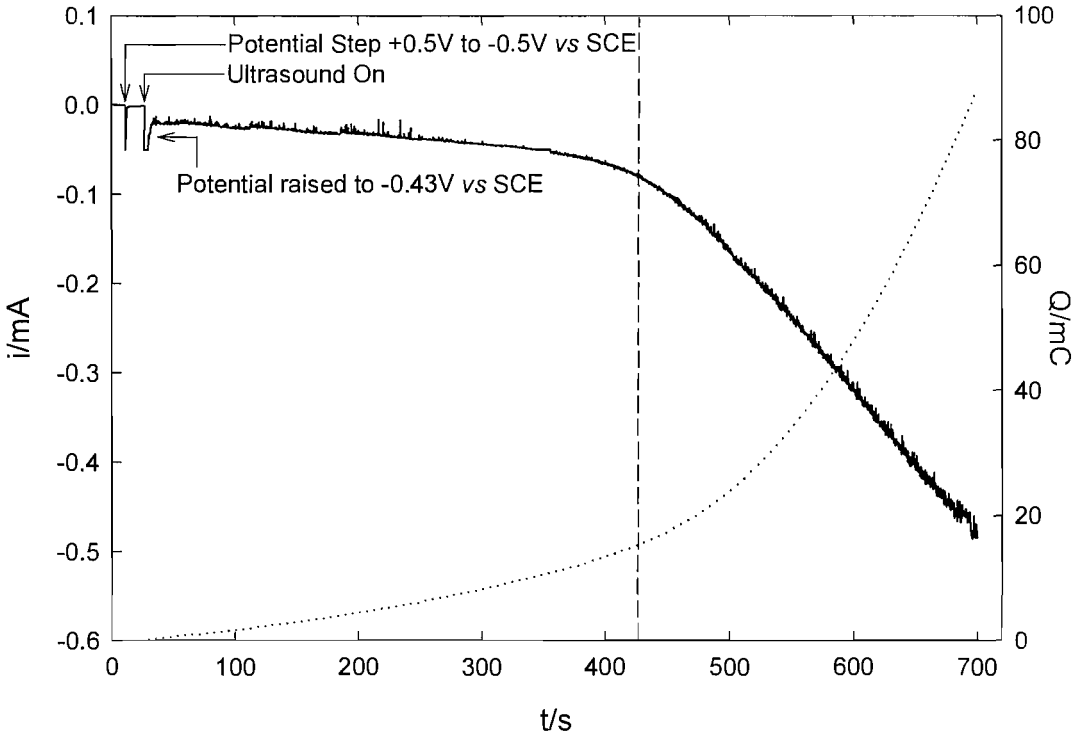


**Figure 2.11** Plot showing the current (—) and charge (····) as a function of time during the deposition of lead at the recessed electrode.

The electrode was initially held at a potential of +0.5 V *vs.* SCE. The potential was then stepped to –0.5 V *vs.* SCE, which is in the potential region where lead deposition occurs (see Figure 2.10). Ultrasounic irradiation of the electrode was then initiated, leading to an increase in the cathodic current due to enhanced mass transfer . At this point the potential was adjusted such that the current density was of the order of 200 mA $cm^{-2}$, which was found to give good lead deposition. Over the first 400 seconds the current increases gradually as the cavity fills with lead. There is then a clear transition between 400 and 500 seconds after which the current increase was much faster. The total charge passed up to this point ((— —) in Figure 2.11) was ~15 mC. Using a simple Faradic relationship (assuming 100% efficiency) and a molar volume of 18.26 mol $cm^{-3}$, this equates to 1.42 $\times 10^6$ $\mu m^3$ of lead. For a diameter of 125 µm, this

charge corresponds to a cylinder of lead 115 µm deep. This is in good agreement with the image of the recessed electrode shown in Figure 2.10 and indicates that the rapidly incresing current seen after 500 s is the result of lead deposition outside of the cavity. This change in behaviour is an effective indicator as to when the deposition is complete.

Following the deposition the electrode was polished with an aqueous alumina slurry (1.0 µm). On some occasions this would cause some of the lead to be removed from the cavity. If this was the case more lead was deposited, the electrode polished and the process repeated until a relatively uniform lead surface (as deemed by optical microscopy) had been achieved.

**Lead/lead dual electrode**

Lead/lead dual electrodes were constructed using a similar method to the Pb/Pt dual electrode, using 125 µm diameter lead microwire (99.5%, Goodfellow). Two 4 cm lengths of wire were cut and one was insulated by means of a lacquer, which was painted onto the wire leaving approximately 1 cm exposed. Connections were made to coaxial wire with silver paint as for the Pb/Pt dual electrode, one connection was insulated with electrical tape and the two wires were twisted together, before being sealed within a Pasteur pipette using epoxy casting resin. After the resin had set the glass was removed from tip of the electrode and the face polished with increasing grades of silicon carbide paper and aqueous alumina slurries (1.0 µm and 0.3 µm) to a mirror finish. An SEM of the electrode after polishing is shown in Figure 2.12.

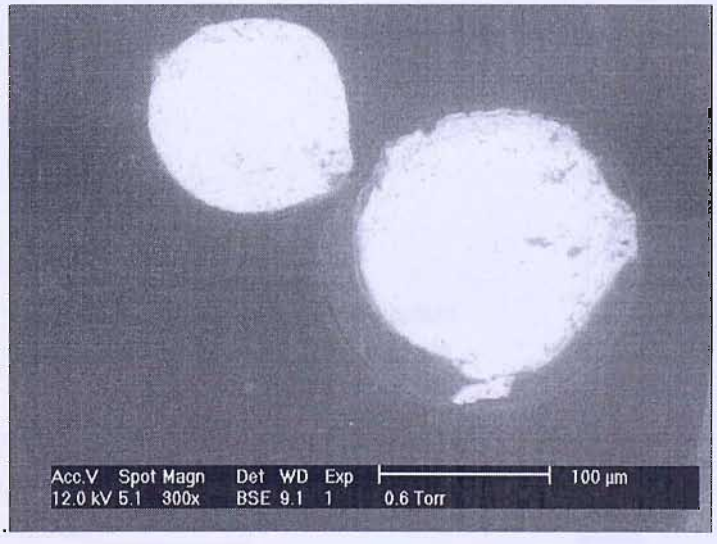


**Figure 2.12** SEM of the surface of the lead/lead dual electrode. The lacquered lead is on the right and shows some distortion from the insulating process.

This shows that the insulating process has distorted the soft lead wire (right-hand microdisc). However, the microdiscs remain electronically isolated from each other but within 200 μm (centre-to-centre).

**Carbon steel electrodes**

Two sizes of carbon steel electrodes were used in this work. The first was a large electrode, which was constructed by sealing a 3 cm length of steel rod (5 mm diameter) in epoxy casting resin (Struers Epofix). This was achieved by using a Gilson pipette tip (1 mL volume cut to size), temporarily fixed to a Teflon plate as a mould. After the resin had set the mould was removed and the surface was polished flat with silicon carbide paper and to a mirror finish using aqueous alumina slurries (1.0 μm and 0.3 μm). The elemental composition of the steel was analysed by means of EDX analysis (using a Philips XL 30 ESEM) and found to be Fe = 92.6%, C = 6.7%, S = 0.7% by weight. While it is desirable to employ microelectrodes because of their high spatial and temporal resolution, it was impossible to obtain sufficiently thin carbon steel wire to construct such electrodes in the conventional manner. Hence, small carbon steel electrodes were constructed using the following method, which is illustrated schematically in Figure 2.13. First, a steel rod (3 cm long, 5 mm diameter) was milled to a point and then sealed in casting resin as above. The face was then polished extremely carefully so as to only expose the tip of the sharpened seal. This resulted in a relatively small area of exposed steel (≈ 75 μm radius) but it was difficult to achieve a good seal around the disc. An SEM image of the surface is shown in Figure 2.14 and a photograph of the entire electrode in Figure 2.15.

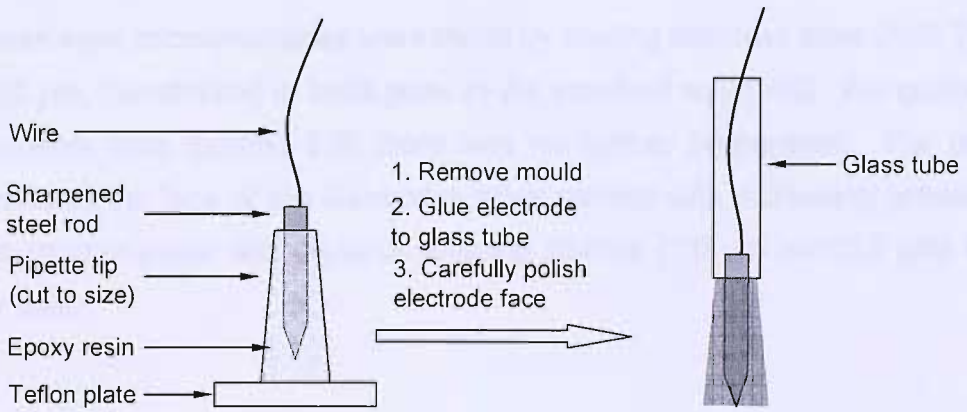


**Figure 2.13** Schematic showing the procedure used for the construction of carbon steel microelectrodes.

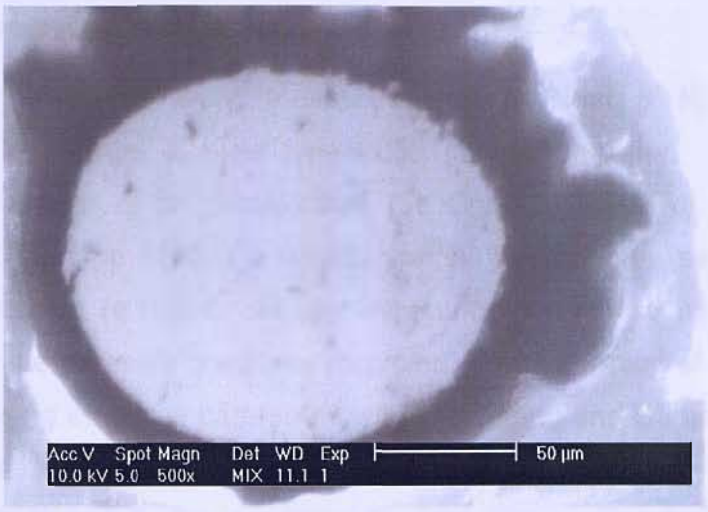


**Figure 2.14** SEM image of the surface of the carbon steel microelectrode.


**Figure 2.15** Photograph of the carbon steel microelectrode. The scale is in cm.

### Stainless steel microelectrodes

Stainless steel microelectrodes were made by sealing stainless steel (AISI Type 302, 25 µm, Goodfellow) in soda glass in the standard way [160]. For guillotine experiments (see Section 2.9) there was no further preparation. For other experiments the face of the electrodes were sanded with increasing grades of silicon carbide paper and aqueous alumina slurries (1.0 µm and 0.3 µm) to a mirror finish.

## 2.3 Measurement of the acoustic pressure

All acoustic pressures were measured with a Brüel & Kjær type 8103 hydrophone and Brüel & Kjær type 2635 charge amplifier. The data was recorded by means of an oscilloscope (Le Croy 9310 AM or Tektronix TDS 220). Whilst the type 8103 is a relatively small hydrophone (see Figure 2.16), the active element (a hollow cylinder measuring 6 mm × 6 mm) is still large compared to the pressure gradients expected. Consideration of this in terms of spatial averaging effects is paramount when recording and interpreting pressure measurements. This is discussed in more detail in Chapter 4. The element is small enough to satisfy the condition that the dimensions are less than one tenth of the wavelength of the driving sound wave used in this work (~ 7 cm), which implies that the hydrophone is omnidirectional with respect to the driving pressure wave [30].

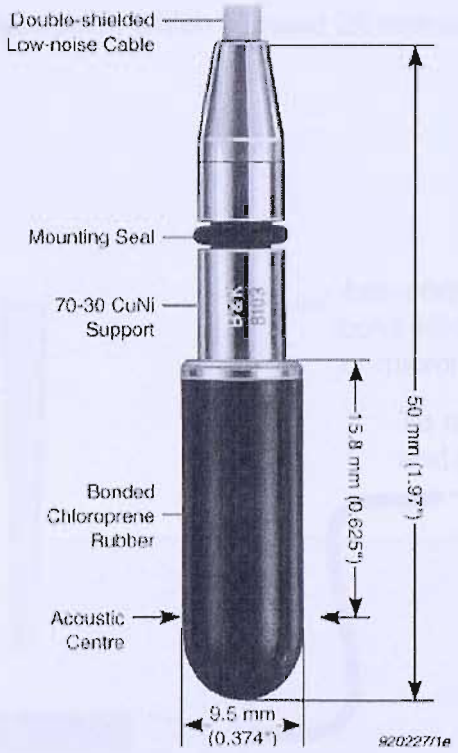


**Figure 2.16** Picture of Brüel & Kjær type 8103 hydrophone with dimensions and location of acoustic centre. Taken from Brüel & Kjær product literature.

### 2.3.1 Measurement of the axial pressure profile

The axial profile of the pressure field generated by the sound source in water was measured in a large tank, measuring 1 m × 1 m × 2 m filled with tap water

at ambient temperature (~22 °C). The large size of the vessel was essential to ensure that the pressure measured was dominated by the direct field generated by the sound source and not any secondary, reverberant sound field. The transducer and horn were positioned such that the tip of the horn was 15 mm below the surface of the water. The hydrophone was fixed to the arm of a computer controlled XYZ scanning rig and positioned below the tip of the horn, ensuring that the acoustic centre (as determined from data supplied by the manufacturer) was on the axis of symmetry of the horn. A schematic of the experimental set-up is shown in Figure 2.17. The axial pressure profile was generated by moving the hydrophone away from the tip of the horn in steps of 1 or 2 mm (depending on the experiment) and recording the pressure at each point. For experiments in castor oil the large tank was replaced with a 5 $dm^3$ beaker (20 cm diameter), which was filled with 3 $dm^3$ of castor oil. The tip was placed 15 mm below the surface of the liquid and the hydrophone was positioned as before. In this case the hydrophone was moved by means of a micrometer and stage (Newport), which allowed 25 mm of movements with 0.02 mm resolution.

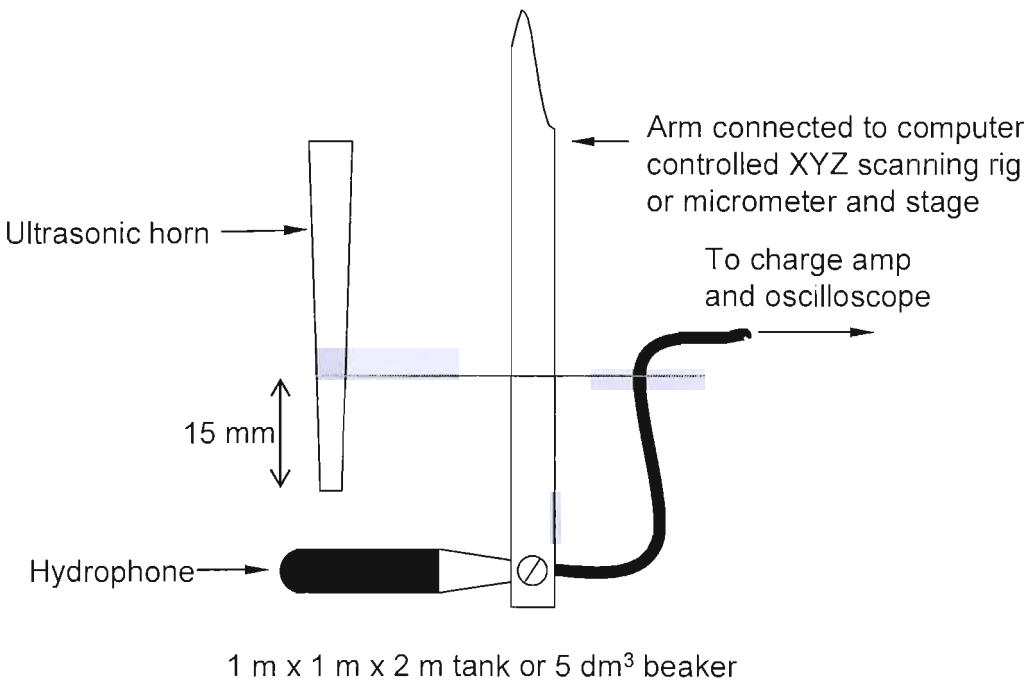


**Figure 2.17** Experimental set-up for measurement of the axial pressure profile.

### 2.3.2 Measurements in the presence of a baffle

In order to investigate the effect of a rigid baffle on the pressure profile, a copper plate was added to the experimental set-up described above. The plate was 15 cm × 15 cm and was 2 mm thick. A hole (4 mm diameter) was drilled in the centre of the plate. The plate was clamped such that the tip of the horn passed through the hole and the plate was just below (and parallel to) the surface of the water. All experiments were carried out in a large water tank (45 cm × 45 cm × 30 cm), filled with 50 L of tap water at ambient temperature (~22 °C). The horn was submerged to a depth of 15 mm. The pressure was recorded using Brüel & Kjær type 8103 hydrophone, Brüel & Kjær type 2635 charge amplifier and Tektronix TDS 220 oscilloscope. The hydrophone was positioned horizontally below the horn, with the acoustic centre on the axis of symmetry of the horn, as shown in Figure 2.17. The horn to hydrophone distance was controlled by means of a micrometer and stage (Newport), which allowed 25 mm of movements with 0.02 mm resolution.

## 2.4 Calorimetry

The calorific power of the horn was measured in the standard way [161]. A vacuum jacketed cell was filled with 15 g of pure water and the temperature increase following the application of ultrasound was measured by means of a homemade thermocouple. An example of the effect of sonication on the sample temperature is shown in Figure 2.18. The calorific power, $W_c$ is given by

$$W_c = \left(\frac{dT}{dt}\right)_{t_{ON}} MC_p$$

where $\left(\frac{dT}{dt}\right)_{t_{ON}}$ is the initial gradient of the temperature *vs.* time plot (following the activation of ultrasound), $M$ is the mass of the sample and $C_p$ is heat capacity of the sample (4.184 J $g^{-1}$ $K^{-1}$ for pure water). The value of $\left(\frac{dT}{dt}\right)_{t_{ON}}$ was determined through a quadratic curve fit using commercial graphing software (SigmaPlot, SPSS Inc.). The calorific power was found to be 56 ± 5 W $cm^{-2}$. This is the 'power' quoted in appropriate figure legends.

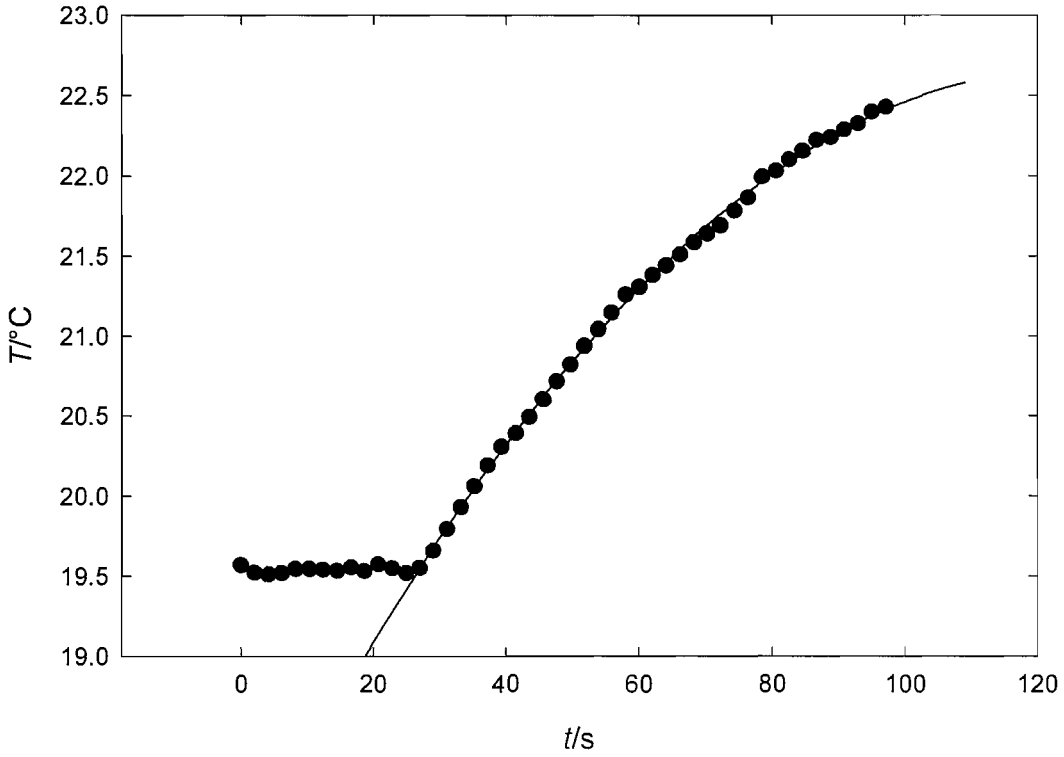


**Figure 2.18** Plot showing the effect of ultrasound on the temperature of a sample of pure water. The ultrasound was turned on at $t$ = 25 s. The symbols (•) represent experimental points and the line (—) the quadratic best fit.

## 2.5 Low light level imaging

The light output generated by cavitation (see Chapter 4) was recorded in a number of different ways. In all cases the data were recorded in a darkroom.

### 2.5.1 Image intensified pictures

Initially, MBSL and MBSCL images were recorded by means of a JAI CV-A50 CCD camera and a Phototek MCP 325 image intensifier using the set-up shown in Figure 2.19. Light is focused onto the intensifier, which consists of a photocathode input, microchannel plate to provide electron gain and a luminescent output window. The gain (maximum $2 \times 10^7$) was controlled by a Phototek MCPCU 2.3 control unit. The CCD camera was focused on the luminescent image and the data recorded by means of a PC *via* a frame grabber and software (PXC 200A, Imagenation Vision). This system allows extremely low light level, real time imaging. However, it was found that this set-up did not allow the tip of the horn to be imaged with sufficient magnification. High magnification was necessary in order to determine the spatial extent of

MBSL (see Section 4.3.1). An alternative system was therefore used for this purpose. This alternative system is described in the following section.

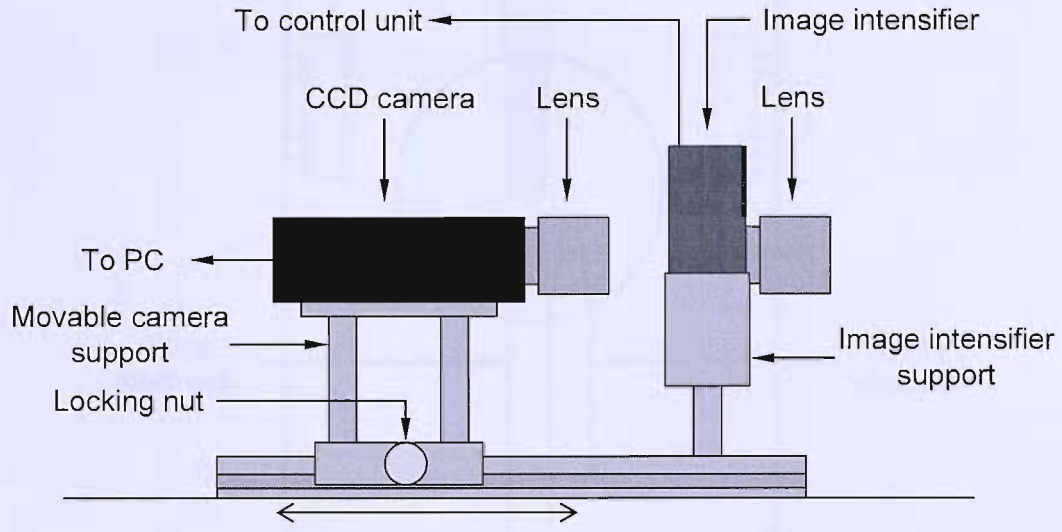


**Figure 2.19** Experimental set-up for recording images using image intensifier technology.

### 2.5.2 Long time exposure CCD camera

High magnification MBSL pictures were taken by means of a Starlight Xpress HX516 long time exposure CCD camera, which was interfaced with a PC using software supplied by the manufacturer. The exposure times used (usually 10 min) are given in the appropriate figure legends. In all cases the acoustoelectrochemical cell type B was used (see Figure 2.6). For experiments where the effect of electrode material was investigated (see Section 4.4.2) the arrangement shown in Figure 2.20 was employed. An electrode, whose body was constructed from epoxy resin was cut to size and glued to a glass electrode with fast setting epoxy resin. This was then placed in the cell, which was on a stand (as shown in Figure 2.1). This set-up allowed three experimental conditions (no electrode, epoxy electrode and glass electrode) to be studied with the minimum of disturbance by simply moving the cell in the X direction to position the chosen electrode under the fixed horn.

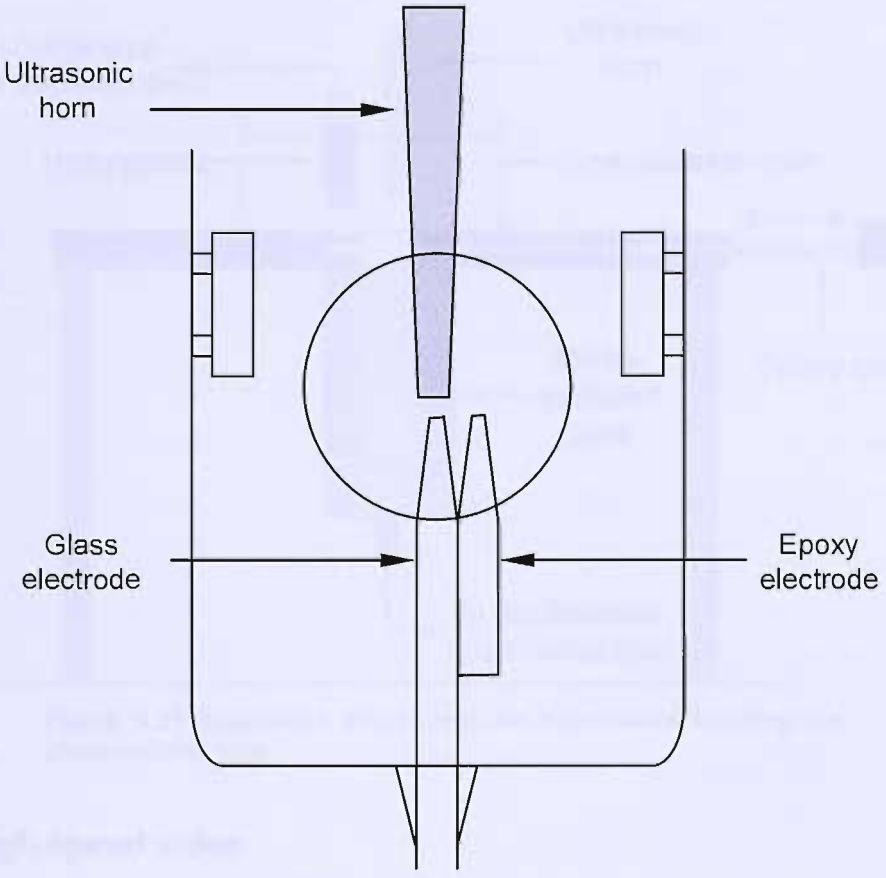


**Figure 2.20** Experimental set-up used to investigate the effect of electrode material on multibubble sonoluminescence.

### 2.5.3 Photomultiplier tube

The temporal characteristics of MBSL were investigated using an EMI-Gencon Inc. RFI/B-293 photomultiplier tube (PMT) powered by 2 kV power supply (Brandenburg 475R). The experimental set-up was as shown in Figure 2.21. The PMT was fixed to the underside of a wooden platform, which had a hole (10.5 cm diameter) in the centre. A sliding cover allowed the hole to be covered when not in use. The cell, which was a Pyrex crystallisation dish (internal diameter, 93 mm depth, 50 mm), was placed above the PMT and the horn was positioned such that the tip was 15 mm below the surface of the solution (0.75 M $Na_2SO_4$). In order to measure the pressure and light output simultaneously a hydrophone was placed in the cell such that the acoustic centre was at a lateral distance of 15 mm from the centre of the tip of the horn. An oscilloscope (Tektronix TDS 224) was used to record the output from the PMT and the hydrophone simultaneously, allowing the pressure signal and light output to be temporally correlated.

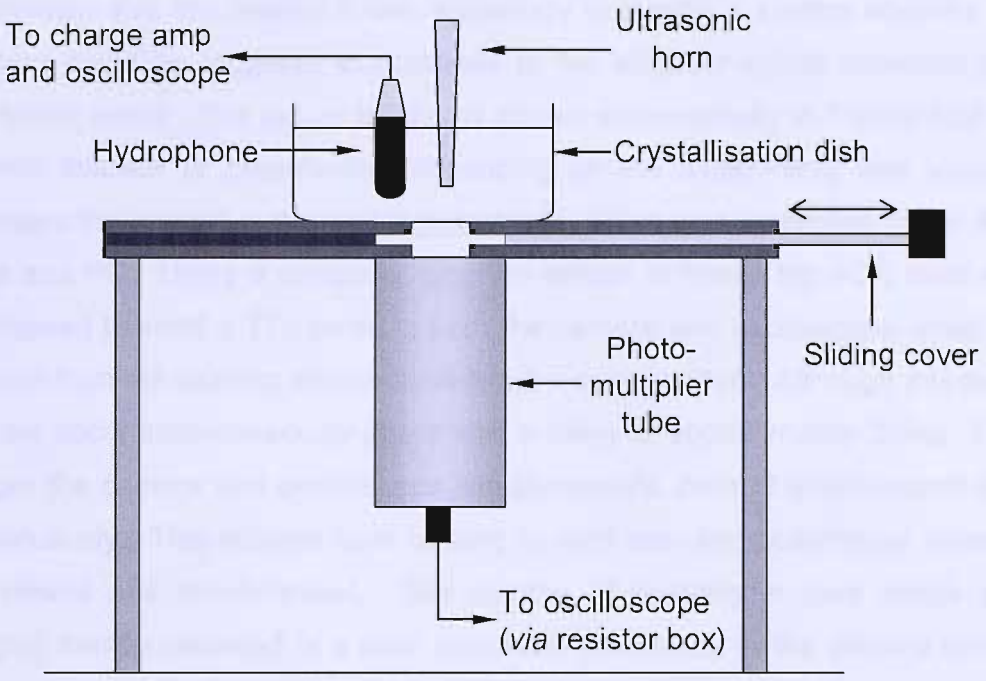


**Figure 2.21** Experiment set-up used for experiments involving the photomultiplier tube.

## 2.6 High-speed video

High-speed video footage was recorded using a Photosonics Phantom V7 digital video camera fitted with a monozoom lens. The camera is capable of recording at up to 150,000 frames per second depending on the resolution (see Table 2.1).

| Resolution (pixels) | Maximum Rate (f.p.s) |
|---|---|
| 800 × 600 | 4,800 |
| 512 × 512 | 8,300 |
| 256 × 256 | 27,000 |
| 128 × 128 | 68,500 |
| 128 × 64 | 102,000 |
| 64 × 64 | 121,000 |
| 32 × 32 | 150,000 |

**Table 2.1** Table showing selected resolution and corresponding maximum recording rates obtainable using the Phantom V7 high-speed camera.

It is possible to store over 1 second of data and hence more than 150,000 images. However, this can be problematic when studying phenomena such as cavitation where the events of interest occur randomly and on a microsecond

timescale. For this reason it was necessary to design a system whereby the camera could be triggered in response to the electrochemical detection of a cavitation event. The set-up for this is shown schematically in Figure 2.22. A current follower or potentiostat (depending on the experiment) was used to measure the current at the working electrode, which was monitored by an ADC card and PC. Using a computer program written in house the ADC card was configured to send a TTL pulse to both the camera and oscilloscope when the current from the working electrode satisfied a set condition. Although this pulse did not occur instantaneously (there was a delay of approximately 2 ms), it did trigger the camera and oscilloscope simultaneously, both of which record data continuously. This allowed data relating to both pre- and post-trigger times to be viewed and synchronised. The number of post-trigger (and hence pre-trigger) frames recorded is a user selectable parameter in the camera control software. In order to provide sufficient light for the camera it was necessary to backlight the subject producing a silhouette of the horn and/or electrode.

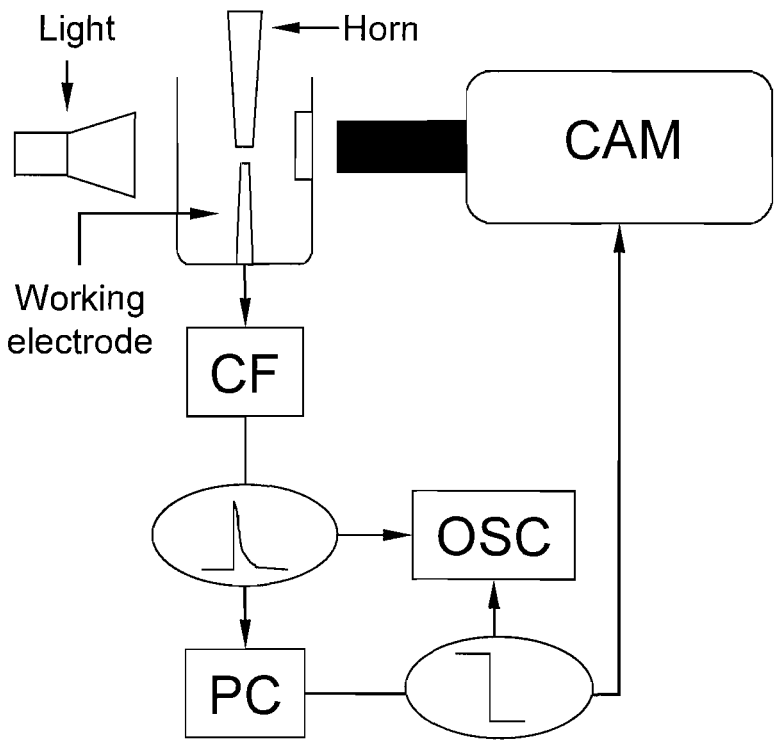


**Figure 2.22** Experimental set-up for recording high speed video footage synchronously with electrochemical data. CAM = camera, CF = current follower, OSC = oscilloscope, PC = computer and ADC card.

## 2.7 Laser scattering experiments

Laser scattering experiments (Chapter 5) were performed using the set-up shown schematically in Figure 2.23.

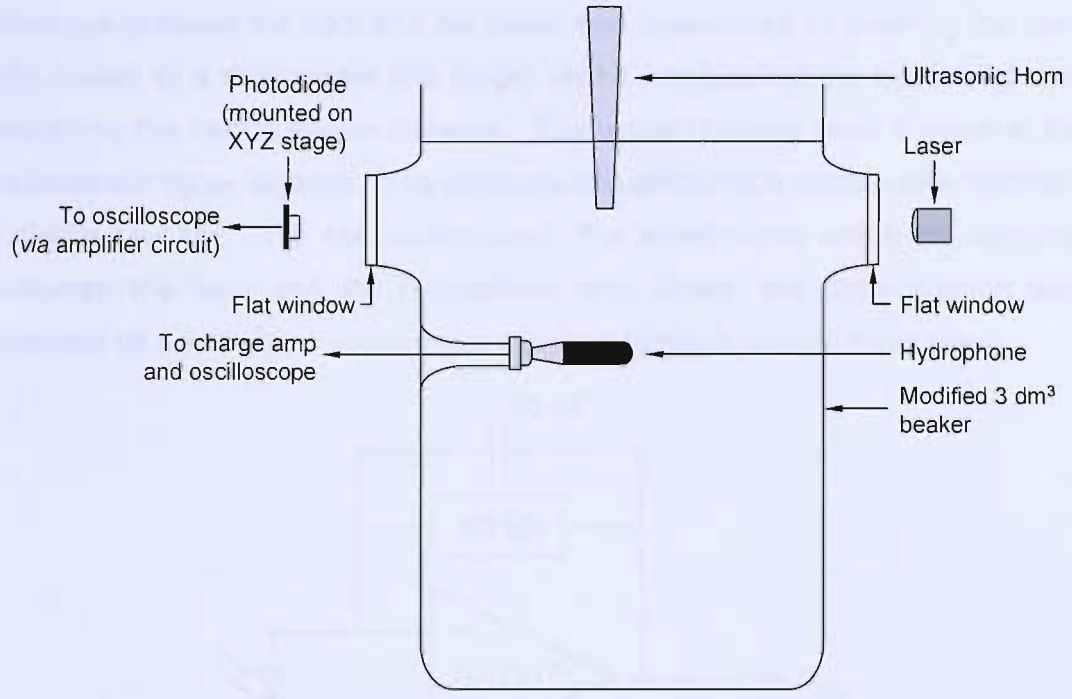


**Figure 2.23** Experimental set-up used for laser scattering experiments.

A 3 $dm^3$ beaker was modified by the scientific glass blowing service in the School of Chemistry at the University of Southampton to include optically flat windows (4 cm diameter) on opposite sides of the beaker. Also included was a hollow glass support, which was terminated with an SQ 13 fitting, allowing a hydrophone to be positioned in the centre of the beaker at a height of 12 cm. The overall height of the beaker was 23 cm and the internal radius was 7 cm. The beaker was filled to a height of 19 cm with pure water and the ultrasonic horn was positioned such that it was in the centre of the beaker submerged to a depth of 15 mm. A laser (UG 5001-21 diode laser, 1 mW, 635 nm, RS) was shone through the beaker and detected by means of a photodiode (AEPX65, RS) and home made amplifier circuit (see Figure 2.24). The photodiode had an active area of 0.8 $mm^2$. The electronics were such that under daylight conditions the output, $V_{PD}$ was 0 V, while the maximum output (under direct illumination by the laser) was -1.2 V. Thus, any scattering of the beam resulted in an increase in the output voltage (*i.e* less negative). Prior to each

experiment, the position of the photodiode was adjusted by means of and XYZ stage (Newport, 0.02 mm resolution) such that the output was at a maximum negative value. The laser beam was flat with a width of 3 mm and was orientated such that it was parallel with the face of the ultrasonic horn. The distance between the horn and the beam was determined by lowering the horn (by means of a micrometer and stage) until it just blocked the beam and then retracting the horn a known distance. The actual distance used is given in the appropriate figure legends. The pressure and photodiode output were recorded using a Le Croy 9310 AM oscilloscope. For experiments where the distance between the horn and the hydrophone was varied, the glass support was blanked off and the hydrophone was clamped in place using a retort stand.

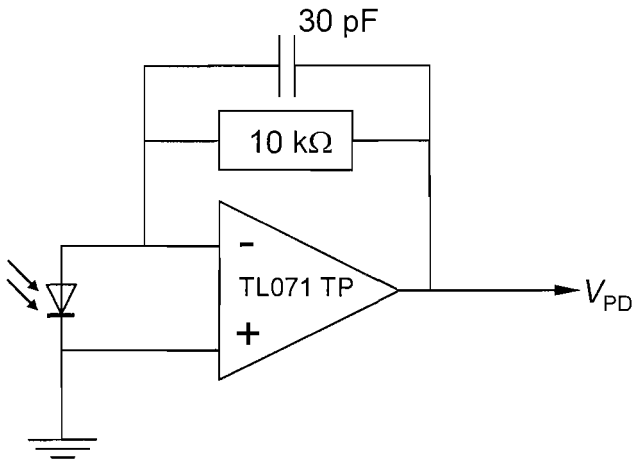


**Figure 2.24** Photodiode amplifier circuit used for laser scattering experiments.

## 2.8 Speed of sound measurements

Speed of sound measurements (as used in Section 4.4.2) were performed using a Brüel & Kjær type 8103 hydrophone, Brüel & Kjær type 2635 charge amplifier and the ultrasonic transducer controlled as described in Section 2.1. For the solid samples, the experimental set-up was that shown in Figure 2.25. In this experiment, the function generator sends a pulse (in the form of a square wave of frequency 40 Hz) to the transducer. The rising part of this wave triggers the oscilloscope. The hydrophone detects the resulting acoustic signal after it has passed through the sample and it is recorded by the oscilloscope *via* the charge amplifier. The repetitive nature of the input allowed the averaging function of the oscilloscope to be used to improve the signal to noise ratio. In all cases the signal was averaged over 128 responses. A comparison of the single and averaged responses is shown in Figure 2.26.

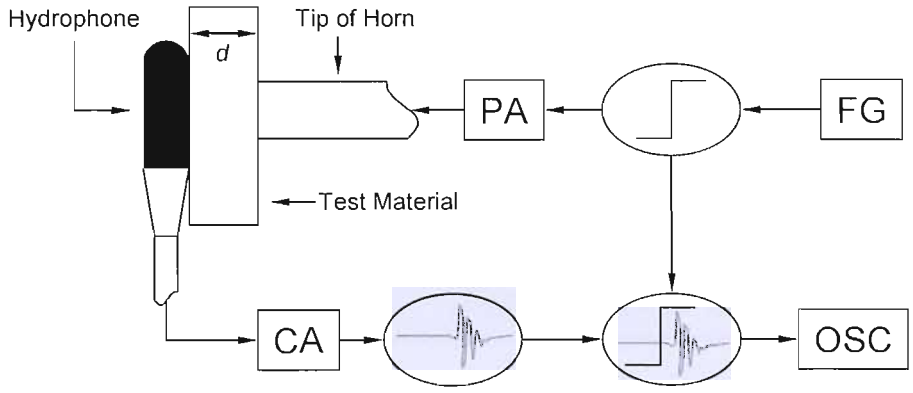


**Figure 2.25** Experimental set-up for the measurement of the speed of sound. FG = function generator, PA = power amplifier, CA = charge amplifier, OSC = oscilloscope.

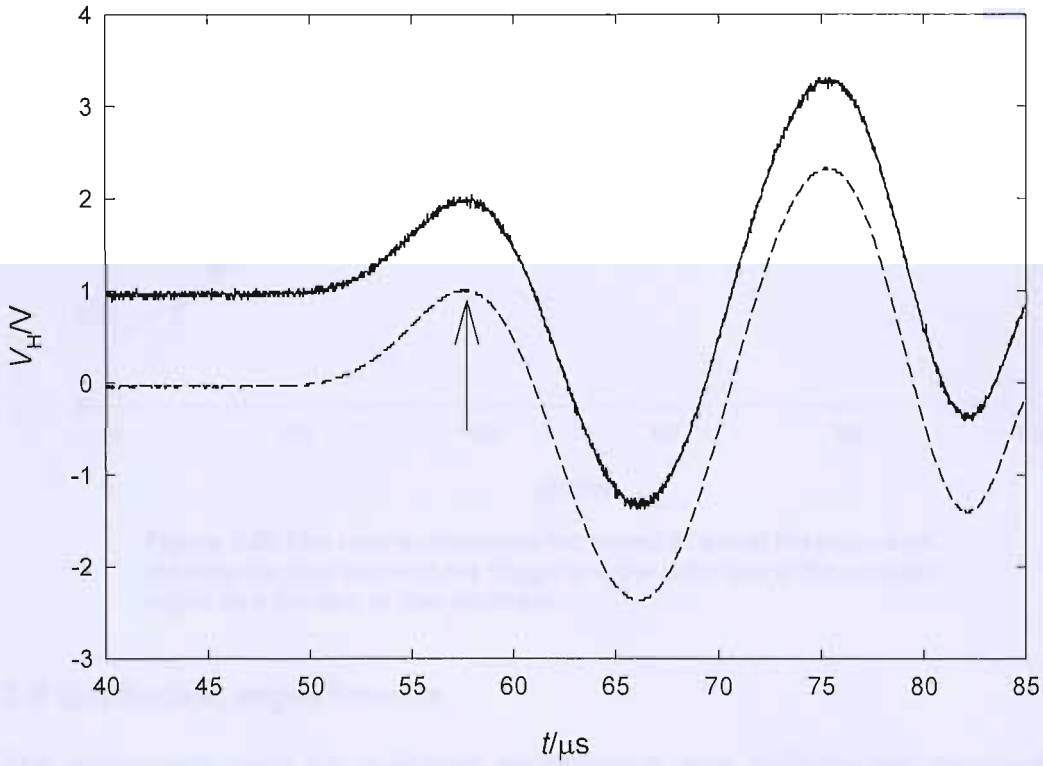


**Figure 2.26** Plot showing the comparison of single (—) and averaged (— —) hydrophone responses. The single response is offset by +1 V for clarity. The number of averages was 128. The arrow indicates peak 1.

The delay between the trigger and detection of the signal is proportional to the speed of sound in the test material, although care must be taken as there are numerous sources of additional time delays in this system. For this reason discs of various thicknesses, *d*, were used in order to construct a linear plot of distance *vs.* time from which the speed of sound could be determined as the

reciprocal of the gradient. In all cases the time used was that between the trigger and the first peak in the signal (shown by the arrow in Figure 2.26). As an example, Figure 2.27 shows the data for epoxy resin (Epofix, Struers). For the electrolyte the same technique was used except the hydrophone was placed in the solution and the horn-to-hydrophone distance was controlled by a micrometer and stage (Newport) which allowed 25 mm of movement with 0.02 mm resolution.

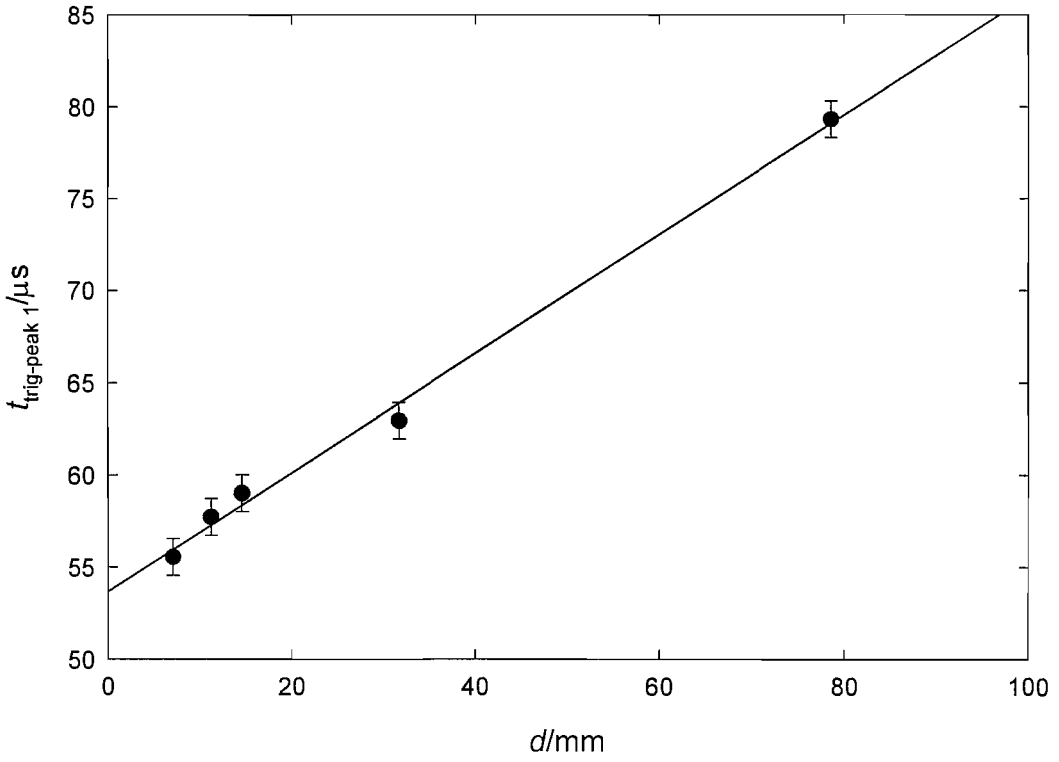


**Figure 2.27** Plot used to determine the speed of sound in epoxy resin, showing the time between the trigger and the detection of the acoustic signal as a function of disc thickness.

## 2.9 Guillotine experiments

The equipment used for guillotine experiments was built by the mechanical workshop at the University of Southampton and is shown in Figure 2.28. It consists of a stainless steel cell with a spring-loaded arm mounted on a Teflon bearing. Stainless steel microelectrodes sealed in soda glass were scored approximately 1 cm from the tip with a glass cutter prior to being loaded from below such that they were in the path of the guillotine arm. On release the arm fractures the microelectrode exposing the stainless steel to the solution. The current was recorded both before and after the guillotine event by means of a

current follower and oscilloscope (Tektronix TDS 220). The casing of the guillotine itself was used as a counter/reference electrode.

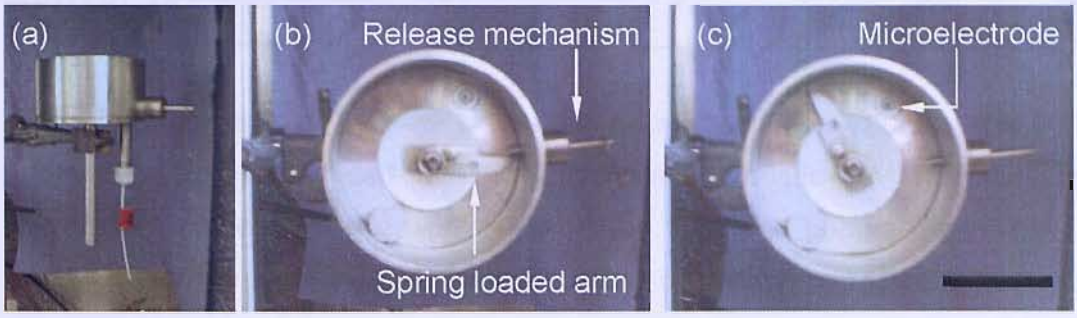


**Figure 2.28** Equipment used for guillotine experiments. **(a)** Side view. **(b)** Top view prior to release of the spring loaded arm. **(c)** Top view after the release of the spring loaded arm. The scale bar in (c) represents 50 mm.

## 2.10 Chemicals and solutions

All solutions were made up using water from an USF Elga Purelab Option E10 water purification system. Water purified in this manner had a conductivity of below 0.1 μS $cm^{-1}$ and a low organic content (manufacture quoted TOC < 30 ppb). A list of all chemicals employed, suppliers and purity (no further purification was carried out) is shown in Table 2.2.

| Chemical | Supplier | Purity/Grade |
|---|---|---|
| 3-aminophthalhydrazide | Aldrich | 97 % |
| 3-methyl-2-pyrazoline-5-one | Avocado | > 98 % |
| Castor oil | Aldrich | - |
| $CO_2$ | BOC | - |
| EPOFIX epoxy resin | Struers | - |
| EDTA | Lancaster | 99 % |
| $H_2O_2$ | BDH | 30 % w/w |
| $K_2CO_3$ | Fisher | Analytical |
| $K_4Fe(CN)_6$ | Aldrich | 99 % |
| KCl | Fisher | Analytical |
| KI | Timstar | Analytical |
| $Na_2SO_4$ | BDH | AnalaR |
| NaCl | BDH | AnalaR |
| $NaNO_3$ | BDH | AnalaR |
| $Ru(NH_3)_6Cl_3$ | Strem | 99 % |
| $PbSO_4$ | Aldrich | 99.999 % |

**Table 2.2** List of chemicals employed, purity and supplier

# Chapter 3 Pb/Pt dual electrode: A novel sensor for acoustoelectrochemistry

3

One of the key aims of the work presented in this thesis was to characterise the physical effects associated with sonication and acoustic cavitation and the correlation of these effects with the pressure field and bubble dynamics. A large part of the work involved the use of a novel dual microelectrode, which consists of lead and platinum microwires sealed in close proximity (see Section 2.2.3). Through the employment of suitable experimental conditions, it can be used as an excellent sensor for the study of acoustoelectrochemistry. Its properties and deployment are described in this chapter.

## 3.1 The concept of the dual electrode

The use of microelectrode technology is highly advantageous in the study of the effects of sonication and acoustic cavitation owing to their small size[2] and fast response times. As discussed in Section 1.6, these effects can be separated into those which affect the mass transfer characteristics of the electrode [41, 74, 77-87, 89-93] and those which lead to erosion of the electrode surface [77, 94-96, 98]. Although investigation of these phenomena has been reported previously, each process is normally considered individually. The concept of the dual electrode presented in this work is to use lead and platinum electrodes together to study the mass transfer and erosive effects of cavitation simultaneously. Lead was chosen to study erosion events as it can be easily passivated with a layer of insoluble $PbSO_4$, while platinum is an excellent material for probing mass transfer effects, using well characterised redox reactions.

## 3.2 Voltammetric characterisation

Cyclic voltammograms of the platinum and lead electrodes in a solution of 10 mM $K_4Fe(CN)_6$ and 0.75 M $Na_2SO_4$ are shown in Figure 3.1. The voltammetry at the platinum electrode shows the characteristic sigmoidal shape for the oxidation of $Fe(CN)_6^{4-}$ at a microelectrode, with a well defined plateau signifying

[2] Relative to cavitation bubbles expected, which are anticipated to have maximum radii (during pulsations) of at least 100-200 of microns (see Figures 1.1 and 1.2).

a mass transfer limited reaction from +0.3 to +0.7 V *vs.* SCE. At the lead electrode there is a large anodic peak (labelled A), due to the oxidation of Pb metal to insoluble $PbSO_4$ at -0.45 V *vs.* SCE. At potentials more positive than this the lead electrode is essentially passivated and there is no current following. The corresponding reduction peak (labelled B) is seen on the reverse sweep of the Pb electrode at -0.7 V *vs.* SCE. The relative potentials of the electroactive regions associated with both electrode materials are important and, together with other properties make this dual electrode a powerful tool for the study of acoustoelectrochemistry. These are discussed in the following section.

## 3.3 Properties of the dual electrode

Consider the voltammetry shown in Figure 3.1 and in particular two potential regions (labelled 1 and 2 respectively). At all potentials positive of -0.45 V *vs.* SCE the Pb electrode is covered with a layer of $PbSO_4$, which is essentially insoluble. Hence, in this state it can be used to detect erosive events, which have been associated with inertial cavitation [98].

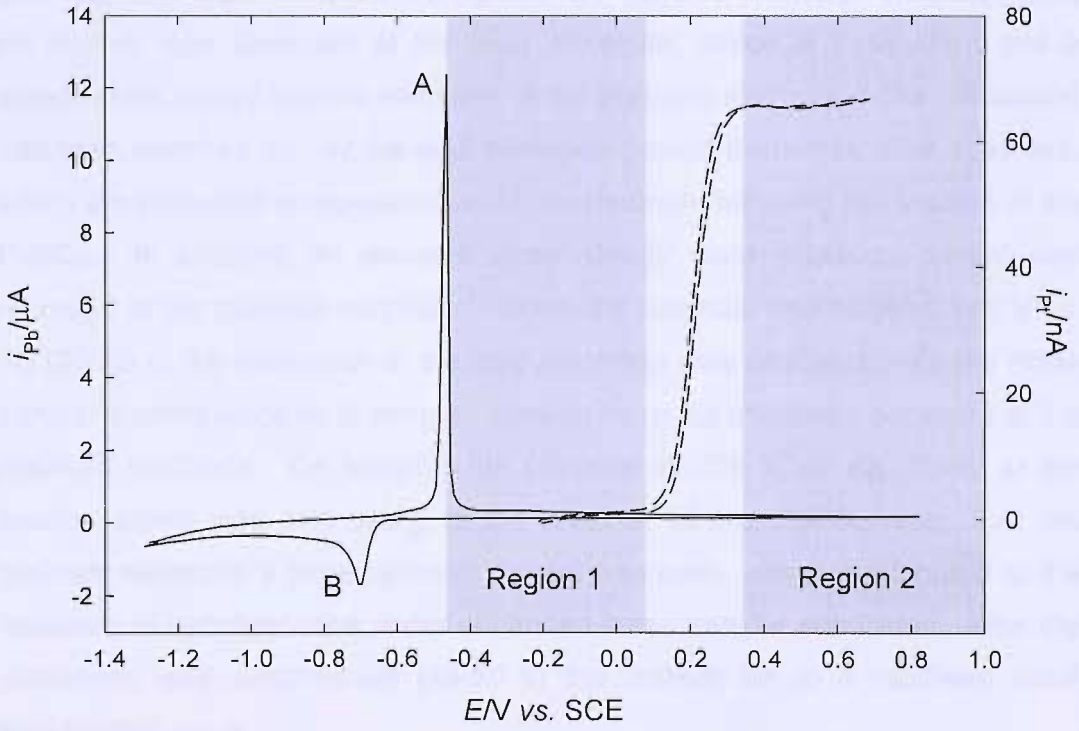


**Figure 3.1** Cyclic voltammogram of the 125 μm diameter lead disc (—) and 50 μm diameter platinum disc (– –) of the dual electrode in a solution containing 10 mM $K_4Fe(CN)_6$ and 0.75 M $Na_2SO_4$. For lead the sweep rate was 50 mV $s^{-1}$ and for platinum the sweep rate was 5 mV $s^{-1}$. Both experiments were performed under aerobic conditions at 25 ± 1 °C.

In contrast, there are important differences in the electrochemistry occurring at the platinum electrode in the two regions. In region 1 there is no net current flowing, while in region 2 there is a mass transfer limited current for the oxidation of ferrocyanide ions. If the potential of the platinum electrode is held in region 1 it is insensitive to mass transfer effects. However, if the potential of the platinum electrode is held in region 2 (*i.e.* positive of +0.35 V *vs.* SCE) it acts as a sensor sensitive to all hydrodynamic processes associated with sonication. In general these are seen as increased current due to enhancements in mass transfer caused by acoustic streaming, bubble oscillation and other bubble motion (see Section 1.6.1).

The location of these potential regions means that this dual electrode has the capability to detect both erosion and mass transfer effects of sonication and cavitation. However, the mass transfer component can be 'switched on and off' through control of the applied potential. This effect can be seen in Figure 3.2, which shows the current recorded simultaneously at the lead and platinum electrodes under various potential conditions. In the first 10 seconds the potential[3] was held at +0.8 V *vs.* Ag and the ultrasound was off. As expected, no current was observed at the lead electrode, which is passivated and a steady state anodic current was seen at the platinum electrode. The ultrasound was then switched on. At the lead electrode current transients were observed, which are attributed to repassivation of the electrode following the erosion of the $PbSO_4$. In addition, an elevated quasi steady state oxidation current was recorded at the platinum microdisc. When the potential was stepped to 0 V *vs.* Ag (20-30 s) the behaviour of the lead electrode was unaffected but the mass transfer current dropped to zero, as there is no redox chemistry occurring at the platinum electrode. On stepping the potential to -0.8 V *vs.* Ag (30-40 s) the erosion signal was lost owing to the removal of the $PbSO_4$ layer. At the platinum electrode a large cathodic current was seen, which is attributed to the reduction of hydrogen ions under enhanced mass transfer conditions. After the ultrasound was switched off (40-50 s) the current fell to a relatively small steady-state value.

[3] Ag wire was used as a counter/reference electrode. The potential of the wire was measured to be +0.04 V *vs.* SCE under the conditions employed here.

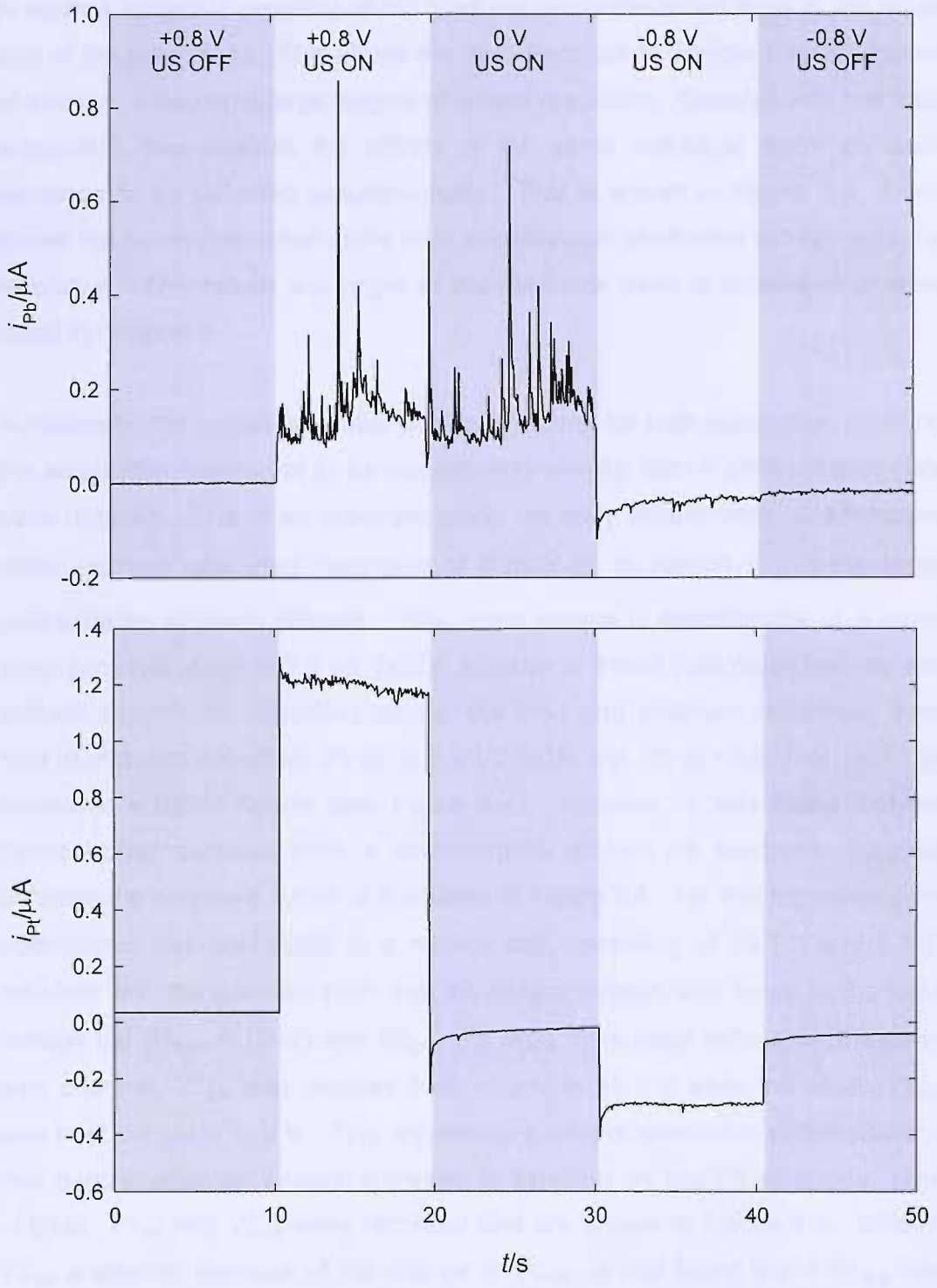


**Figure 3.2** Current-time traces from lead (125 μm diameter, upper plot) and platinum (50 μm diameter, lower plot) discs of the dual electrode under various experimental conditions recorded at low temporal resolution. The electrode-to-horn separation was 1.4 mm. The solution contained 20 mmol $dm^{-3}$ $K_4Fe(CN)_6$ and 0.75 mol $dm^{-3}$ $Na_2SO_4$ and the experiment was performed under aerobic conditions at 25 ± 1°C. The ultrasound frequency was 22.83 kHz and the power was 56 ± 5 W $cm^{-2}$.

A second attractive property of the dual electrode described here is the small size of the microdiscs. This allows the dual electrode to sample a small volume of solution, affording a large degree of spatial resolution. Coupled with fast data acquisition, this enables the effects of the same individual event on each electrode to be detected simultaneously. This is shown in Figure 3.3, which shows the current recorded at the lead and platinum electrodes at high temporal resolution. The nature and origin of the response seen is discussed in more detail in Chapter 5.

Additionally, the applied potential can be the same for both electrodes, enabling the acquisition electronics to be considerably simpler than if different potentials were required. This is an important point. In early experiments an alternative redox reaction was used (reduction of $Ru(NH_3)_6^{3+}$ to $Ru(NH_3)_6^{2+}$) in the same concentrated sulphate solution. This redox couple is electroactive at a much lower potential ($E_{1/2}$= -0.2 V *vs.* SCE). In order to detect both mass transfer and surface erosion, as described above, the lead and platinum electrodes were held at different potentials (Pt at -0.5 V *vs.* SCE and Pb at +0.8 V *vs.* SCE) by means of a bipotentiostat (see Figure 3.4). However, it was found that the bipotentiostat suffered from a considerable amount of electronic coupling between the channels, which is illustrated in Figure 3.5. For this experiment the potentiostat was connected to a dummy cell consisting of 10 kΩ and 1 MΩ resistors with the gain set such that the output voltage was equal to the input voltage (*i.e* $R1_{gain}$.= 10 kΩ and $R2_{gain}$ = 1 MΩ). The input voltage on the lower gain channel, $V1_{app}$ was stepped from –1.2 V to +1.0 V while the other, $V2_{app}$ was kept constant at 0 V. This represents a simple simulation of the situation that occurs when an erosion transient is detected on the Pb electrode. The outputs, $V1_{out}$ and $V2_{out}$ were recorded and are shown in Figure 3.5. Clearly, $V2_{out}$ is affected because of the change in $V1_{out}$. It was found that if $V1_{app}$ was stepped in the opposite sense (*i.e.* from high voltage to low voltage) the spike in $V2_{out}$ also changed direction. This electronic coupling problem is compounded if a reductive redox probe is employed. An anodic current transient, generated by the repassivation of the lead electrode leads to a 'cathodic' event due to electronic coupling and it is impossible to discern genuine mass transfer transients from artefacts. It is therefore desirable to employ an oxidative redox

probe, as used in this work, in order to distinguish genuine mass transfer events from electronic coupling.

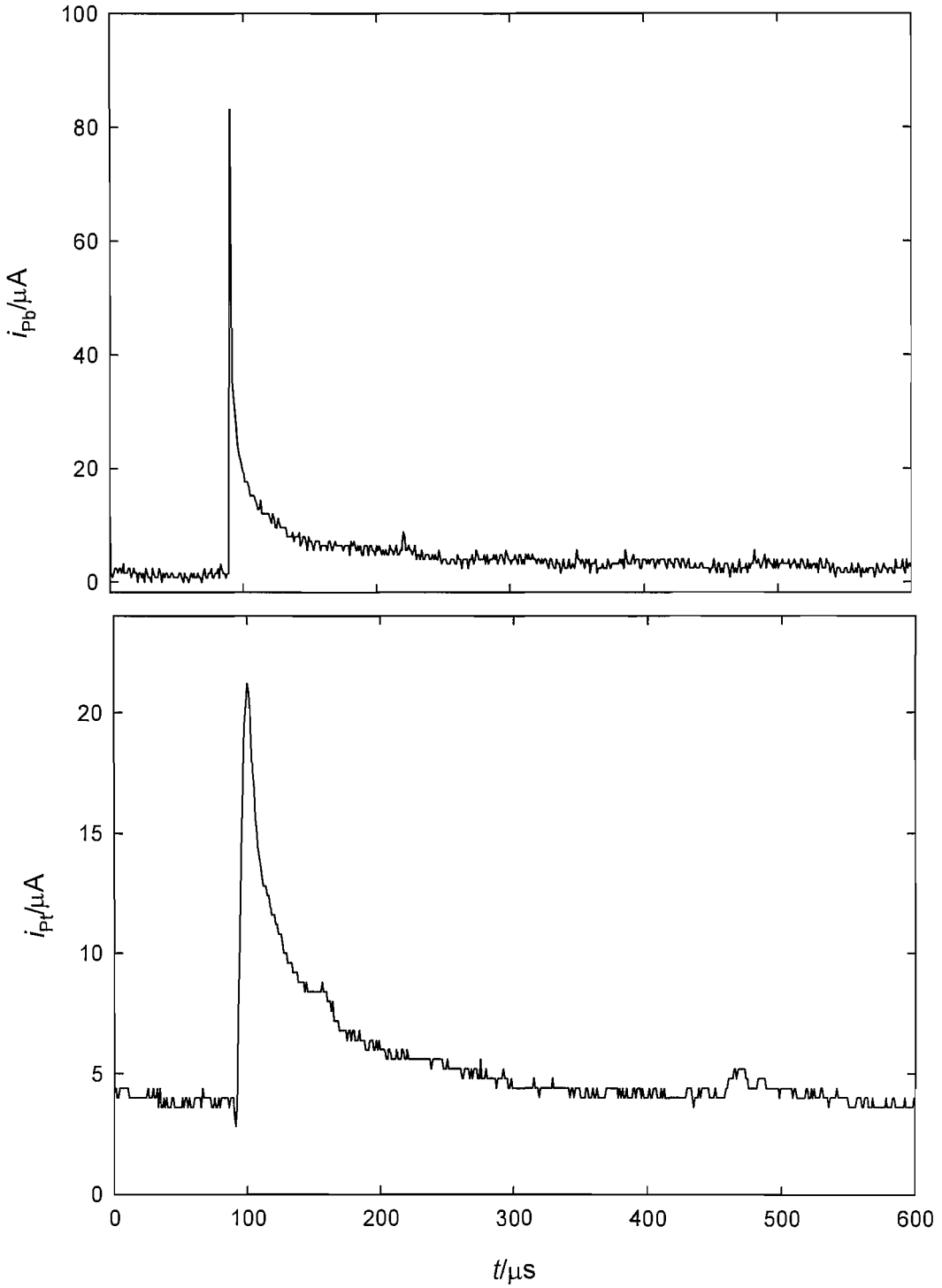


**Figure 3.3** Current traces from lead (125 μm diameter, upper plot) and platinum (50 μm diameter, lower plot) discs of the dual electrode under exposure to ultrasound. The electrode-to-horn separation was 1.4 mm. The solution contained 20 mmol $dm^{-3}$ $K_4Fe(CN)_6$ and 0.75 mol $dm^{-3}$ $Na_2SO_4$ and the experiment was performed under aerobic conditions at 25 ± 1°C. Both electrodes were held at +0.8 V *vs.* Ag. The ultrasound frequency was 22.83 kHz and the power was 56 ± 5 W $cm^{-2}$.

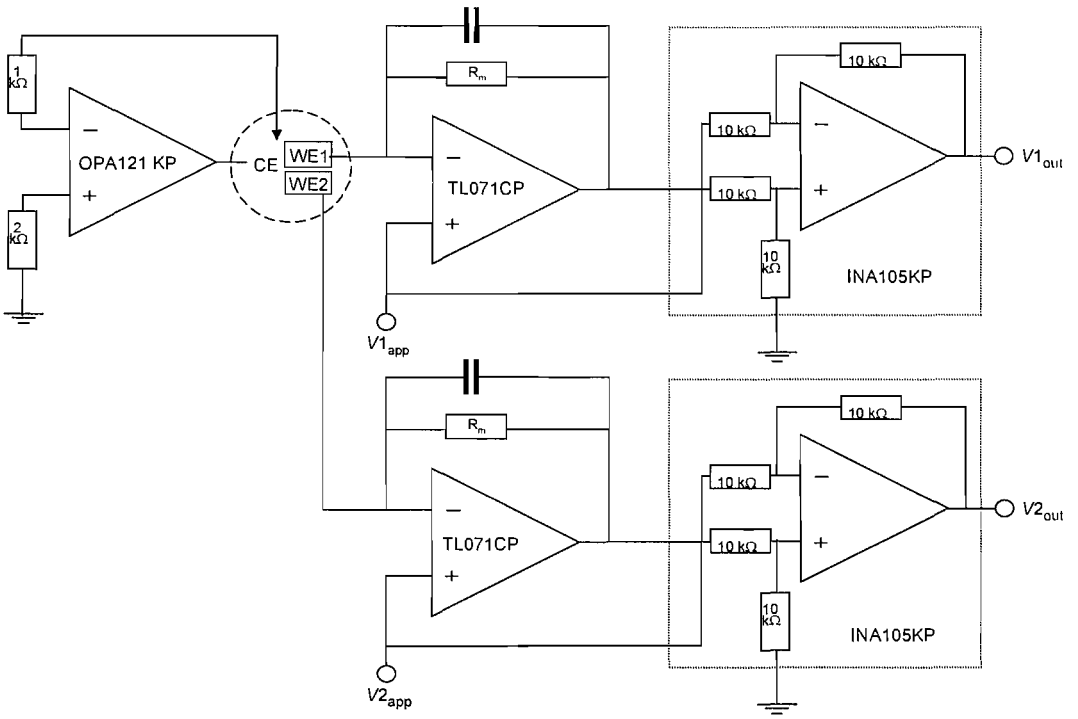


**Figure 3.4** Circuit diagram of the bipotentiostat used for initial experiments.

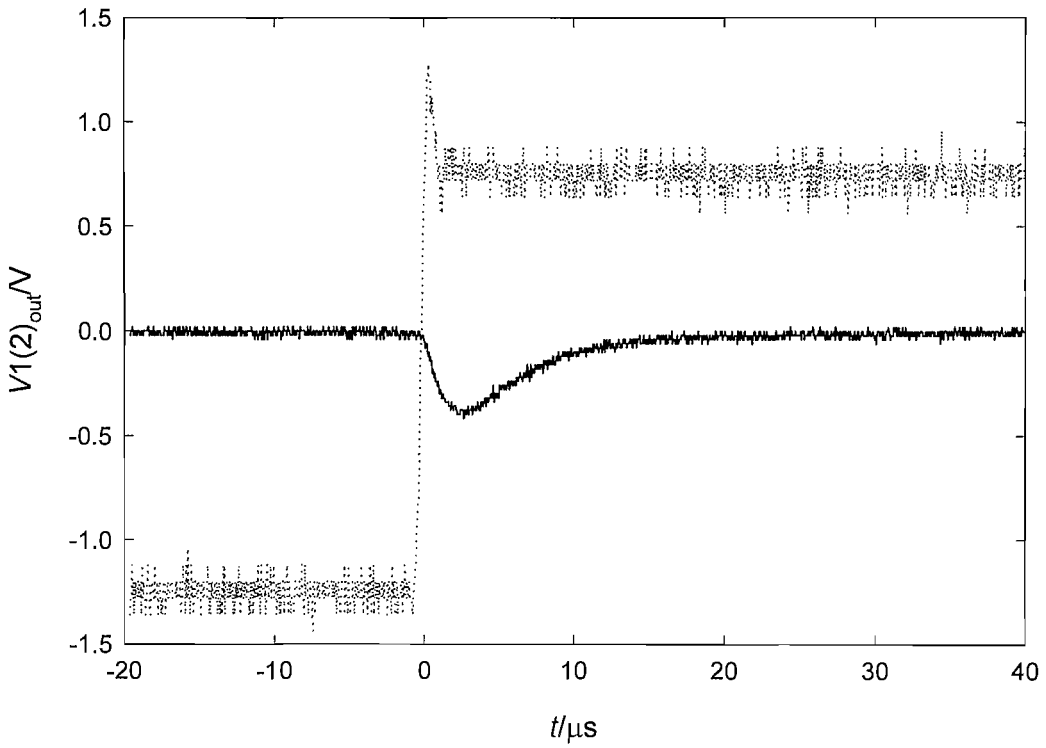


**Figure 3.5** Plot showing the output of the bipotentiostat following a step in $V1_{app}$ (-1.2 V to +1.0 V). (····) shows $V1_{out}$ and (—) shows $V2_{out}$. $V2_{app}$ was kept constant at 0 V. The gain for channel 1 was 10 kΩ and the gain for channel 2 was 1 MΩ.

## 3.4 Confirmation of the erosion mechanism

In Chapter 4, the dual electrode will be used to probe a region close to the tip of the ultrasonic horn. The lead electrode will be employed as a sensor for erosive processes in an attempt to locate the inertial cavitation threshold in terms of distance from the tip of the horn. Although current transients recorded at a passivated lead electrode have been reported previously [98] and associated with erosive processes caused by inertial cavitation events, it is important to consider other possibilities. It has recently been suggested that the transient current increase is due to an accelerated dissolution mechanism rather than an erosion process. The origin of the transient current increase is discussed in this section.

Although $PbSO_4$ is relatively insoluble in water there will be limited dissolution. The concentration of $Pb^{2+}$ ions in solution at the $PbSO_4/Na_2SO_4$ interface can be calculated from the solubility product.

$$K_{SP} = [Pb^{2+}][SO_4^{2-}] = 1.82 \times 10^{-8} \text{ mol}^2 \text{ dm}^{-6} \qquad (3.1)$$

The concentration of sulphate in solution is 0.75 M and hence the concentration of dissolved lead ions at the surface of the sulphate modified electrode is $2.43 \times 10^{-11}$ mol $cm^{-3}$. If the action of a cavitation event is to replace this lead-rich liquid with lead-free solution, then a transient current increase may be observed as a result of accelerated dissolution of the $PbSO_4$. However, this seems unlikely for a number of reasons. First, the timescale of a dissolution process would be expected to be longer than the very rapid event shown in the upper trace in Figure 3.3. Second, the charge associated with the current transient in the upper trace of Figure 3.3 is 2.7 nC. Using Faraday's law and the concentration of lead ions given above (Equation 3.1), this equates to a volume of lead-rich solution of $5.8 \times 10^8$ $\mu m^3$ or assuming hemispherical geometry, a hemisphere of radius 650 µm. This represents an unrealistic physical scenario. It is unfeasible that this volume of lead-rich solution could be replaced by lead free solution in a transient fashion so as to result in the short time scale current responses such as that shown in the upper trace of Figure 3.3. There is continuous mixing in the cell, caused by acoustic streaming (which is expected to remain constant with time). This would result in a steady state current enhancement rather than the transient responses seen here.

However, in order to prove that dissolution cannot account for the transients recorded at the Pb electrode two experiments were performed. First, a dual electrode was constructed, which consisted of two lead wires rather than lead and platinum (see Section 2.2.4). The potential of both discs was held at +0.8 V *vs.* SCE and the electrode was exposed to ultrasound as above. If the accelerated dissolution mechanism was correct, it would be impossible to detect current transients at only one of the electrodes because overlap of the lead-rich hemispheres described above (Figure 3.6 shows the hemispheres drawn to scale).

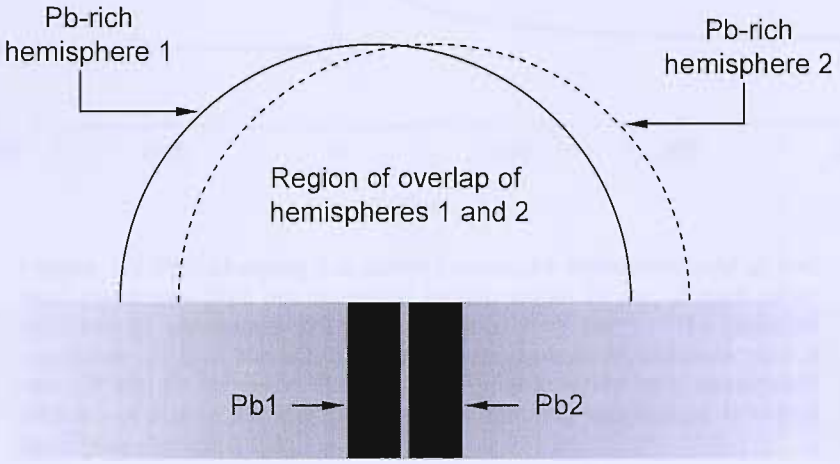


**Figure 3.6** Scale drawing of the 'lead-rich' hemispheres which would be necessary if the accelerated dissolution mechanism was feasible.

However, Figure 3.7 (which shows the current recorded at both discs simultaneously) demonstrates that this is not the case. Current transients were recorded at only one of the lead microdiscs. In a second experiment the 0.75 M $Na_2SO_4$ solution was saturated with $PbSO_4$. Under these conditions there can be no dissolution and as such the alternative mechanism predicts that no current transients can be recorded. This was found not to be the case, and transients similar to those shown in Figure 3.3 and 3.7 were recorded. Finally, if an enhanced mass transfer-based accelerated dissolution was responsible it may be expected that an elevated background current would be observed, due to continual dissolution of the $PbSO_4$ layer. However, inspection of Figure 3.7 shows that outside the occurrences of anodic transients there is no current flowing. This confirms that the origin of such responses is an erosion-based mechanism.

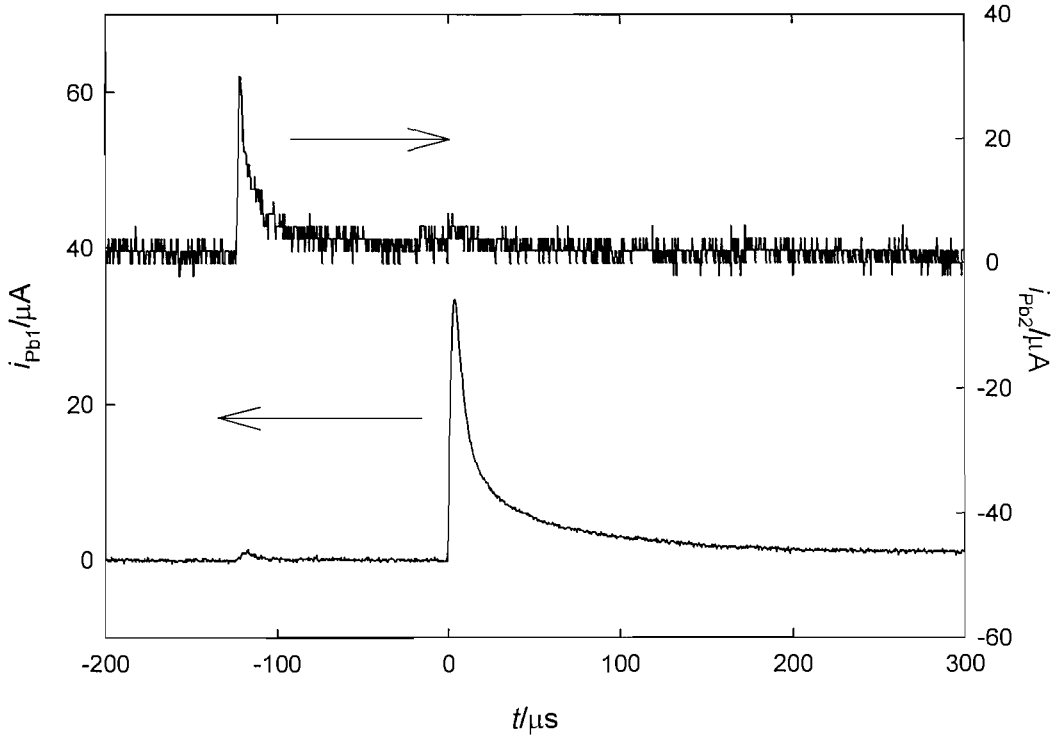


**Figure 3.7** Plot showing the current recorded simultaneously at two lead electrodes (125 μm diameter) sealed within 20 μm of each other exposed to ultrasound (22.83 kHz, 56 ± 5 W $cm^{-2}$). The solution contained 0.75 M $Na_2SO_4$ and the electrode-to-horn distance was 1 mm. It should be noted that the low signal to noise ratio associated with $i_{Pb2}$ is due to the low gain of the measuring electronics, which is fixed (see Section 2.2.2).

## 3.5 Estimation of the eroded area

In order to estimate the area eroded by a cavitation event, the procedure detailed in reference [98] was employed. Briefly, the area eroded can be calculated by comparing the charge passed during the repassivation of the surface following a cavitation event with the charge passed during passivation of the entire electrode following a potential step (assuming that double layer charging is negligible and that the cavitation event removes the entire thickness of the passivating layer). The charge consumed by the transient shown in the upper plot of Figure 3.3 (in the first 100 μs) was 1.13 nC. This compares with the charge consumed (in the first 100 μs) following a potential step from -0.8 V *vs.* SCE (where bare lead exists, see Figure 3.1) to +0.8 V *vs.* SCE (the potential employed in Figure 3.3) of 239 ± 5 nC. Given that the area of the entire electrode is ~12300 $\mu m^2$, the area removed by the cavitation event can be calculated to be approximately 58 $\mu m^2$. If the eroded area is considered to be circular this is equates to a radius of ~4 μm (7 % of the radius of the entire

electrode). It was not possible to image any individual erosion sites. However, erosion over the entire surface of the lead electrode can be clearly seen in Figure 3.8, which shows an SEM of the dual electrode following exposure to ultrasound (22.83 kHz, 56 ± 5 W $cm^{-2}$) for 500 s at an electrode-to-horn distance of 1.4 mm.

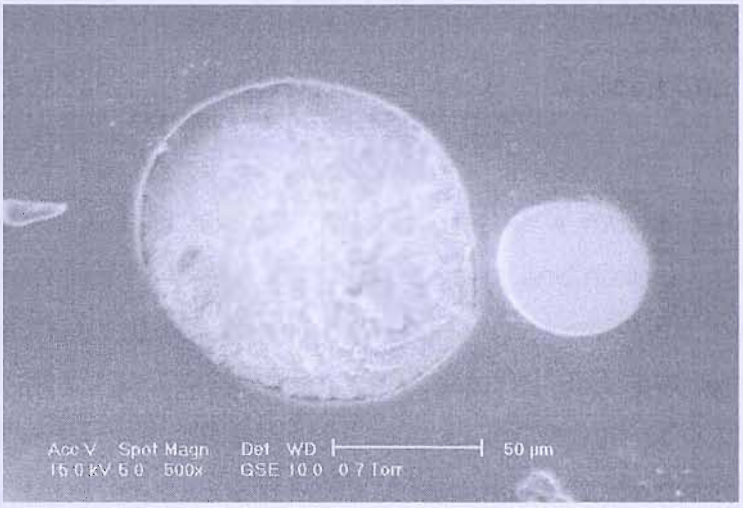


**Figure 3.8** SEM of the surface of the lead/platinum dual electrode following exposure to ultrasound (22.83 kHz, 56 ± 5 W $cm^{-2}$) for 500 s at an electrode-to-horn distance of 1.4 mm.

## 3.6 Conclusions

In this chapter a novel sensor for use in acoustoelectrochemical experiments has been introduced. Its capability to detect the erosion and mass transfer effects associated with sonication simultaneously has been shown briefly. It should be noted that the nature of these responses (and others) will be discussed in more detail in Chapter 5, which will correlate the responses with the local environment and bubble dynamics prevalent in the vicinity of the horn. This environment is the subject of the next chapter.

# Chapter 4 The sound field and the invasive nature of the electrode

4

In this, and the following chapter the environment prevalent in the vicinity of the ultrasonic horn is discussed, in terms of the sound field generated and the nature of the cavitation present. Bubble behaviour is highly dependent on the local physical conditions at the nucleation point and in particular the local acoustic pressure amplitude. In order to derive meaningful conclusions based on experimental results, it is therefore vital to consider the sound field generated by the sound source. In this chapter a model, based on those available in standard texts [30, 162] is discussed, and pressure measurements are presented from both above and below the inertial cavitation threshold. Two experiments (one based on sonoluminescence and the other a novel electrochemical experiment) designed to map the extent of inertial cavitation within the electrochemical cell are described and the comparisons with the sound field model made.

## 4.1 Theoretical sound field

The experimental set-up used in this work consists of a vibrating horn with a tip radius of 1.5 mm, submerged to a depth of ~15 mm, operating at a frequency of ~23 kHz. Under these conditions the tip of the horn is less than a wavelength from the surface of the liquid. An appropriate approximation for sound field modelling purposes would therefore be a rigid disc baffled by a free surface (although it is noted that the horn will distort the air/liquid interface). Simulation of this complex scenario is beyond the scope of this work. For the purpose of the work presented here the sound source will be represented as a rigid disc within a rigid baffle oscillating with simple harmonic motion at circular frequency, $\omega$. The entire surface of the disc is assumed to oscillate in phase and with the same amplitude. This arrangement is widely discussed in the acoustic literature (see, for example [162, 163]). It will be shown later that this is a reasonable approximation for the experimental set-up used here.

### 4.1.1 Three-dimensional pressure field

In order to calculate the three dimensional pressure field, the disc can be subdivided into an array of surface elements of area $dS$, which act as point

sources, each emitting spherical waves. The baffled nature of the disc means that acoustic emissions that are not emitted into the liquid are reflected. Thus all the acoustic energy is projected into the half-space in front of the disc. With reference to Figure 4.1, the contribution of a source, d$S$ on the disc to the pressure at a point A, which lies in the XZ plane at a distance, $r$ from d$S$ is

$$dP \propto \frac{e^{j(\omega t - kr)}}{r} dS \tag{4.1}$$

The total pressure at A is found by simply summing all the point sources over the surface of the disc

$$P \propto \int_S \frac{e^{j(\omega t - kr)}}{r} dS \tag{4.2}$$

where from Figure 4.1, $r = \sqrt{(x_A - x)^2 + y^2 + z_A^2}$ .

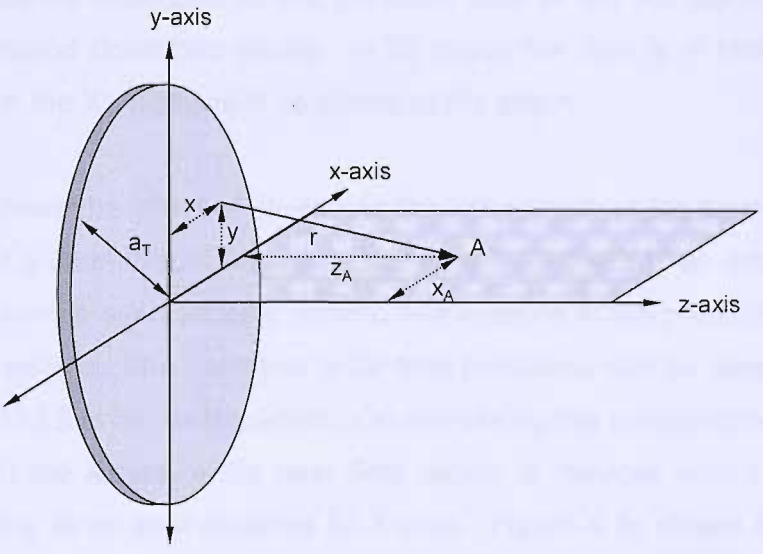


**Figure 4.1** Geometry used in the calculation of the pressure field generated by a baffled disc.

Through numerical evaluation of this integral in a plane perpendicular to the disc and passing through the centre, the entire pressure field can be calculated. The circular symmetry of the disc implies that pressure field calculated for one plane is the same for all such planes, and hence the entire pressure distribution can be described. There are two important extremes to consider. If the point A is close to the disc then, depending on the wavelength of the sound and the

radius of the disc, the difference in the path length from the point sources to the observer (point A) can be significant. In this situation constructive and destructive interference due to phase differences in the waves arriving at the observation point lead to a complicated pressure field with local minima and maxima. This is the near field region. In contrast, far from the disc the path difference is negligible compared with the wavelength, the waves are essentially in phase and the pressure field displays a simple decay with distance due to geometrical spreading of the acoustic power. This is the far field region. The extent of the near field region is dependent on the overall size of the sound source and the wavelength. For a disc the transition from near to far field behaviour occurs at an axial distance, $r_{ax} = a_T^2/\lambda$, where $a_T$ is the radius of the disc. For sound where the wavelength is short compared to the radius of the source the near field is extensive, whereas at longer wavelengths the near field only exists close to the disc, if at all. As the wavelength becomes much larger than the radius of the disc there are effectively no near field characteristics in the pressure profile. This evolution in behaviour can be clearly seen in Figure 4.2, which shows examples of the pressure field in the XZ plane, calculated using the method described above. In all cases the disc is of radius 20 units and is lying in the XY plane with its centre at the origin.

Figure 4.2 shows the effect of increasing the wavelength of the sound from (a) 3 units to (b) 7.5 units to (c) 300 units. In Figure 4.2a there is an extensive near field, which can be seen as local minima and maxima in the pressure amplitude close to the source. The transition to far field behaviour can be seen at an axial distance of 133.3 units, as expected. On increasing the wavelength to 7.5 units (Figure 4.2b) the extent of the near field region is reduced with the transition point occurring at an axial distance 53.3 units. Figure 4.2c shows the pressure field in the case where the wavelength is much greater than the radius of the disc. Here, there is no near field and the pressure is greatest at the surface of the disc and decays as the distance from the surface increases. This is the situation which is expected under the experimental conditions used in this work, where the wavelength of the ultrasound employed (~7 cm) is much larger than the radius of the tip of the horn (1.5 mm).

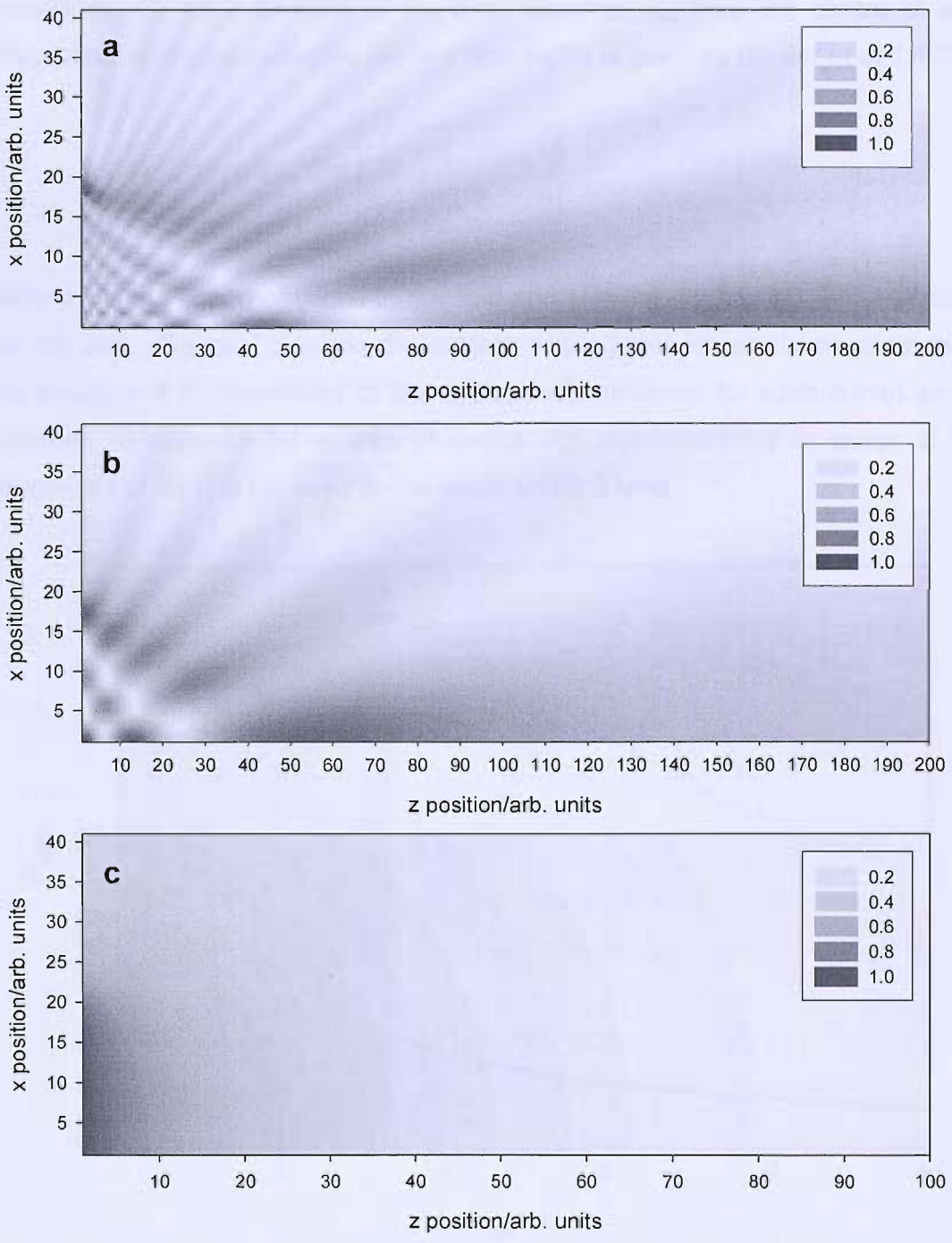


**Figure 4.2** Greyscale plots showing the pressure field generated in the XZ plane by a baffled disc of radius 20 units, lying in the xy plane centred on the origin. **(a)** $\lambda = 3$ units. **(b)** $\lambda = 7.5$ units. **(c)** $\lambda = 300$ units. The legend shows the pressure amplitude normalised to the maximum pressure amplitude for each plot.

### 4.1.2 Axial pressure profile

The three-dimensional representation of the pressure field given in the previous section is useful in visualising its form; however it is also helpful to consider the axial pressure profile more closely. A useful analytical solution for the pressure

amplitude, $P_A$ as a function of the axial distance, $r_{ax}$ from the centre of an oscillating rigid disc, radius $a_T$ within a rigid baffle is given by Kinsler *et al.* [162].

$$P_A = 2\rho cU\left|\sin\left\{\frac{kr_{ax}}{2}\left[\sqrt{1+\left(\frac{a_T}{r_{ax}}\right)^2}-1\right]\right\}\right| \qquad (4.3)$$

where $c$ is the speed of sound in the fluid and $U$ is the amplitude of the velocity of the disc. Figure 4.3 shows the axial acoustic pressure amplitude predicted by Equation 4.3 (normalised to the appropriate maximum for each curve) as a function of distance for a disc of radius 1.5 mm operating in water at a frequency of 23 kHz (as used in this work) and 2.3 MHz.

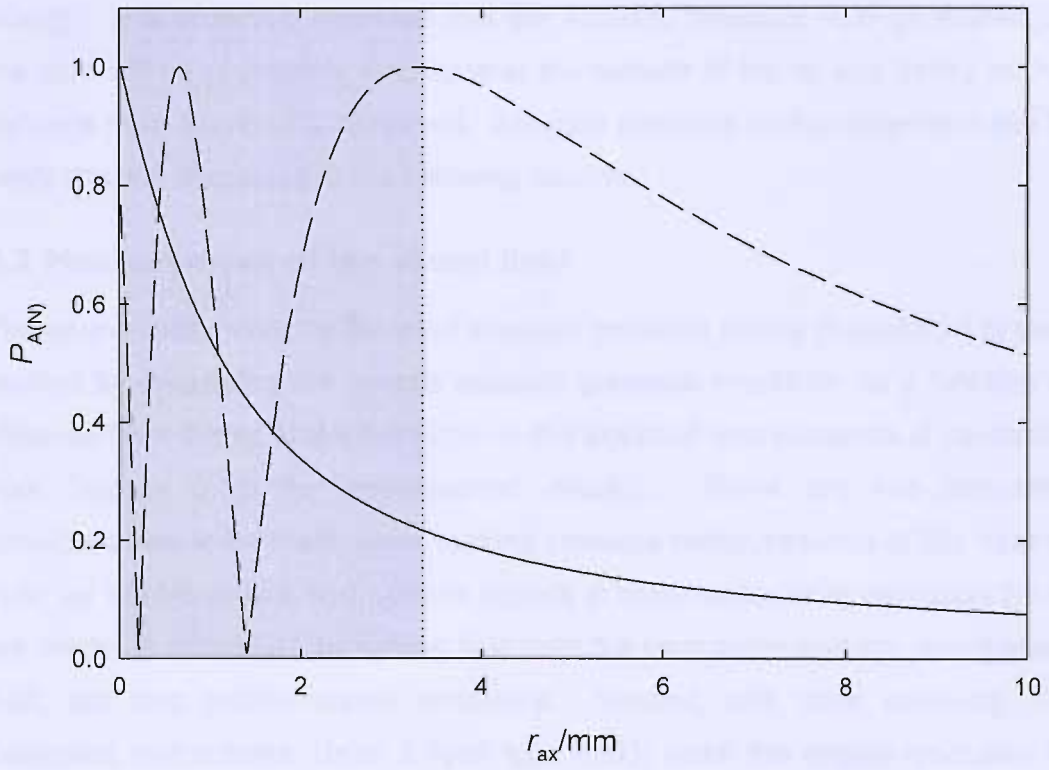


**Figure 4.3** Plot showing the axial acoustic pressure amplitude (normalised to the appropriate maximum for each curve), $P_{A(N)}$ as a function of the axial distance from the tip of the horn, $r_{ax}$. Calculated for a disc of radius, $a_T$ = 1.5 mm operating in water ($c$ = 1480 ms$^{-1}$, $\rho$ = 1000 kg m$^{-1}$) at frequency of 2.3 MHz (- - - ) and 23 kHz (—). The dotted line (·····) indicates the transition from near field to far field behaviour for the 2.3 MHz case.

Again it is possible to consider near and far field behaviour. The 2.3 MHz case exhibits near field behaviour (indicated by the shaded region in Figure 4.3), displaying local maxima and minima. The locations of the maxima and minima

in terms of axial distance from the centre of the disc are given by Equation 4.4 [162],

$$r_{ax(m)} = \frac{4a_T^2 - m^2\lambda^2}{4m\lambda} \tag{4.4}$$

where $m$ represents an integer value. Maxima are observed for $m$ = 1,3,5... and minima for $m$ = 0,2,4... The position of $r_{ax(1)}$ (in this case 3.34 mm, shown by the dotted line in Figure 4.3) demarcates the near field from the far field. In the lower frequency case however, the wavelength is much longer than the radius of the disc and there is no near field ($r_{ax(1)}$ is not physically real). In this situation (as in Figure 4.2c) the pressure amplitude is greatest at the surface of the disc and decays with distance due to geometric spreading of the acoustic energy. It is therefore expected that the acoustic pressure field generated by the horn will be of greatest amplitude at the surface of the tip and decay as the distance from the horn is increased. Acoustic pressure measurements made to verify this are discussed in the following section.

## 4.2 Measurement of the sound field

The sound field model for the axial acoustic pressure profile (Equation 4.3) was verified by measuring the on-axis acoustic pressure amplitude as a function of distance from the tip of the horn both in the absence and presence of cavitation (see Section 2.3.1 for experimental details). There are two important considerations to be made when making pressure measurements of this nature. First, as will be shown, hydrophone signals in continuous-wave cavitation fields are made up of not just the driving field from the transducer and any reverberant field, but also bubble-related emissions. Second, and more seriously, the calibrated hydrophone (Brüel & Kjær type 8103) lacks the spatial resolution to measure acoustic pressures close to the tip of the horn with sufficient accuracy. The active element of the hydrophone is a 6 mm × 6 mm hollow cylinder which, considering the pressure field profile expected (solid line in Figure 4.3) is too large to make meaningful measurements in the region close to the tip of the horn as a result of spatial averaging. Of course smaller hydrophones are available but in general they lack the robustness necessary to survive the harsh conditions generated in a cavitation field. For these reasons pressure measurements were made at large distances (>5 mm) from the tip of the horn

(where the pressure gradients are smaller) and the data fitted to Equation 4.3, to yield a calibrated axial pressure profile. Also, the measurements were made in a large water tank (1 m × 2 m × 1 m) in order to minimise the reverberant field. This allows comparison with the model described in Section 4.1.2, which assumes free field conditions.

### 4.2.1 Below the inertial cavitation threshold

Initially, the pressure was measured below the inertial cavitation threshold. This was achieved by applying a low drive voltage to the transducer such that the pressure signal was purely sinusoidal and there were no audible or visual signs of inertial cavitation. The sinusoidal nature of the pressure wave was confirmed by FFT analysis of the signal, which showed a single peak at the driving frequency. The measured acoustic pressure amplitude is shown as a function of axial distance in Figure 4.4.

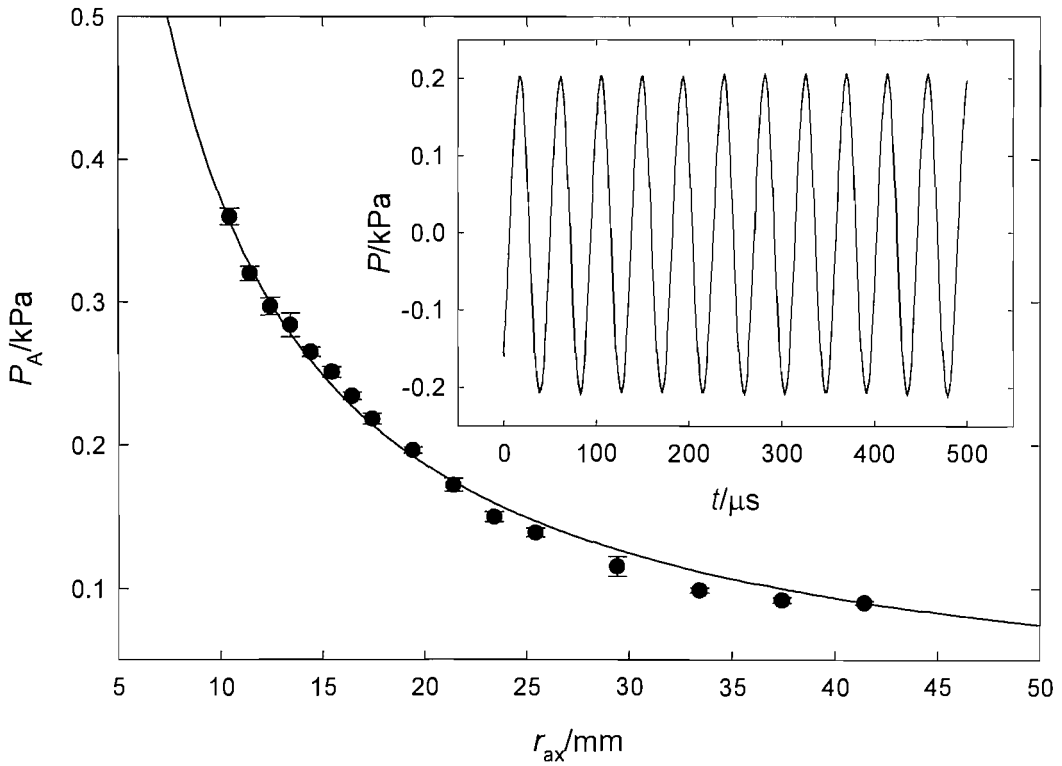


**Figure 4.4** Plot showing the acoustic pressure amplitude as a function of axial distance, $r_{ax}$ in the absence of any inertial cavitation. (•) represent the experimental points and (—) is the curve fit to Equation 4.3. The error bars are 95% confidence limits based on 5 measurements. **Insert** Plot showing an example of the pressure signal recorded at a distance of 17.4 mm.

The insert to Figure 4.4 shows an example of the pressure signal recorded at an axial distance[4] of 17.4 mm. The solid line in the Figure 4.4 represents the fit of Equation 4.3 to the experimental data, preformed using commercial graphing software (SigmaPlot, SPSS Inc.). The parameters used for the fitting routine were; $\rho$ = 1000 kg $m^{-3}$, $f$ = 22800 Hz, $c$ = 1480 m $s^{-1}$, $U$ was allowed to vary. A good fit to the data was achieved (residuals were all less than 0.01 kPa). However, although the shape of the curve fits well, there is uncertainty in the absolute magnitude of each point. This uncertainty arises because the experimental set-up used here does not comprise of a rigid disc within a rigid baffle, as modelled by Equation 4.3. Rather the baffle is a free surface (the liquid-air interface).

In order to investigate the discrepancy introduced through this assumption, the pressure was measured in the presence of a rigid baffle as a function of distance (see Section 2.3.2 for full details). This was then compared to the pressure measured using the experimental set-up employed throughout the research presented this thesis. This is shown in Figure 4.5. The open circles (○) show the pressure recorded using the experimental set-up used throughout this thesis (a horn immersed to a depth of 15 mm). The dashed line (– – –) shows the fit of these data to Equation 4.3. The closed circles (●) show the pressure measured in the presence of a rigid baffle. The solid line (—) shows the fit of these data to Equation 4.3. The values used in the curve fitting routines were $\rho$ = 1000 kg $m^{-3}$, $f$ = 22800 Hz, $c$ = 1480 m $s^{-1}$, $U$ was allowed to vary. In both cases good fits were achieved (residuals were all less than 0.01 kPa). In the absence of the rigid baffle, the pressure amplitude was found to be 78% of that recorded in its presence. However, the shape of the curve is not changed. This can be seen clearly in the insert to Figure 4.5, which shows both sets of data normalised to the baffled case through the values of $U$ generated from the curve fits. This shows that Equation 4.3 can be used to model the shape of the axial pressure profile generated by the experimental set-up used throughout this work. However, the values of $U$ obtained from curve fitting will be underestimates of the true value by 22%.

[4] For all pressure measurements reported in this work the distances quoted relate to the centre of the active element of the hydrophone.

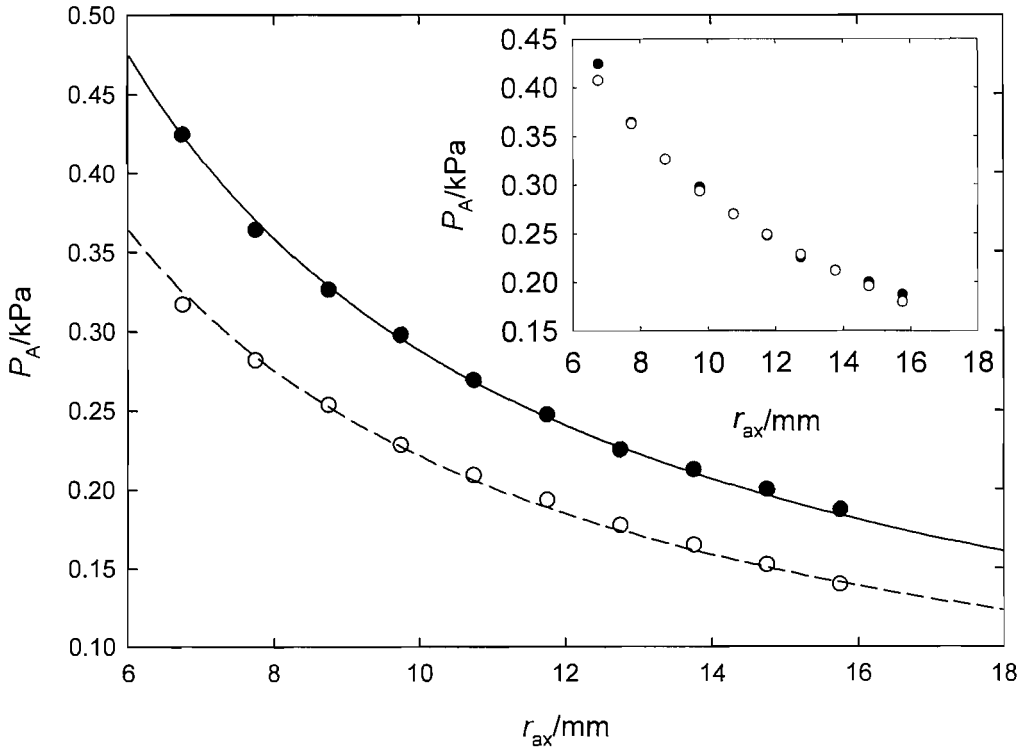


**Figure 4.5** Acoustic pressure amplitude measured as a function of distance. The open circles (○) show the pressure record under the conditions used throughout this thesis. The dashed line (– – –) shows the fit to Equation 4.3. The closed circles (●) show the pressure measured in the presence of a rigid baffle. The solid line (—) shows the fit to Equation 4.3. **Insert** The same data as in the main figure normalised to rigid baffled case.

### 4.2.2 Above the inertial cavitation threshold

In the presence of inertial cavitation the pressure signal recorded is much more complex than that seen in its absence. Figure 4.6 shows an example of the signal recorded at a distance of 8.8 mm. There is an underlying pressure wave, which is approximately sinusoidal at the driving frequency[5], superimposed with high amplitude pressure pulses every 3-4 cycles. The origin of these pulses is of fundamental importance in the understanding of the pressure field generated when the transducer is operated at high drive voltages. Shock waves produced during inertial cavitation activity have been associated with cavity cluster collapse [71, 72, 164]. These have been suggested previously by Vyas and Preece in relation to the erosion of a solid material in a cavitation cloud [164]. Vyas and Preece measured the stress in a solid surface placed below an

[5] Nominally 23 kHz. The exact frequency used was that which gave the maximum pressure amplitude (peak-to-peak/2). Although this frequency varied slightly as the horn eroded (and was polished flat) the value for the pressure maximum was found to be reproducible. Exact frequencies used are given in the appropriate figure legends.

ultrasonic horn by means of a quartz transducer and postulated that erosion of materials was dominated by a single, large shock wave emitted by the concerted collapse of a bubble cloud and not the effect of shock waves or jetting during individual bubble collapses.

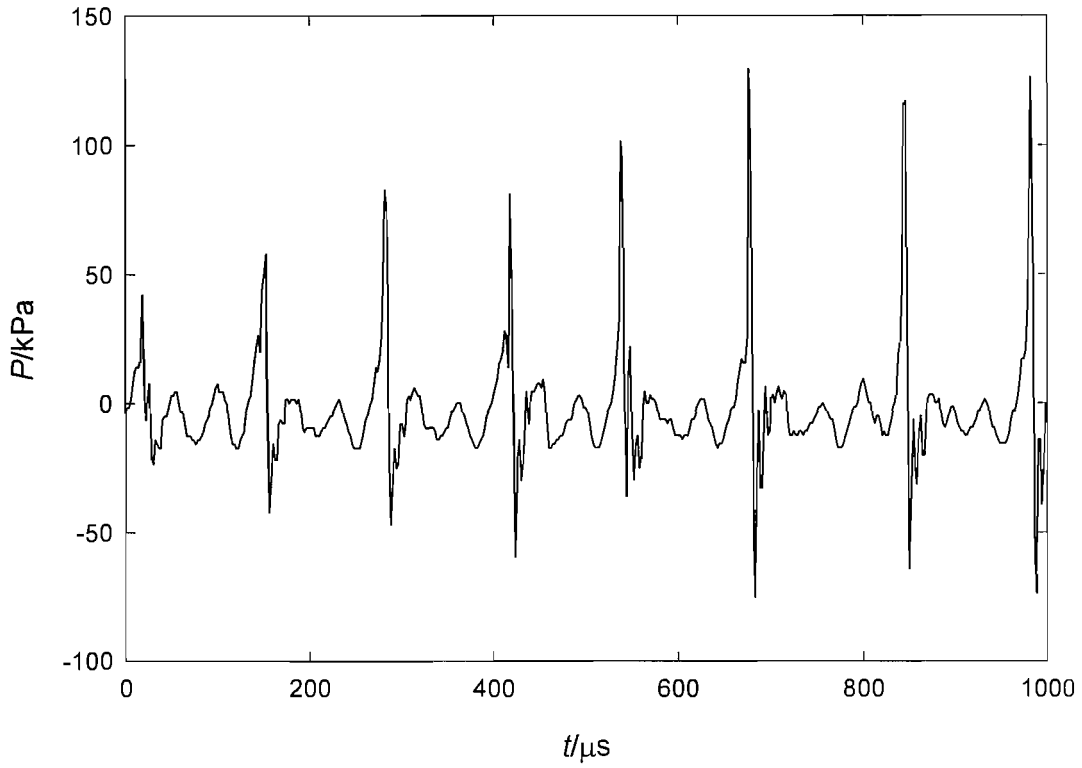


**Figure 4.6** Plot showing the pressure as a function of time in water. Recorded in the presence of inertial cavitation (as deemed by visual and audible observation). The distance between the acoustic centre of the hydrophone and the tip of the horn was 8.8 mm.

The treatment of the bubble cloud as a single entity was drawn from experimental results, which showed periodic high stress levels at the frequency of the sonication, which was observed as a sharp, well defined peak in the measured stress. Vyas and Preece argued that if the erosive effects associated with cavitation were caused by the collapse of individual bubbles the stress measured on each cycle would be more erratic. This is because, although the collapse is considered to be concerted, the exact collapse time of each bubble would depend on its location, size and other factors. Subsequently Hansson *et al.* produced models and further experimental verification of the dynamics of cavity clusters [71, 72]. In short, Hansson *et al.* proposed that clusters of bubbles collapse in such a way that the energy from an outer shell of bubbles is transferred to the neighbouring shell and so on, such that the collapse of bubbles in the centre of the cluster is extremely energetic and can cause

surface erosion. It is important to note that, in contrast to the work of Vyas and Preece, this model suggests that surface erosion is caused by individual bubble collapses; the effect of the cluster is to concentrate the energy into the final bubble collapse. In both cases however, an energetic shock wave is expected to be associated with cluster collapse and it may be that the pressure shocks reported in Figure 4.6 are the result of such events. However, this assumption must be made with caution. During the research of this thesis, the proposition was made that it is possible that the pressure spikes could be an intrinsic property of the transducer when driven at the high voltages used to generate cavitation. Rather than being the result of emission from cavitation activity, the pressure spikes could be the cause of the phenomenon (the manufacturers were unable to advise on the origin of the subharmonic signal).

In order to confirm which of the above scenarios was true, the pressure signal was measured using the same driving conditions as Figure 4.6, but in castor oil rather than water. This is shown in Figure 4.7.

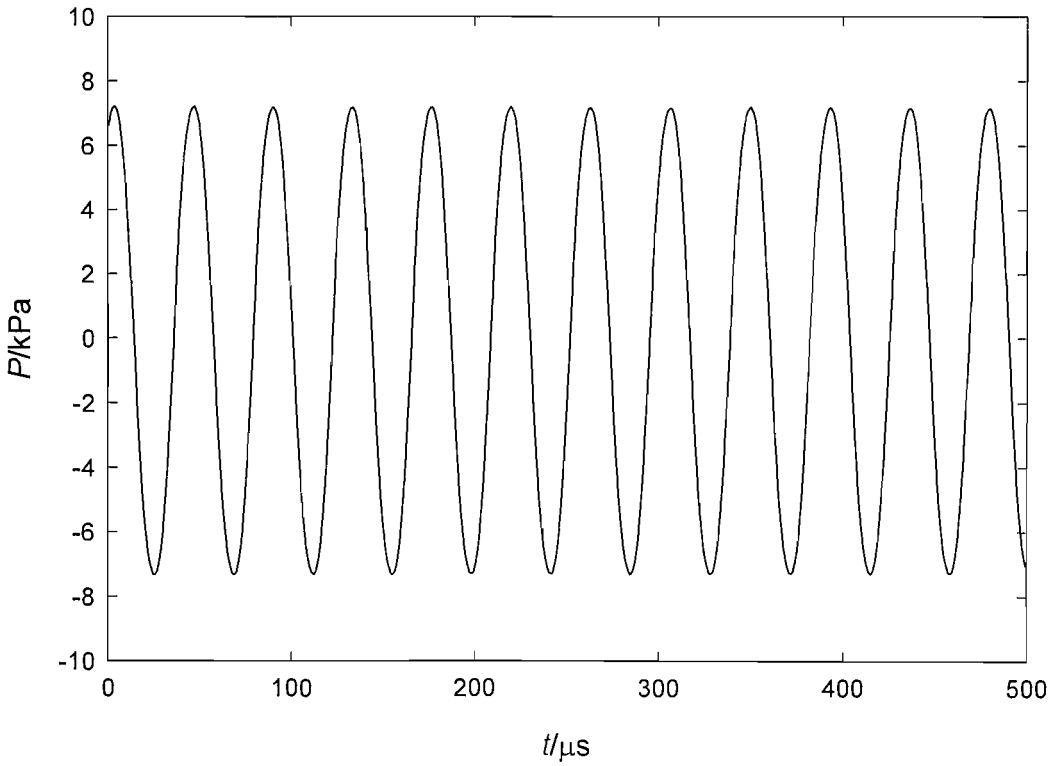


**Figure 4.7** Plot showing the pressure as a function of time in castor oil. Recorded under the same conditions as used in Figure 4.6. The distance between the acoustic centre of the hydrophone and the tip of the horn was 6.8 mm.

The large dynamic viscosity of castor oil (0.96 kg $m^{-1}$ $s^{-1}$ at 20 °C) compared to water (8.91 × $10^{-4}$ kg $m^{-1}$ $s^{-1}$ at 20 °C) means that the cavitation threshold in castor oil is significantly higher; of the order of 400 kPa at 23 kHz (calculated using the method described in Section 1.3.3). It is therefore expected that under the conditions used here, there will be no inertial cavitation and hence no third-order subharmonic signal. This is indeed the case. When the castor oil was subjected to sonication there were no audible or visual signs of cavitation and the pressure wave measured was sinusoidal at the selected drive frequency (see Figure 4.7). This confirms that the spikes seen at high drive voltages in water are not due to the properties of the transducer, but the result of emissions from the cavitation process.

Further evidence of cluster collapse and an insight into the dynamics of the process was obtained from high-speed photography. Figure 4.8 shows a sequence of 40 frames recorded at a rate of 100,000 f.p.s. The dark oblong at the top of each frame is the tip of the horn. A bubble cloud is clearly visible below the tip, which can be seen to collapse, resulting in frames in which no bubbles can be seen. The data sequence covers a total of 400 μs (~9 cycles of the driving wave) during which time three complete collapses can be seen (frames 7, 20 and 33). The fact that total collapse of the cavity cluster is not observed on every pressure cycle is consistent with previous work [71, 72]. Hansson and Mørch [71] have shown that the collapse time for a bubble cluster, $\tau$ is given by,

$$\tau = R_C \sqrt{\frac{\rho\beta}{P_0}} \tag{4.5}$$

where $R_C$ is the radius of the cluster and β is the volume fraction of cavities in the cluster at its maximum size. It should be noted that this was derived for a cluster under quasi-static pressure conditions. However, it has been applied to clusters formed during continuous wave sonication [71, 72]. In order for cluster collapse to be seen on every cycle, the collapse time must be less than half the period of the driving wave, here less than 21.9 μs. This would equate to a volume fraction of approximately 0.02 (assuming a cluster radius of 1.5 mm). Inspection of frame 24 in Figure 4.8 (where the cluster appears at its maximum size), shows that this is unreasonable. It should be noted that Figure 4.8 is a

two-dimensional representation of a three-dimensional situation. Bubbles are overlapping and it is therefore difficult to determine the volume fraction of cavities accurately. However, the collapse time of the cluster can be estimated. The cluster can be seen at a maximum radius in frame 24 and has collapsed by frame 33. This gives a collapse time of 90 ± 10 μs. From this, the volume fraction of cavities in the cluster at the maximum radius can be calculated as 0.37 ± 0.08. This appears to be a reasonable estimate. It is nevertheless noted that a more accurate determination of β would be worthwhile. This may be possible using a laser diffraction technique [165].

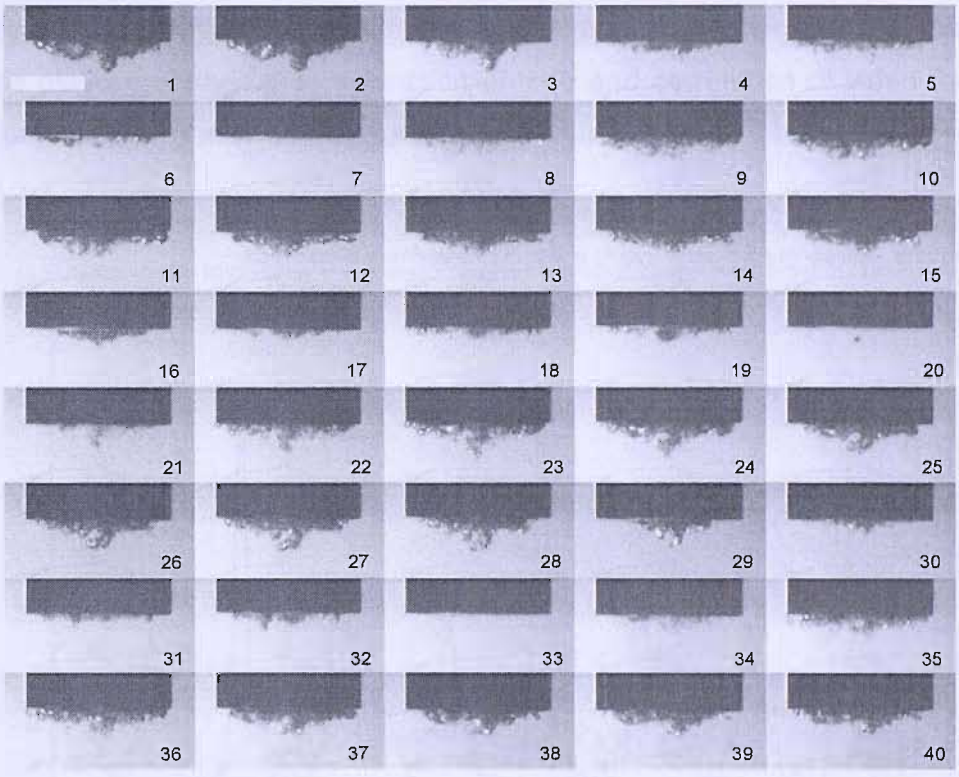


**Figure 4.8** 40 consecutive frames taken at 100,000 f.p.s showing the tip of the ultrasonic horn operating (dark oblong at the top of each frame) under the same conditions as used for Figure 4.6. The scale bar in frame 1 represents 1.5 mm.

In order to investigate the relationship between the cluster collapse and the acoustic pressure, the pressure was measured at the same time as the video footage shown in Figure 4.8 was recorded. This is shown in Figure 4.9. It has the same form as that shown in Figure 4.6; shock waves can be seen superimposed on the lower amplitude driving wave. In order to correlate the pressure data and video footage temporally, the speed of sound in the liquid must be considered. It will be shown in Section 5.1.3 that the speed of sound

under the conditions used here can be estimated to be 780 ± 120 m $s^{-1}$. The distance between the horn and the hydrophone was 14.2 mm, which means that there is a delay of 18 ± 4 μs in the hydrophone data. In order to take this into account 18 μs has been added to the time of each video frame. The timing of the frames is shown by the white circles (○) in Figure 4.9. The error bars represent the error due to the uncertainty in the speed of sound measurement. However, it is noted that there will be an additional errors because it is not clear where different components of the pressure originate from. Pressure shocks associated with cavitation will originate within the liquid, while the driving wave originates from the horn itself. Also, the environment generated by the horn is highly dynamic, with a rapidly varying bubble population. Hence, the speed of sound may be changing as a function of time and correlation of video footage and pressure data may be inaccurate.

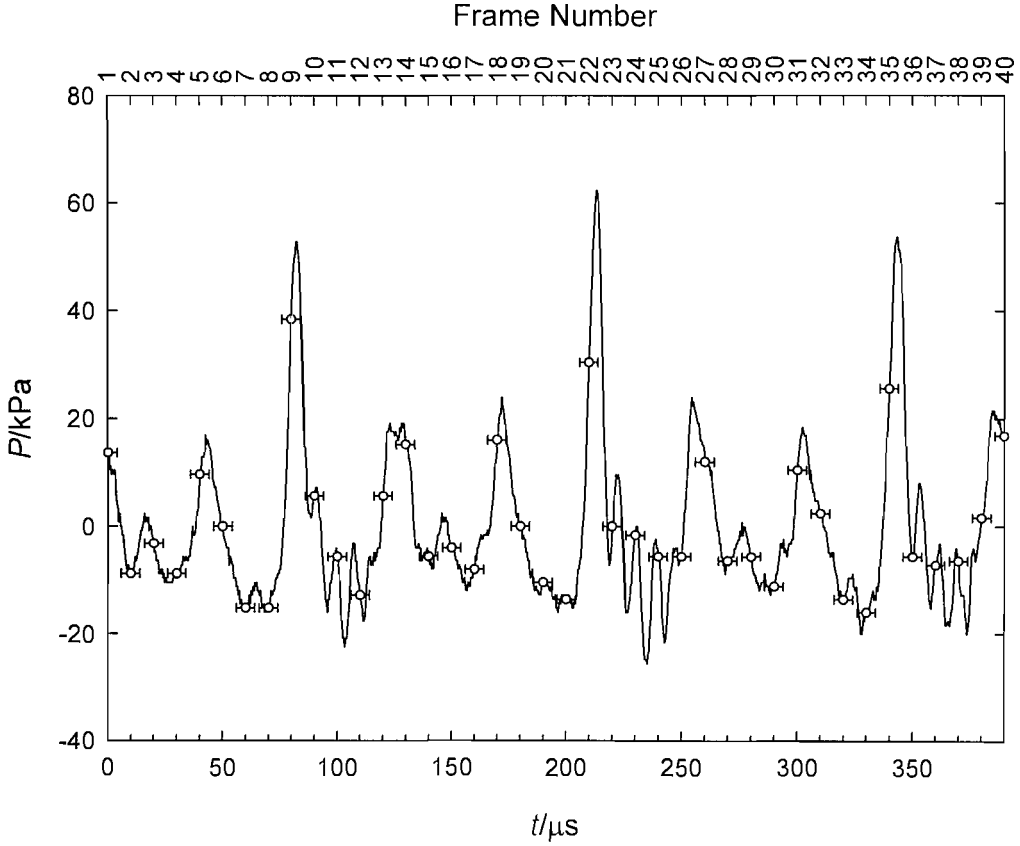


**Figure 4.9** Plot showing the pressure recorded simultaneously with the video shown in Figure 4.8. The horn-to-hydrophone distance was 14.2 mm. The frame numbers on the top axis relate to Figure 4.8. The symbols (○) indicate the timing of individual frames.

Nevertheless, inspection of the time correlated pressure and video footage suggests that the shock waves are not associated with the cluster collapse

itself. The three occurrences of high pressure spikes shown in Figure 4.9 occur during frames 8/9, 21/22 and 34/35. Rather than being associated with the collapse of the bubble cluster, this is after the bubble cloud has undergone total collapse, which occurs in frames 7, 20 and 33. There is nothing evident in the video footage presented in Figure 4.8 that can be deemed responsible for the shock waves. However, from the data presented here, it appears that the collapse of the large cluster may be ruled out as the source. This will be discussed further in Section 5.1.4. Presently however, given that it is the driving wave that generates the cavitation activity, it is necessary, for sound field modelling purposes, to extract the magnitude of the driving wave from the complicated pressure signal. Although this is the case and the subject of the remainder of this section the shock waves, which result from cavitation, cannot be ignored as will be shown later.

In order to separate the underlying driving signal FFT analysis was employed. An example of a FFT spectrum taken from pressure-time data is shown in Figure 4.10. There is a large peak at the driving frequency as well as various harmonic frequencies. In order to calibrate the magnitude of the sinusoidal wave at the driving frequency, sine waves of frequency 22.8 kHz and various amplitudes, $A_{sine}$ were generated and FFTs performed. A plot of the amplitude of the sine waves against their FFT magnitude is shown in the insert to Figure 4.10. From this data it is possible to construct a plot of the acoustic pressure amplitude at the driving frequency as a function of axial distance. This is shown in Figure 4.11. The solid line in the figure shows the fit of the experimental data to Equation 4.3. The parameters used for the fitting routine were as follows, $\rho$ = 1000 kg $m^{-3}$, $f$ = 22800 Hz, $c$ = 1480 m $s^{-1}$. From the fit it is possible to extract a value for the amplitude of the velocity of the horn, $U$ and from this the amplitude of the displacement. The curve fit shown in Figure 4.11 yields a value for $U$ of 0.70 ± 0.05 m $s^{-1}$ (95%) and a peak-to-peak displacement of 9.80 ± 0.05 µm (95%). However, inspection of Figure 4.12, which shows sections of two frames from high speed video footage, indicates that the displacement is in fact larger than this. Figure 4.12a shows the right hand edge of the tip of the horn (dark area labelled H) at the top of the range of motion. The light area (labelled S) is the solution.

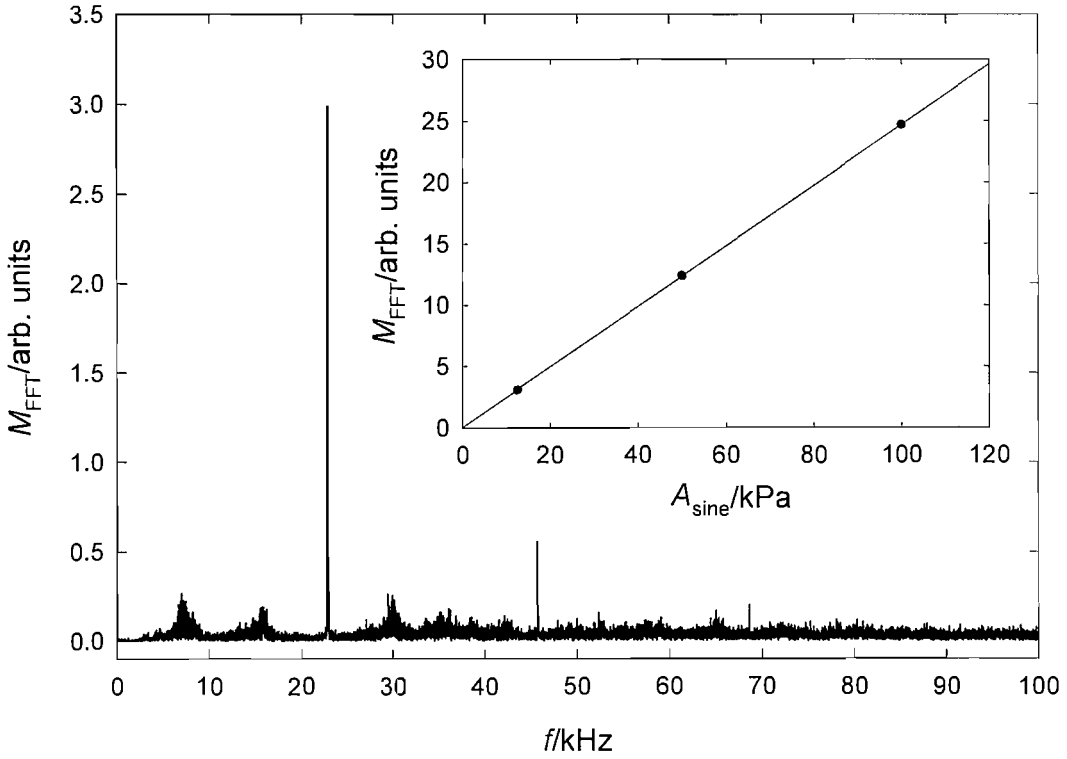


**Figure 4.10** Plot showing the fast Fourier transform spectrum for the pressure wave shown in Figure 4.6.

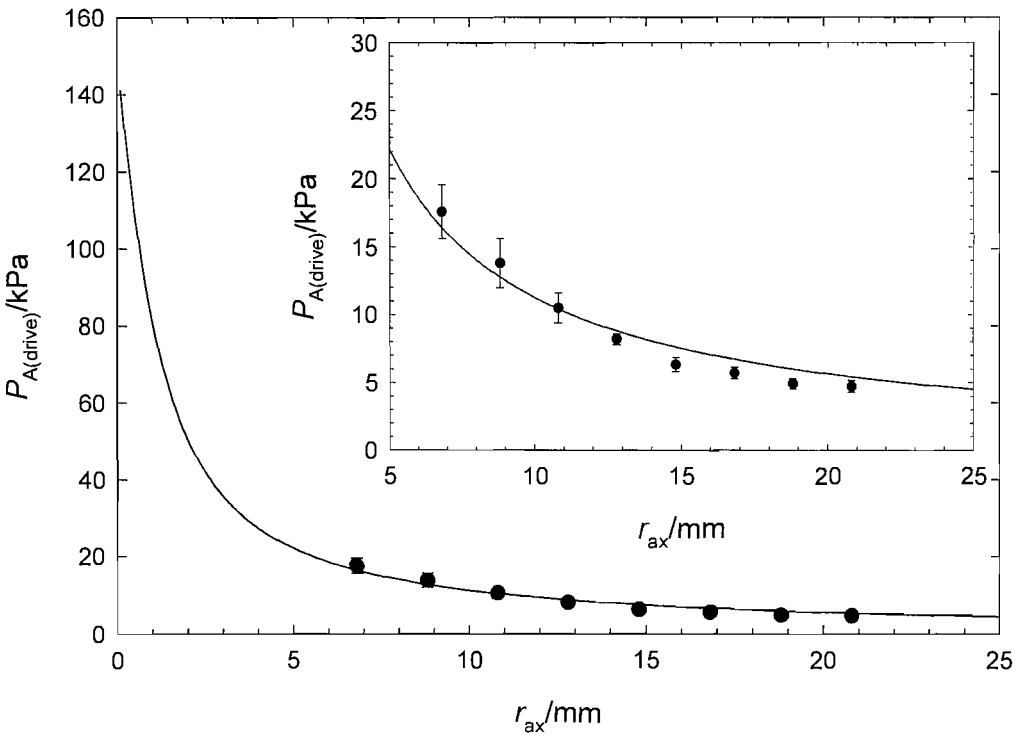


**Figure 4.11** Plot showing the acoustic pressure amplitude at the driving frequency as a function of axial distance, $r_{ax}$ in the presence of inertial cavitation. (•) represents the experimental points and (—) is the curve fit to Equation 4.3. The error bars are 95% confidence limits based on 5 measurements. **Insert** Expansion of the data from 5 to 25 mm.

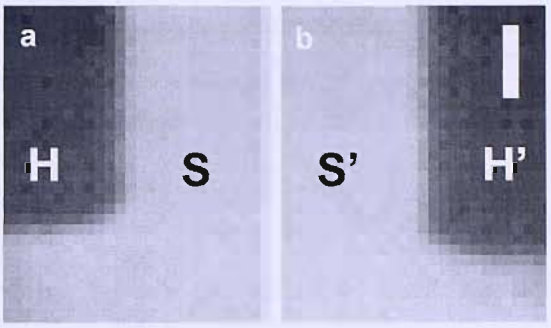


**Figure 4.12** Sections of two frames to show the peak-to-peak displacement of the horn. The frames are taken from video footage recorded at 100,000 f.p.s. The scale bar represents 50 μm.

Figure 4.12b shows the left hand edge of the tip of the horn (labelled H') at the bottom of the range of motion. Again, the light area (labelled S') is the solution. It should be noted that 'top' and 'bottom' refer to the extremities visible in the video footage and the actual displacement may be greater. It is difficult to determine the exact peak-to-peak displacement but it is approximately 20 ± 5 μm. The curve fit is to be expected to generate an underestimation of $U$ because, as discussed in Section 4.2.1 the horn is not within a rigid baffle (as Equation 4.3 models). However, it was shown that the underestimation is expected to be only 22 %. The underestimation seen here is greater than this (it is up to 50%) and may be due to the inhomogeneous nature of the fluid in the presence of cavitation. Equation 4.3 can take account of neither the bubbles which are present, nor their effect on the fluid properties prevalent in the region of the horn. The presence of bubbles in solution will decrease the density and may alter the sound velocity and attenuation coefficient. Equation 4.3 predicts that the pressure amplitude scale linearly with density and hence an overestimation in the density of the fluid would lead to an underestimation in the displacement of the horn, as seen here. However, this assumes that variations in the speed of sound have no effect on the pressure profile. The influence of the speed of sound in the solution is depicted in Figure 4.13, which shows the pressure amplitude predicted by Equation 4.3 as a function of distance for four different sound speeds (500, 1000, 1500 and 2000 m $s^{-1}$). All other parameters are as in Figure 4.11. The wide range of sound velocities was chosen as it is known that the speed of sound in bubbly liquids can be greater or less than the bulk value (here assumed to be 1480 m $s^{-1}$) depending on the bubble population, size distribution and frequency of sonication. For example Fox *et al.* [166] have reported speeds of sound in the range 500-2500 m $s^{-1}$.

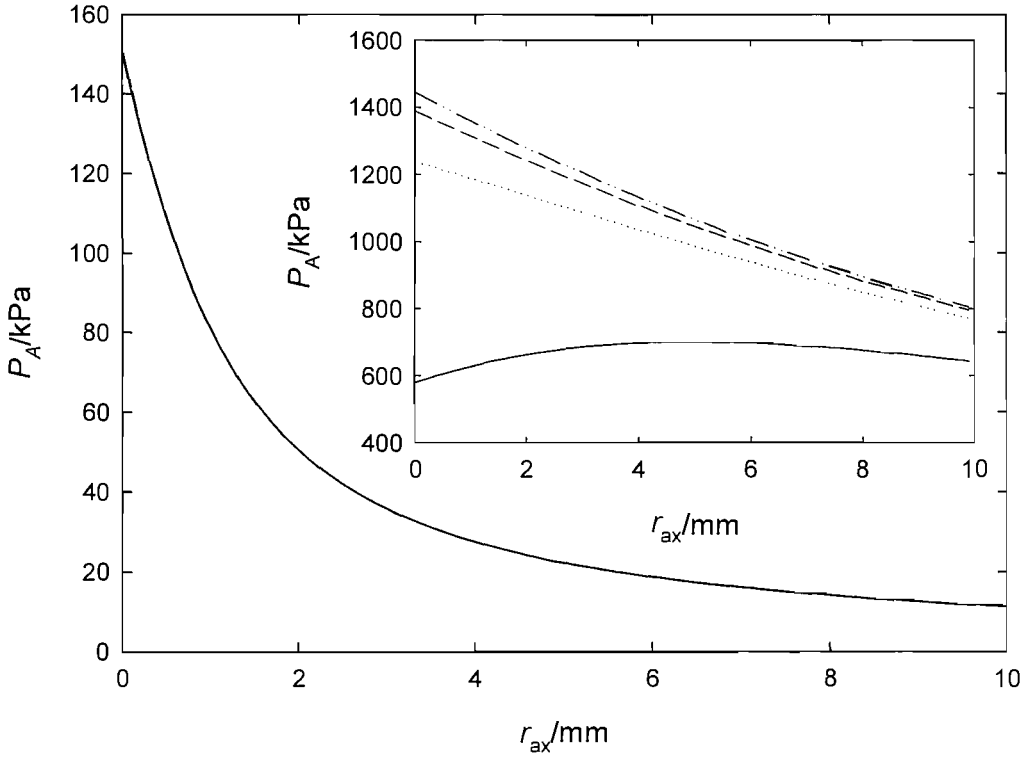


**Figure 4.13** Plots showing the acoustic pressure amplitude predicted by Equation 4.3 calculated for four different speeds of sound (500 (—), 1000 (·····), 1500 (——) and 2000 (—··—) m $s^{-1}$) and two different horn radii (1.5 mm main figure and 15 mm insert).

Clearly under the conditions used here, large variations in the speed of sound have very little effect on the pressure field (the curves overlay each other). However, it is worth noting that this will not always be the case. Consider a horn of radius 15 mm rather than 1.5 mm as used here. Under the same sonication frequency a decrease in the speed of sound of the sonicated medium has a large effect as the influence of near field behaviour is increased (see insert to Figure 4.13). This is particularly apparent in the 500 m $s^{-1}$ case, where there is a maximum ($r_{ax(1)}$) at a distance of 4.9 mm, which as discussed in Section 4.1.1 above, demarcates the near field from the far field. This effect is due to the wavelength tending toward a value similar to or less than the radius of the horn as the speed of sound decreases. Shielding by the bubble cloud itself will also have an effect on the pressure field. It has been shown that intense cavitation at the tip of an ultrasonic horn can shield the bulk solution from the sound field [32, 167, 168]. If this was the case here, then it may be expected that the value of *U* determined from the pressure measurements reported in Figure 4.11 would be lower than the true value. Also, the presence of bubbles will alter the attenuation coefficient. However, without detailed

knowledge of the bubble radii and population distributions it is impossible to determine to what degree.

## 4.3 The inertial cavitation threshold pressure

The form of the pressure profile shown in the previous sections implies that, if inertial acoustic cavitation is to occur anywhere within the solution, it will do so close to the faceplate of the vibrating horn, where the acoustic pressure amplitude is highest. As the distance from the tip of the horn is increased, there will be a point at which inertial cavitation ceases and only non-inertial bubbles exist. The location of this point is of vital importance given the very different bubble behaviours and physical effects associated with inertial and non-inertial cavitation. Estimates of the inertial cavitation threshold were discussed in Section 1.3.3. Under the conditions used in this work a value of approximately 110-120 kPa is expected. Consideration of Figure 4.11 shows that at axial distances of less than ~0.6 mm the acoustic pressure amplitude at the driving frequency is greater than this and hence effects commonly associated with inertial cavitation (e.g. erosion, luminescence, radical production) are expected at these short distances. In this section two experiments are described, which were used to map the extent of two of these effects (MBSL and surface erosion). The results yield interesting conclusions about the extent of inertial cavitation effects in sonoelectrochemical cells, and in particular the effect of the electrode itself on the results obtained.

### 4.3.1 Sonoluminescence imaging

The first experiment was based on imaging of the sonoluminescence output of the operating ultrasonic horn. Imaging of multibubble sonochemiluminescene (MBSCL) has been used for determining the spatial distribution of inertial cavitation [99, 101, 169]. The generation of light during MBSCL relies on a chemical reaction between radical species generated during the collapse of a bubble and a suitable chemical species (see Section 1.7.1). However, this has important implications for the use this technique in the experimental set-up used in this work. It is well known that acoustic streaming generates a large amount of forced convection in the electrochemical cell and as such may carry reaction products away from the tip of the horn. This may lead to an expansion of the luminescent area and a false impression of the extent of inertial cavitation. In contrast, multibubble sonoluminescence (MBSL) originates directly from the

inertial collapse of a cavitation bubble and would not be subject to such complications.

**Comparison of MBSCL and MBSL**

A comparison of the MBSCL and MBSL output of the horn recorded during cavitation is shown in Figure 4.14a and b respectively.

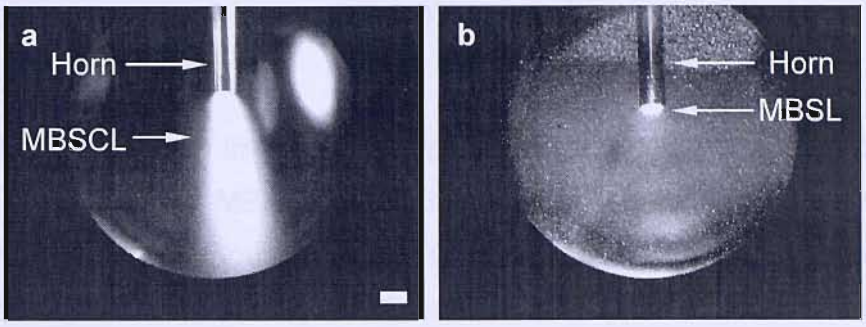


**Figure 4.14** A comparison of the MBSCL (a) and MBSL (b) output of the ultrasonic horn operating under the same sonication conditions (22.85 kHz, 56 ± 5 W $cm^{-2}$). For (a) the solution contained 0.1 M $Na_2CO_3$, 0.1 mM EDTA, 0.1 mM $H_2O_2$ and 50 μM Luminol (3-aminophthalhydrazide) and for (b) the solution contained 0.75 M $Na_2SO_4$. Both experiments were performed under ambient conditions (25 °C, aerobic solutions). Recorded by means of a JAI CV-A50 CCD camera and a Phototek MCP 325 image intensifier. The scale bar in the lower right corner of (a) represents 3 mm.

The tip of the horn can be seen entering from the top of each frame. It should be noted that these are composite images, consisting of an image taken under daylight conditions (to visualise the position of the horn) and an image taken in a darkroom using an image-intensifying camera (see Section 2.5.1) to see the luminescence output. The light and dark images were than combined using a commercial image stacking software package (Tawbaware ImageStacker). In the case of MBSCL (Figure 4.14a) there is a large amount of light below the horn. It seems unreasonable that inertial cavitation is present in such a wide area (the sound field model predicts inertial cavitation at distances of less than 1 mm from the horn) and it is postulated that the large extent of luminescence is due to flow of luminescent reaction products away from the horn as discussed above. The light area to the right of the horn is due to a reflection of light from the glass wall of the cell. In contrast, MBSL (Figure 4.14b) is only seen close to the tip of the horn, in agreement with the sound field model described in Section 4.2. While this suggests that imaging of MBSL is an effective means of mapping the extent of inertial cavitation within the electrochemical cell, the

camera set-up used here does not provide sufficient spatial resolution to determine this extent accurately. For this reason a second camera system was used (see Section 2.5.2) to determine the distance to which MBSL extends from the tip of the horn. It is important to note that although MBSCL is not suitable for imaging the extent of inertial cavitation in the experimental geometry used here, it can still be applied effectively to standing wave systems where there is little forced convection in the cell [73, 101, 169].

**The extent of MBSL**

Figure 4.15a shows an image of the tip of the horn taken with the alternative camera system. The MBSL output of the horn, operating under the same conditions as used in Figure 4.14b is shown in Figure 4.15b. These images were taken by means of a Starlight Xpress HX516 CCD camera. For the image taken in daylight (Figure 4.15a) the exposure time was one tenth of a second and for the dark image (Figure 4.15b) the exposure time was 10 minutes. As above, luminescence and by assumption inertial cavitation is concentrated close to the tip of the horn in agreement with the sound field model. However, light production extends to an axial distance of 0.9 ± 0.05 mm from the centre of the horn, which is somewhat further than may be expected.

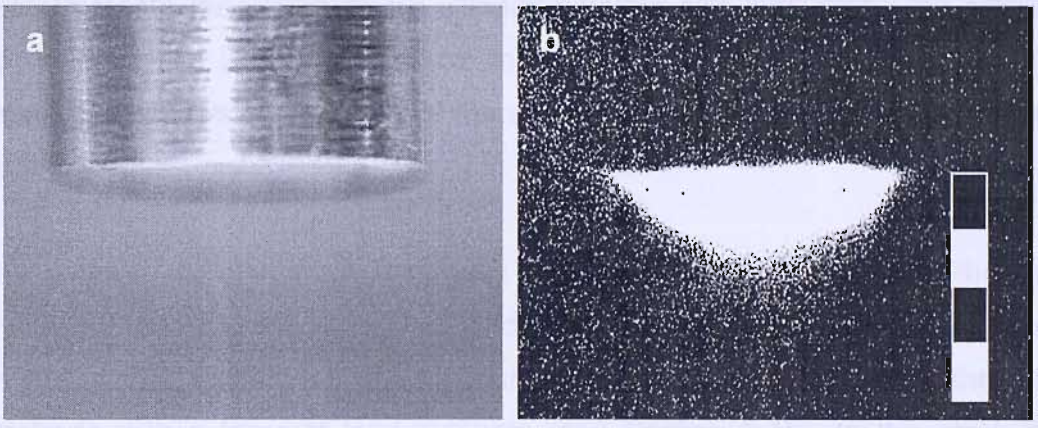


**Figure 4.15** Images of ultrasonic horn taken with a cooled CCD camera. Frame (a) was taken under normal daylight conditions while (b) was taken in a dark room. Frame (a) shows the tip of the ultrasonic horn and (b) the corresponding light emission (exposure time 10 mins) in the presence of continuous ultrasonic irradiation (22.85 kHz, 56 ± 5 W $cm^{-2}$). The solution contained 0.75 mol $dm^{-3}$ $Na_2SO_4$. The experiment was performed under ambient conditions (25 °C, aerobic solutions). The scale bar represents 2 mm in 0.5 mm increments.

Figure 4.11 shows that the pressure amplitude of the driving pressure wave at this distance is only 85 ± 3 kPa, lower than the predictions of the inertial

cavitation threshold pressure, which are of the order of 110-120 kPa (see Section 1.3). It should be noted however, that 85 ± 3 kPa is the amplitude of the driving pressure wave and takes no account of the effects associated with the acoustic signal produced by inertial bubble collapses close to the transducer. These shock waves occur at the pressure maximum in the driving signal (see Figure 4.6); hence bubbles which are compressed by the driving pressure signal are also exposed to a high pressure shock. Note the pressure maximum[6]. from the cavity collapse shock is 130 kPa at 8.8 mm compared to 14 kPa from the driving signal Hence one may expect the shock pressures to scale up to the order of 1 MPa close to the tip of the ultrasonic probe. These high pressure shocks may collapse bubbles, which are sub-inertial in the driving pressure field, giving rise to luminescence at a greater distance than expected. In order to investigate the spatial extent of inertial cavitation further, a second, electrochemical experiment was performed. This is described in the following section.

### 4.3.2 Electrochemical investigation

A second measure of the spatial extent of inertial cavitation made use of a novel electrochemical erosion technique. A dual Pt/Pb electrode (see Chapter 3) was used to locate the centre of the ultrasonic plume and then probe the erosion boundary, which is assumed to be linked to the inertial cavitation threshold. Figure 4.16 shows a schematic of the experimental approach used, which was as follows.

The potential of both microdiscs was held at +0.8 V *vs.* SCE. In the test electrolyte of 20 mM $K_4Fe(CN)_6$ and 0.75 M $Na_2SO_4$ this results in mass transfer limited oxidation at the platinum electrode and passivation of the lead electrode with a layer of lead sulphate (see Section 3.1). In this state the platinum electrode is sensitive to all hydrodynamic processes whilst the lead electrode is only sensitive to high energy events capable of causing surface erosion. The centre of the plume generated by the ultrasonic horn was found by mapping the enhancement in mass transfer of $Fe(CN)_6^{4-}$ to the platinum electrode in a 12 mm × 12 mm plane below the tip. This was done at a distance

[6] It should be noted that the Brüel & Kjær type 8103 hydrophone has an upper frequency limit of ~180 kHz, after which the signal begins to be attenuated. This suggests that the estimations of shock wave pressures are underestimates of the real signal.

where no erosion was detected (6 mm tip to plane of electrode motion) in order to protect the soft lead sulphate modified electrode from damage. The current was recorded for five seconds at each point and a map of the average current (normalised to the silent MTL current) is shown in Figure 4.17.

**Figure 4.16** Schematic showing the experimental protocol for centring the dual electrode and approaching the ultrasonic tip. Not to scale.

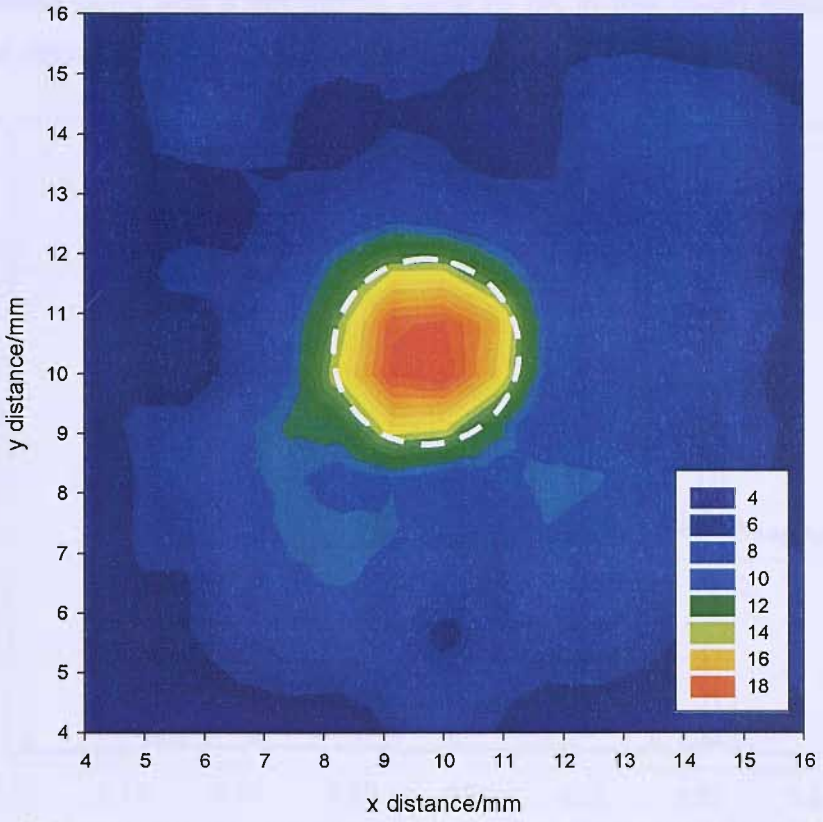


**Figure 4.17** Contour map showing the average mass transfer signal in a plane 6 mm below the tip of the ultrasonic horn. The electrode was held at +0.8 V *vs.* SCE in a solution of 20 mM $K_4Fe(CN)_6$ and 0.75 M $Na_2SO_4$ The legend indicates the average current normalised to the silent steady state current of 132 nA. The white dashed circle represents the size of the horn.

It is recognised that the averaged mass transfer enhancement is associated with a number of physical process (see Section 1.6.1); however it is reproducible and represents an effective *in-situ* method of centring the electrode below the tip of the horn. With the microelectrode centred on the mass transfer maximum, the current at the lead sulphate modified electrode was recorded for a fixed time (0.4 s) at decreasing electrode-to-horn separations. An example of a current-time trace recorded at a distance of 0.9 mm from the tip of the ultrasonic horn is shown in Figure 4.18. A number of current transients are evident, which are attributed to repassivation of the electrode following erosion of a portion the $PbSO_4$ layer. If it is assumed that the erosive process is the result of inertial cavitation, then the onset of these erosion events can be used to determine the location of the inertial cavitation threshold in terms of axial distance from the centre of the horn. In order to locate this onset the number of current transients detected at the lead electrode was counted at each distance using a peak finding program, which defines a peak as any point greater than

the previous point and a set trigger value (5 μA in this case) followed by four points of decreasing value (see Section A.4).

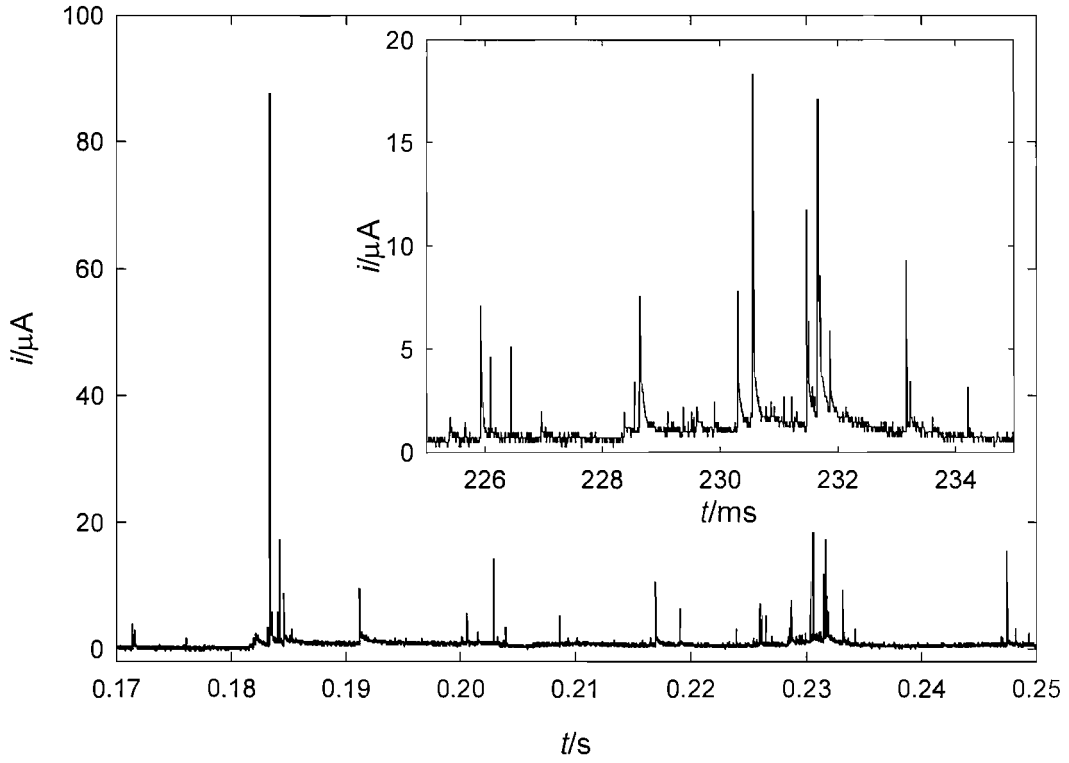


**Figure 4.18** Plot showing a current-time trace for a passivated lead electrode (125 μm diameter) exposed to ultrasound (22.85 kHz, 56 ± 5 W $cm^{-2}$). The electrode-to-horn separation was 0.9 mm and the potential was held at +0.8 V *vs.* SCE. **Insert** Expansion of the data around 0.23 s.

Figure 4.19 shows the number of events detected by the lead electrode as a function of electrode-to-horn separation for five separate experiments. There is clearly a threshold distance, which was measured to be at 1.3 ± 0.2 mm (95%, 5 measurements). This is significantly further than the boundary measured for MBSL (0.9 mm) and corresponds to an acoustic pressure amplitude at the driving frequency of 68.8 ± 6.5 kPa (see Figure 4.11). This is below the theoretical inertial cavitation threshold and less than the threshold measured using MBSL (see Section 4.3.1). The disagreement (between the erosion and the theoretical thresholds and between the erosion and MBSL thresholds) could be the result of a number of factors. First, as with the MBSL data above, the erosion threshold takes no account of the shock waves evident in Figure 4.6. Second and more importantly, the electrode cannot be regarded as non-invasive as it will, depending on the frequency of the pressure fluctuation considered, the materials employed and the geometry, affect the sound field

and consequently the results observed. This is the subject of the following section.

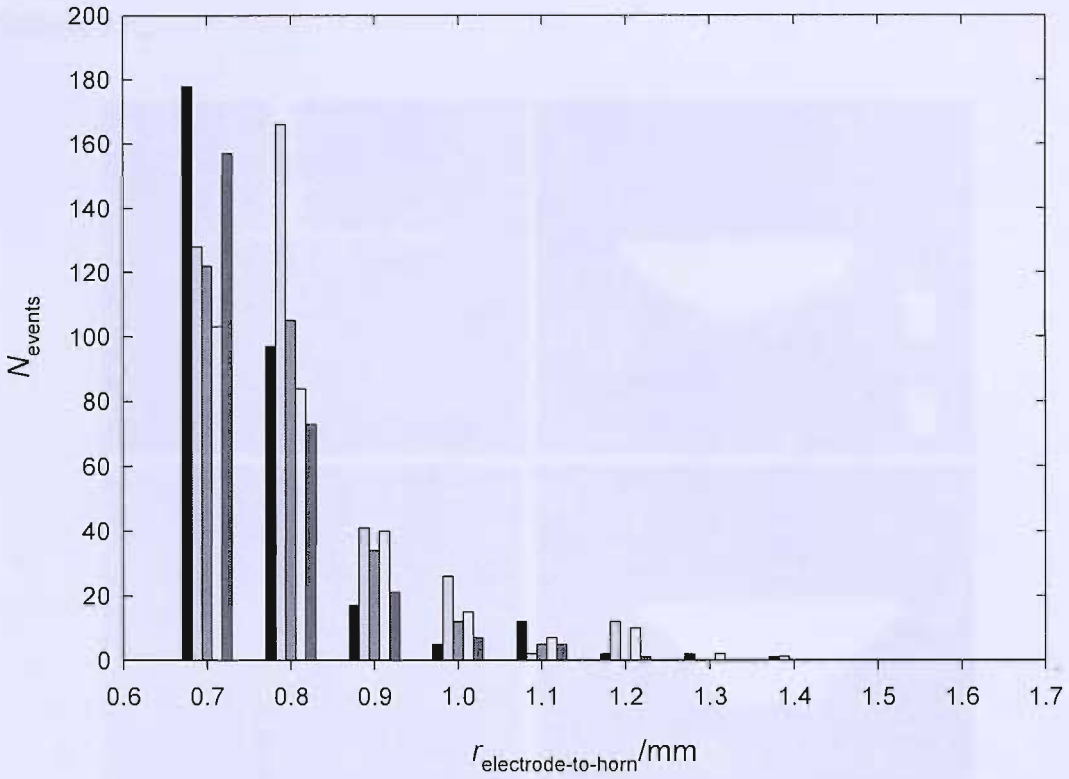


**Figure 4.19** Plot showing the number of peaks identified by peak finding software as a function of electrode-to-horn distance. The figure shows data for 5 repeat experiments. The trigger current was 5μA.

## 4.4 The invasive nature of the electrode

In the previous sections, two experiments designed to locate the inertial cavitation threshold in terms of the axial distance from the tip of the ultrasonic horn were described. One experiment was based on MBSL and the second on the erosion of a passivated lead electrode; both effects have been associated with inertial cavitation. However, it was found that the threshold for erosion was further from the tip of the horn than the threshold for luminescence. This implies that the electrode is invasive in nature. The pressure at its face is greater than the pressure at the same point in space in the absence of any electrode. This statement must be made with caution for a number of reasons.

First, it implicitly assumes that the threshold pressure required for MBSL and erosion are the same and, in this analysis, equal to the inertial cavitation threshold. Support for this assumption (as opposed to the electrode having no

effect on the pressure field and MBSL and surface erosion being subject to different threshold conditions) is given in Figure 4.20, which shows the MBSL output of the horn (labelled H) in the absence and presence of an electrode (labelled E).

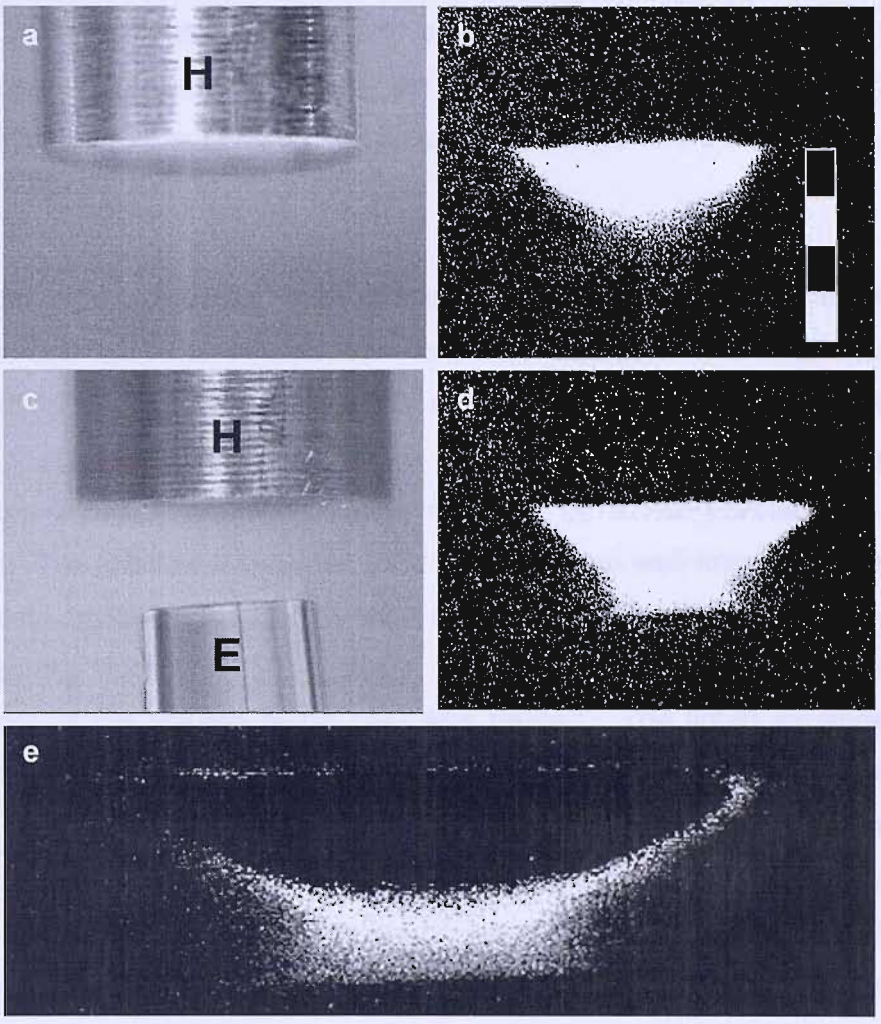


**Figure 4.20** Images of ultrasonic horn (labelled H) and electrode (labelled E) taken with a cooled CCD camera. Frames (a) and (c) are taken under normal daylight conditions while (b) and (d) are taken in a dark room. Frame (a) shows the ultrasonic horn on its own and (b) the corresponding light emission (exposure time 10 mins) in the presence of continuous ultrasonic irradiation (22.85 kHz, 56 ± 5 W $cm^{-2}$). Frame (c) shows the horn and an electrode and (d) the corresponding light emission (exposure time 10 mins) in the presence of continuous ultrasonic irradiation (22.85 kHz, 56 ± 5 W $cm^{-2}$). Frame (e) shows a subtraction of (b) from (d). The solution contained 0.75 mol $dm^{-3}$ $Na_2SO_4$. The experiment was performed under ambient conditions (25 °C, aerobic solutions). The scale bar represents 2 mm in 0.5 mm increments (not applicable to frame (e)).

Figure 4.20a shows the tip of the horn on it own under daylight conditions and Figure 4.20b shows the corresponding MBSL output. Figure 4.20c shows the horn and a glass electrode placed 1 mm below the tip of the horn. The MBSL

output under these conditions is shown in Figure 4.20d. The presence of the electrode clearly extends the light output. Figure 4.20e shows a subtraction of b from d, which emphasises the extra luminescence in the presence of the electrode. The extension of light output in the presence of an electrode indicates that the electrode is indeed invasive in nature, as discussed above. If it were the case that the MBSL and erosion threshold pressures are different and the electrode had no effect on the pressure field it would be expected that the addition of an electrode would make no difference to the MBSL output of the horn.

A second important point, when considering the effect of the electrode, is that the insertion of solid objects can influence cavitation in ways other than perturbation of the pressure field. For example, *via* the distribution of cavitation nuclei. This effect goes beyond the simplistic assertion that volumes, from which the liquid is displaced, to be replaced by a non-porous solid cannot cavitate. The interfaces between solid and liquid are well-known for their ability to nucleate cavitation [170]. The work of Berthelot [171] illustrates this point. In a pioneering study in 1850, a closed glass tube almost filled with water (the remainder of the volume being gas) was heated. The liquid expanded more than the glass, forcing the gas into the liquid sample so that the latter filled the vessel. On cooling, the liquid adhered to the glass and was constrained from contraction. As a result tension was generated in the sample, which increased as the sample cooled until cavitation occurred. Using this technique Berthelot measured the 'tensile strength' of water to be around 50 bar. However, it is important to note that the cavitation initiated at the walls of the sample vessel rather than within the liquid. It was therefore the adhesive forces acting between the glass and the water that were overcome, not the intermolecular forces of the water sample. This demonstrates an important point: it is not the properties of the liquid *per se* that determine the maximum tension the liquid can sustain but often other bodies present within the liquid sample [172].

Berthelot's tests were static and demonstrate the invasiveness of the insertion of a solid with respect to nucleation. They do not contain information on the relative magnitude of this effect, compared to the perturbation of the pressure field by the solid. However, Figure 4.20e shows that the majority of the

additional sonoluminesence, which results from the insertion of the solid electrode, occurs at the boundary that divided, prior to the insertion of the electrode the region in which inertial cavitation existed from that where it did not. This boundary is defined by the local values of the acoustic pressure amplitude, which in the free field decreases as the distance from the tip of the horn is increased (see Figure 4.11). The theory described in the following section however, predicts that scattering of the incident pressure wave from the surface of the solid will increase the pressure in this region, and this will have the exact effect of allowing the boundary to extend further from the horn than it did in the absence of the electrode. The assertion, that the observed effect is attributable to perturbation of the pressure field rather than nucleation effects is further supported by the observation that the majority of additional sonoluminesence seen in Figure 4.20 is not at the interface of the solid/liquid boundary. Also, there is no additional MBSL at the sides of the electrode which, unlike the highly polished (0.3 μm alumina) face, would be expected to provide numerous nucleation sites. The results presented here are not to say that the magnitude of the invasive effect on nucleation will always be less than that on the pressure field; however the evidence from Figure 4.20 suggests that this is the case here. The invasive nature of the electrode can therefore be attributed to scattering of the incident pressure waves by the electrode, which is discussed in detail in the following section.

### 4.4.1 Modelling the effect of the electrode on the sound field

In this model the effect of the electrode on the incident sound field has been characterised by calculating the total (incident plus scattered) pressure at the face of the electrode using linear acoustic theory. The electrode is assumed to be a rigid disc of radius $a_E$ (see Figure 4.21) and the sound field is assumed to be single-frequency plane waves. The use of linear acoustic theory, as opposed to non-linear theory, is justified by calculating the error associated with neglecting harmonics of order 2 and above. It can be shown that a plane wave of amplitude, $P_A$, which has propagated a distance of $h$ in an aqueous medium, will have a second-harmonic component, $P_A(2^{nd})$ of [173]:

$$\left[\frac{P_A(2^{nd})}{\text{bar}}\right] = \frac{h}{1910\lambda}\left[\frac{P_A}{\text{bar}}\right]^2 \qquad (4.6)$$

At the driving frequency of ~23 kHz, assuming a pressure amplitude of 10 bar (much higher than those observed here, see Figure 4.11) and a propagation distance of 4 mm (the worst case scenario of twice the electrode-to-horn distance), the pressure invested in the second harmonic is only ~0.03% of the fundamental. At high frequencies (for example the shocks reported in Figure 4.6), the pressure invested in the second harmonic is also negligible. For example, after propagating a distance of 4 mm, a 1 Mhz pressure wave of amplitude 10 bar will have a second harmonic component of ~0.14 bar (1.4%). The driving sound field is assumed to be normally incident on the face of the electrode. The normal component of the particle velocity vanishes at the surface of the disc and hence the following relationship exists between the particle velocity of the incident wave, $u_i$ and the particle velocity produced in the fluid immediately adjacent to the disc, $u_s$,

$$u_s = -u_i \tag{4.7}$$

The plane wave assumption allows the particle velocity of both the incident and scattered waves to be related to the incident acoustic pressure, $P_i$

$$u_i = -\frac{P_i}{\rho c} \tag{4.8}$$

By making the simplifying assumption that the axial particle velocity in the plane of the disc for $r' > a_E$ is zero, where $r'$ is the radial displacement from the centre of the electrode, Rayleigh's 2nd integral can be applied to compute the scattered acoustic pressure at any position **x** in space, including points on the disc surface.

For a time-harmonic axial velocity distribution $u_s$ of frequency ω, uniformly distributed over the disc surface $S$, the scattered pressure, $P_s$ may be written as

$$P_s(\mathbf{x},t) = \frac{jk\rho c u_s e^{j\omega t}}{2\pi} \int_S \frac{e^{-jk|\mathbf{x}-\mathbf{y}|}}{|\mathbf{x}-\mathbf{y}|} dS(\mathbf{y}) \tag{4.9}$$

Together with the geometry shown in Figure 4.21, Equation 4.9 gives the radial pressure distribution on the surface of the disc due to scattering of the incident pressure in the form,

$$P_s(r',t) = \frac{jkP_i e^{j\omega t}}{2\pi} \int_{-\pi}^{\pi} \int_{0}^{R'_{\lim}(r',\theta)} \frac{e^{-jkR'}}{R'} R'\,dR'\,d\theta \tag{4.10}$$

where, from Figure 4.21 $R'_{\lim}(r',\theta) = r'\cos\theta + \sqrt{a_E^2 - r'^2\sin^2\theta}$. Whilst the integral in $R'$ is straightforward, the $\theta$ integral has no closed form solution. The final result for the total acoustic pressure as a function of $r'$ may be written in the form,

$$P_t(r',t) = P_i + P_s(r',t) \tag{4.11}$$

$$P_t(r',t) = P_i e^{j\omega t}[2 - H(ka_E,\bar{r})] \tag{4.12}$$

where $\bar{r} = r'/a_E$ and $H(ka_E,\bar{r})$ is a scattering function given by,

$$H(ka_E,\bar{r}) = \frac{1}{\pi}\int_0^{\pi} \exp[-j\,\Psi(\bar{r},\theta)]\,d\theta \tag{4.13}$$

where

$$\Psi = ka_E\left(\bar{r}\cos\theta + \sqrt{1-\bar{r}^2\sin^2\theta}\right). \tag{4.14}$$

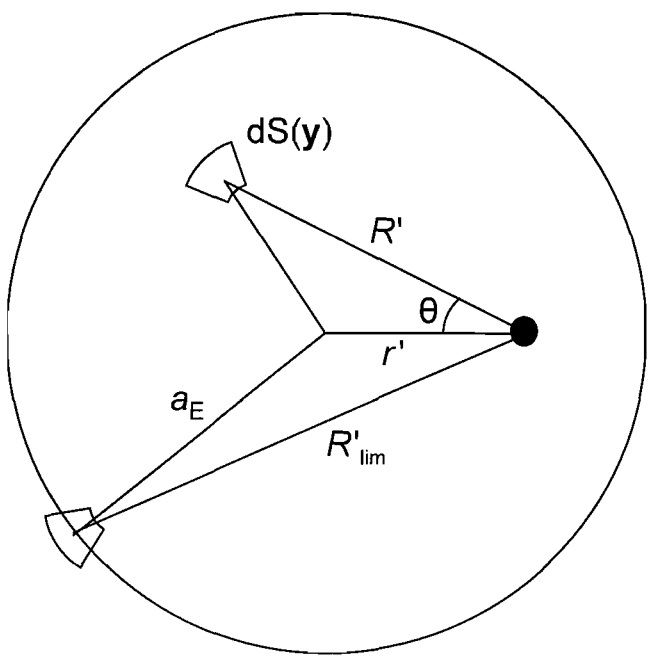


**Figure 4.21** Geometry used in the calculation of the surface pressure at the face of the electrode.

Note that Equation 4.14 indicates that the total pressure variation is completely defined by two non-dimensional quantities: the Helmholtz frequency, $ka_E$ and the fractional radial distance from the centre of the electrode, $\bar{r}$. The general behaviour of the total pressure (expressed as the time averaged mean square total pressure normalised to the time averaged mean square incident pressure, where $\overline{P_i^2} = (1/2)|P_i|^2$) as a function of $r'/a_E$ for various $ka_E$ values is shown in Figure 4.22.

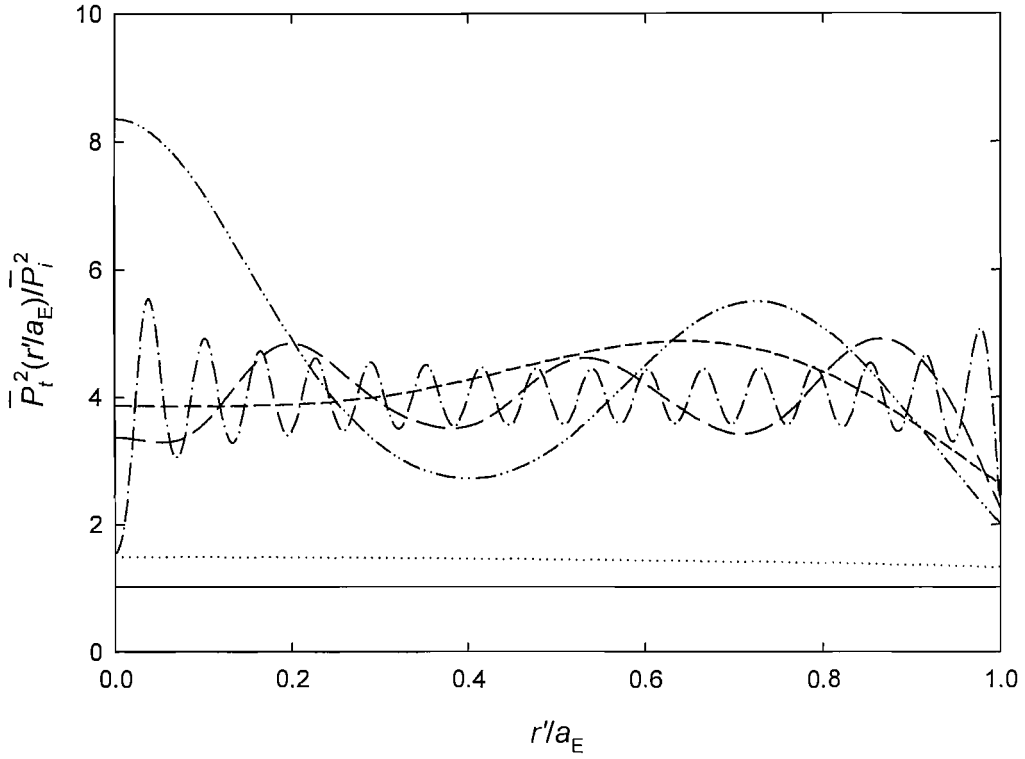


**Figure 4.22** Plot showing the total pressure at the surface of the electrode (normalised to the incident pressure) as a function of the radial position for various values of $ka_E$. (—), (·····), (—— —— ——), (—··), (— — —) and (—·) represent $ka_E$ = 0.1, 0.5, 5, 10, 20 and 100 respectively.

There are three interesting limiting cases:

1) At the centre of the electrode

$$\overline{P_t^2}(r') \rightarrow \overline{P_i^2}[5 - 4\cos ka_E]; \qquad \text{as } r'/a_E \rightarrow 0$$

2) The low frequency limit

$$\overline{P_t^2}(r') \rightarrow \overline{P_i^2}; \qquad \text{for all } r' \text{ as } ka_E \rightarrow 0$$

3) The high frequency limit

$$\overline{P_t^2}(r') \rightarrow 4\overline{P_i^2}\,; \qquad \text{for all } r' \text{ (except } r'=0) \text{ as } ka_E \rightarrow \infty$$

**Average surface pressure**

In order to assess the average effect of the electrode on the sound field, consider the pressure averaged over the face of the electrode, which is defined by

$$\langle P \rangle = S^{-1} \int_S P(\mathbf{x}) dS(\mathbf{x}) \tag{4.15}$$

Substituting Equations 4.12 and 4.13 into 4.15 yields

$$\langle P \rangle = P_i e^{j\omega t} \left[ 2 - \frac{2}{\pi} \int_0^{\pi} \int_0^{1} \exp[-j\,\Psi(\bar{r},\theta)] d\theta\, \bar{r} d\bar{r} \right] \tag{4.16}$$

The calculation required in Equation 4.16 is precisely equivalent to the calculation of the radiation impedance of a circular piston, first deduced by Lord Rayleigh [174]. His solution is expressed in terms of tabulated functions. Following an identical approach the surface-average pressure may also be written as

$$\langle P \rangle = P_i e^{j\omega t} \left[ 2 - \frac{2J_1(2ka_E)}{2ka_E} + j\frac{2K_1(2ka_E)}{2ka_E} \right] \tag{4.17}$$

where $J_1$ and $K_1$ are the Bessel function of the first kind, and the Struve function of order 1, respectively. Figure 4.23 shows a plot of Equations 4.16 and 4.17 versus $ka_E$ where Equation 4.16 has been computed by trapezoidal integration. Agreement between the two curves is generally very close, which confirms the consistency between the numerical and analytical approaches. Figure 4.23 shows that at values of $ka_E$ < 0.1 the scattering of the disc is insignificant. Considering the drive signal (~23 kHz) and electrode support radius (~1 mm) employed here a value of $ka_E$ = 0.098 is obtained. Under these circumstances the scattering from the disc is only 8 % of the incident sound field. However, for high $ka_E$ values (e.g. $ka_E$ > 1) the scattering in this model approaches 100 % of the incident beam. Hence for frequencies of sound > 230 kHz (e.g. the high frequency components that accompany shock waves (see Figure 4.6)) the disc

behaves as a perfect reflector. This implies that shock waves emitted by inertial cavitation activity will be reflected from the solid/liquid boundary of the electrode and in turn will add to the sound field. This enhancement in pressure at the electrode surface can account for both the extension of the spatial distribution of MBSL in the presence of an electrode and detection of erosion events at greater distances from the tip of the ultrasonic horn than expected.

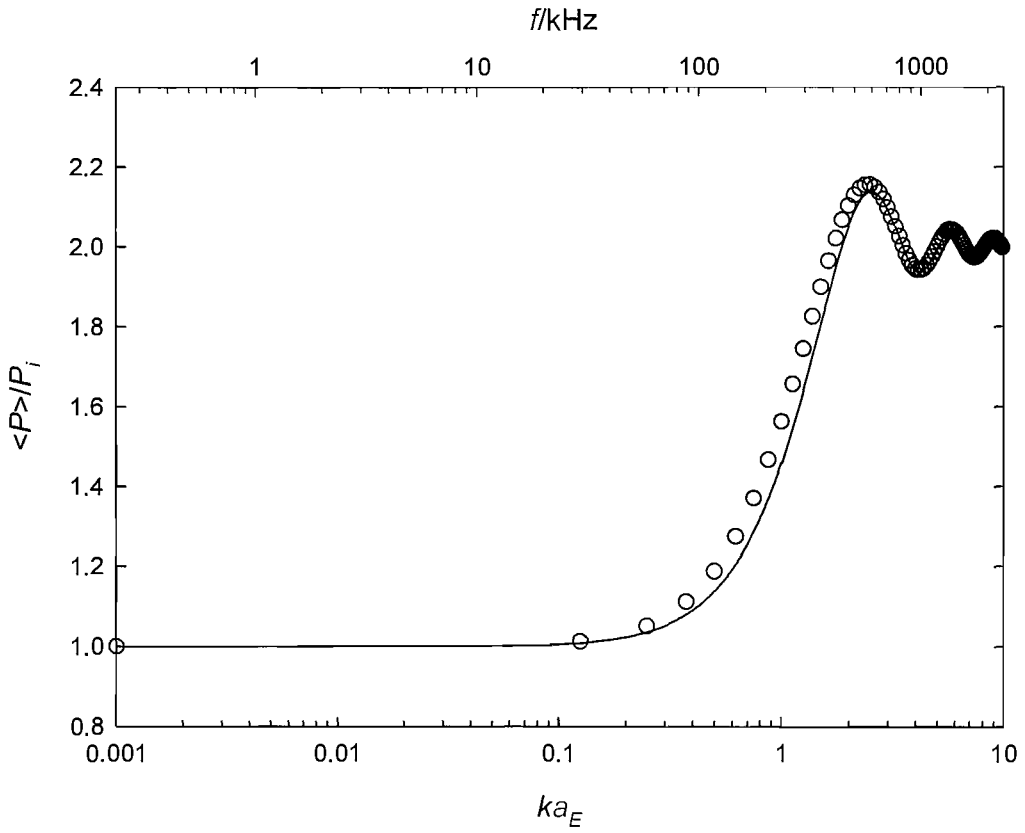


**Figure 4.23** Plot showing the average pressure amplitude over the surface of the electrode (normalised to the incident pressure amplitude) as a function of $ka_E$, where $k$ is the wavenumber and $a_E$ is the radius of the face of the electrode. The symbols (○) represent the numerical model (Equation 4.16) and the solid line (—) represents the analytical model (Equation 4.17). The frequencies quoted on the upper axis assume an electrode radius, $a_E$ of 1 mm.

### 4.4.2 Material dependence of the invasive effect

In addition to the frequency dependence described in Section 4.3.1, the degree of scattering of the incident sound wave also depends on interfacial materials used. By employing a simple fluid/fluid interface model, it is possible to define a reflection coefficient (assuming normal incidence), $\Lambda$,

$$\Lambda = \frac{\rho_E c_E - \rho_S c_S}{\rho_E c_E + \rho_S c_S} \tag{4.18}$$

where $\rho_E$ is the density of the electrode material, $\rho_S$ is the density of the solution, $c_E$ is the speed of sound in the electrode material and $c_S$ is the speed of sound in the solution. It must be recognised that a variety of complex waves may be generated at a solid/liquid interface, however this simple fluid/fluid model provides a reasonable first order illustration of the effect. The reflection coefficient can be used to correct for the physical properties of the interfacial materials such that $u_s = -\Lambda u_i$ and, following Section 4.4.1, Equation 4.12 may be rewritten as:

$$P_t(r',t) = P_i e^{j\omega t}[1+\Lambda(1-H(ka_E,\bar{r}))] \tag{4.19}$$

Equally, Equation 4.17 may be rewritten as:

$$\langle P \rangle = P_i e^{j\omega t}\left[1+\Lambda\left(1-\frac{2J_1(2ka_E)}{2ka_E}+j\frac{2K_1(2ka_E)}{2ka_E}\right)\right] \tag{4.20}$$

or, in the high frequency limit:

$$\langle P \rangle = (1+\Lambda)P_i \tag{4.21}$$

For the rigid model $\Lambda$ = 1 but as shown above the value of $\Lambda$ is material dependent and hence the pressure amplitude at the surface of the electrode depends on the material used in its construction. This can be shown through the use of electrodes for which glass is used in the construction of the main body of the electrode instead of epoxy resin. Given the different material properties of glass compared with epoxy resin it would be expected that a glass bodied electrode would exhibit a greater invasive effect on the sound field. This is owing to the higher value of $\Lambda$ (see Table 4.1), leading to a greater enhancement of the surface pressure. Initially this will be demonstrated through the use of MBSL imaging.

| Material | Density/kg m$^{-3}$ | Speed of Sound[7]/m s$^{-1}$ | $\Lambda$ |
|---|---|---|---|
| Electrolyte | 1110 ± 20 | 1610 ± 20 | - |
| Epoxy Resin | 1120 ± 70 | 3100 ± 350 | 0.32 ± 0.09 |
| Glass | 2300 ± 100 | 4000 ± 500 | 0.67 ± 0.13 |

**Table 4.1** Physical properties of the materials used in this work.

[7] See Section 2.8 for experimental details of speed of sound measurements.

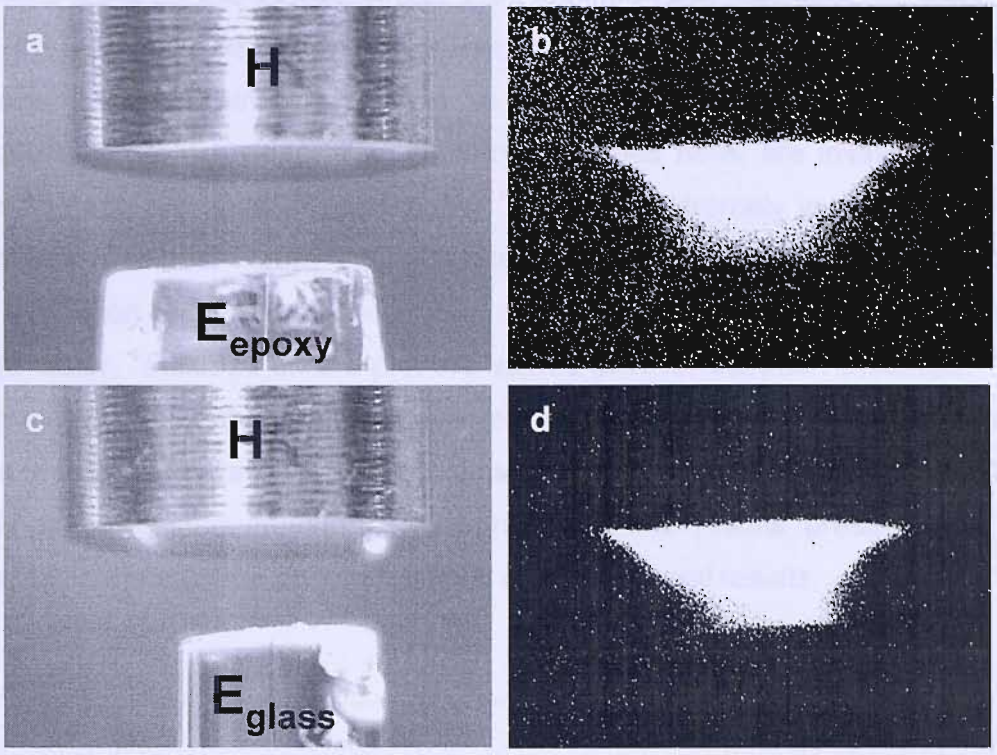


**Figure 4.24** Images of ultrasonic horn and electrode taken with a cooled CCD camera. Frames (a) and (c) are taken under normal daylight conditions while (b) and (d) are taken in a dark room. Frame (a) shows the ultrasonic horn and a epoxy electrode and (b) the corresponding light emission (exposure time 10 mins) in the presence of continuous ultrasonic irradiation (22.85 kHz, 56 ± 5 W $cm^{-2}$). Frame (c) shows the horn and a glass electrode and (d) the corresponding light emission (exposure time 10 mins) in the presence of continuous ultrasonic irradiation (22.85 kHz, 56 ± 5 W $cm^{-2}$). The solution contained 0.75 mol $dm^{-3}$ $Na_2SO_4$. The experiment was performed under ambient conditions (25 °C, aerobic solutions).

Figure 4.24 shows the MBSL output in the presence of epoxy and glass electrodes. Figure 4.24a and c show images taken in daylight of the horn (labelled H) and the electrode (labelled $E_{epoxy}$ and $E_{glass}$) for epoxy and glass respectively. The MBSL output for each case is shown in Figure 4.24b and d respectively. It can clearly be seen that in the presence of a glass electrode the extra light is more extensive, supporting the fact that the magnitude of the invasive effect of the electrode is increased for glass and that this effect is material dependent. Further evidence of this was obtained using the electrochemical approach described in Section 4.3.2. In this case, however the electrode used employed glass as the main body (see Section 2.2.3 for details of the construction). The results of this are presented in Figure 4.25, which shows the average number of events recorded as a function of distance for the epoxy and glass electrodes. It was found that the threshold distance for erosion

using a glass bodied electrode was 2.3 ± 0.2 mm compared with 1.3 ± 0.2 mm for the epoxy bodied electrode. This, together with the MBSL data shown above, provides strong evidence to suggest that acoustoelectrochemical experiments, which adopt the geometry described here, are invasive and the effects seen are material dependent. This is an extremely important result in this field. Consider Figure 4.26, which is a plot showing the reflection coefficient as a function of the density and speed of sound assuming the interface is with pure water. Included on the plot are values of Λ for common materials. It is interesting to note that the invasive effect is most pronounced when comparing epoxy resin with glass; two of the most common electrode support materials. This highlights the importance of considering the results presented in this chapter in the analysis and comparison of experimental results.

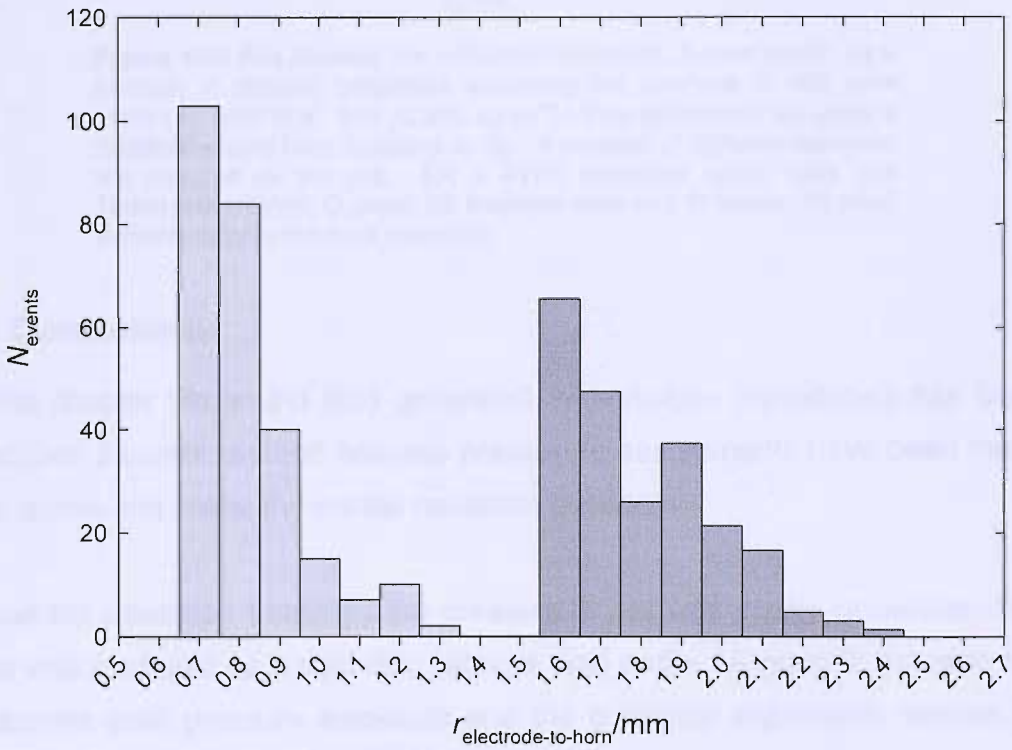


**Figure 4.25** Plot showing the average number of erosion events detected as a function of electrode-to-horn distance for epoxy (light grey) and glass (dark grey) bodied electrodes. Note that the experiment was stopped when the count exceeded ~80 events. The number of events detected is expected to increase as the electrode-to-horn distance is reduced.

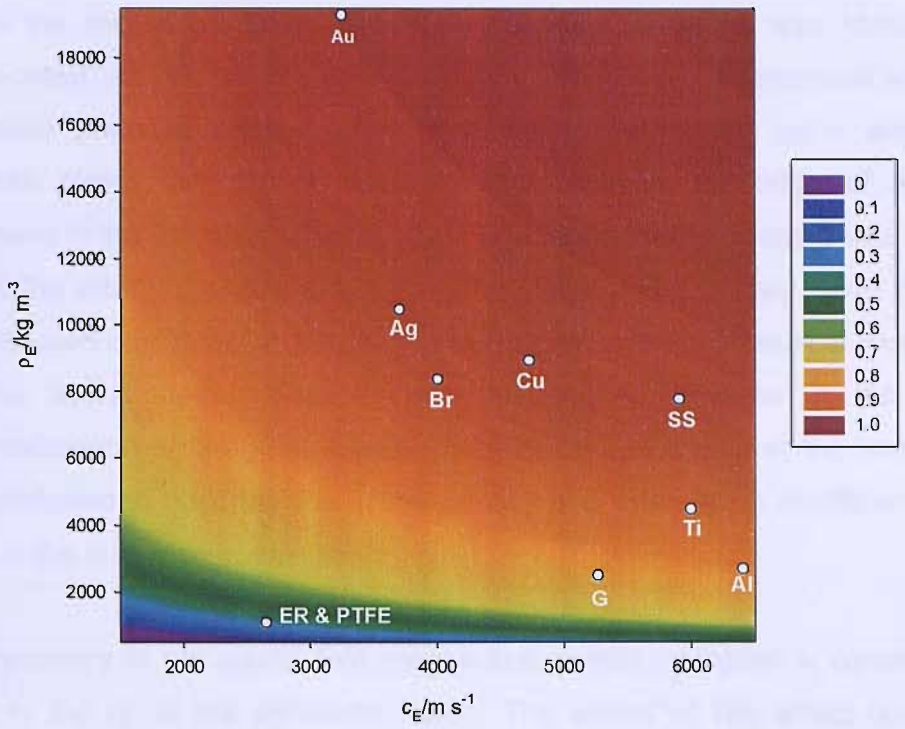


**Figure 4.26** Plot showing the reflection coefficient, Λ (see scale), as a function of material properties assuming the interface is with pure water ($c_S$ 1480 m s$^{-1}$ and $\rho_S$ 990 kg m$^{-3}$). This calculation assumes a fluid/fluid model (see Equation 4.18). A number of different materials are included on the plot. ER & PTFE represent epoxy resin and Teflon respectively, G glass, SS stainless steel and Br brass. All other symbols refer to the pure elements.

## 4.5 Conclusions

In this chapter the sound field generated by horn-type transducers has been described theoretically and acoustic pressure measurements have been made both above and below the inertial cavitation threshold.

Below the cavitation threshold the pressure signal was purely sinusoidal. The horn was modelled as a rigid disc within a rigid baffle. A good fit between the measured axial pressure amplitude and the analytical expression derived by Kinsler *et al.* was obtained, which showed that the pressure is greatest at the tip of the horn. Although the axial profile was a good fit in terms of shape, it was shown that the values of $U$ obtained from the curve fits were likely to be underestimates of the true values. This is because in reality the horn is not within a rigid baffle but rather a free surface (the liquid-air interface). Experiments showed that the rigid baffle assumption introduced a discrepancy in the value of $U$ of 22%.

Above the inertial cavitation threshold the pressure signal was found to be complicated, with an underlying driving pressure wave superimposed with high amplitude pressure spikes. The pressure spikes, which occur every 3-4 pressure cycles, can be attributed to shock waves, the origin of which is discussed in the following chapter. Fast Fourier transform analysis was used to isolate the driving pressure wave from the signal and a fit was made between the pressure amplitude at the driving frequency and the analytical expression for the sound field. The fit was reasonable; however it led to an underestimation of the peak-to-peak displacement of the tip of the horn. This was attributed to uncertainties in the density and attenuation coefficient of the liquid in the presence of cavitation.

The geometry of the sound field means that inertial cavitation is concentrated close to the tip of the ultrasonic horn. The extent of two effect commonly associated with inertial cavitation (MBSL and surface erosion) was measured. It was found that MBSL extended to greater distances than expected, which was attributed to the action of shock waves generated during cavity collapse. Surface erosion (measured electrochemically) was found at even greater distances. This was explained by scattering of the incident sound field by the electrode. Shock waves are efficiently scattered by the electrode and add to the pressure at the surface forcing bubbles, which would not collapse violently in the absence of the electrode, to become inertial. The degree of this scattering depends on the frequency of the incident pressure wave, the size of the electrode and the material used in its construction.

# Chapter 5 Correlation of observed physical effects with bubble dynamics

5

In the previous chapter the sound field generated by the ultrasonic horn was modelled and verified experimentally. Also, a novel dual Pb/Pt microelectrode was used to explore the extent of erosive processes associated with inertial cavitation. In this application the lead and platinum electrodes were used independently. This chapter presents results obtained by recording the current at both microdiscs simultaneously, allowing both the erosive and mass transfer effects of individual cavitation events to be detected. This is a novel approach and represents a major development in the use of electrochemistry as a probe for such effects. In addition, high-speed video (up to 120,000 f.p.s) has been used to image processes above the electrode surface and acoustic pressure measurements have been made in order to correlate the observed physical effects with the bubble dynamics prevalent in the region of interest. This is further investigated by a laser scattering experiment. Two regions are probed. First, close to the horn, within the 'inertial cavitation zone' identified in Chapter 4. Second, the electrode was moved further away from the horn to an area where interesting periodic mass transfer enhancement has been reported [91, 93].

## 5.1 Within the 'inertial cavitation zone'

Initially, the region within 1.4 mm of the tip of the horn was investigated. As shown in the previous chapter, this is in the region in which inertial cavitation exists (or, more correctly, in which the effects widely assumed to be due to inertial events are observed) as well as non-inertial cavitation. The bubble dynamics which lead to the observation of inertial cavitation effects were studied by means of a combination of electrochemistry, MBSL, laser scattering and high speed video.

### 5.1.1 Simultaneous high-speed video and electrochemistry

Figure 5.1 shows 78 frames from a video taken at 120,000 f.p.s, which shows the surface of the electrode (at the bottom of each frame) and a small volume of the solution above the electrode. The horn was 1.4 mm above the electrode and is out of the frame of view. For the majority of the time the solution appears

relatively free from bubble activity. There are four frames however (6 ($t$ = 1343 µs), 28 ($t$ = 1525 µs), 48 ($t$ = 1690 µs) and 70 ($t$ = 1871 µs)), which show bubble activity in the vicinity of the electrode.

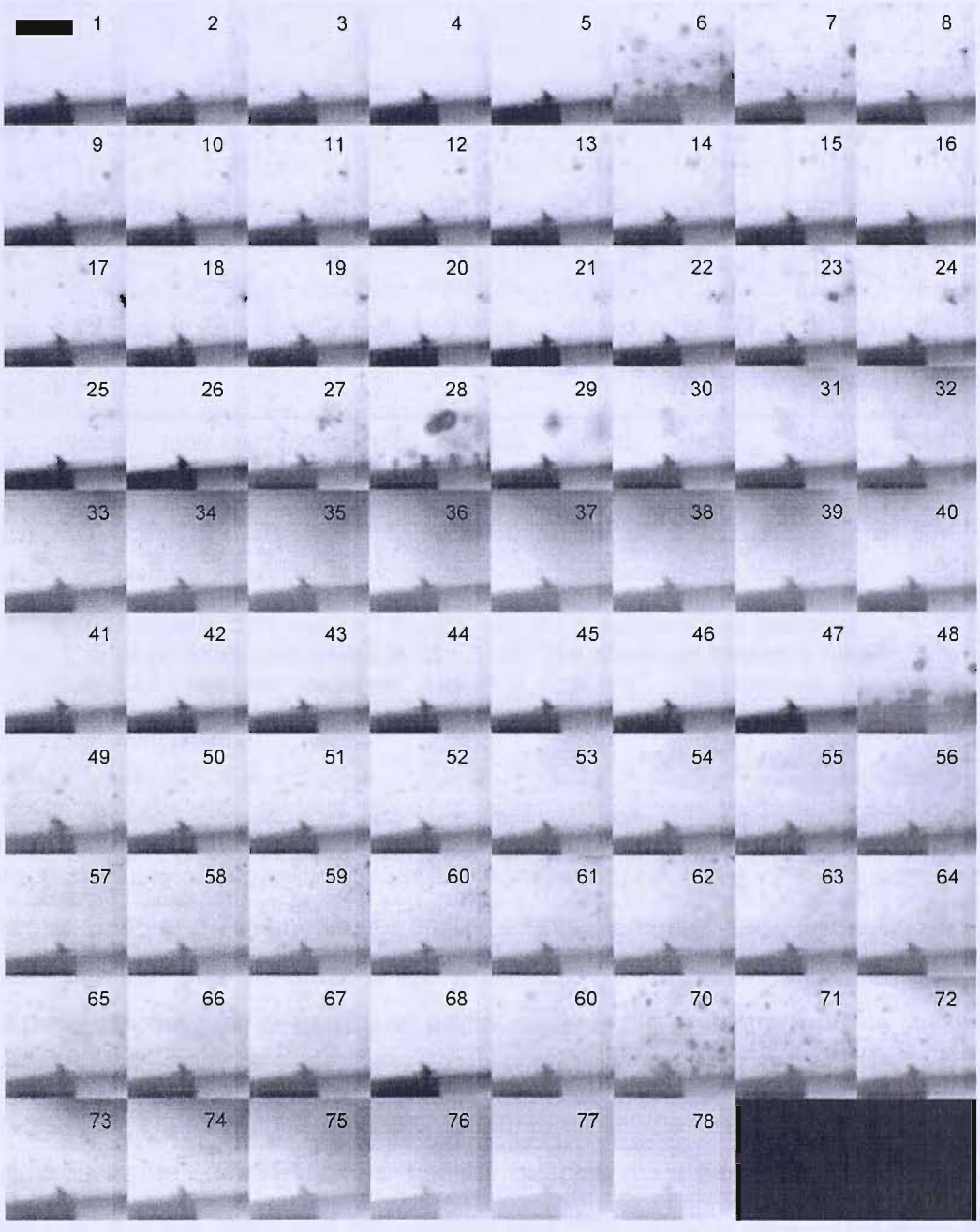


**Figure 5.1** 78 frames recorded simultaneously with the current data shown in Figure 5.2. The first frame is at $t$ = 1302 µs and the capture rate was 120,000 f.p.s. The electrode entres from the bottom of each frame. The dark area at the bottom left of each frame is the silhouette of the lead and platinum electrodes. The scale bar in the first frame represents approximately 150 µm.

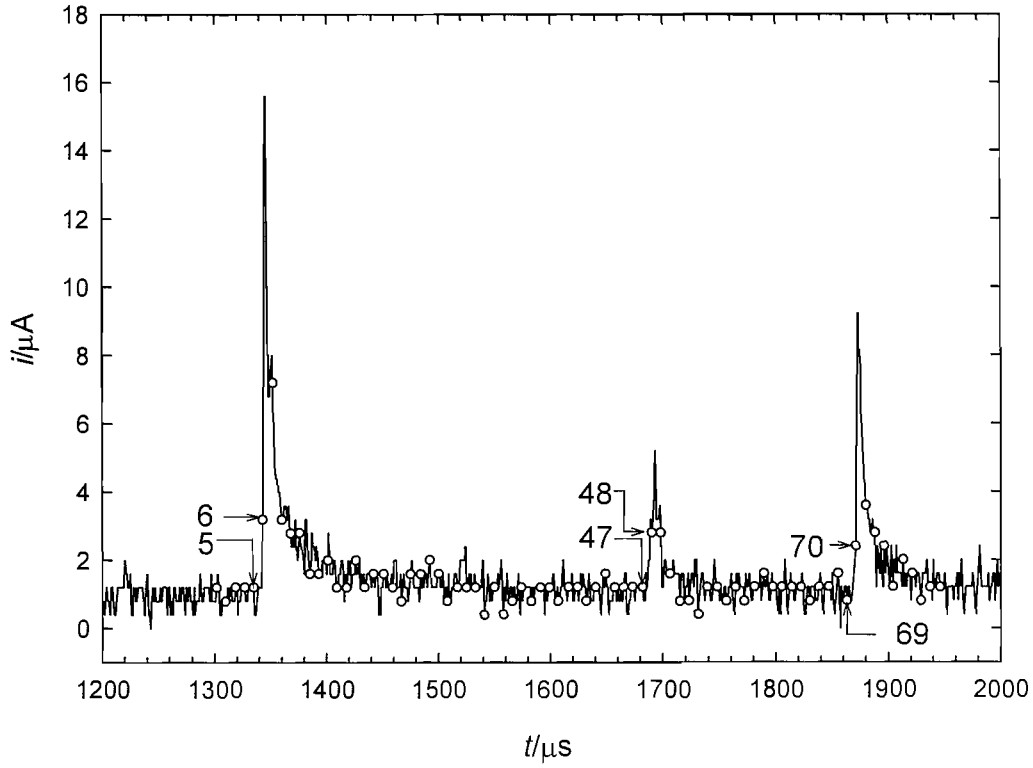


**Figure 5.2** Current trace recorded at a lead microelectrode (125 μm diameter) exposed to ultrasound. The electrode-to-horn separation was 1.4 mm. The potential was held at +0.8 V *vs.* Ag. The solution contained 0.75 mol $dm^{-3}$ $Na_2SO_4$ and the experiment was performed under aerobic conditions at 35 ± 3 °C. The ultrasound frequency was 22.83 kHz and the power was 56 ± 5 W $cm^{-2}$. The symbols (○) represent the timing of the frames in Figure 5.1. Selected frames are numbered.

It can be seen from Figure 5.2, which shows the current recorded simultaneously at a passivated lead electrode that on three of these occasions (frames 6, 48 and 70) anodic current transients were detected. From Figure 5.1 it can be seen that the bubbles are small (~10-50 μm maximum diameter) and exist both in the bulk solution and at the surface of the electrode. The life time of these bubble events was noted to be very short. Consider the first event (frame 6). There are no bubbles visible in either the preceding frame or the following frame. This indicates that the bubbles must expand and collapse in less than 8.3 μs, given that the capture rate was 120,000 f.p.s. The short life time and small radii of these bubbles means that they are not visible in the video footage presented in Chapter 4 (Figure 4.7), which shows a large bubble cluster at the tip of the horn. It should be noted that the majority of this large bubble cloud cannot be seen in Figure 5.1 because it is out of the field of view; however it is partially evident in frames 33-39. It was shown in Chapter 4 that the collapse of this large bubble cloud occurs every 3-4 pressure cycles. It was

also shown that shock waves detected in the pressure trace (see Figure 4.6) were not associated with the collapse of this bubble cloud. Rather, it was found that shock waves were detected after the bubble cloud disappeared from view. In order to establish the timing of the shock waves with respect to erosion of the passivated lead electrode the current and pressure were measured simultaneously, which is discussed in the following section.

### 5.1.2 Simultaneous electrochemistry, MBSL and acoustic pressure

The current recorded at a passivated lead electrode (125 μm diameter held at +0.8 V *vs.* SCE) and acoustic pressure, measured at the same time, under exposure to ultrasound in a solution of 0.75 M $Na_2SO_4$ is shown in Figure 5.3.

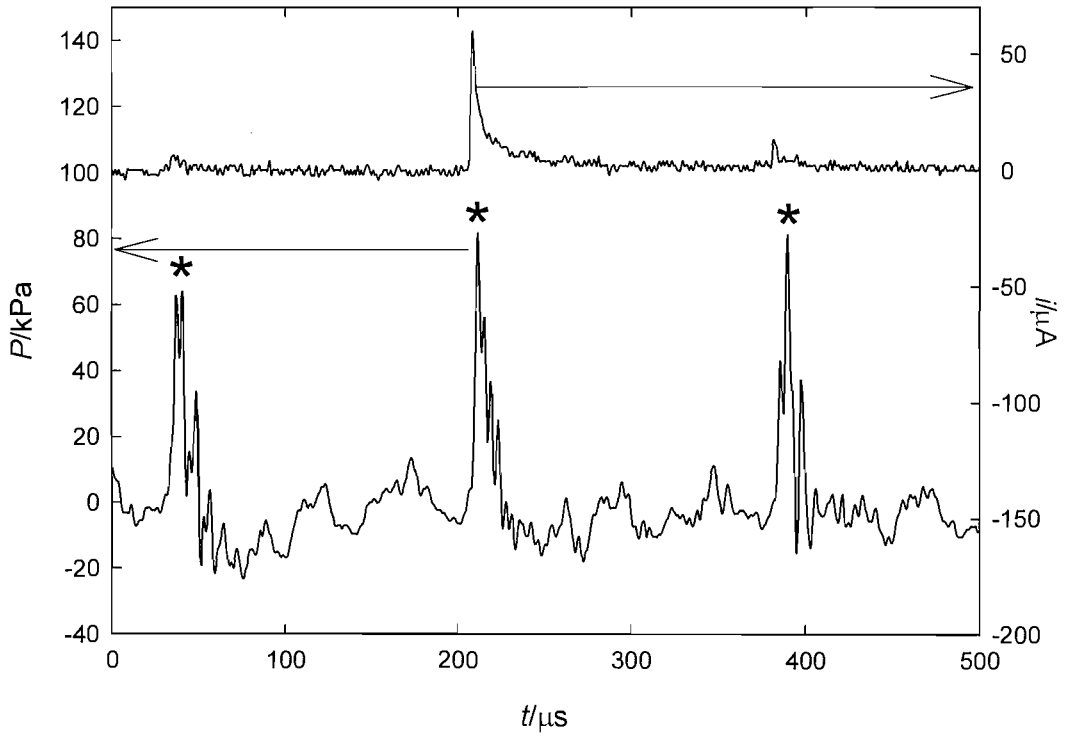


**Figure 5.3** Acoustic pressure and current recorded at a passivated lead electrode (125 μm diameter). The electrode-to-horn distance was 1 mm and the horn-to-hydrophone distance was 10 ± 1 mm.

The lower trace shows the acoustic pressure trace, which is somewhat distorted because this data was recorded in a relatively small cell (type B see Figure 2.6). As a result the hydrophone was subject to reverberant field effects in addition to the direct field and signals associated with cavitation activity. Nevertheless, pressure spikes (labelled *) can be seen to occur periodically, in a similar fashion to those shown in Figures 4.6 and 4.9. The upper trace shows the current recorded at the same time. The electrode was positioned 1 mm from

the tip of the horn and the hydrophone was 10 ± 1 mm from the tip of the horn. In order to correlate the current and pressure data 13 µs has been added to the current trace. This is to account for the delay caused by the finite speed of sound in the liquid. Owing to uncertainties in the speed of sound (as discussed in Section 4.2.2) and the location of the hydrophone, there is an error of at least ± 4 µs. However, a repassivation transient can be seen to occur at $t$ ~ 210 µs, which correlates temporally with a pressure spike. A second, much smaller small transient can be seen at $t$ ~ 380 µs (4 pressure cycles later), which also correlates with a large pressure spike. While it must be noted that the timing of the shock wave is by no means exact, it is clear that the erosion of the electrode is associated with the shock wave. This confirms that the small, short lived bubbles (see Figure 5.1, frame 6), which are associated with erosion of the electrode are also associated with shock wave emission. The exact nature of this association is discussed further in Section 5.1.4. In addition to this erosion data, temporally correlated pressure and MBSL data was also recorded, which is shown in Figure 5.4.

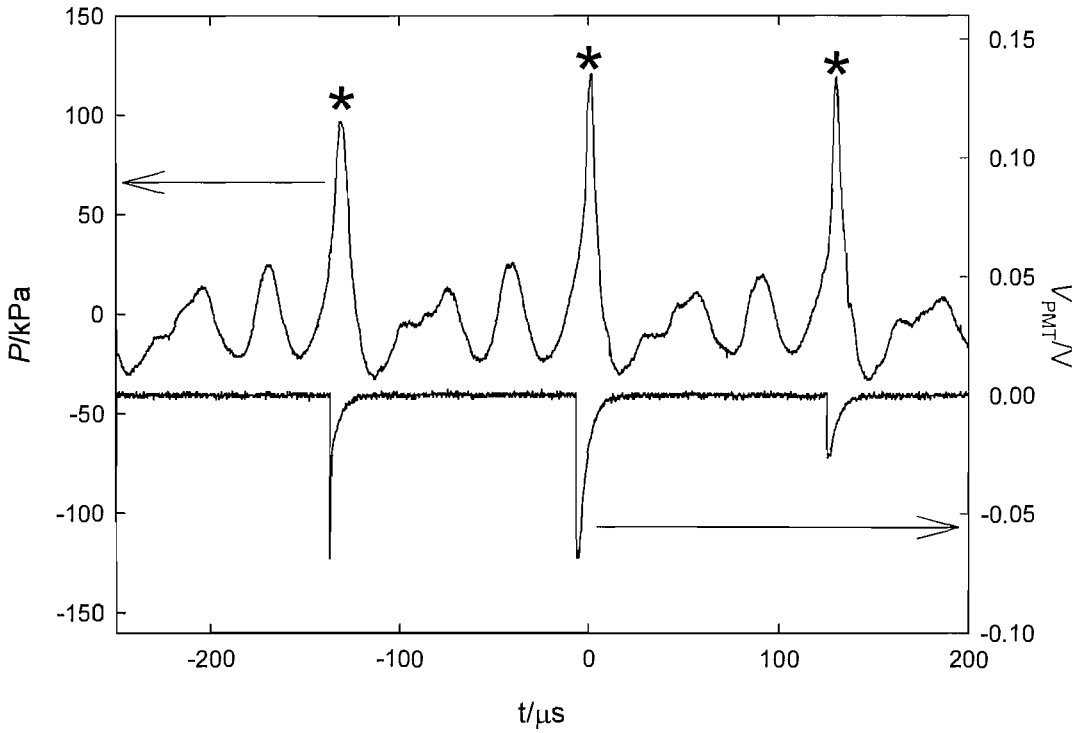


**Figure 5.4** Plot showing the acoustic pressure (upper trace) and output from the PMT (lower trace) as a function of time. The horn-to-hydrophone distance was 15 ± 1 mm.

High time resolution MBSL was recorded by means of a photomultiplier tube (see Section 2.5.3). The upper trace in the figure shows the acoustic pressure

and the lower trace shows the output from the PMT. It is clear that light output (negative voltage spikes) correlates temporally with the high pressure spikes, suggesting that MBSL is also associated with the small, short lived bubbles shown in Figure 5.1. It is interesting to note that in the case of MBSL (see Figure 5.4), for every shock wave seen in the pressure signal there is corresponding light output. In contrast, not every shock wave seen in Figure 5.3 leads to a repassivation transient. Similarly, only three of the four bubble events seen in Figure 5.1, generate an electrochemical response. This suggests that although a global shock wave is generated, which can be detected by the hydrophone, it is the action of a localised event that leads to surface erosion. The lead microelectrode represents a small target, whereas the PMT collects light from a wide area. Only events, which occur in a suitable location, will be detected by the passivated electrode.

### 5.1.3 Simultaneous laser scattering and acoustic pressure

In order to further confirm the dynamics of the bubble population, a laser scattering experiment was performed (see Section 2.7 for experimental details). Similar experiments have been performed in order to monitor bubble formation during lithotripsy procedures [175]. For the experiment described here, a laser beam was passed below the tip of the ultrasonic horn at a distance of 1.4 mm. A photodiode was aligned with the laser beam and the output of the photodiode monitored during sonication. The photodiode amplification electronics (see Figure 2.24) were such that under daylight conditions the output, $V_{PD}$ was 0 V, while the maximum output (under direct illumination by the laser, through the cell) was -1.2 V. Thus, any scattering of the beam resulted in an increase in the output voltage (*i.e* less negative). At the same time as recording the output from the photodiode, the acoustic pressure was also measured. Figure 5.5 shows the photodiode output and acoustic pressure measured simultaneously under exposure to ultrasound. Initially the output from the photodiode (upper trace) is high (-0.7 V), indicating that the laser light is scattered, presumably by bubbles at the tip of the horn. The scattering of the laser light can be seen in Figure 5.6b, which shows a photograph of the experiment with ultrasound operating. Comparison with Figure 5.6a, which shows the corresponding situation without ultrasound, reveals scattering of the laser light at the tip of the ultrasonic horn. The value of $V_{PD}$ is then seen to decrease, reaching a minimum (~-1.2 V), which is followed by a positive spike (labelled A). The

output then increases to the original value (labelled C) before this cycle of decrease followed by positive spike (labelled A') and increase is repeated. The decrease in $V_{PD}$ indicates that the solution is clearing of bubbles.

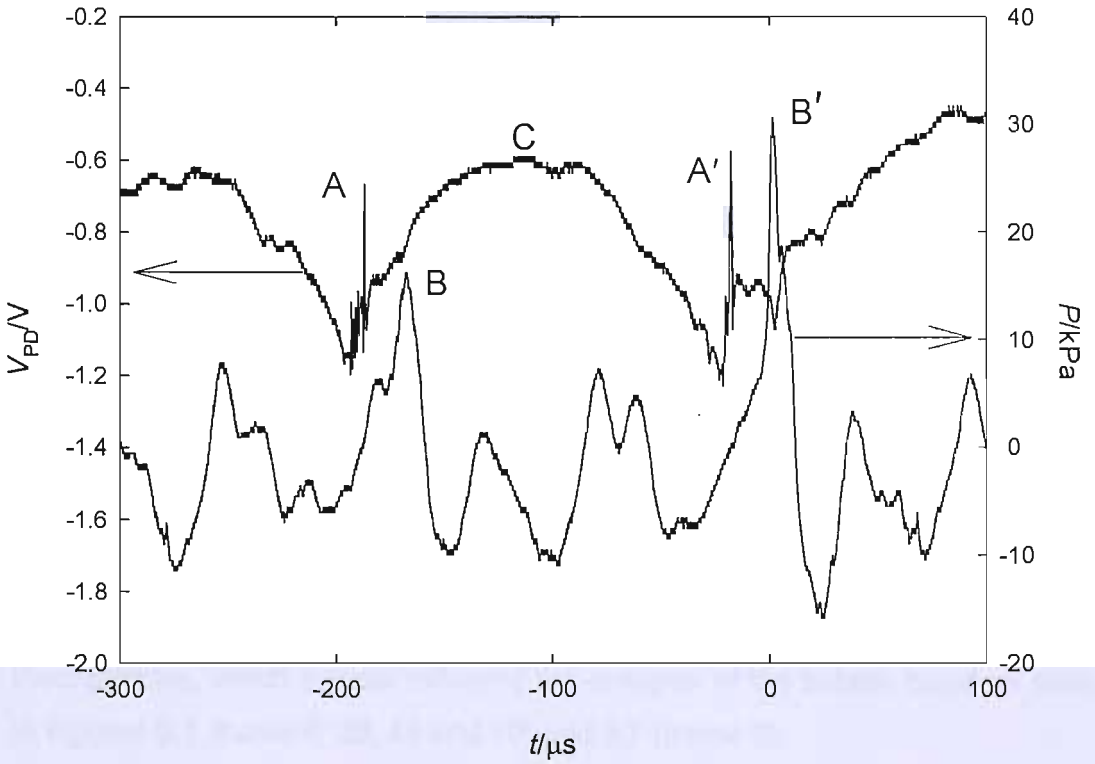


**Figure 5.5** Plot showing the acoustic pressure (lower trace) and output from a photodiode (upper trace) recorded simultaneously under exposure to ultrasound (23.10 kHz, 56 ± 5 W cm$^{-2}$). The photodiode was aligned with a laser beam, which was passing below the tip of the horn at a distance of 1.4 mm. The distance between the horn and the hydrophone was 20 ± 1 mm.

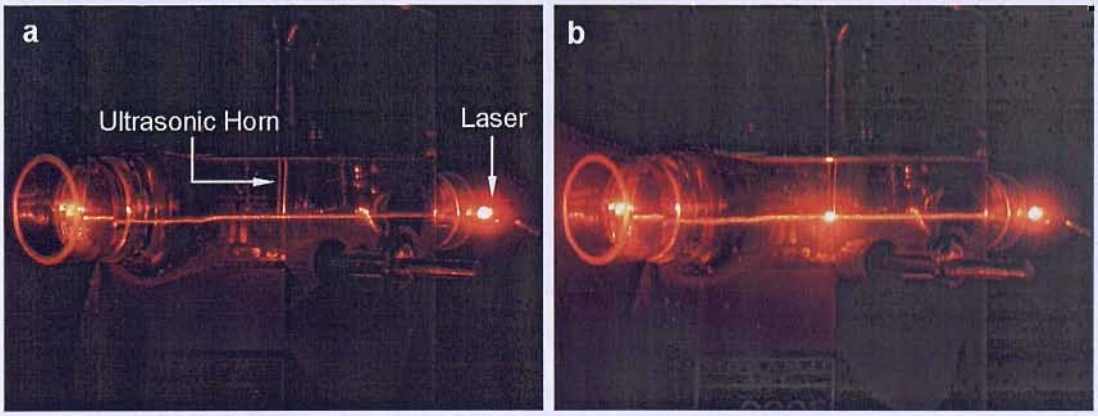


**Figure 5.6** Photographs showing laser scattering experiment. **(a)** No ultrasound. **(b)** With ultrasound (23.10 kHz, 56 ± 5 W cm$^{-2}$). The photodiode is out of the field of view to the left of each picture.

The periodic clearing of the solution is consistent with the video footage presented in Figure 4.7, which shows a bubble cloud of oscillating volume at the tip of the horn that can be seen to undergo complete collapse every 3-4 pressure cycles. Figure 4.7 does not show the small, short lived bubbles, which can be seen in Figure 5.1. However, these short lived bubble events can be seen in Figure 5.7, which shows frames from high speed video footage of a volume of solution between the horn (shown by the dotted line in frame 1) and an electrode (at the bottom of each frame). A large bubble cloud can be seen at the tip of the horn. This undergoes a collapse from frames 1 to 7 and the solution appears clear in frame 8. The collapse time for the bubble cloud is 75 ± 5 μs (given the frame rate of 100,000 f.p.s). This is consistent with the data presented in Chapter 4. In frame 9 small bubbles can be seen in the bulk solution (highlighted by the dotted ellipse), similar to those shown in Figure 5.1. This sequence of events (cloud collapse followed by the appearance of small bubbles) is supported by the laser scattering data presented in Figure 5.5. Following the clearing of the solution (seen as a decrease in $V_{PD}$) positive spikes (A and A') are seen. These spikes are therefore attributed to the short lived bubbles, which appear following the collapse of the bubble cloud as seen in Figures 5.1 (frame 6, 28, 48 and 70) and 5.7 (frame 9).

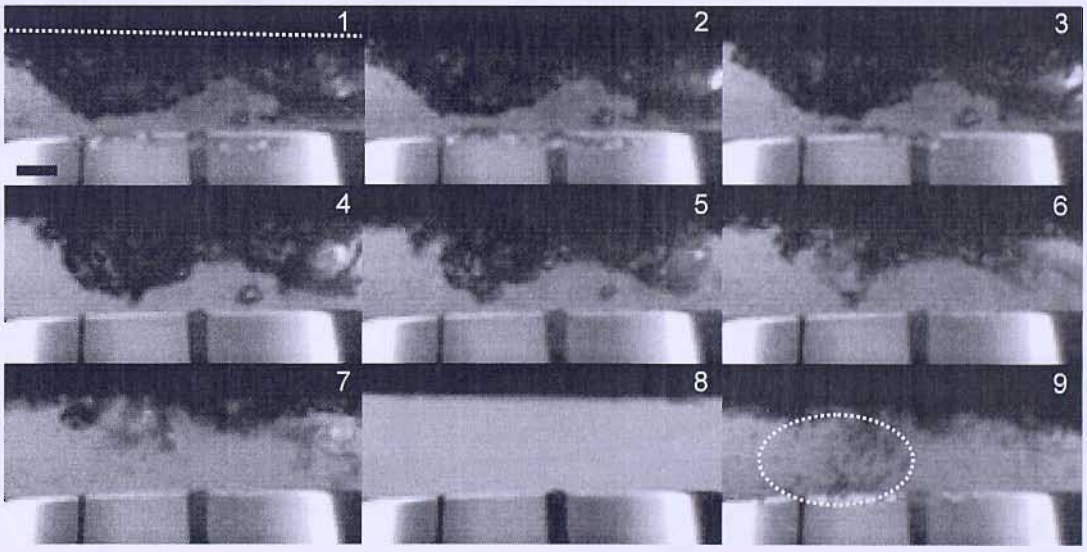


**Figure 5.7** 9 frames taken from high speed video footage recorded at 100,000 f.p.s. The tip of the horn is at the top of each frame (shown by the dotted line in frame 1). An electrode can be seen at the bottom of each frame. The scale bar in frame 1 represents 250 μm.

While it appears from Figure 5.5 that the short lived cavities exist prior to the occurrence of shock waves, which can be seen in the pressure data and

labelled B and B′, care must be taken owing to the finite speed of sound within the liquid. The photodiode records real time dynamics of the bubble population, while the hydrophone is subject to a delay, which is proportional to the speed of sound within the liquid. This was further investigated by altering the distance between the tip of the horn and the hydrophone. Figure 5.8 shows three data sets recorded with the hydrophone at an axial distance ($r_{ax}$) of (a) 14.2 mm, (b) 28.2 mm and (c) 52.2 mm.

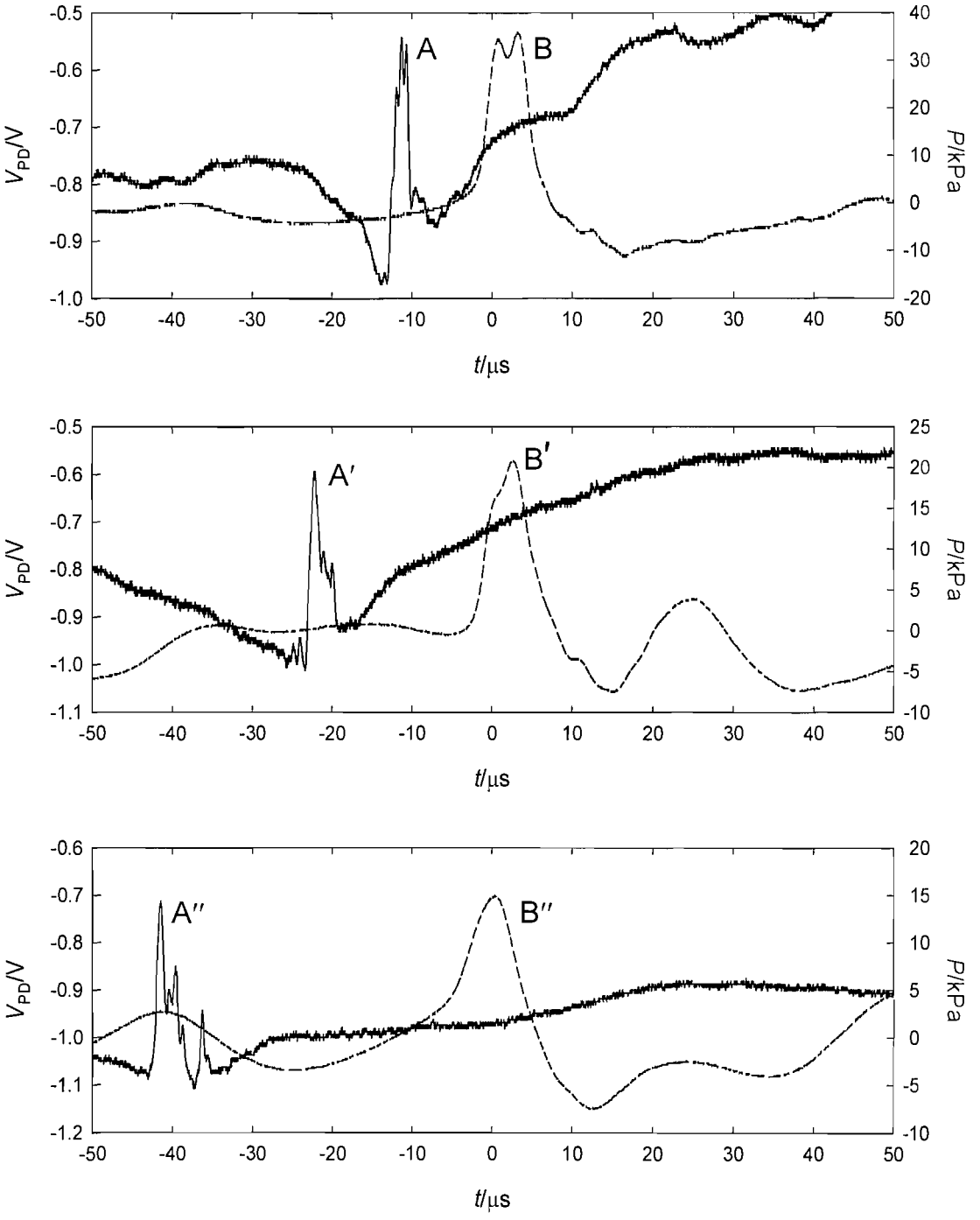


**Figure 5.8** Plot showing the acoustic pressure (— — —) and output from a photodiode (——) recorded simultaneously under exposure to ultrasound at three horn-to-hydrophone distances. **(a)** 14.2 mm **(b)** 28.2 mm **(c)** 52.2mm.

In all cases the pressure, shown by the dotted line, exhibits a large spike, labelled B, B′ and B″. This was used to trigger the oscilloscope, which was employed to collect the data. As in Figure 5.5, the output from the photodiode shows a positive spike (labelled A, A′ and A″) prior to the shock wave. In Figure 5.8a, for which the distance between the tip of the horn and the hydrophone was 14.2 mm, the peak in the photodiode output (A) occurs 13 ± 2 μs prior to the pressure shock (B). On increasing the distance between the tip of the horn and the hydrophone the time between the peak in $V_{PD}$ and the shock wave can be seen to increase. A plot showing the delay between the peak in the photodiode data and the pressure shock ($\Delta t$) plotted as a function of distance between the tip of the horn and the hydrophone ($r_{ax}$) is shown in Figure 5.9.

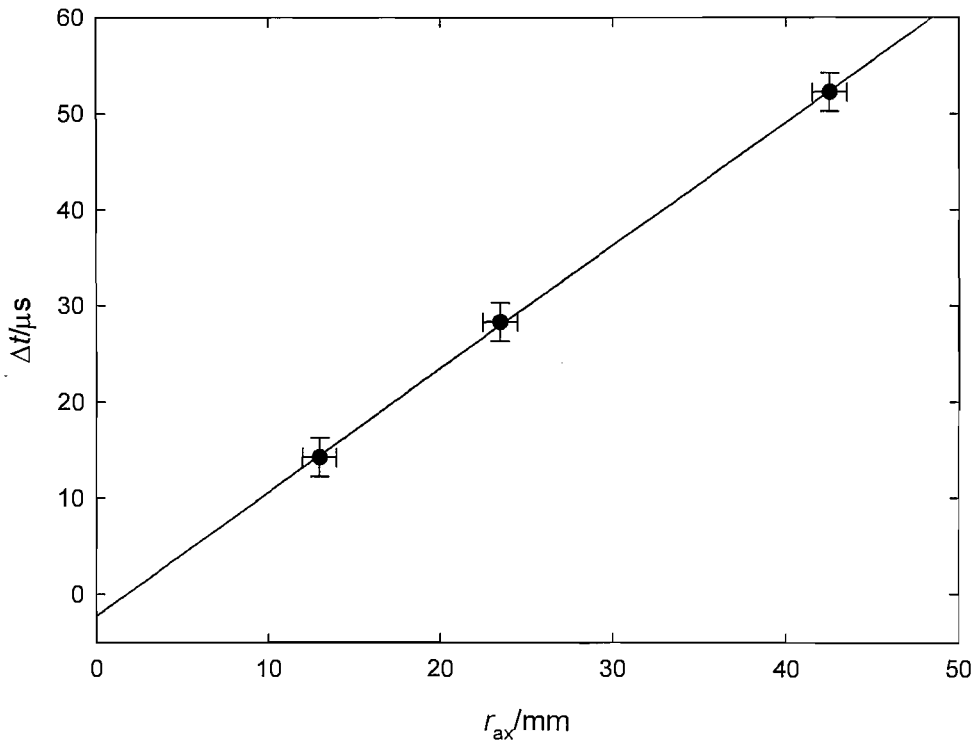


**Figure 5.9** Plot showing the delay between the peak in the photodiode output (measured from the initial rise) and the pressure shock as a function of axial distance between the tip of the horn and the hydrophone.

There appears to be a linear relationship between the delay and the distance which is to be expected. The inverse of the gradient gives a value for the speed of sound in the liquid as 780 ± 120 m $s^{-1}$. This is much less than the speed of sound in bulk water, however retardation of sound velocity in bubbly liquids is well known [101, 166]. The intercept (*i.e* the delay at zero distance) is -2.2 ±

6.2 μs. The fact that this is close to zero is further evidence that the shock waves seen in the pressure traces are associated with the short lived bubbles seen in Figures 5.1 and 5.7. The exact nature of this association will now be discussed further.

### 5.1.4 Explanation of observed effects: Shielding *vs.* rebound

In the preceding sections it was shown that shock waves, surface erosion and MBSL are all associated with small, short lived bubbles. These become visible in the solution following the collapse of a large bubble cloud at the tip of the ultrasonic horn. Consider Figure 5.10, which shows the dynamics of these cavities in greater detail. This is taken from the same footage as Figure 5.1. The frame numbers do not correlate between the figures. The dark area at the bottom of each frame is an epoxy electrode and the light area is the solution (0.75 M $Na_2SO_4$). The electrode was 1.4 mm from the horn, which is out of the field of view at the top of each frame. The contrast has been increased compared with Figure 5.1. In frame 1 a number of small bubbles can be seen. One such bubble is indicated with an arrow. These remain visible and of roughly the same size until frame 5. In frame 6 they can be seen to have expanded to many times their original size. There are two possible mechanisms, which may explain this behaviour. First, the removal of the shielding effect of the bubble cloud and second, bubble rebound. These will now be discussed.

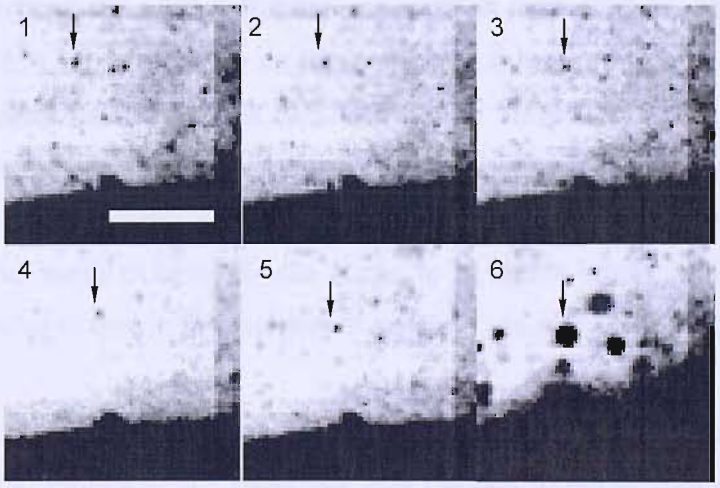


**Figure 5.10** 6 frames from high speed video footage recorded at 120,000 f.p.s. The dark area at the bottom of each frame is an electrode. The scale bar in frame 1 represents 150 μm.

**Shielding**

It is well known that bubble clouds at the tip of operating ultrasonic horns can shield the bulk solution from the pressure wave [32, 167, 168]. It may be that the collapse of the large bubble cloud exposes the solution to a greater negative pressure than in the presence of the cloud. This may exceed the threshold required for explosive growth. This would lead to the appearance of cavitation bubbles, such as those in Figure 5.1 (frames 6, 28, 48 and 70) and Figure 5.7 (frame 9). The subsequent violent collapse of these bubbles may be responsible for the observed effects. Inspection of Figure 4.6 does indicate that the peak negative pressure for the cycle immediately before the shock wave is greater than the preceding cycle, suggesting that this may be the case[8]. However, in order to confirm this it would require complex experimental procedures. Large volumes of solution are required to minimise reverberant field effects. However, the techniques described in this thesis to detect inertial cavitation (MBSL and electrochemical detection of surface erosion) lend themselves to small scale experiments. MBSL requires dark conditions and the ability to place the PMT relatively close to the ultrasonic horn. The electrochemical technique makes use of concentrated sulphate solution. Scale up of both procedures, to allow simultaneous measurement of the unperturbed acoustic pressure and effects of inertial cavitation, would therefore be difficult.

**Bubble rebound**

The second possible explanation for the bubble behaviour shown in Figures 5.1 and 5.7 is bubble rebound. Bubble rebound is well known, for example in lithotripsy [176, 177]. Following an initial shock a bubble (or cloud of bubbles) is compressed and then rebounds to many (up to 1000) times the original size. Following this the bubbles collapse again and emit pressure pulses. The bubbles may then undergo further rebounds or fragment. It is possible that the collapse of the large bubble cluster leads to a shock wave, which generates behaviour similar to this in the cavities in solution, as shown in Figure 5.10.

A comparison of the shielding and bubble rebound mechanisms is shown schematically in Figure 5.11. However, it is difficult to either rule out or confirm

[8] It should be noted that Figure 4.6 is the only 'clean' pressure trace recorded in the presence of inertial cavitation that is presented in this work. All other pressure traces were recorded in relatively small cells and as such were subject to greater reverberant field effects.

either mechanism as supporting evidence for both can be found in the data presented here. Consider Figures 5.1 and 5.2. The initial rise of the first anodic transient in Figure 5.2 can be seen to occur between frames 5 and 6 (*i.e* prior to the growth of the short lived bubbles). This suggests that the erosion is generated by a shock wave, which then causes bubbles to rebound and become visible. However, it should be noted that an error of only 1 μs in the synchronisation of video and electrochemical data could suggest that the transient occurs after frame 6. This could support the shielding argument, whereby erosion is caused by the collapse of the cavities seen in, for example, frame 6 of Figure 5.1. An error of this size is possible as the time resolution on the camera is 1 μs. The shielding mechanism is further supported by the data presented in Figures 4.8 and 4.9, which appeared to show that shock waves are not associated with the cluster collapse. However, uncertainties in the speed of sound in the complex environment generated by the horn mean it is impossible to rule out the rebound mechanism based on this alone.

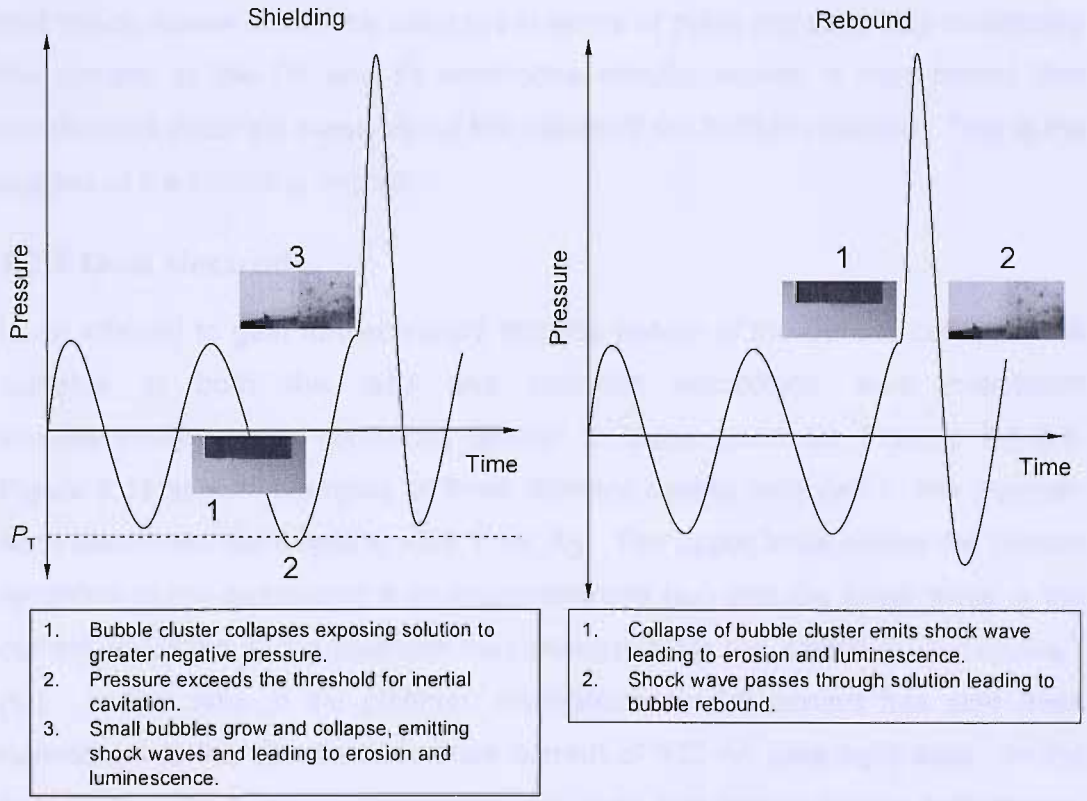


**Figure 5.11** Schematic comparison of the shielding and bubble rebound mechanisms. For full details see the main text.

Although the exact mechanistic detail of the bubble behaviour observed has not been ascertained here, the data presented in the previous sections (5.1.1-5.1.3) is notable for a number of reasons. The high-speed video footage shows multibubble acoustic cavitation (as opposed to laser-induced cavitation or other single bubble studies) at unprecedented frame rates. It is also the first time that simultaneous high-speed video and electrochemical data, and time correlated pressure and electrochemistry recorded under exposure to cavitation has been presented. The application of laser scattering to studying the dynamics of the bubble population is also novel and, together with acoustic pressure measurements made at the same time, this data gives a unique insight into the behaviour of the multibubble cavitation system.

In an attempt to further elucidate the mechanism responsible for erosion effects, a Pb/Pt dual electrode was employed. As discussed in Chapter 3, the dual electrode can detect both the erosive and mass transfer effects of cavitation. These effects have been associated with different mechanisms (it is assumed that shock waves cannot be detected in terms of mass transfer). By monitoring the current at the Pb and Pt electrodes simultaneously, it was hoped that conclusions could be drawn about the nature of the bubble collapse. This is the subject of the following section.

### 5.1.5 Dual electrode

In an attempt to gain further insight into the nature of the bubble collapse, the currents at both the lead and platinum microdiscs were monitored simultaneously under conditions similar to those used for Figures 5.1-5.8. Figure 5.12 shows examples of three different events recorded in this manner. Both electrodes were held at +0.8 V *vs.* Ag. The upper trace shows the current recorded at the passivated lead microelectrode ($i_{Pb}$) and the lower trace is the current recorded at the platinum microelectrode for the oxidation of $Fe(CN)_6^{4-}$ ($i_{Pt}$). In the case of the platinum microelectrode the current has also been normalised to the silent steady state current of 132 nA (see right axis). In the section labelled A, current transients are seen simultaneously on both traces. The magnitude and duration of the transients are in good agreement with previous work [83, 90, 98] and are indicative of an inertial bubble collapse, showing for the first time that both the mass transfer and erosion effects of the same inertial cavitation event can be recorded simultaneously.

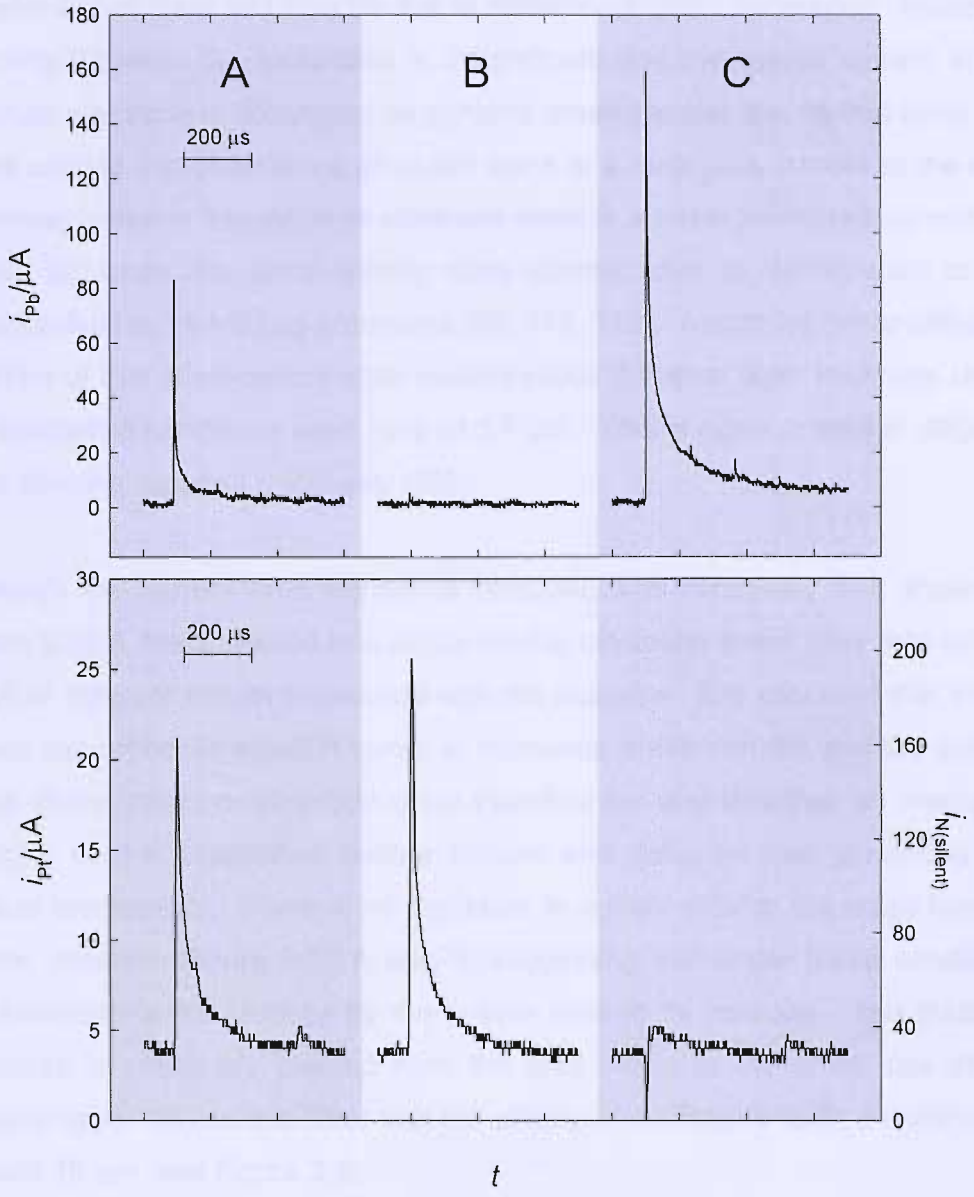


**Figure 5.12** Current traces from lead (125 µm diameter, upper plot) and platinum (50 µm diameter, lower plot) discs of the dual electrode under exposure to ultrasound. The electrode-to-horn separation was 1.4 mm. The solution contained 20 mmol $dm^{-3}$ $K_4Fe(CN)_6$ and 0.75 mol $dm^{-3}$ $Na_2SO_4$ and the experiment was performed under aerobic conditions at 25 ± 1°C. Both electrodes were held at +0.8 V *vs.* Ag. The ultrasound frequency was 22.83 kHz and the power was 56 ± 5 W $cm^{-2}$. The mass transfer data has been normalised with respect to the steady state current recorded under silent conditions (132 nA).

It is also possible to detect cavitation events, which either produce mass transfer or erosion signals alone. Examples of these types of event are shown in Figure 5.12 B and C respectively and are discussed further later. However, this clearly shows that the simultaneous current transients are genuine and not the result of coupling in the acquisition electronics. There is a minor transient, seen in the lower trace of part C, which does not have the form of a mass

transfer disturbance and may be due to minor electronic interference. However, coupling between the electrodes is insignificant and the overall current at the platinum electrode is dominated by genuine mass transfer events that occur. At times outside the occurrence of peaks there is a negligible current at the lead electrode, while at the platinum electrode there is a much increased current, up to *ca.* 30 times the silent steady state current, due to deformation of the diffusion field by streaming processes [96, 178, 179]. Assuming linear diffusion, analysis of this quasi-steady state current yields diffusion layer thickness under the sonication conditions used here of 0.7 μm. This is close to limit of diffusion layer thinning reported previously [88].

Although the current time transients recorded simultaneously and shown in Figure 5.12 A are attributed to a single inertial cavitation event, they may be the result of different effects associated with the collapse. It is assumed that shock waves cannot be detected in terms of increased mass transfer and the current spike at the platinum electrode must therefore be due to either an impinging microjet or the associated bubble motion and collapse that generated the erosive mechanism. There is no depletion in current prior to the mass transfer spikes shown in Figure 5.12 A and B, suggesting that under these conditions the electrode is not blocked by the bubble prior to its collapse. The platinum electrode is effectively isolated from the lead owing to the small size of the diffusion layer and so it is clear that the effects of a collapse span a distance of at least 10 μm (see Figure 2.8).

Mass transfer enhancement without associated erosion events (Figure 5.12 B) could be caused by non-inertial cavitation, which will occur in the region under investigation or by bubble motion in the vicinity of the Pt microdisc. However, mass transfer events of the magnitude and duration shown in the figure ceased when the electrode-to-horn distance was increased to more than 1.5 mm (*i.e.* beyond the location of the inertial cavitation threshold identified in Chapter 4). Non-inertial cavitation would still be expected at this distance as would other bubble motion; hence it is unlikely that the events shown are due to non-inertial bubble oscillation/motion. It is perhaps more likely that the location of the bubble collapse limits the effects to the platinum electrode. An event at the

edge of the platinum electrode cannot be detected in terms of surface erosion because of the short range nature of the erosive mechanisms.

Assuming that the bubble collapse occurs at the centre of the Pb and Pt microdiscs, it may be that an erosion event without mass transfer enhancement (Figure 5.12 C) is the result of a collapse, which results in a shock wave emission but no associated microjet formation. However, as with Figure 5.12 B, this scenario could equally be explained by considering the location of the bubble collapse. An event at the edge of the lead electrode occurs up to 130 μm from the platinum microdisc, well beyond the limits of mass transfer detection given the highly deformed diffusion layer.

These spatial limitations are disappointing. It may be desirable to investigate the construction of a micro ring-disc electrode, which would alleviate the problem. It would also be desirable to reduce the size of the dual electrode considerably. It appears from the video footage in Figure 5.1 that the cavitation bubbles, which lead to erosion of the surface, are smaller than anticipated. Nevertheless the concept of the dual electrode is still valid but further development is necessary if it is to be used to its full potential.

## 5.2 Response outside the 'inertial cavitation zone'

On increasing the separation between the horn and the electrode very different behaviour was observed. Initially a Pb/Pt dual electrode was used and placed at a distance of 4.5 mm from the tip of the horn. As in Section 5.1.5, the potential of both microdiscs was held at +0.8 V *vs.* SCE. An example of a typical current time trace is shown in Figure 5.13. The electrode was well outside the region in which erosion was detected in the previous chapter and as expected no current can be seen at the passivated lead electrode. At the platinum electrode, where there is mass transfer limited oxidation of $Fe(CN)_6^{4-}$ the current is initially (at $t$ = -2 ms) stable at approximately 1.8 μA. This is *ca.* 14 times greater than the silent steady state current (132 nA). This elevated steady state current is attributed to streaming processes as seen in Section 5.1.5.

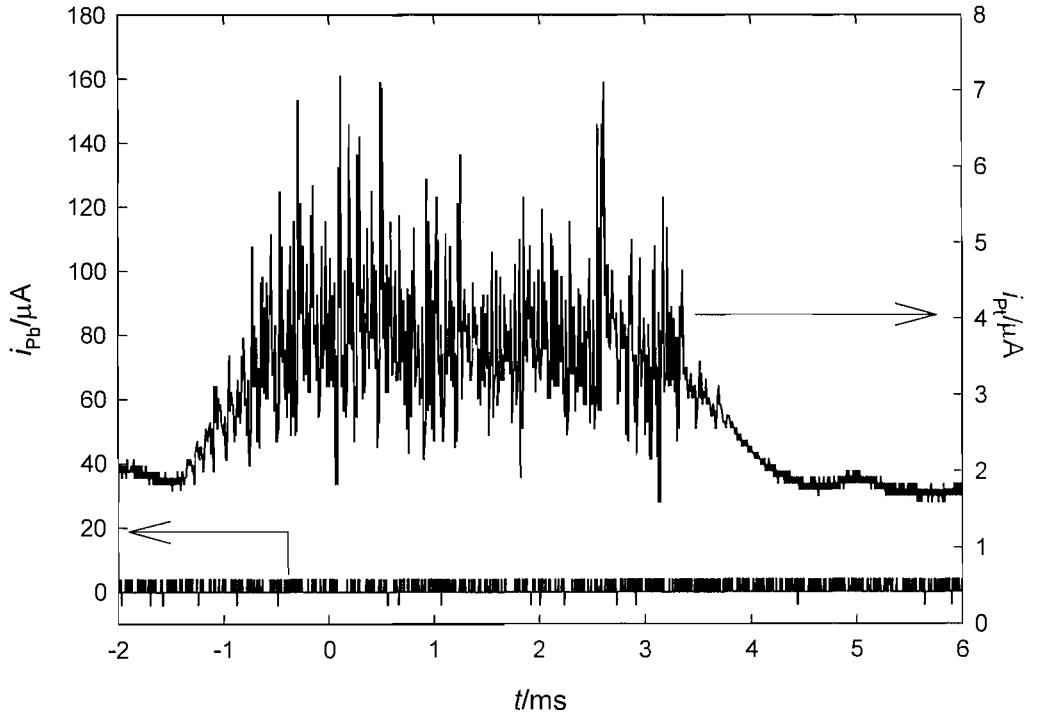


**Figure 5.13** Current traces recorded simultaneously from lead (125 μm diameter) and platinum (50 μm diameter) microdiscs of a dual electrode under exposure to ultrasound (22.83 kHz, 56 ± 5 W $cm^{-2}$). The electrode-to-horn separation was 4.5 mm. The solution contained 20 mM $K_4Fe(CN)_6$ and 0.75 M $Na_2SO_4$ and the experiment was performed under aerobic conditions. The potentials of both discs was held at +0.8 V *vs* Ag.

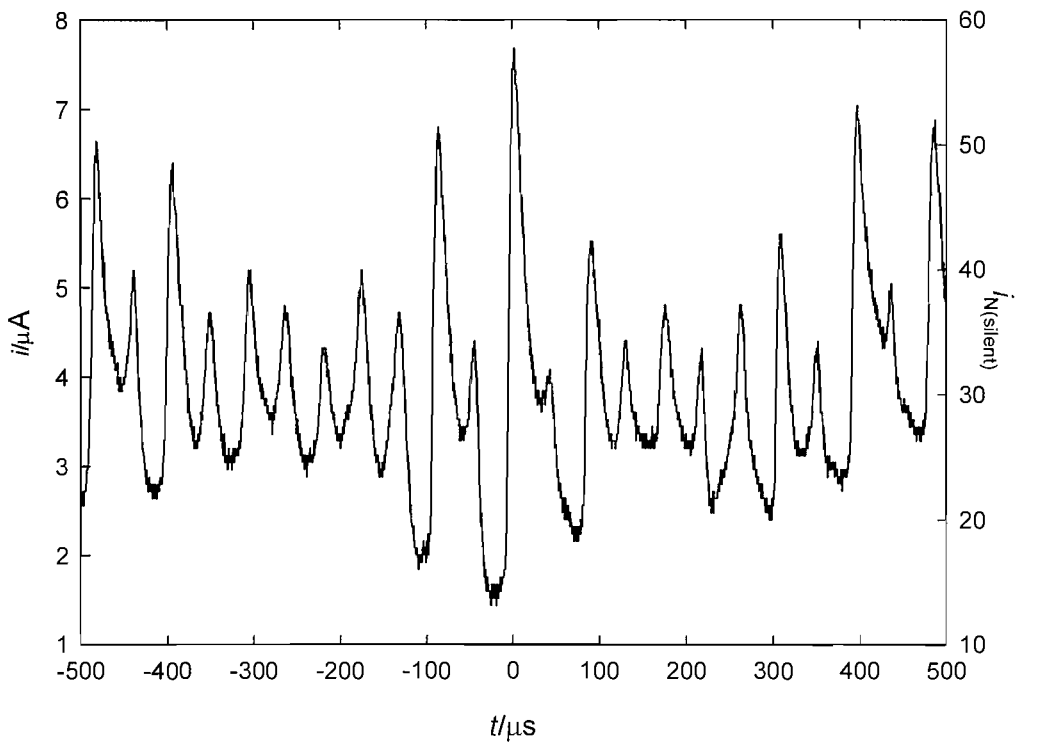


**Figure 5.14** Expansion of Figure 5.13 around $t$ = 0.

The magnitude of the enhancement is around half that than seen in Figure 5.12, presumably because of the lower streaming velocities seen at the greater distances employed for the data shown in Figure 5.13 (4.5 mm rather than 1.4 mm). At $t$ = -1.25 ms the current begins to rise and between $t$ = -1 ms and $t$ = 3.25 ms there is a period of further current enhancement, above the already elevated background current. The current then falls back to the initial steady state value of ~1.8 μA. Figure 5.14 shows an expansion of the data around $t$ = 0. This reveals that the current enhancement, seen between -1.25 and 3.25 ms is periodic in nature. Individual current spikes of up to nearly 60 times the silent current were observed. The duration of the individual events is short, of the order of 50 μs. The frequency of these events is the same as the driving frequency. Current-time traces of a similar nature have been reported previously by Maisonhaute *et al.* [91, 93]. Also, enhancements at subharmonics of the driving frequency have been reported [91]. Frames taken from high-speed video recorded at the same time as the data presented in Figure 5.14 (although not temporally correlated) are shown in Figure 5.15.

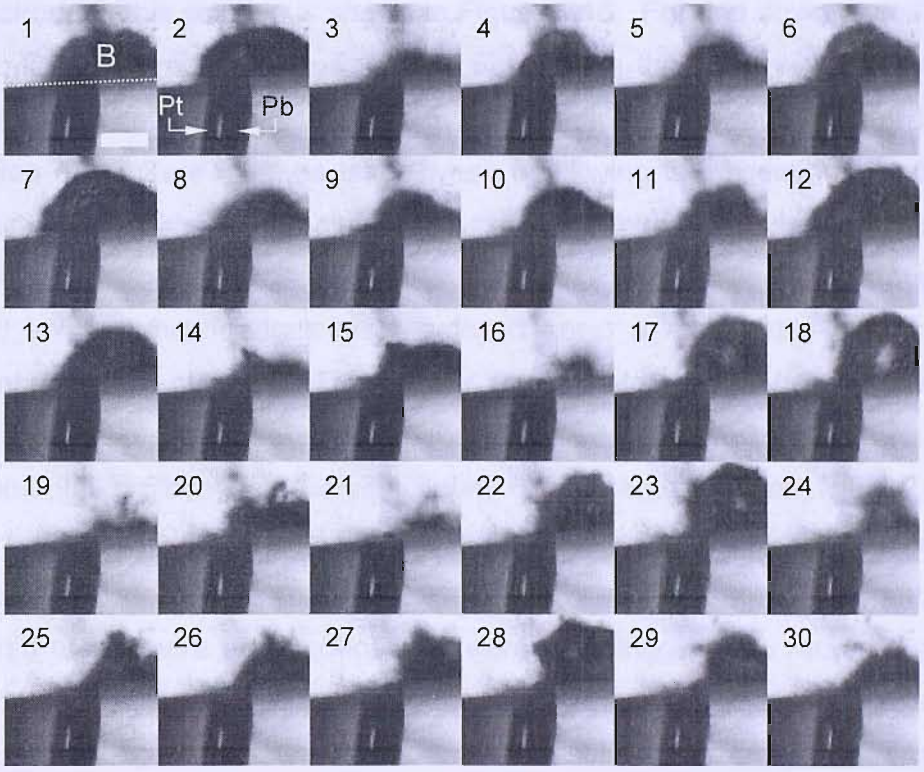


**Figure 5.15** 30 frames from high-speed video recorded at the same time as the data shown in Figures 5.13 and 5.14. The capture rate was 60,000 f.p.s. The microwires can be seen at the bottom of each frame. Platinum (25 μm diameter) on the left and lead (125 μm diameter) on the right. The scale bar in frame 1 represents 175 μm.

In contrast to the video shown in Figure 5.1, there is a bubble (labelled B in frame 1) on the surface of the electrode (shown by the dotted line in frame 1). The bubble is comparatively large (~ 400 μm diameter) compared with those seen in Figure 5.1. Although the bubble can be seen to undergo volume and shape variations the dynamics are not clear. It may be expected that the relatively high driving pressure amplitudes at the surface of the electrode[9] lead to a plethora of surface modes making interpretation of the video footage difficult. Therefore, in order to study the nature of the surface-bound bubble further, a novel 'ring down' experiment was performed, which is described in the following section.

### 5.2.1 A novel ring down experiment

The ring down experiment was designed to study the relaxation of the bubble after the termination of the ultrasound. It was found that the intense lighting necessary for the video led to rapid degradation of $Fe(CN)_6^{4-}$ and hence for this experiment (which does not include any erosion component) the solution contained 2 mM KI and 0.5 M KCl. A cyclic voltammogram of a 25 μm diameter Pt electrode in this solution is shown in Figure 5.16. For ring down experiments the working electrode was positioned 4.5 mm from the tip of the horn and the potential was held at +0.6 V *vs.* SCE, which resulted in mass transfer limited oxidation of $I^-$. Care must be taken when employing the oxidation of iodide in this fashion. It is known that plating of $I_2$ can contaminate the electrode surface, leading to an erratic response. However, Power [180] showed that through the use of low $I^-$ concentrations (as employed here) a reasonable steady state response can be attained. The current was monitored during sonication and signals similar to those reported in Figure 5.13 were observed. The experimental protocol for the ring down experiments was as follows. The current at the Pt electrode was monitored and the system described in Section 2.6 was used, to ensure that if an event, such as that shown in Figure 5.13 occurred the camera and oscilloscope were both triggered to record data. In addition to this the signal from the function generator (which was computer controlled and generated the signal to be amplified and drive the horn) was terminated. As well as the current and video data, a hydrophone was placed in the cell and the acoustic pressure measured as a function of time.

[9] From Figure 4.11, $P_A$(drive) ~25 kPa at 4.5 mm.

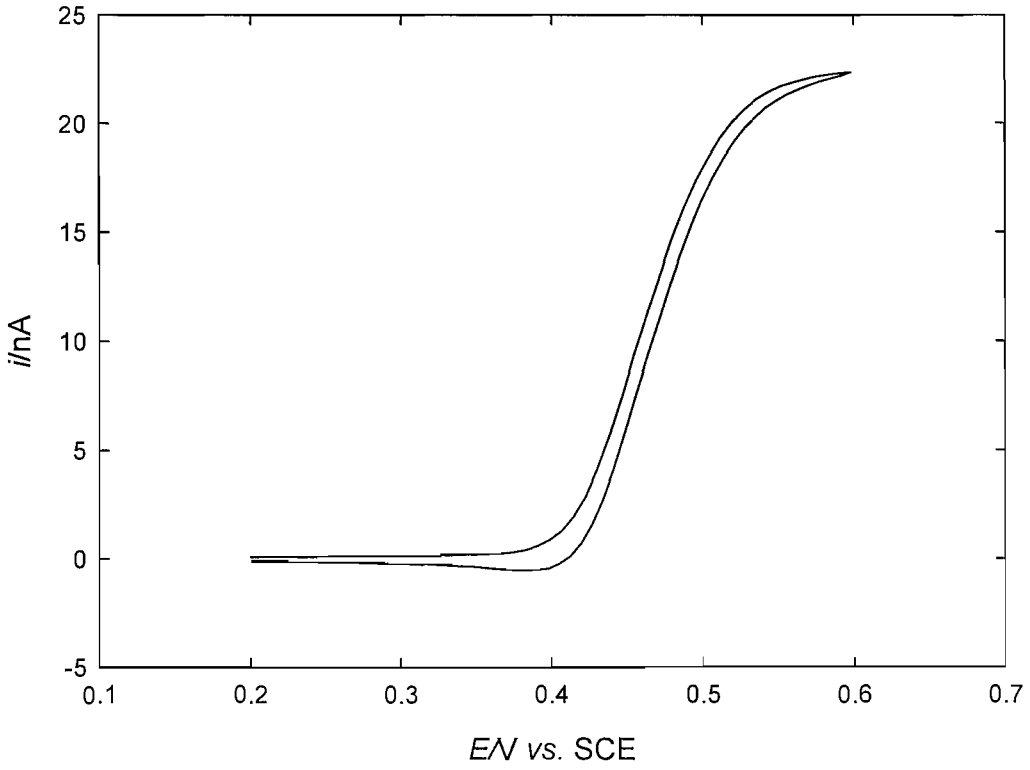


**Figure 5.16** Cyclic voltammogram recorded at a 25 µm diameter Pt electrode in a solution of 2 mM KI and 0.5 M KCl. The sweep rate was 10 mV $s^{-1}$ and the temperature was 25 ± 1 °C.

Typical results obtained during a ring down experiment are shown in Figures 5.17 (pressure *vs.* time), 5.18 (current *vs.* time) and 5.20 (frames from high-speed video). First, consider the acoustic pressure signal. The trigger point is at $t$ = 0 s. However, there was a delay (caused by the response time of the function generator to commands sent from the PC) before the ultrasound actually ceased, which is shown by the dotted line. Following the termination of the input signal there is a decay in the pressure over approximately 80 ms due to the ringing down of the transducer. It must be noted that the pressure amplitudes reported in Figure 5.17 are not those that exist at the electrode surface. This is because the hydrophone was positioned approximately 3 cm from the horn and was not aligned with the central axis of the horn. It is expected that the pressure experienced at the surface of the electrode will be somewhat higher but exhibit a similar decay in amplitude. The current recorded at the platinum electrode, which was measured simultaneously, is shown in Figure 5.18.

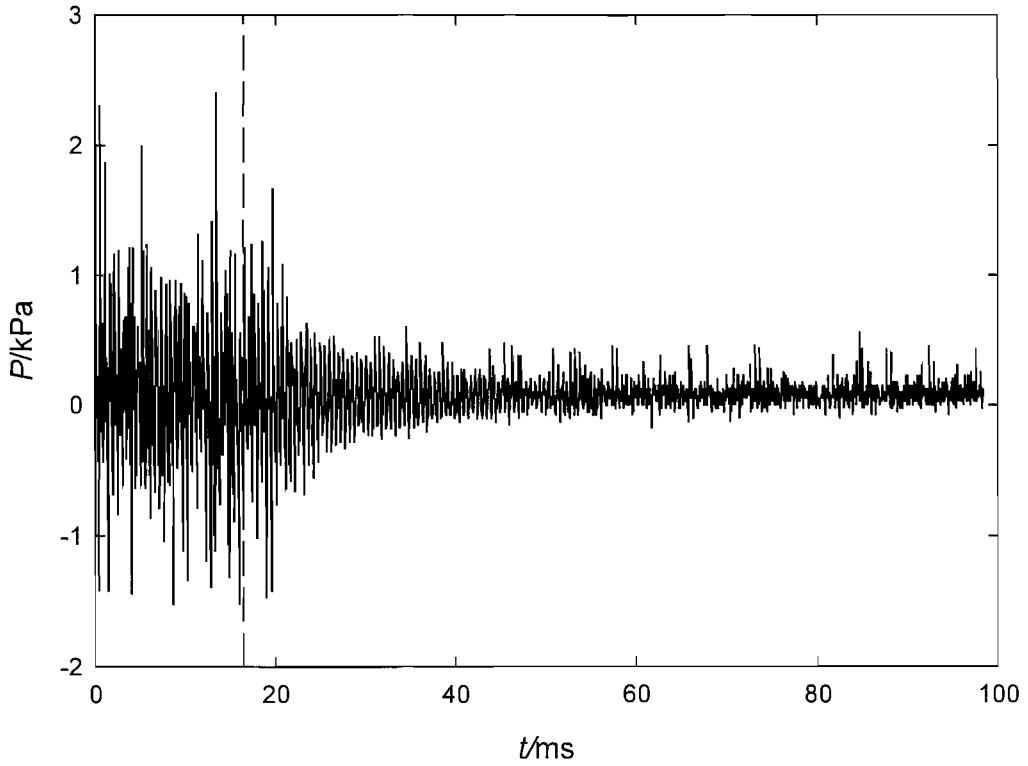


**Figure 5.17** Plot showing the pressure trace recorded during a ringdown experiment. The dotted line shows the time at which the ultrasound (22.85 kHz, 56 ± 5 W $cm^{-2}$) was terminated. The temperature was 40 ± 3 °C (elevated temperature due to intense lighting necessary for high-speed video).

Initially the current is enhanced in a similar fashion to that reported in Figure 5.13. Following the termination of drive signal (indicted by the dotted line) the current continues to exhibit enhancement for ~2 ms before decreasing to ~4 times the silent steady state current for the oxidation of $I^-$ (22 nA, see Figure 5.16). Over the next 80 ms the current shows an overall decrease to approximately twice the silent steady state current, however this reduction in the magnitude of the current is punctuated by periods of current enhancement. This behaviour can be explained through consideration of Figure 5.20, which shows 200 frames from high-speed video footage recorded synchronously with the data shown in Figures 5.17 and 5.18. In order to aid the interpretation of the video footage, Figure 5.19 shows the layout and scale of the individual frames.

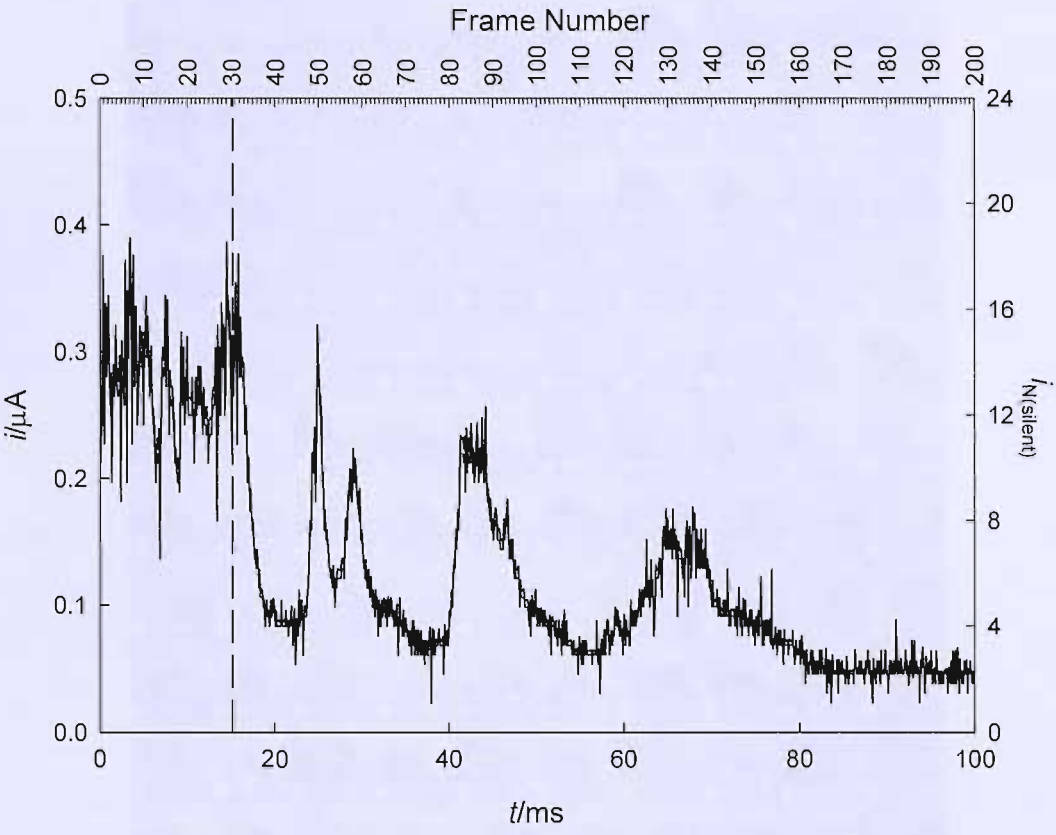


**Figure 5.18** Current recorded at a 25 μm diameter platinum electrode in a solution of 2 mM KI and 0.1 M KCl during a ringdown experiment (see main text for full details). The potential of the electrode was held at +0.6 V vs. SCE. The dotted line shows the time at which the ultrasound (22.85 kHz, 56 ± 5 W $cm^{-2}$) was terminated. The temperature was 40 ± 3 °C (elevated temperature due to intense lighting necessary for high-speed video). The frame numbers given on the top axis relate to Figure 5.20.

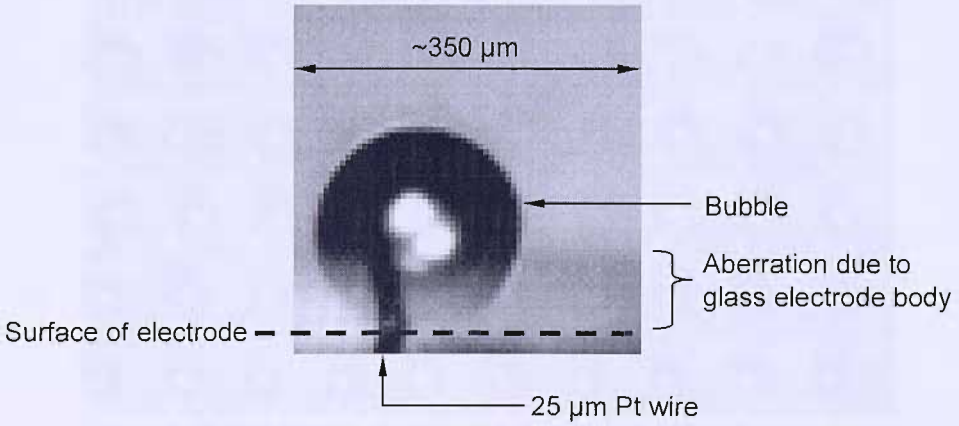


**Figure 5.19** Diagram to illustrate the layout and scale of the individual frames shown in Figures 5.20 and 5.21.

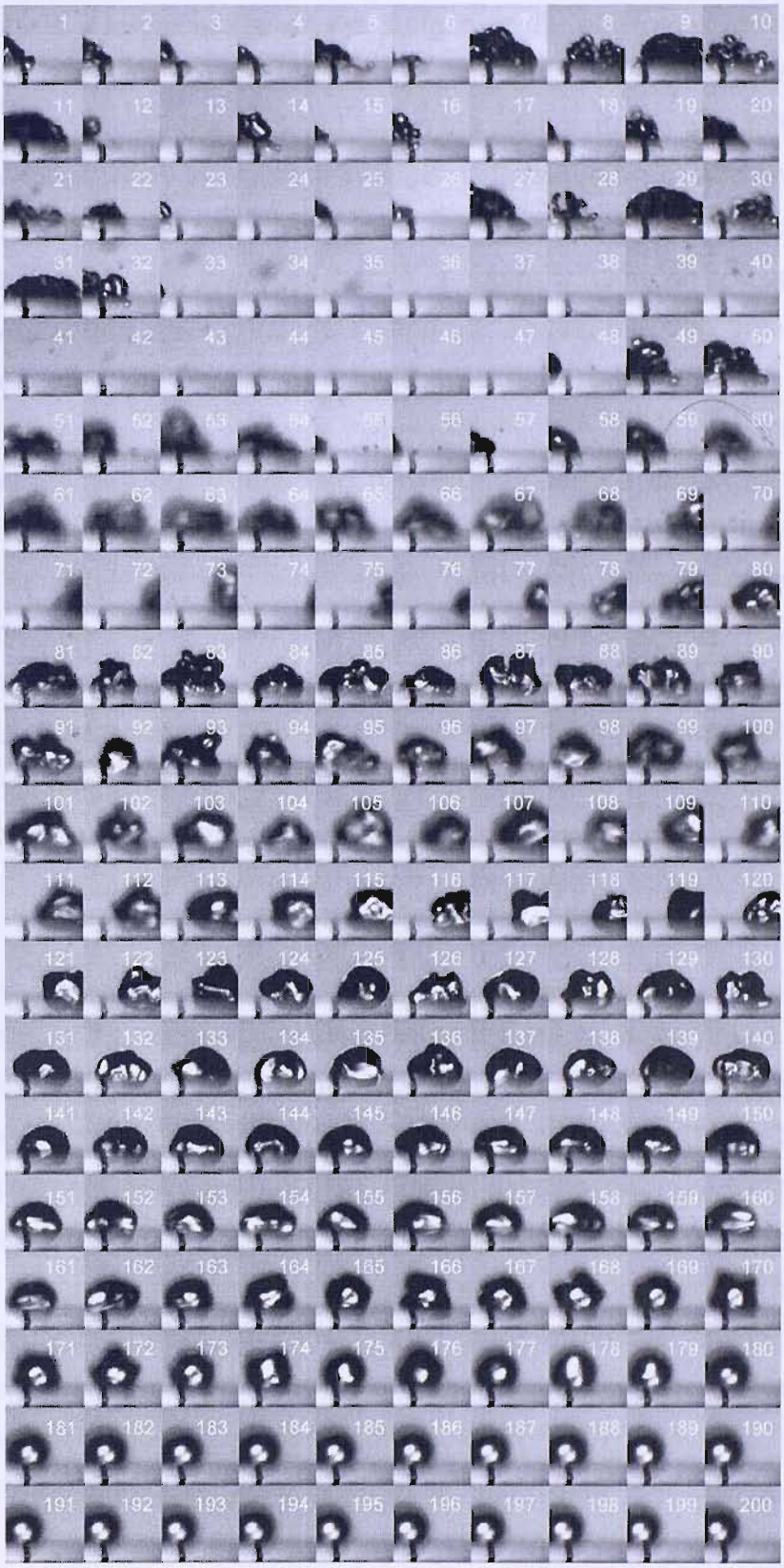

**Figure 5.20** 200 frames showing the bubble behaviour during a ring down experiment. The interframe time is 0.5 ms (every 50$^{th}$ frame from data recorded at 100,000 f.p.s). Recorded simultaneously with the data shown in Figures 5.17 and 5.18. The frames read left to right top to bottom. The first frame is at $t$ = 0.007 ms and the ultrasound (22.85 kHz, 56 ± 5 W cm$^{-2}$) was terminated after ~15 ms (frame 30). For layout and scale of individual frames see Figure 5.19.

Initially there is a large bubble on the surface of the electrode, which can be seen to oscillate and translate. The bubble remains in the vicinity of the electrode until frame 33 ($t$ = 16.5 ms), when the bubble moves out of the field of view. This corresponds to first drop in current. Between frames 34 and 47 ($t$ = 17 - 23.5 ms) there is no bubble activity visible in the video footage and the current remains relatively low. The bubble re-enters at frame 48 and appears in focus above the electrode in frames 49 and 50. During this time the current is again enhanced. The bubble can then be seen to translate away from the electrode, although on this occasion this is evidenced by the bubble moving out of focus rather than out of the field of view. Again the current drops. The movement of the bubble on the electrode surface continues as the acoustic pressure amplitude drops, with each period of current enhancement corresponding to bubble activity close to the electrode. After 100 ms the acoustic pressure amplitude fell to close to zero and the bubble remained on the surface of the electrode. This is interesting as it may be expected that the bubble would rise away from the surface under buoyancy forces. The fact that the bubble remains on the surface may be indicative of contamination of the surface.

Indeed, the behaviour described in this section was not observed on every occasion raising the possibility that surface bound bubble activity such as this is indicative of electrode fouling. During the ring down process the bubble can be seen to relax; large amplitude oscillations and shape variations at the beginning of the experiment decrease until the bubble exhibits discrete surface wave modes (see, for example, frame 172). Although details such as these can be seen, and the high interframe time allows an entire ring down experiment to be studied, Figure 5.20 does not show the full range of bubble motion. For this purpose high frame rate (100,000 f.p.s) video sequences recorded at various times during a ring down experiment are shown in Figure 5.21 a-d. The layout and scale of the individual frames is shown in Figure 5.19.

In Figure 5.21a the first frame is at $t$ = 9287 μs. At this time the system was still under sonication. A large bubble can be seen on the surface of the electrode, which undergoes large volume oscillations (compare frames 36 and 38). The frequency of the volume oscillation appears to be the same as the driving

frequency. The bubble radius can be seen at successive maxima in, for example frames 36 and 40 or 53 and 57. This corresponds to a period of ~40 μs, which agrees well with the driving pressure wave at 23.10 kHz. As well as volume oscillation, the bubble is subject to high amplitude surface waves, which results in fragmentation of the bubble and subsequent re-coalescence. This is particularly evident in frames 64-69.

The oscillation of the bubble at the driving frequency agrees with the high time resolution electrochemistry shown in Figure 5.14, which exhibited periodic current enhancement at the driving frequency. Signals of this nature have been attributed to periodic blocking of the electrode [91, 93]; the video footage presented here cannot confirm or refute this. However, it is worth noting that the current in Figure 5.14 does not fall to zero indicating that blocking of the electrode is an unlikely mechanism in this case. Rather forced convection due to the bubble motion is the most likely mechanism for the periodic enhancement seen here.

In Figure 5.21b the first frame is at $t$ = 27187 μs. This is approximately 12 ms after the termination of ultrasound. Nevertheless the bubble can still be seen to undergo volume and shape oscillations. The amplitude of the oscillation is somewhat less than that seen in Figure 5.21a, which may be expected owing to the decreasing acoustic pressure amplitude. However, fragmentation is still evident; the generation of a daughter bubble can be seen in frames 59-70. Unlike the fragmentation present in Figure 5.21a, the daughter bubble is small and moves away from the parent rather than undergoing re-coalescence. This may be expected. If two bubbles are pulsating, and one is smaller than resonance and one is larger than resonance size, they will repel each other through secondary Bjerkness forces. At 23 kHz the resonance radius is ~120 μm. The daughter bubble is clearly smaller than this and the parent is larger.

In Figure 5.21c the first frame is at $t$ = 67007μs, approximately 52 ms after the termination of ultrasound. By this time the bubble oscillations have relaxed further and are of smaller amplitude, again owing to the decrease in the acoustic pressure amplitude. Surface waves are clearly evident on the bubble, however more than one mode is excited, leading to chaotic oscillation. The

bubble appears to be of a more spherical nature than that seen in Figure 5.21a and b, which exhibits a hemispherical geometry. This may be due to decreased acoustic streaming velocities as the acoustic pressure amplitude decreases. High streaming velocities in the liquid would tend to force the bubble towards the electrode surface. Also, the high amplitude oscillations visible in Figure 5.21a and b are likely to generate secondary Bjerkness forces, which would attract the bubble to the rigid interface [30].

In Figure 5.21d the first frame is at $t$ = 81717 μs. At this time, 67 ms after the ultrasound had been turned off the acoustic pressure amplitude is relatively low. A discrete surface mode ($n$ = 5) is visible on the bubble. The period of the surface wave is approximately 80 μs (for example, consider frames 36-44, which show one oscillatory cycle). Surface oscillation at half the driving frequency is indicative of the Faraday wave (the surface wave with the lowest threshold). The existence of Faraday waves may explain the subharmonic current enhancements, which have been reported previously [91]. The observation of Faraday waves generated on bubbles using a horn-type transducer is interesting. The electrochemical detection of surface waves on large gas bubbles (2-3 mm), exposed to audible sonic excitation has been reported previously [60, 181, 182]. However, to the author's knowledge this is the first time that the phenomenon has been suggested as a mechanism to explain the periodic enhancements seen in the mass transfer of redox species to an electrode under ultrasonic irradiation. It should be noted that for this to be the case under continuous wave sonication (as opposed to the ring down experiment described here) the acoustic pressure amplitude would have to be somewhat lower than that used in this work. This is likely in the case of reference [91], which employed large electrode-to-horn separations (7-10 mm compared with 4.5 mm here) and a lower acoustic power (7.8 W $cm^{-2}$ compared with 56 ± 5 W $cm^{-2}$ used here). Unfortunately, as is common with much sonoelectochemical work reported in the literature, no acoustic pressure measurements were made in reference [91] and hence it is difficult to make firm comparisons.

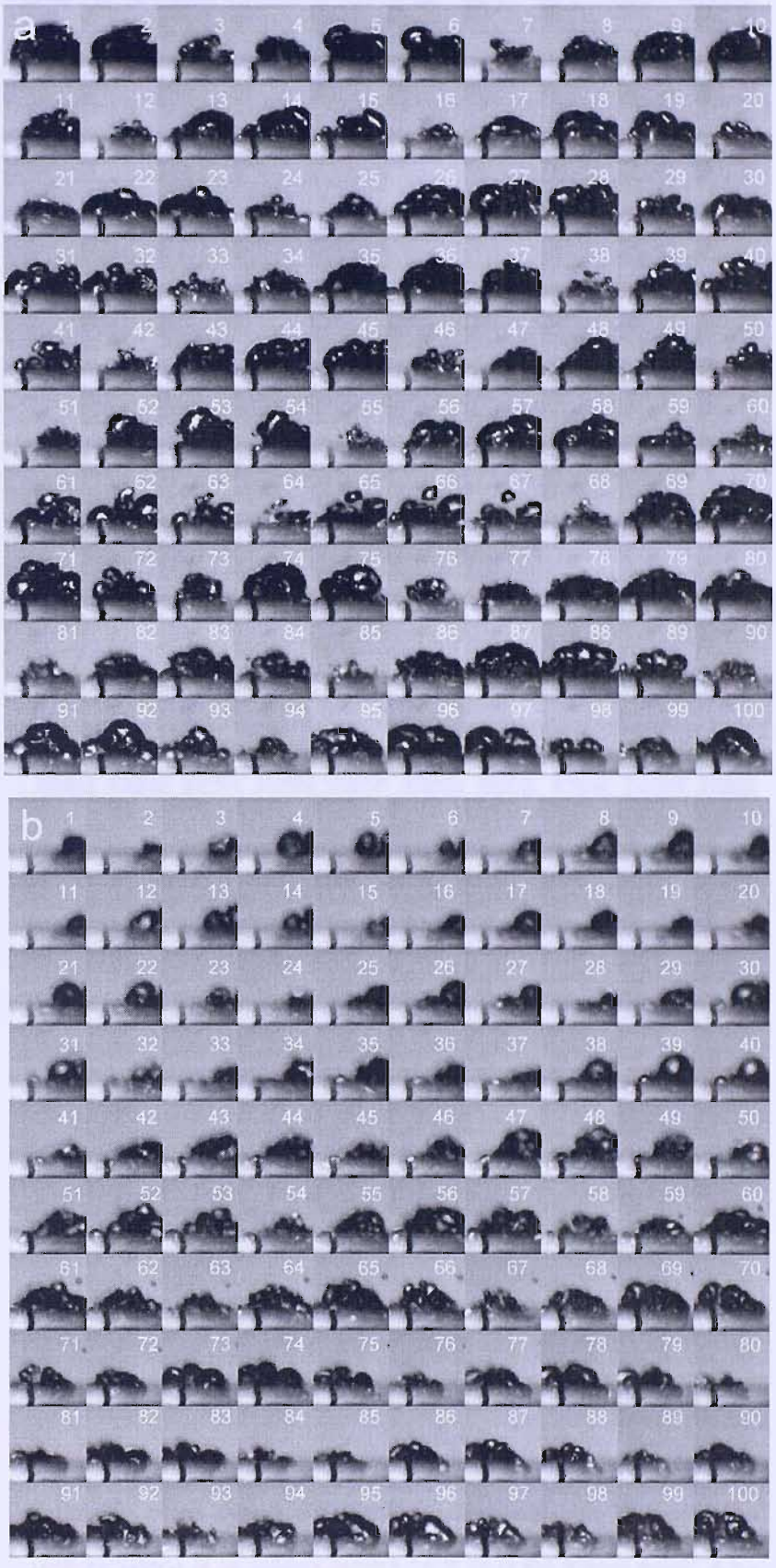


**Figure 5.21** Continues overleaf

**Figure 5.21 a-d** Video sequences showing the bubble behaviour at increasing times during a ringdown experiment. In all cases the capture rate was 100,000 f.p.s. The time for the first frame ($t_{1st}$) in each sequence is as follows (where $t$ = 0 µs is the trigger point): **a** $t_{1st}$ = 9287 µs, **b** $t_{1st}$= 27187 µs, **c** $t_{1st}$= 67007 µs, **d** $t_{1st}$= 81717µs. For layout and scale of individual frames see Figure 5.19.

A plot of the threshold acoustic pressure amplitude required to stimulate surface waves with mode numbers 3-7 on a bubble of equilibrium radius[10] 130 μm is shown in Figure 5.22. This plot was constructed by solving Equation 1.25 using the conditions given in Table 5.1.

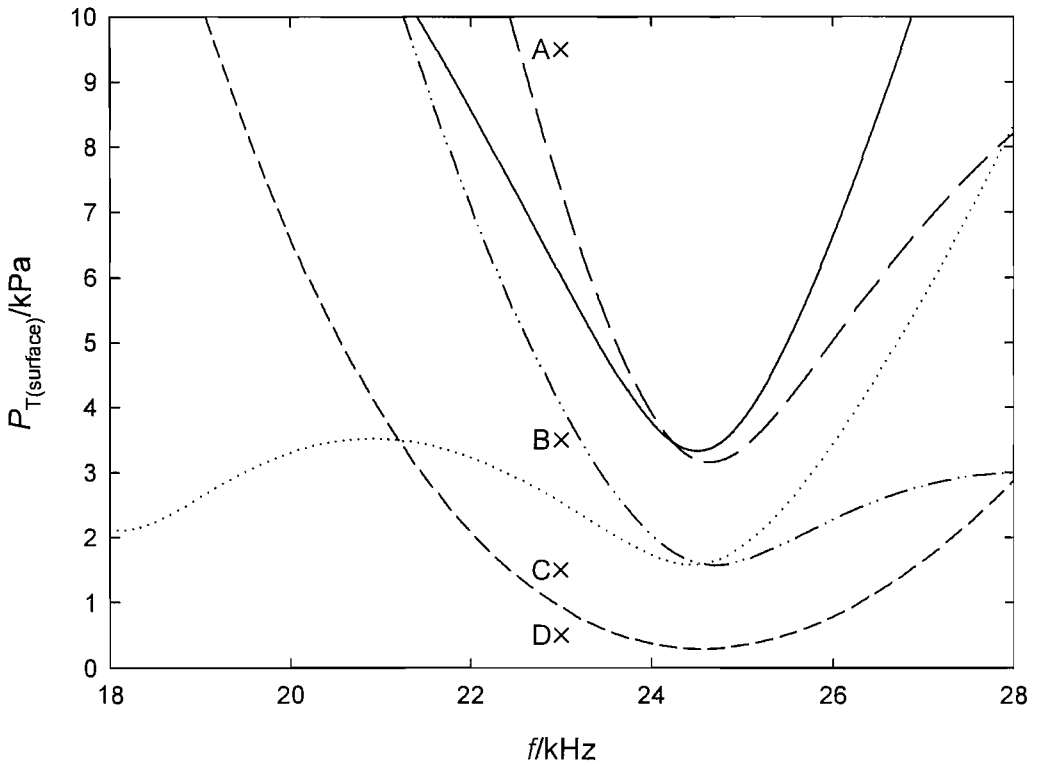


**Figure 5.22** Plot showing the predicted pressure thresholds for the onset of surface waves for modes n = 3 (—), 4 (·····), 5 (– – –), 6 (–·–) and 7 (—— ——). Calculated using Equation 1.25 and the parameters in Table 5.1.

| Parameter | Value |
|---|---|
| Equilibrium radius ($R_0$) | 130 μm |
| Hydrostatic pressure ($P_0$) | 1.01 ×$10^5$ Pa |
| **Liquid Properties** | |
| Density (ρ) | 1000 kg $m^{-3}$ |
| Viscosity (η) | 8.91 ×$10^{-4}$ kg $m^{-1}$ $s^{-1}$ |
| Surface tension (σ) | 7.70 ×$10^{-2}$ N $m^{-1}$ |
| Speed of sound ($c$) | 1480 m $s^{-1}$ |
| Vapour pressure ($P_v$) | 3450 Pa |
| **Gas Properties** | |
| Thermal conductivity ($K_g$) | 2.53 ×$10^{-2}$ W $m^{-1}$ $K^{-1}$ |
| Density ($\rho_g$) | 1.616 kg $m^{-3}$ |
| Specific heat capacity ($c_{p(g)}$) | 1007 J $kg^{-1}$ $K^{-1}$ |
| Polytropic index (κ) | 1.38 |

**Table 5.1** Parameters using in the construction of Figure 5.22.

[10] Estimated from Figure 5.19.

Figure 5.22 shows that at 23 kHz the surface mode, $n$ = 5 is indeed the mode with the lowest threshold pressure. It is also informative in illustrating the evolution of bubble behaviour during a ring down experiment. Consider the (illustrative) points A-D marked on the figure. Initially, under sonication the acoustic pressure is high (point A). Under these conditions a number of surface modes are excited and the bubble motion is seen as chaotic owing to superimposition of the modes. This is the situation seen in Figure 5.21a and b. Point B indicates a situation, which may lead to the bubble behaviour similar to that exhibited in Figure 5.21c. Here, the pressure is lower and only two surface modes are excited. As the pressure amplitude decreases further it enters a region in which only one surface mode is excited (the Faraday wave), which is shown by point C and in Figure 5.21d. Eventually the pressure drops below the threshold required for surface wave excitation (point D) and only the zero order breathing mode of the bubble exists. The amplitude of this oscillation is much less than that exhibited by surface waves [183] and is not visible in the video data presented here.

## 5.3 Conclusions and further work

In this chapter a number of techniques have been used in conjunction with each other, in order to correlate some the observable physical effects of sonication with the bubble dynamics, which cause them.

Initially the environment close to the horn, within the 'inertial cavitation zone' identified in Chapter 4 was studied (< 1.4 mm). A combination of electrochemistry, MBSL and laser scattering was used to investigate the dynamics of the bubble population. It was found that erosion and MBSL are associated with the shock waves seen in the pressure traces in Chapter 4. High-speed video footage revealed small bubbles that become visible in the solution following the collapse of the bubble cluster at the tip of the horn. However, it is unclear what the origin of these bubbles is. Two mechanisms are proposed. The first is that, following the collapse of the bubble cluster, the pressure in the solution falls to more negative values allowing explosive growth and subsequent collapse. The second is that the bubbles which are visible are the result of rebound following the collapse of the bubble cluster. However, even at 120,000 f.p.s the video footage was not of high enough time resolution

these mechanisms. The Pb/Pt dual electrode, introduced in Chapter 3 was employed in an attempt to elucidate the actual erosive mechanism. While it was shown that the erosive and mass transfer aspects of an individual bubble collapse could be recorded simultaneously, it was found that the 'side-by-side' construction limited the interpretation of experimental data if the location of a collapse was unknown. This may be improved upon by investigating the possibility of constructing a micro ring-disc Pb/Pt electrode, possibly through the use of sputtering techniques. This has recently been used to construct a Au/Pt micro ring-disc electrode for SECM applications [184]. A symmetric sensor of this nature would be advantageous as the location of the bubble collapse would be much less important. It was also noted that it would be desirable to reduce to overall size of the dual electrode.

Following this, focus was turned to bubble behaviour further from the horn (4.5 mm). Here, very different behaviour was observed. The dual electrode detected no erosion, as expected, but periodic mass transfer enhancement was detected. High-speed video footage showed that this was due to a large (100's of microns radius), surface bound bubble undergoing oscillations at the driving frequency. Further insight into the behaviour of the bubble was gained from a novel ring down experiment, in which the relaxation of the bubble following the termination of ultrasound was monitored using video and electrochemical techniques. During this relaxation the bubble was seen to initially exhibit a plethora of superimposed surface waves and eventually, as the pressure decreased sufficiently the discrete Faraday wave. It was suggested that this Faraday wave oscillation may be the source of subharmonic current enhancement, which has been reported by other workers [91], however no electrochemical evidence was presented here. Further investigation of this would be a worthwhile extension to this work.

# Chapter 6 Ultrasound as a tool for the study of surface processes

6

It is well known that inertial cavitation can lead to the erosion of a solid surface [47]. It has been shown in the preceding chapters and elsewhere [98] that through the use of microelectrode technology and fast data acquisition, it is possible to detect the erosive effects of inertial cavitation as electrochemical transients. The aim of the work presented in this chapter was to determine whether these ideas could be extended to other systems, particularly those of commercial significance. Two initial studies are presented. The first concerns the kinetics of passive film formation and the second the effects of ultrasound and cavitation on additives designed to inhibit corrosion of carbon steel.

## 6.1 Kinetics of passive film formation

The passivity of stainless steel (and many other metals and alloys) is a vital characteristic but is inherently difficult to study owing to the formation of the passive film at very low potentials (primarily due to the low equilibrium potential of the chromium/chromium oxide couple in water [185]). This makes the de-convolution of the film formation from hydrogen evolution difficult. In order to study the initial stages of film growth, it is necessary to expose bare metal and monitor the subsequent oxidation electrochemically. The use of inertial cavitation lends itself to this and may have significant advantages over current techniques (see Section 1.9.1), as outlined below.

First, the removal of the passivating film is very fast. The collapse time of inertial cavitation bubbles is on the microsecond timescale. Second, the exposed area is small. From experiments on the relatively soft lead/lead sulphate system, the eroded area was calculated to be approximately $0.6 \times 10^{-6}$ $cm^2$ (see Section 3.4). This is ~170 times less than that exposed by the breaking electrode technique [129] and ~700-2400 times less than the scratched electrode technique [118, 120]. Finally, it is possible to record hundreds of events in seconds (see Section 4.3) enabling a large amount of data to be collected and analysed. One drawback of this method is that the size of the inertial cavitation bubbles, and hence the eroded area, varies and is not known precisely. Whilst this does not restrict the analysis of the kinetics, it does

limit quantitative information regarding current density. In Sections 6.1.2 and 6.1.3 experimental data concerning the erosion/corrosion of a Type 302 stainless steel microelectrode exposed to inertial cavitation is presented. However, prior to cavitation studies the system was characterised by means of cyclic voltammetry. The results of this are presented in the following section.

### 6.1.1 Voltammetry

A cyclic voltammogram recorded using a stainless steel microelectrode (25 μm diameter) in a solution of $K_2CO_3$ is shown in Figure 6.1.

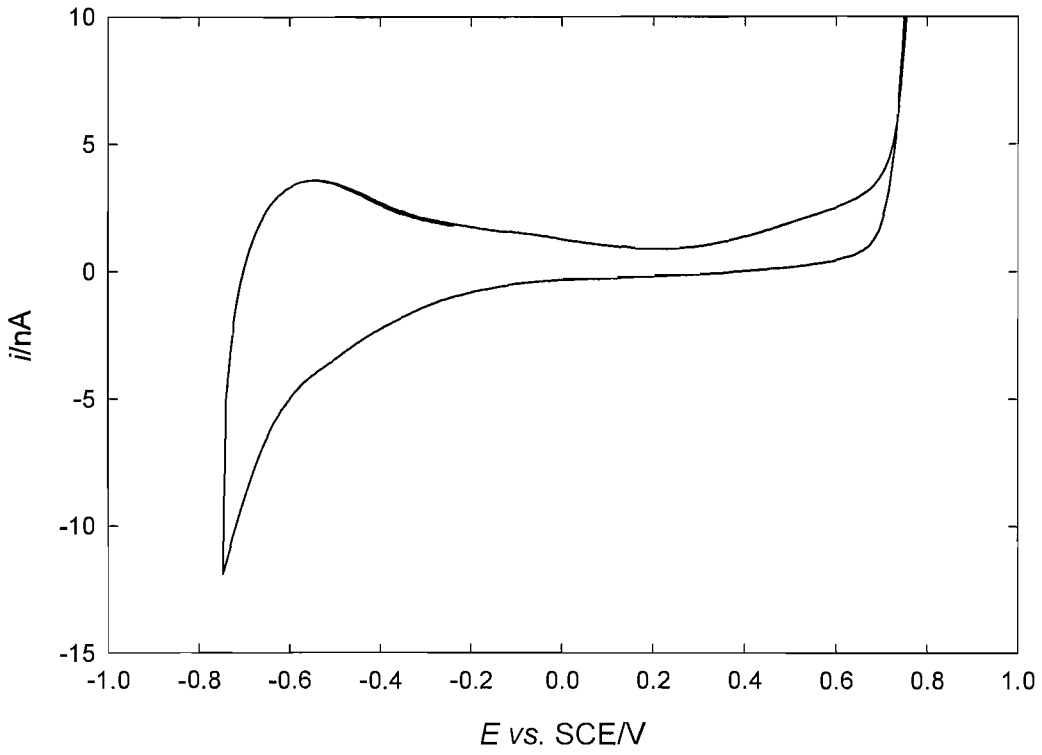


**Figure 6.1** Cyclic voltammogram of a stainless steel microelectrode (25 μm diameter) in a solution of 0.5 M $K_2CO_3$. The sweep rate was 10 mV $s^{-1}$.

This shows the characteristic shape for a metal undergoing passivation. The scan starts at -0.7 V *vs.* SCE. The metal initially corrodes but quickly passivates and from ~-0.2 V *vs.* SCE to ~0.6 V *vs.* SCE the surface of the stainless steel is covered with an oxide film. At higher potentials oxygen evolution occurs and the passive film breaks down, leading to a large anodic current. In the experiments described in the following sections the potential of the stainless steel microelectrode was held at +0.25 V *vs.* SCE. Under these conditions the surface is passivated and any removal of the oxide film is

expected to result in repassivation transients, similar to those already presented for the lead/lead sulphate system (see Figures 3.3, 5.2 and 5.12).

### 6.1.2 Effect of inertial cavitation

In order to study the effect of inertial cavitation, the electrode was positioned centrally below the ultrasonic horn at a distance of 0.3 mm. The small distance ensured that the electrode was within the zone where inertial cavitation exists (as shown in Section 4.3). Figure 6.2 shows the current recorded in the presence of ultrasound as a function of time.

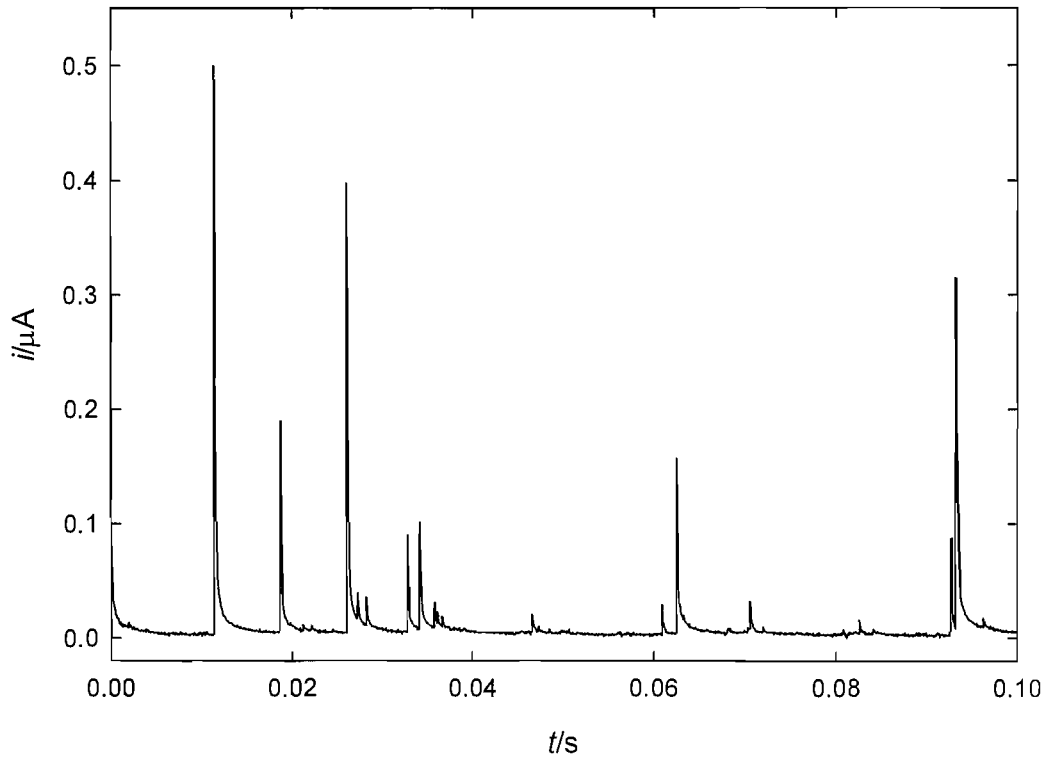


**Figure 6.2** Plot showing the current recorded as a function of time for a stainless steel microelectrode (25 μm diameter) exposed to inertial cavitation. The electrode-to-horn distance was 0.3 mm and the potential was held at +0.25 V *vs.* SCE. The solution contained 0.5 mol $dm^{-3}$ $K_2CO_3$.

A series of transient oxidation currents can be observed, which are attributed to repassivation following removal of the oxide film. Clearly the individual current-time transients are of differing height. This range of event size is expected if the production of inertial cavitation events occurs randomly throughout the solution in front of the microelectrode. In essence the microelectrode can be thought of as a target. Events directly above the stainless steel electrode will erode the greatest area and hence generate the largest event. However, inertial

cavitation at the edge of the microdisc will remove less material and subsequently produce a smaller oxidation transient. The degree of surface erosion is also expected to be highly dependent on the distance of the cavitation event from the surface of the electrode. This has been shown to be true in the case of laser generated cavitation events [67]. In addition to the spatial considerations outlined, a range of bubble sizes is expected, which would result in a distribution in the amount of material eroded by each cavitation event. Similar current distributions have been seen for the $Pb/PbSO_4$ system [98]. Figure 6.2 shows that a significant number of oxidation transients (>10) can be detected in a short period of time (100 ms). By employing a trigger function on the ADC card (controlled by software written in-house, see Section A.2.3) and the use of a high sampling rate (4 MHz) it is possible to record many individual erosion transients with high temporal resolution, which can then be used for further analysis. An example of this is shown in Figure 6.3.

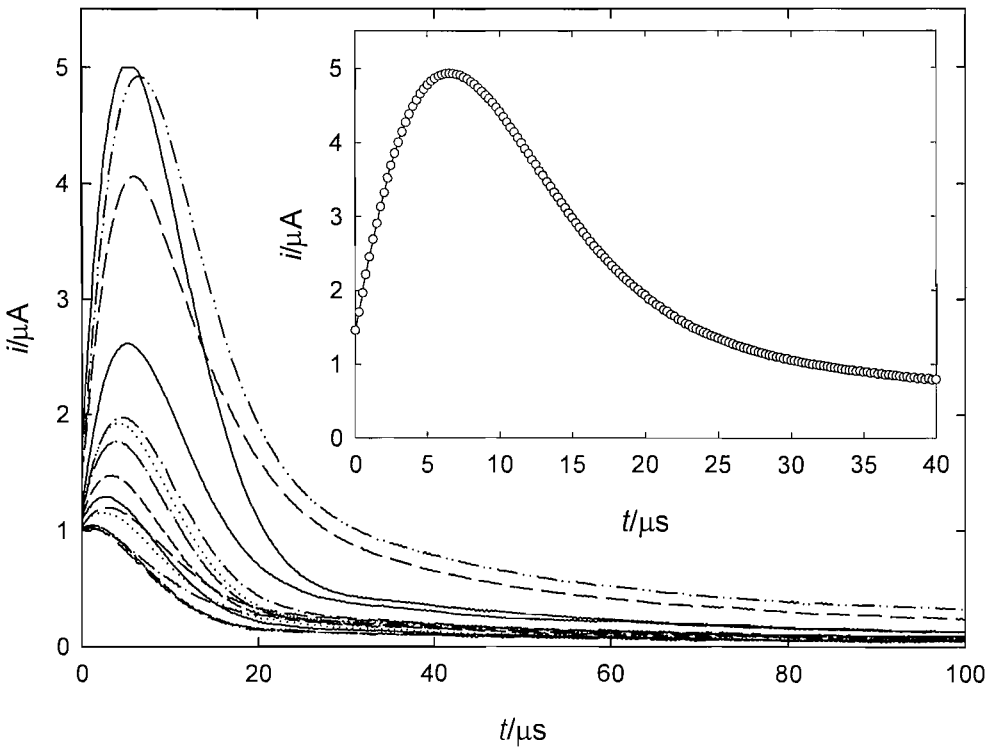


**Figure 6.3** Plot showing a set of 16 transients recorded in 1 second using a stainless steel microelectrode (25 μm diameter) exposed to ultrasound at a distance of 0.65 mm. The trigger current was 1 μA and the solution contained 0.5 M $K_2CO_3$. This figure shows 100 μs out of 500 μs of data recorded. Insert One of the transients showing the data points to illustrate the temporal resolution.

Figure 6.3 shows a set of 16 transients recorded at the microelectrode during a 1 second exposure to ultrasound. Also shown in the figure as an insert is a

transient with the data points included to illustrate the temporal resolution of the apparatus employed. As in Figure 6.2, there is a distribution in the magnitude of the transients. However, it should be noted that the current of the maximum erosion event (~5 μA) is two orders of magnitude smaller than the mA events produced by other erosion/fracture techniques [128, 129]. The low currents should reduce the effects of solution resistance.

### 6.1.3 Kinetic analysis

The two major mechanisms for passive film growth under high electric fields are ion migration and place exchange (see Section 1.9). Burstein and Davenport [186] have described in detail an analysis, which can be used to differentiate between the mechanisms from current-time data plotted in an appropriate manner. Their findings are summarised in Table 6.1. They also consider the effect of ohmic potential drop within the electrolyte for the ion migration case. Figure 6.4 shows the theoretical curves expected for various values of electrolyte resistance for film growth according to the ion migration model. In both cases the effect of solution resistance is to distort the curves from linearity. Figure 6.5 shows similar plots for a repassivation transient recorded using the trigger-based method for recording transients with high temporal resolution described in Section 6.1.2.

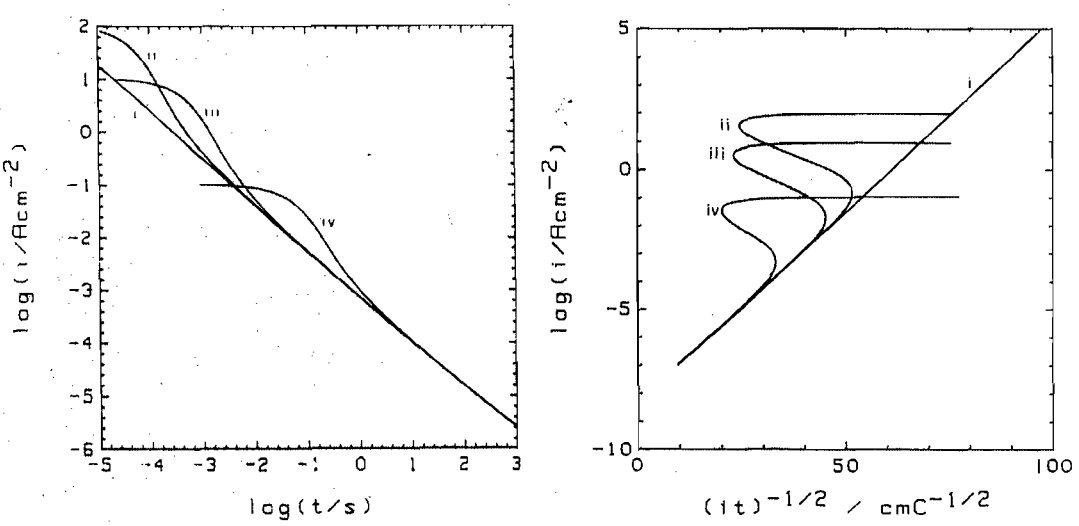


**Figure 6.4** Plots showing the effect of electrolyte resistance, $R_\Omega$ on the theoretical curves log(*i*) *vs.* log(*t*) and log(*i*) *vs.* $(it)^{-1/2}$. $R_\Omega$ = 0 (i), 0.01 (ii), 0.1 (iii) and 10 (iv). After Burstein and Davenport [186].

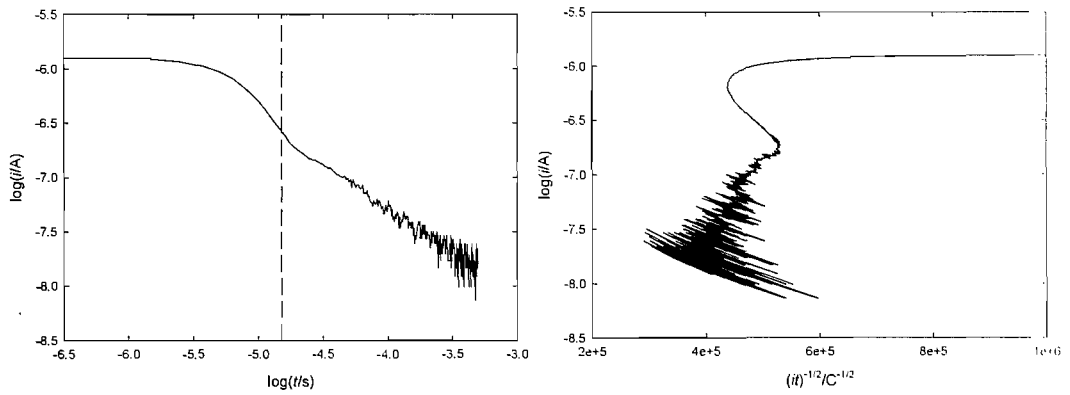


**Figure 6.5** Plots of log(*i*/A) *vs.* log(*t*/s) and log(*i*/A) *vs.* $(it)^{-1/2}$ for a current transient recorded using the method described in this chapter. The dotted line indicates $t$ = 15 μs.

Clearly, both curves are not linear over the entire acquisition time and exhibit the effects of the resistance of the solution. However, this is only at the shortest times. For the log(*i*/A) *vs.* log(*t*/s) plot the data shows distortion from linearity in a similar fashion to that shown in Figure 6.4 at times[11] less than 15 μs (indicated by the dotted line). However, at greater times the data is linear and can be used for kinetic analysis. Similarly, the log(*i*/A) *vs.* $(it)^{-1/2}$ plot exhibits a distortion analogous to that seen in the corresponding plot in Figure 6.4. It should be noted that 15 μs is rapid when compared with conventional techniques, such as the scratched electrode and guillotine, which respond on a millisecond timescale [118, 120] but similar to short time data for breaking electrode techniques [129]. Analysis of the data shown in Figure 6.5 (at times greater than 15 μs) yields a value for dlog(*i*/A)/dlog(*t*/s) of -0.8, which together with the positive slope in the plot of log(*i*/A) *vs.* $(it)^{-1/2}$ indicates that the ion migration mechanism is controlling the passive film growth. However, it was found that this was not always the case.

| **Model** | **Plot of log(*i*) *vs.* log(*t*)** | **Plot of log(*i*) *vs.* $(it)^{-1/2}$** |
|---|---|---|
| Ion migration | Slightly curved with gradient less negative than -1 | Straight line of constant positive gradient for given film |
| Place exchange | Straight line of gradient -1 | Vertical line |

**Table 6.1** Summary of current-time behaviour for ion migration and place exchange models of passive film growth.

[11] In this and all subsequent cases $t_0$ is defined as the value of $t$ for which $i$ is maximum.

Consider Figure 6.6, which shows four transients and Figure 6.7, which shows plots of log(*i*/A) *vs.* log(*t*/s) and log(*i*/A) *vs.* $(it)^{-1/2}$ for the data shown in Figure 6.6 (the symbols used correspond in all cases). There are differences in the kinetics of the passivation process, which is reflected in the values of dlog(*i*/A)/dlog(*t*/s) (see Table 6.2) and the slopes of the plot log(*i*/A) *vs.* $(it)^{-1/2}$. It is difficult to determine values in the latter case, however Figure 6.7 clearly shows a variation in behaviour from vertical (◆ and ■) to sloped (• and ▼). This indicates that the former events exhibit place exchange type kinetics while the latter proceed *via* an ion migration mechanism. The variation in the value of dlog(*i*/A)/dlog(*t*/s) from close to -1 (◆ and ■) to somewhat less than -1 (• and ▼) also supports this.

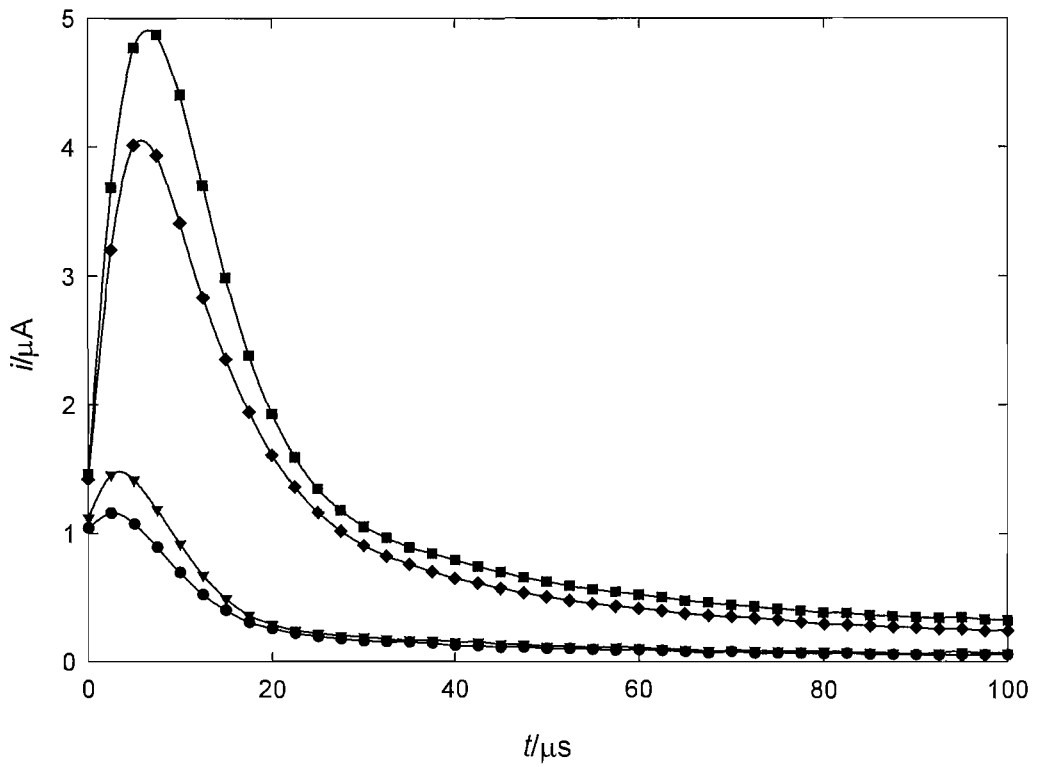


**Figure 6.6** Plot showing 4 transients recorded using a stainless steel microelectrode (25 μm diameter) exposed to ultrasound at a distance of 0.65 mm. The trigger current was 1 μA and the solution contained 0.5 M $K_2CO_3$. This figure shows 100 μs out of 500 μs of data recorded and the symbols represent every twenty fifth data point for clarity.

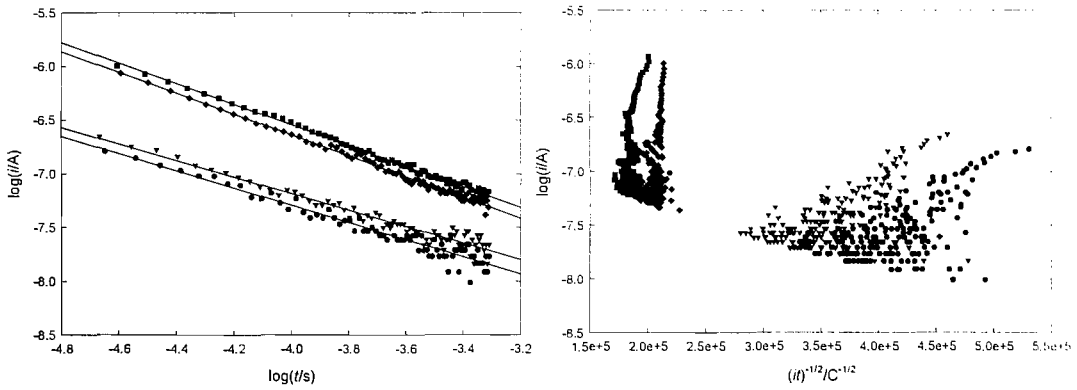


**Figure 6.7** Plots of log(*i*/A) *vs.* log(*t*/s) and log(*i*/A) *vs.* $(it)^{-1/2}$ for the data shown in Figure 6.6. The data symbols used correspond in all plots.

| Curve | dlog(*i*/A)/dlog(*t*/s) |
|---|---|
| ◆ | -0.97 |
| ■ | -0.96 |
| ● | -0.80 |
| ▼ | -0.77 |

**Table 6.2** Gradients of the double log plots shown in Figure 6.7

In Figures 6.6 and 6.7 it was shown that different transients, recorded under the same experimental conditions can exhibit different passivation mechanisms. It was noted that the transients with higher current maxima show place exchange kinetics, whilst the smaller current transients exhibit kinetics associated with an ion migration mechanism. In order to investigate this relationship further a series of transients was recorded and the value for dlog(*i*/A)/dlog(*t*/s) plotted as a function of peak current. This is shown in Figure 6.8. There is a broad correlation between the peak current and the value of dlog(*i*/A)/dlog(*t*/s), which may be expected and will now be discussed.

Following the discussion above, the y-axis in Figure 6.8 is effectively an indicator of the passivation mechanism, where -1 indicates the place exchange mechanism and lower gradients suggest ion migration. As stated in Section 6.1.2, the peak current depends on a number of factors, such as bubble size and collapse location. Given that the place exchange mechanism is only applicable to the initial stages of oxide film formation (see Section 1.9.2), it follows that those transients with gradients close to -1 represent occasions on which the entire oxide layer has been removed to reveal bare metal. In contrast

transients for which dlog(*i*/A)/dlog(*t*/s) has a less negative value are indicative of cases in which the entire thickness of the oxide layer is not eroded and the film thickens *via* an ion migration mechanism. It is possible to consider four scenarios, which may result from erosion of the passive film by an inertial cavitation event. These are detailed below and shown schematically in Figure 6.9. The distribution of the data shown in Figure 6.8 can be understood through consideration of the physical feasibility of each scenario.

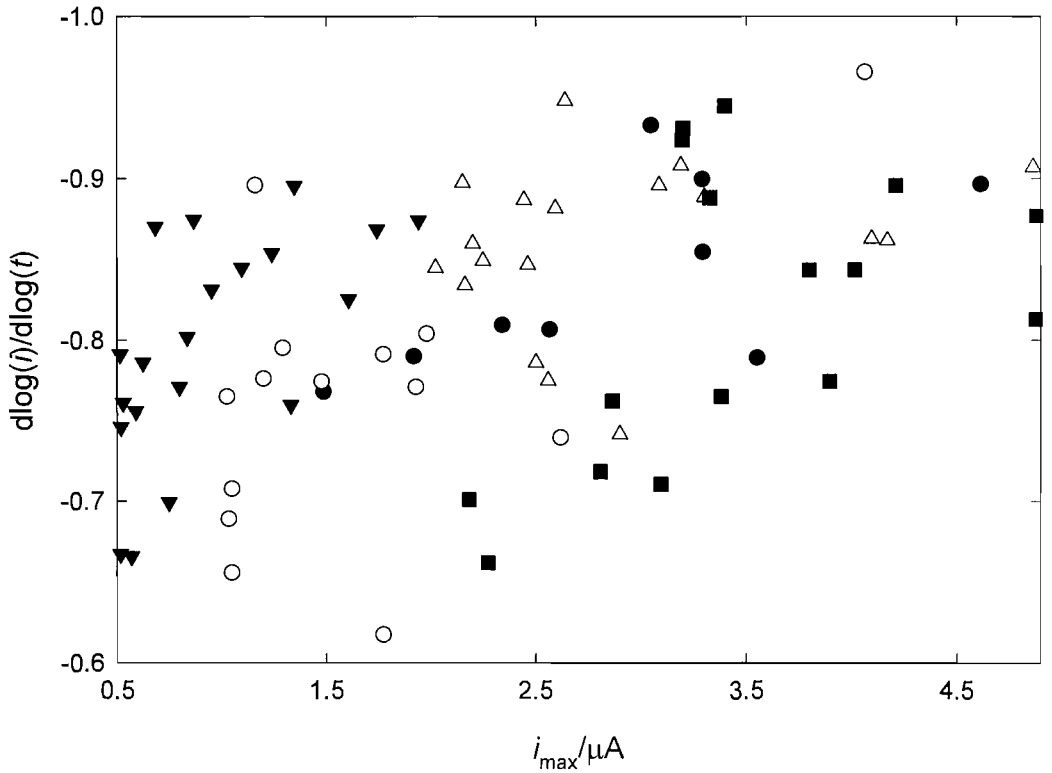


**Figure 6.8** Plot showing the gradient of double log plot as a function of peak current. Different symbols denote separate sets of experiments performed under nominally identical conditions.

Scenario I: In this scenario a small amount of the passive film is removed to reveal bare metal. This would result in a small peak current but a value for dlog(*i*/A)/dlog(*t*/s), which is close to -1 indicating place exchange kinetics. This is unlikely to occur unless the cavitation event occurs at the edge of the electrode and hence there were only a small number of data points recorded in this region.

Scenario II: Here a large amount of the passive film is removed and the underlying metal is exposed. As in Scenario I this would result in place exchange kinetics (dlog(*i*/A)/dlog(*t*/s) close to -1) as the bare

metal is revealed, however the peak current would be large. This is a physically realistic scenario, which is reflected in the large number of repassivation transients that occurred in this part of the figure.

Scenario III: In this case, a small amount of the passive film is removed, however bare metal is not exposed and hence the film thickens *via* the ion migration mechanism. This would lead to a small peak current and a value for dlog(*i*/A)/dlog(*t*/s) less negative than -1. As with Scenario II, this is physically reasonable and again there was a large amount of data, which occurred in this region.

Scenario IV: In this scenario a large amount of the passive film is removed, however as with Scenario III bare metal is not exposed and hence ion migration controls the thickening of the film. This would result in a large peak current and a value for dlog(*i*/A)/dlog(*t*/s) less negative than -1. This is the most unrealistic scenario and hence no data was recorded in this region of the figure.

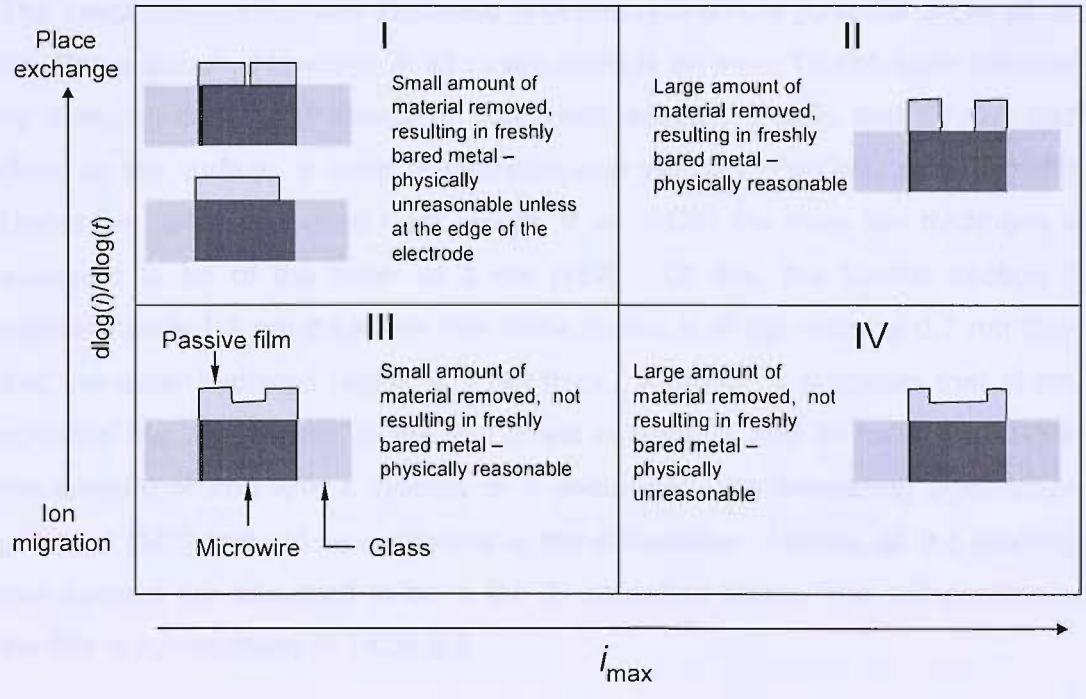


**Figure 6.9** Schematic of four scenarios, which can result from passive film erosion by an inertial cavitation event. For more detail see the main text.

In cases where the film growth kinetics are best described by the place exchange mechanism it may be expected that a transition would occur as the film thickens and ion migration dominates the film growth process. Indeed, this has been reported for the passivation of stainless steel in 1 M $MgCl_2$ using a scratched electrode technique [121]. However, this transition was seen more than 10 ms after the initial scratch. In the technique described in this work intervals of this duration between erosion events are rarely seen and hence no such effect was observed. This represents a drawback associated with the multi bubble inertial cavitation erosion technique described here, which may need to be addressed in future work.

### 6.1.4 Estimation of the eroded area

It is possible to estimate the amount of material removed by a cavitation event through simple Faradic relationships. In order for this to be possible it is necessary to consider the structure of the oxide film. Films grown potentiostatically under conditions similar to those used in this work have been studied using a variety of surface techniques [187-189]. It has been shown that the passive film formed under potential control in alkaline solution on 304 stainless steel consists of $Cr_2O_3$, iron oxide species and hydrated iron species. The exact composition and thickness is dependent on the potential under which the film is grown. However, in all cases there is an inner Cr-rich layer followed by a region consisting mainly of iron oxide species ($Fe_2O_3$ and $Fe_3O_4$) and, close to the surface, a layer of hydrated iron species ($Fe(OH)_2$ and FeOOH). Under the conditions used here (+0.25 V *vs.* SCE) the total film thickness is expected to be of the order of 3 nm [187]. Of this, the Cr-rich section is approximately 1.3 nm thick, the iron oxide region is of the order of 0.7 nm thick and the outer hydrated region is 1 nm thick. Although it is known that at this potential the iron present in the film exists in both 2+ and 3+ oxidation states, the amount of iron with a valency of 2 decreases with increasing polarisation potential [187] and will be neglected in the calculation. Hence, all the oxidised iron species are assumed to be in the 3+ oxidation state. The composition of the film is summarised in Table 6.3.

The total charge passed during a repassivation event consists of contributions from three oxidative processes and can be written as:

$$Q_T = 3F(b_{FeOOH} + 2b_{Fe_2O_3} + 2b_{Cr_2O_3}) \quad (6.1)$$

where, $F$ is Faradays constant, and $b_X$ is the number of moles of each species formed in the reaction. This equation can be used in conjunction with the molar ratio of the reaction products to calculate the total amount of material removed by an erosion event.

| Species | Density/ g cm$^{-3}$ | Mol. Mass/ g mol$^{-1}$ | % by Volume | % by Moles |
|---|---|---|---|---|
| FeOOH | 4.18 | 88.85 | 33.33 | 41 |
| $Fe_2O_3$ | 5.24 | 159.69 | 23.33 | 20 |
| $Cr_2O_3$ | 5.21 | 151.99 | 43.33 | 39 |

**Table 6.3** Expected composition of the passive film formed on stainless steel under the conditions employed

Consider the repassivation transient shown by curve (■) in Figure 6.6. This transient was chosen for analysis as the gradient of -0.96 indicates complete removal of the film. Also, it is one of the largest transients recorded and as such gives an indication of the upper limit of the eroded area. The charge passed during this event (over a period of 500 µs) was 140 pC, which would equate to an area of 2.7 µm$^2$ assuming the film grows to the 3 nm thickness within this time. However, film thickness measurements are usually recorded over extended periods of time (~2 hours). Hence the estimation of film thickness over the time scale of Figure 6.6 may be inaccurate. In order to gain a more meaningful estimation extrapolation to longer time periods is necessary. The spectroscopic data concerning the structure of the film pertains to quasi-steady state conditions after a polarisation period of ~2 hours; however EQCM data for the growth of passive films on stainless steel under anodic polarisation shows that the majority of film growth occurs within 100 seconds [190]. The transient was therefore extrapolated by extending the linear plot of log($i$/A) *vs.* log($t$/s) to a time of 100 s. Over this period a total charge of 2.3 nC would be passed, which equates to an exposed area of 45 µm$^2$. This is in reasonable agreement with the calculated erosion area for the lead/lead sulphate system (see Section 3.5) It should be noted that this assumes that double layer effects are relatively small compared to the charge consumed in oxide film growth as shown to be the case for the lead system [98].

In an attempt to calibrate the erosion events detected with ultrasound further, a guillotine experiment was performed. In this experiment a 25 μm diameter stainless steel microelectrode was fractured in a glass surround under electrochemical control (see Section 2.9). Figure 6.10 shows an oxidation transient recorded from such a fracture experiment. The oxidation event is significantly larger than the transients observed in the inertial cavitation experiments.

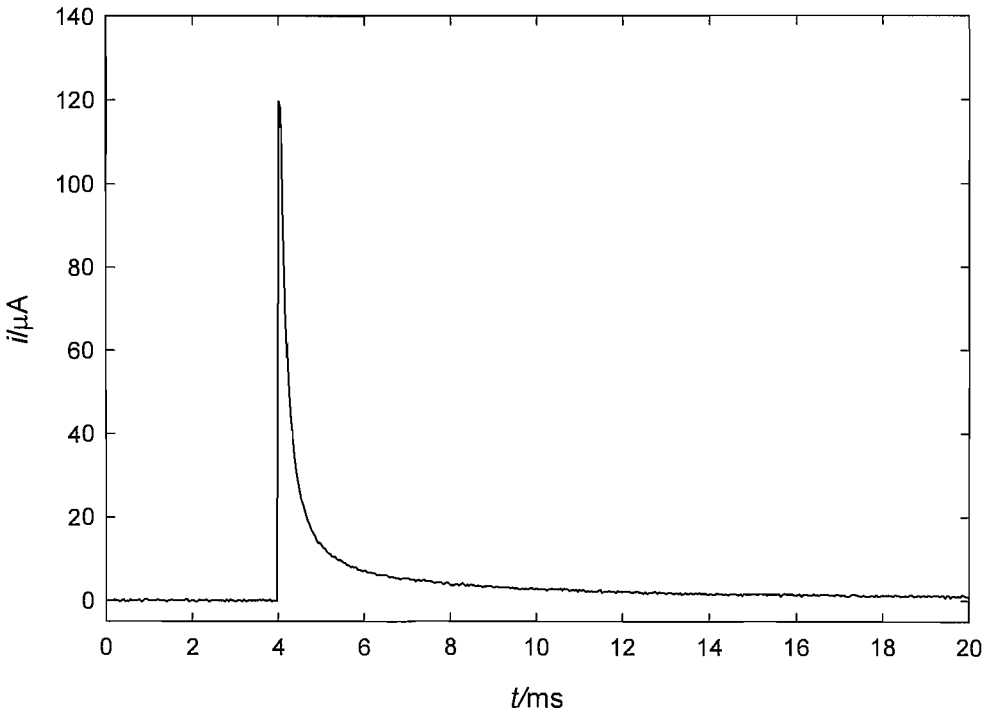


**Figure 6.10** Plot showing the current as a function of time for a guillotine experiment on a 25 μm diameter stainless steel microelectrode sealed in glass. The solution contained 0.5 mol $dm^{-3}$ $NaNO_3$ and the electrode potential was held at +0.75 V *vs.* stainless steel (the guillotine itself).

This is as expected as the guillotine experiment theoretically exposes the entire 490 $\mu m^2$ microelectrode surface at one time. However, Figure 6.11 shows an SEM of a post fracture microelectrode. This clearly indicates that the fracture of the microelectrode is not clean and a significant elongation and fracture process has occurred. This increases the fresh area exposed to the solution in the fracture event. In the case shown an area was estimated to be in excess of 3500 $\mu m^2$. Under these circumstances it is inappropriate to calculate the surface area exposed by cavitation using this calibration method. It is recognised that while the calculation shown above is worthwhile in estimating

the amount of material eroded by a cavitation event, a more robust calibration is required, which may be the subject of future work.

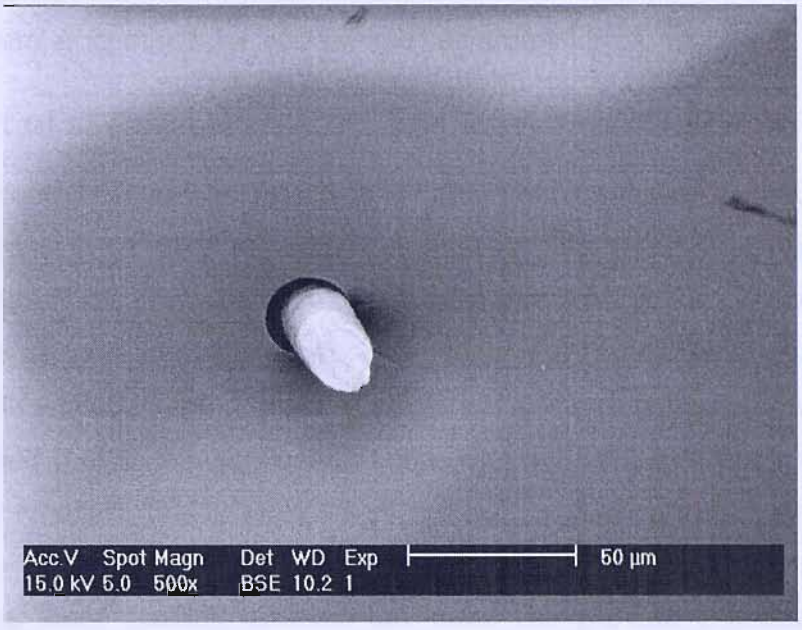


**Figure 6.11** SEM of a 25 µm diameter stainless steel microelectrode following fracture in a guillotine experiment.

### 6.1.5 Conclusions and further work

In this subsection a novel technique for the study of passive film formation using inertial cavitation has been described. Passivation of stainless steel under potential control has been monitored electrochemically. It has been shown that through the use of microelectrode technology and fast data acquisition (4 MHz) it is possible to record numerous current transients, which have been attributed the repassivation of the electrode surface following erosion caused by individual cavitation events.

The kinetics of the repassivation process have been analysed and it has been found that both place exchange and ion migration mechanisms are in evidence. It has been shown that there is a broad correlation between the peak current associated with a cavitation event and the film growth mechanism. Events with a large current lead to film growth controlled by a place exchange mechanism, while smaller currents lead to ion migration control. This has been explained in terms of the degree of film removal; large currents are associated with complete removal of the film to expose bare metal whilst smaller currents are the result of only partial removal of the passive film. The area exposed by individual

cavitation events has been estimated from a Faradic relationship to be up to 45 $\mu m^2$ for the largest events recorded. However, it has been recognised that more robust calibration is necessary. Other further work may extent the study to other systems of commercial interest such as aluminium.

## 6.2 Effect of cavitation on corrosion inhibition

The acoustoelectrochemical set-up, which has been developed in course of this (and previous work [89, 90, 98]), provides a straight forward method for studying the effects of cavitation on surface processes. In the previous section the kinetics of passive film formation on stainless steel was investigated. The subject of this section is the effect of cavitation on corrosion inhibition. While it is recognised that in this application hydrodynamic cavitation is perhaps more industrially relevant, this is much more difficult to generate and control in the laboratory environment, as well has being significantly more costly. Considering these factors, acoustic cavitation can provide a cheap and well controlled alternative (providing it has been well characterised, as advocated in the previous chapters) in which to conduct preliminary work.

### 6.2.1 Characterisation of the inhibitor

In this initial study, the inhibition of sweet corrosion of carbon steel in 1 M NaCl by 3-methyl-2-pyrazoline-5-one (MPO) was studied. MPO is a heterocyclic ketone (see Figure 6.12), which has been shown to inhibit corrosion of steel in sulphuric acid solution through adsorption onto the surface and suppression of the metal dissolution reaction [191].

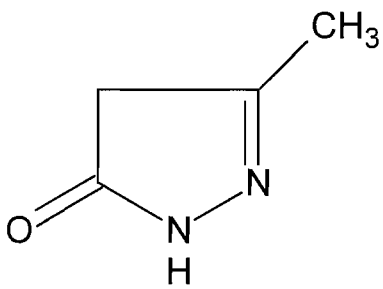


**Figure 6.12 S**tructure of 3-methyl-2-pyrazoline-5-one (MPO).

The effect of MPO on the corrosion potential of a 75 µm radius carbon steel electrode is shown in Figure 6.13. Upon injection of the inhibitor, the corrosion potential immediately rises rapidly from a value of ~-705 mV *vs.* SCE before slowing and achieving a steady value of ~-605 mV *vs.* SCE after approximately

15 minutes. The origin of the anodic shift in the corrosion potential was determined using Tafel analysis.

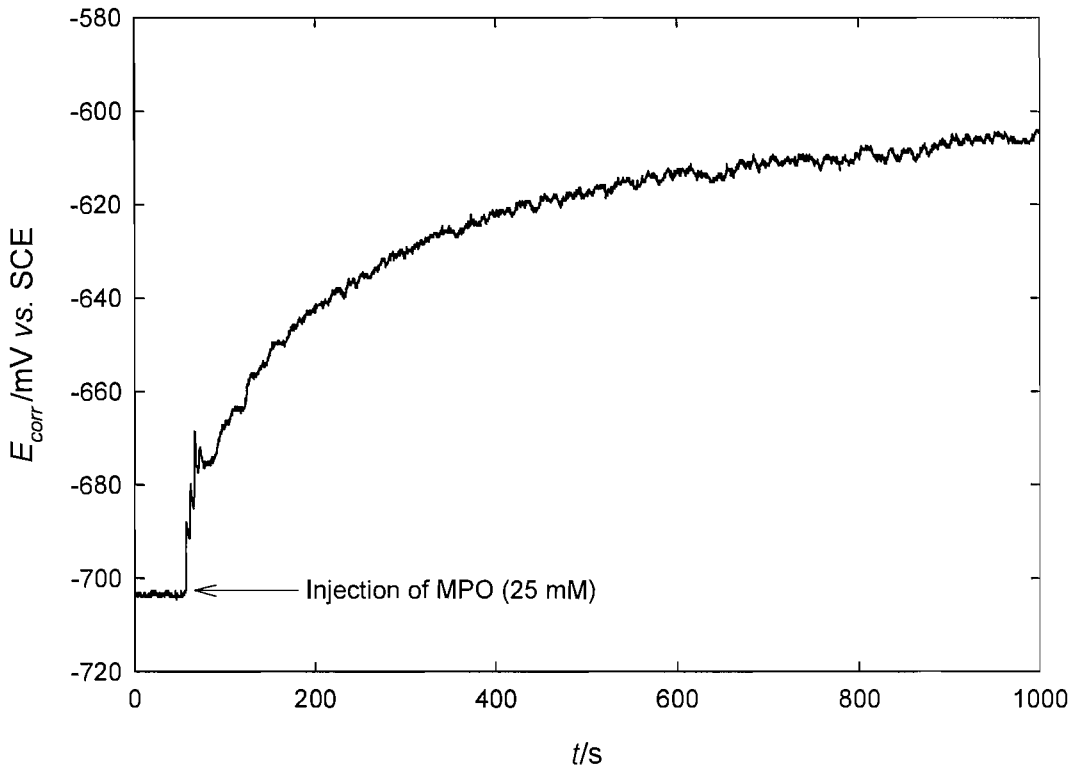


**Figure 6.13** Plot showing the effect of MPO (25 mM) on the corrosion potential of a 75 µm radius carbon steel electrode in $CO_2$ saturated NaCl (1 M) at 25 °C.

Tafel plots for carbon steel in 1 M NaCl saturated with $CO_2$ in the absence and presence of MPO are shown in Figure 6.14. The cathodic Tafel[12] slope is similar in both cases (241 mV decade$^{-1}$ without inhibitor, 223 mV decade$^{-1}$ with inhibitor) but the anodic slopes are very different. Without MPO the slope associated with dissolution of the metal is 105 mV decade$^{-1}$, however after the inhibitor was added (and left to equilibrate for 15 minutes) the value of the Tafel gradient decreased to 45 mV decade$^{-1}$. This indicates that under the conditions used here, MPO acts as an anodic inhibitor, decreasing the rate of active dissolution of the metal as seen previously [191]. The corrosion current can be calculated from the intersection of the anodic and cathodic Tafel lines, which results in values of 0.48 µA in the absence of the inhibitor and 0.22 µA in the presence of MPO. This equates to an efficiency of only 45%. However, it should be noted that the aim of this work was not discovery of novel corrosion inhibitors but to develop a technique for the analysis of such compounds. It is

[12] By convention the inverse of the gradients in Figures 6.14 and 6.15.

convenient at this juncture to consider the effect of ultrasound on the corrosion process in the absence of the inhibitor.

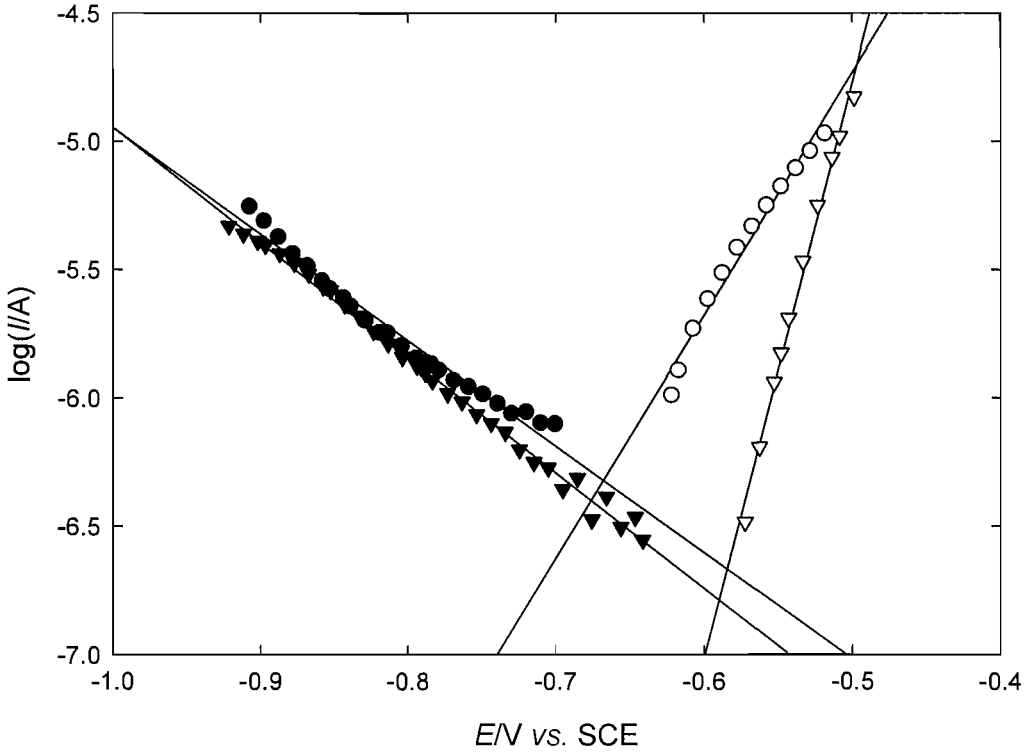


**Figure 6.14** Tafel plots for carbon steel in $CO_2$ saturated 1 M NaCl in the absence (• and ○) and presence (▼ and ▽) of MPO (25 mM). The sweep rate was 5 mV $s^{-1}$ and the temperature was 25 °C. Open symbols represent the anodic data and closed symbols the cathodic data.

Figure 6.15 shows Tafel plots recorded in the absence and presence of ultrasound. Under the conditions used here, the application of ultrasound has little effect on the anodic reaction but a large effect on the cathodic process. The Tafel gradient increases from 240 mV $decade^{-1}$ to 322 mV $decade^{-1}$ and the current density is also enhanced. The $CO_2$ saturated solution had a pH of 3.7 and it is assumed that the predominant cathodic reaction is that given in Equation 6.2.

$$2H^+_{(aq)} + 2e^- \rightarrow H_{2(g)} \qquad (6.2)$$

This is a multi-step reaction with numerous mechanisms and pathways [192]. As such, the mechanism by which sonication/cavitation affects the reaction is complex and difficult to determine. However, the result shown above (increased cathodic gradient and corrosion current density) is consistent with that seen previously for hydrogen evolution at a titanium sonotrode [192].

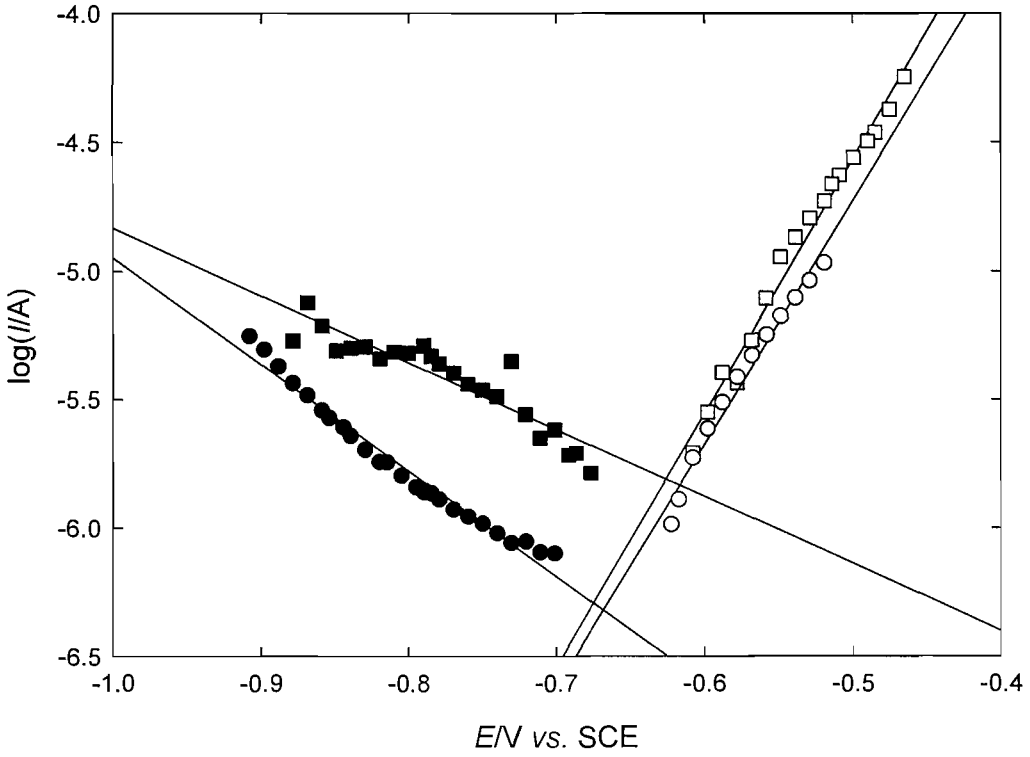


**Figure 6.15** Tafel plots for carbon steel in $CO_2$ saturated 1 M NaCl in the absence (● and ○) and presence (■ and □) of ultrasound (23.10 kHz, 56 ± 5 W $cm^{-2}$, 5 mm electrode-to-horn). The sweep rate was 5 mV $s^{-1}$ and the temperature was 25 °C. Open symbols represent the anodic data and closed symbols the cathodic data.

### 6.2.2 Effect of ultrasound on the inhibitor

The effect of cavitation on the inhibitor was investigated by monitoring the corrosion potential as a function of time for sonication at various electrode-to-horn distances. This was achieved by means of a galvanostat built in house. The effect of ultrasound on the corrosion potential of a 75 µm radius carbon steel electrode in $CO_2$ saturated NaCl (1 M) is shown in Figure 6.16. At large distances (≥ 1.5 mm), sonication leads to an increase in the corrosion potential, however at electrode-to-horn separations of 1 mm and 0.5 mm the value of $E_{corr}$ was seen to decrease when the solution was exposed to ultrasound.

In order to understand the variations in the corrosion potential it is necessary to consider both the electrochemical processes, which are occurring and the physical effects of the sonication process. It is convenient to make use the diagram shown in Figure 6.17, which shows schematically the Tafel plots presented in Figures 6.14 and 6.15.

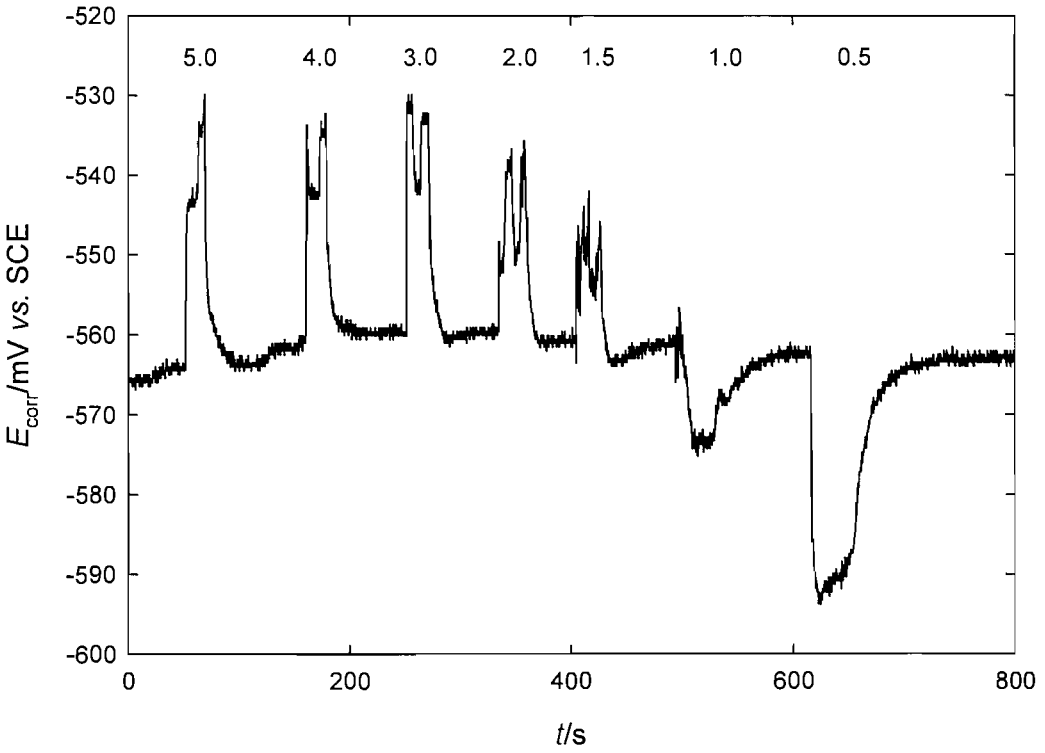


**Figure 6.16** Plot showing the corrosion potential of a 75 μm radius carbon steel electrode as a function of time in a solution of 1 M NaCl with 25 mM MPO saturated with $CO_2$. The solution was sonicated at various electrode-to-horn distances as shown by the numbers at the top of the figure (distances in mm).

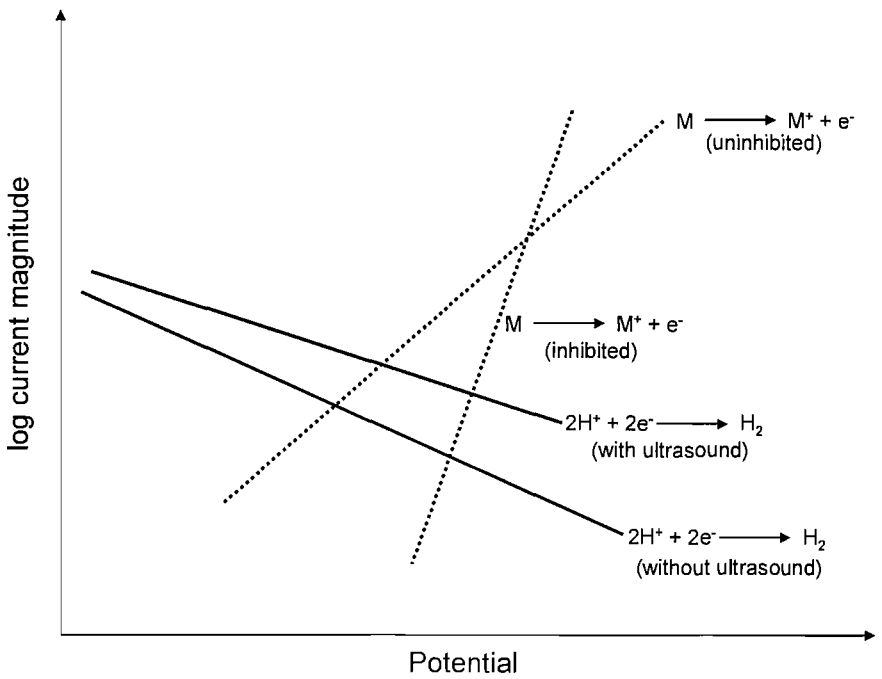


**Figure 6.17** Schematic diagram showing the Tafel slopes relevant to Figure 6.18 and discussion in the main text.

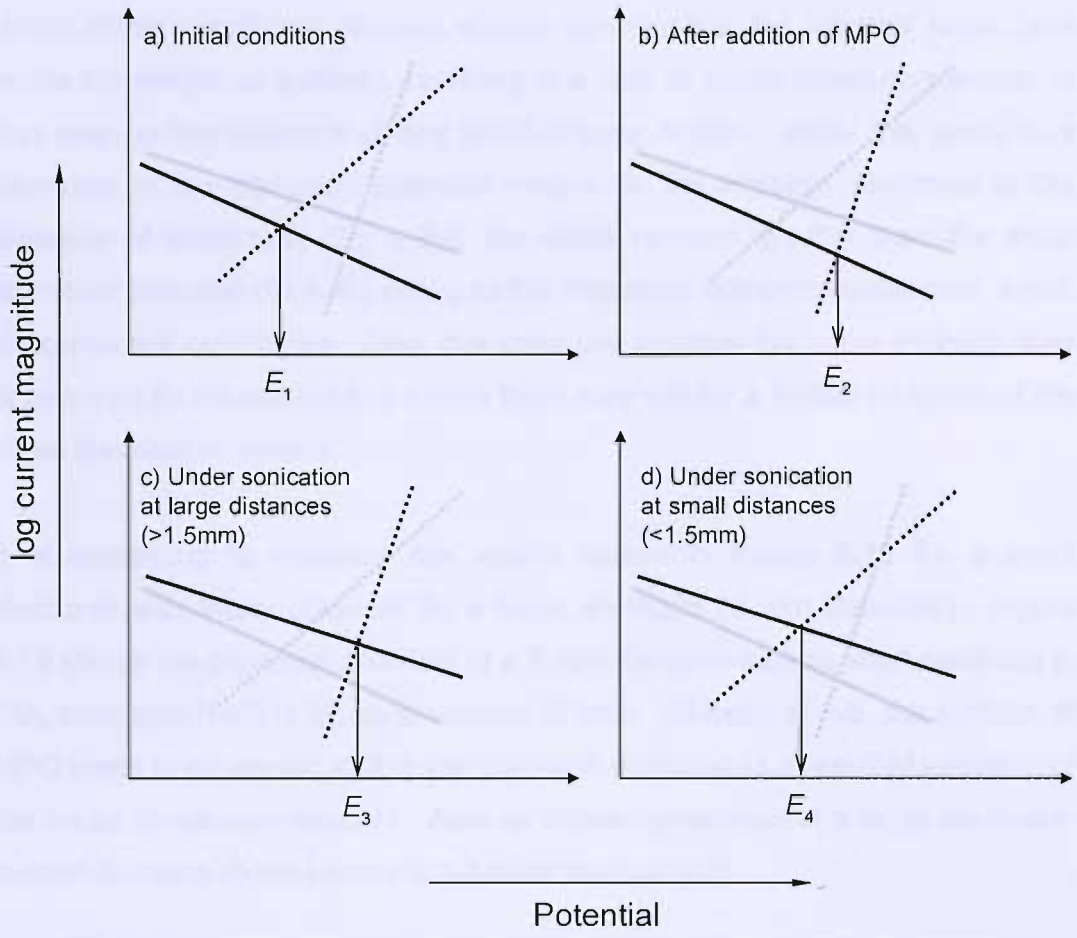


**Figure 6.18** Schematic representation of four experimental scenarios represented in Figure 6.16. Solid lines represent the cathodic reaction and the dotted lines represent the anodic reaction.

There are four lines of interest, two anodic (corresponding to metal dissolution in the absence and presence of MPO) and two cathodic (corresponding to hydrogen evolution in the absence and presence of ultrasound). It has already been shown that MPO has little effect on the cathodic corrosion reaction and that ultrasound has little effect on the anodic corrosion reaction. Also consider Figure 6.18, which represents schematically the four experimental conditions used in Figure 6.16. Initially the corrosion potential has a value, $E_1$, which corresponds to the uninhibited oxidation of the metal and unperturbed hydrogen evolution (shown in Figure 6.18a). Injection of MPO leads to an increased corrosion potential ($E_2$) as the dissolution of the metal is inhibited (Figure 6.18b). Upon sonication at large distances the value of the corrosion potential is seen to rise further to a new value, $E_3$, is due to an increased current density for the cathodic reaction (Figure 6.18c). As the electrode-to-horn distance is decreased the electrode enters the region in which inertial cavitation is present.

Under these conditions, erosive effects can remove the inhibitor layer (and erode the electrode surface), resulting in a rate of metal dissolution similar to that seen in the absence of any MPO (Figure 6.18d). While this leads to a decrease in the corrosion potential relative to the inhibited electrode in the absence of ultrasound ($E_4 < E_3$), the value remains greater than the initial corrosion potential ($E_4 > E_1$) owing to the increased cathodic component, which of course still contributes. Also, it is unknown whether the entire inhibitor layer is removed by ultrasound and hence there may still be a limited inhibition of the metal dissolution reaction.

It is interesting to compare the results shown in Figure 6.16 for a small electrode with those obtained for a large electrode (5 mm diameter). Figure 6.19 shows the corrosion potential of a 5 mm diameter carbon steel electrode in $CO_2$ saturated NaCl (1 M) as a function of time. As seen above, the addition of MPO leads to an anodic shift in the corrosion potential as a result of inhibition of the metal dissolution reaction. Also as above, sonication at a large electrode-to-horn distance (5 mm) leads to a further positive shift.

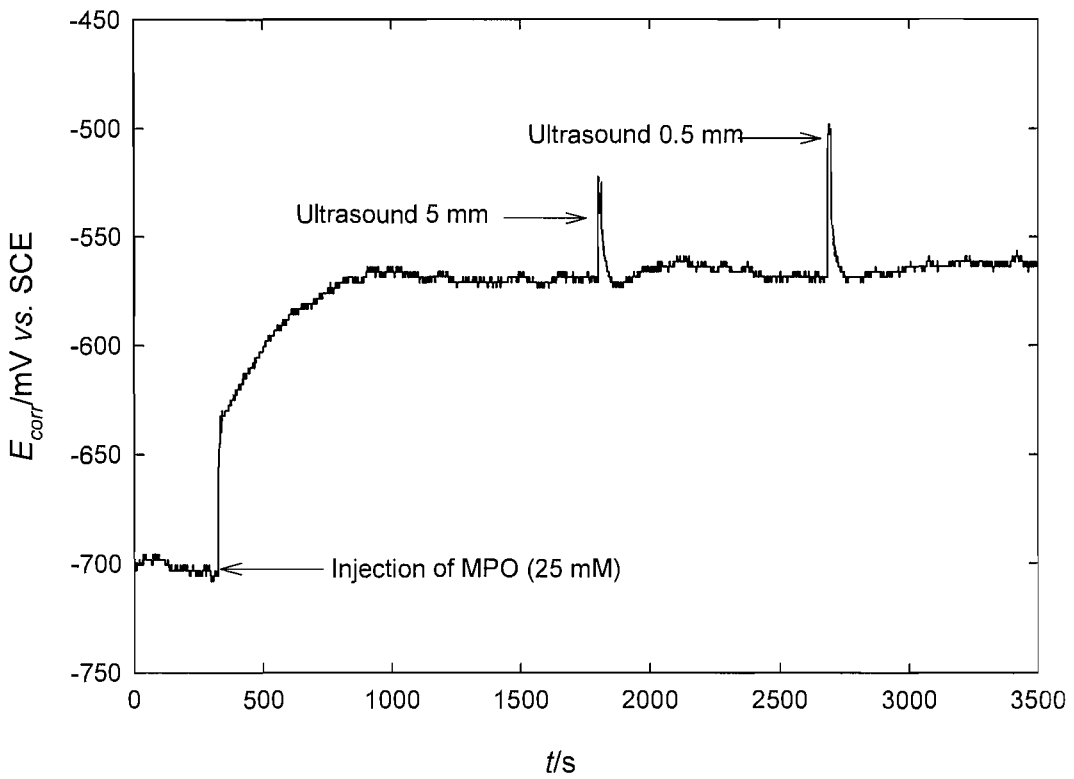


**Figure 6.19** Plot showing the corrosion potential of a 5 mm diameter carbon steel electrode as a function of time in a solution of 1 M NaCl with 25 mM MPO saturated with $CO_2$.

However, sonication at a small distance (0.5 mm) does not show the cathodic shift seen above. This may be expected as the large electrode responds in both a spatially and temporally averaged sense. Although removal of the inhibitor is expected to occur at small electrode-to-horn distances it will do so locally. The response however, is dominated by the global behaviour of the electrode, the majority of which remains covered with an inhibitor layer.

This important point is illustrated in Figure 6.20, which compares the relative sizes of the electrodes with the MBSL output of the horn. The location of the horn is indicated by the solid white line and the electrodes by the dashed white line (the insulating support is not shown). As stated previously (see Section 4.3.1) MBSL is indicative of inertial cavitation and it is expected that within the luminescent region, the corrosion inhibitor will be removed from the surface of the electrode by erosive effects. In the case of the 75 μm radius electrode at 0.5 mm electrode-to-horn separation, the entire surface is within this zone (see Figure 6.20a). In contrast, if the 5 mm diameter electrode is placed at the same electrode-to-horn separation only part of the surface is exposed to inertial cavitation (indicated by the black dashed line in Figure 6.20b) and hence subject to inhibitor removal.

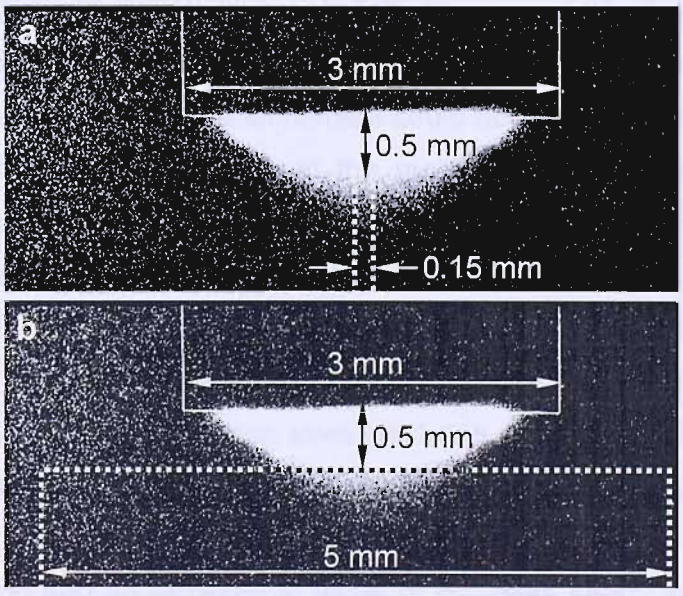


**Figure 6.20** Picture illustrating the size of carbon steel electrodes relative to the MBSL output of the ultrasonic horn.

It must be noted that the MBSL images shown in Figure 6.20 were recorded in the absence of any electrodes. As shown in Section 4.4 the addition of an electrode to the cell will increase the spatial extent of inertial cavitation through shock wave reflection. However, given the small size of the sound source and small distance between the source and the electrode, it is not feasible that the entire surface of the 5 mm diameter electrode could be exposed to inertial cavitation. This illustrates the importance of both the spatial resolution afforded by the use of microelectrodes and a good understanding of the cavitation environment generated by the ultrasonic horn.

### 6.2.3 Conclusions and further work

In this subsection the performance of a corrosion inhibitor in a cavitation environment has been investigated. Erosion/corrosion phenomena are of significant interest owing to their impact on industrial processes. It has been recognised that in an industrial context hydrodynamic cavitation is prevalent, however acoustic cavitation can provide a well controlled environment for initial studies. Here, the inhibition of sweet corrosion of carbon steel in 1 M NaCl by methyl-2-pyrazoline-5-one (MPO) was studied. Initially the effect of sonication on the corrosion process itself was studied and it was found that the corrosion current was enhanced and the corrosion potential was shifted to a more anodic value. It was shown that this can be attributed to increased rate of the cathodic reaction although because of the complex nature of the hydrogen evolution mechanism the source of the enhancement could not be elucidated. Ultrasound had little effect on the dissolution of the metal. Addition of MPO led to a decrease in the corrosion current and a significant anodic shift in the corrosion potential. Tafel analysis showed that this is due to inhibition of the metal dissolution reaction. The effect of ultrasound on the inhibited system was then studied at various electrode-to-horn separations by monitoring the corrosion potential for a 75 μm radius carbon steel electrode. It was found that when the electrode was far from the horn (≥ 1.5 mm (outside the inertial cavitation zone identified in Chapters 4 and 5)) the response was dominated by the enhanced cathodic reaction and an increase in value of $E_{corr}$ was seen. However, when the electrode was close to the horn, removal of the inhibitor layer was evidenced as a decrease in the corrosion potential. When the same experiment was preformed with a large (2.5 mm radius) electrode however, this effect was not seen. Sonication at both large (5 mm) and small (0.5 mm) distances led to

a shift in the value of $E_{corr}$ to more anodic values. This was attributed to the fact that the enhancement of the cathodic reaction is a global effect, whereas the removal of the inhibitor layer is localised. Although the use of microelectrodes has enabled the removal of the inhibitor layer to be seen, the data is still temporally averaged owing to limitations in the response time of the galvanostat used to acquire the data. The use of faster electronics in future work may allow for the resolution of individual erosion events to be recorded in similar fashion to the passivation transients shown in Section 6.1.2. Nevertheless it has been shown that, if properly characterised, acoustic cavitation can provide a convenient methodology for initial studies of inhibitor performance within a cavitation environment.

## 6.3 Overall conclusions

In this chapter the use of ultrasound and inertial cavitation for the study of two surface processes (passive film formation and corrosion inhibition) has been detailed. For detailed conclusions concerning each, readers are directed to Section 6.1.3 and 6.2.3 respectively.

# Chapter 7 Conclusions and further work

This thesis presented an acoustoelectrochemical study of cavitation generated by an ultrasonic horn and its use in the study of surface processes. In order for inertial cavitation to be effectively employed as a tool, thorough characterisation of the system (both the sound field and the nature of cavitation) is required. This was the aim of the first part of this thesis and the results are presented in Chapters 4 and 5. In order to aid this characterisation a novel dual microelectrode consisting of lead and platinum microwires sealed in close proximity was used. The development of this is reported in Chapter 3. In Chapter 6 the application of ultrasound to the study of two industrially relevant systems (passivation of stainless steel and stability of corrosion inhibitors in a cavitation environment) is described.

## 7.1 General Conclusions

Throughout this work the dual microelectrode was employed as a sensor sensitive to both mass transfer and surface erosion. This was achieved through the use of a concentrated (0.75 M) $Na_2SO_4$ solution, which also contained a small amount of $K_4Fe(CN)_6$ (typically 20 mM). In this solution it is possible to passivate the lead electrode with a layer of insoluble $PbSO_4$ and, at the same potential (+0.8 V *vs.* SCE), achieve mass transfer limited oxidation of $Fe(CN)_6^{4-}$. Under these conditions the Pb electrode is sensitive only to erosive events, which can be detected as transient currents, attributed to repassivation of the surface. In contrast, the Pt electrode is sensitive to all hydrodynamic processes, which affect mass transfer of electroactive species to the electrode. It was also noted that on changing the potential of both electrodes to 0 V *vs.* SCE, the lead electrode remained passivated but there was no oxidation at the Pt electrode. This allowed the mass transfer component of the sensor to be 'switched on and off' by simply changing the applied potential.

In the characterisation of the physical environment close the tip of the ultrasonic horn, it was noted that inertial cavitation is a threshold phenomenon, dependent on many factors, but particularly the local pressure amplitude at the point of

interest. In this work attention was therefore paid to characterising the sound field generated, not only by the sound source but also by emissions from cavitation itself. Also, the effect of the electrode on the sound field has been considered. The vibrating horn was modelled as a rigid disc within a rigid baffle. An analytical expression derived by Kinsler *et al.* was used to describe the acoustic pressure amplitude as a function of axial distance from the tip of the horn. Under the conditions employed the sound field exhibits a simple decay with distance owing to the geometric spreading of the acoustic power. This was confirmed by measuring the acoustic pressure amplitude as a function of axial distance in the absence and presence of cavitation. In the absence of cavitation the pressure wave was purely sinusoidal at the driving frequency (as determined by FFT) and the amplitude was plotted as a function of distance to yield the axial pressure profile. This was a good fit to the analytical expression although the magnitude of the horn displacement was found to be an underestimate of the true value. This can be attributed to the fact that the baffle is in reality a free surface rather than rigid. This was confirmed by experiment. In the presence of cavitation the pressure wave was complex, consisting of an underlying wave at the driving frequency, superimposed with high amplitude pressure shocks. The pressure shocks were found to occur every 3-4 cycles of the driving wave. In order to extract the driving wave from the pressure signal FFT was employed. The magnitude of the FFT (calibrated with generated sine waves of known amplitude) was plotted as a function of axial distance to yield the axial pressure profile for the driving pressure wave. This was also a good fit to the analytical expression.

In order to determine the origin of the high pressure shocks, the bubble dynamics close to the horn were investigated using a combination of high-speed video, hydrophone data, erosion of the $PbSO_4$ modified electrode, high time resolution MBSL and laser scattering. A large bubble cloud was visible at the tip of the ultrasonic horn, which could be seen to collapse every 3-4 cycles. Following the collapse of the bubble cloud, small (10's of microns maximum radius) bubbles could be seen in high-speed video and laser scattering data. It was also shown that these bubbles were associated with surface erosion and MBSL. Two possible mechanisms were proposed for the observed dynamics. The first is that the clearing of the large bubble cloud removed its shielding

effect, allowing the pressure in the solution to reach greater negative values and hence initiate inertial cavitation. The second is that, following the collapse of the cloud, bubble rebound occurs. Evidence supporting both mechanisms can be found in the data presented and it was not possible to distinguish between them.

The extent of inertial cavitation within the cell was investigated using MBSL and a novel electrochemical technique. The presence of MBSL was assumed to indicate the presence of inertial cavitation. It was found that MBSL only existed close to the tip of the horn in agreement with the sound field model. MBSL extended to a distance of 0.9 ± 0.05 mm. The pressure of the driving wave at this point was estimated (from the sound field model) to be 85 ± 3 kPa. It was noted that this was less than the theoretical inertial cavitation threshold (~110-120 kPa). The disagreement was attributed to the action of shock waves emitted by collapsing bubbles in higher pressure regions. The electrochemical technique used the dual electrode to first map the enhancement in mass transfer in a plane below the tip of the horn (using the Pt electrode). This allowed the electrode to be centred below the horn. The passivated Pb electrode was then used to measure erosion as a function of distance from the tip of the horn. The onset of erosion was assumed to indicate the onset of inertial cavitation. This was found to occur at an axial distance of 1.3 ± 0.2 mm. From the sound field model, the free field pressure amplitude associated with the driving wave at this point was estimated to be 69 ± 7 kPa. The disagreement between the inertial cavitation threshold pressures measured using MBSL and erosion was attributed to scattering of the incident sound field by the electrode.

The effect of the electrode on the incident sound field was characterised by calculating the total pressure at the surface of the electrode using linear acoustic theory. It was shown that the degree of scattering was dependent on the frequency of the incident sound wave, the radius of the electrode and the fractional distance from the centre of the electrode. Also, the materials used in the construction of the electrode were found to play an important role. Under the conditions used in this work, scattering of the driving pressure wave was found to be insignificant. However, it was shown that the shock waves,

associated with cavity collapse, were strongly scattered by the electrode. In the high frequency limit and assuming a rigid electrode the average pressure at the surface of the electrode was found to be up to twice that in its absence. The material dependence was incorporated by defining a normal incidence, plane wave reflection coefficient, which depended on the acoustic impedance of the interfacial materials. It was shown that a soda glass-bodied electrode had a greater effect on the sound field than an epoxy-bodied electrode, which was due to the higher acoustic impedance of soda glass.

In addition to detecting inertial cavitation close to the tip of the horn the dual electrode was also used to investigate periodic mass transfer events, which occur at larger electrode-to-horn distances. Through the use of synchronous high speed video and electrochemistry, it was found that periodic mass transfer enhancement is caused by oscillation of relatively large (100's of microns radius), surface bound bubbles. Further insight was gained from a novel ring down experiment, in which the ultrasound was terminated and the relaxation of these bubbles was observed. As the pressure decreased the bubble behaviour evolved from chaotic oscillation to discrete surface wave modes. It was postulated that forced convection caused by Faraday waves may be the source of periodic current enhancement at subharmonics of the driving pressure wave, which have been observed.

Following the characterisation of the sound field and cavitation generated by the ultrasonic horn, the application of ultrasound to industrially relevant problems was investigated. The first system studied was the kinetics of stainless steel repassivation under electrochemical control. It was found that under exposure to inertial cavitation removal of the passive film led to transient repassivation currents. It was possible to collect many transients in a short time, which could then be used for kinetic analysis. Kinetic analysis revealed that both the major mechanisms for passive film growth (place exchange and ion migration) were in evidence. It was postulated that this was due to the removal of varying amounts of passive film: on some occasions bare metal was exposed leading to a place exchange mechanism and on some occasions the film was only partially removed, which resulted in ion migration type kinetics. The second system was the performance of corrosion inhibitors in a cavitation environment. The sweet

corrosion of mild steel in NaCl was studied and an anodic inhibitor (3-methyl-2-pyrazoline-5-one (MPO)) was used. It was found that exposure to inertial cavitation removed the inhibitor layer. However, the important conclusion to be drawn was that in order to understand the results obtained it was necessary to employ microelectrodes and to have a good understanding of the nature and location of the cavitation produced by the ultrasonic horn.

## 7.2 Further work

During the course of the work presented in this thesis a good understanding of the environment close to the tip of an operating ultrasonic horn has been obtained. However, further insight into the mechanisms responsible for surface erosion would be useful. The dual electrode presented here was limited in its application by the 'side by side' nature of its construction. It may be possible to develop a Pb/Pt micro ring-disc electrode, possible through sputtering techniques, which would not suffer this limitation. Also, although the high-speed video presented in this thesis has provided a unique insight into the dynamics of acoustic cavitation, faster frame rates would be advantageous. This is difficult because of the stochastic nature of acoustic cavitation events. Often video technology, which allows very high frame rates (>200,000 f.p.s), is limited in the number of frames that can be recorded. However, through the use of a suitable triggering system (such as that used in this work) it may be possible to capture events of interest at high time resolution.

It has been shown briefly that using this understanding ultrasound and cavitation can be applied to industrially relevant systems. In this area there is a large scope for further work. The study of passive film formation could be extended to other systems. For example, aluminium and titanium are well known for their passivity owing to oxide film formation although a more robust calibration would be necessary if quantitative information regarding current density is required. There are numerous systems for which the performance of corrosion inhibitors within a cavitation environment could be investigated.

# Appendix A Visual Basic programs

All the software described as 'in-house' in this thesis was written using Microsoft Visual Basic Version 6. This appendix gives the code for the programs used.

## A.1 Function generator controller

This program was written to interface a Grundig Digimess FG100 function generator with a PC *via* a RS-232 connection.

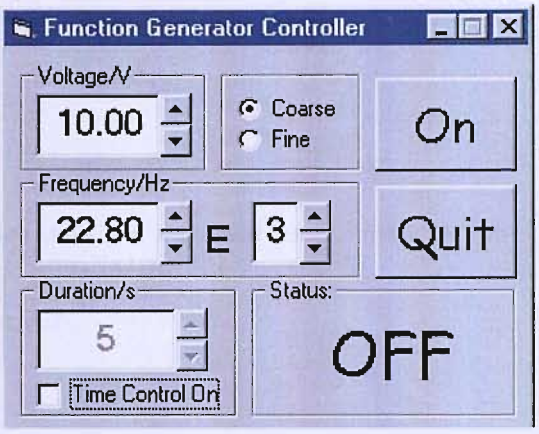


**Figure A.1** Screenshot of the user interface for the function generator controller.

### A.1.1 Visual Basic code

```
Private Sub Form_Load()

    ' Set up comm protocol
    MSComm1.CommPort = 3
    MSComm1.Settings = "9600,n,8,1"
    If MSComm1.PortOpen = False Then MSComm1.PortOpen = True

    MSComm1.Output = Chr$(9) 'Set function generator to remote control
    MSComm1.Output = Chr$(20) 'Initialize comm protocol
    MSComm1.InputLen = 0 'Clear buffer
    MSComm1.Output = "FREQ?" & ";" & Chr$(10) 'File frequency to buffer

    'Delay to allow function generator to file frequency to buffer
    t1 = Timer
repeat:
    t2 = Timer
    t = t2 - t1

    If t > 0.1 Then
       'Read Buffer and display
       frequ$ = MSComm1.Input
       frequval$ = Mid(frequ, 4, 5)
       NumEditFreqval.Value = Val(frequval)
       frequpower = Mid(frequ, 12, 1)
```

```
      NumEditFreqpower.Value = Val(frequpower)
   Else: GoTo repeat
   End If

End Sub
-------------------------------------------

Private Sub cmdOutputOn_Click()

   MSComm1.Output = "OUT_ON" & ";" & Chr(10) 'Set output to ON

   'Configure user interface
   cmdOutputOn.Visible = False
   lblUSOn.Visible = True
   lblUSOff.Visible = False

   DoEvents

   If Check1.Value = 0 Then GoTo noTime 'Check if time limit is on

   'Measure time since output was set to ON
   t1 = Timer
repeat2:
   DoEvents
   t2 = Timer
   t = t2 - t1

   'Wait until duration is reached then turn output to OFF
   If t >= NumEditTime.Value Then
     cmdOutputOff_Click
   Else: GoTo repeat2
   End If

noTime:

End Sub
-------------------------------------------

Private Sub Check1_Click()

   If Check1.Value = 1 Then NumEditTime.Enabled = True
   If Check1.Value = 0 Then NumEditTime.Enabled = False

End Sub
-------------------------------------------

Private Sub cmdOutputOff_Click()

   MSComm1.Output = "OUT_OFF" & ";" & Chr(10) 'Set output to ON

   'Configure user interface
   cmdOutputOn.Visible = True
   MSComm1.PortOpen = False
   lblUSOn.Visible = False
   lblUSOff.Visible = True

End Sub
-------------------------------------------

Private Sub cmdQuit_Click()

   YesNo = MsgBox("Are you sure you want to quit FGControl?",
   vbQuestion + vbYesNo, "FG Control")
   If YesNo = 6 Then End
```

```
End Sub
-----------------------------------------

Private Sub NumEditFreqval_ValueChanged(Value As Variant,
PreviousValue As Variant, ByVal OutOfRange As Boolean)

    'Write frequency to variables
    freqval = NumEditFreqval.Value
    freqpower = NumEditFreqpower.Value

    freq$ = "Freq " & Str$(freqval) & "E" & Str$(freqpower) 'Write
    frequency to string to send to function generator

    MSComm1.Output = freq$ & ";" & Chr(10) 'Send frequency to function
    generator

End Sub
-----------------------------------------

Private Sub NumEditFreqpower_ValueChanged(Value As Variant,
PreviousValue As Variant, ByVal OutOfRange As Boolean)

    'Write frequency to variables
    freqval = NumEditFreqval.Value
    freqpower = NumEditFreqpower.Value

    freq$ = "Freq " & Str$(freqval) & "E" & Str$(freqpower) 'Write
    frequency to string to send to function generator

    MSComm1.Output = freq$ & ";" & Chr(10) 'Send frequency to function
    generator

End Sub
-----------------------------------------

Private Sub NumEditLevel_ValueChanged(Value As Variant, PreviousValue
As Variant, ByVal OutOfRange As Boolean)

    dia1 = NumEditLevel.Value 'Write voltage to variables

    Lev$ = "Level " + Str$(dia1) 'Write voltage to string to send to
    function generator

    MSComm1.Output = Lev$ & ";" & Chr(10) 'Send voltage to function
    generator

End Sub
-----------------------------------------

Private Sub optCoarse_Click()

    NumEditLevel.IncDecValue = 1
    NumEditFreqval.IncDecValue = 1
    NumEditTime.IncDecValue = 1

End Sub
-----------------------------------------

Private Sub optFine_Click()

    NumEditLevel.IncDecValue = 0.1
    NumEditFreqval.IncDecValue = 0.01
    NumEditTime.IncDecValue = 0.1
```

```
End Sub
```

## A.2 Potentiostat interface software

Software was written to interface the potentiostat (or current follower) with a PC *via* a PCI-DAS 4020/12 (Measurement Computing) ADC card. The software consisted of XY, Yt and trigger components.

### A.2.1 XY program

The XY program was used to record cyclic voltammetry.

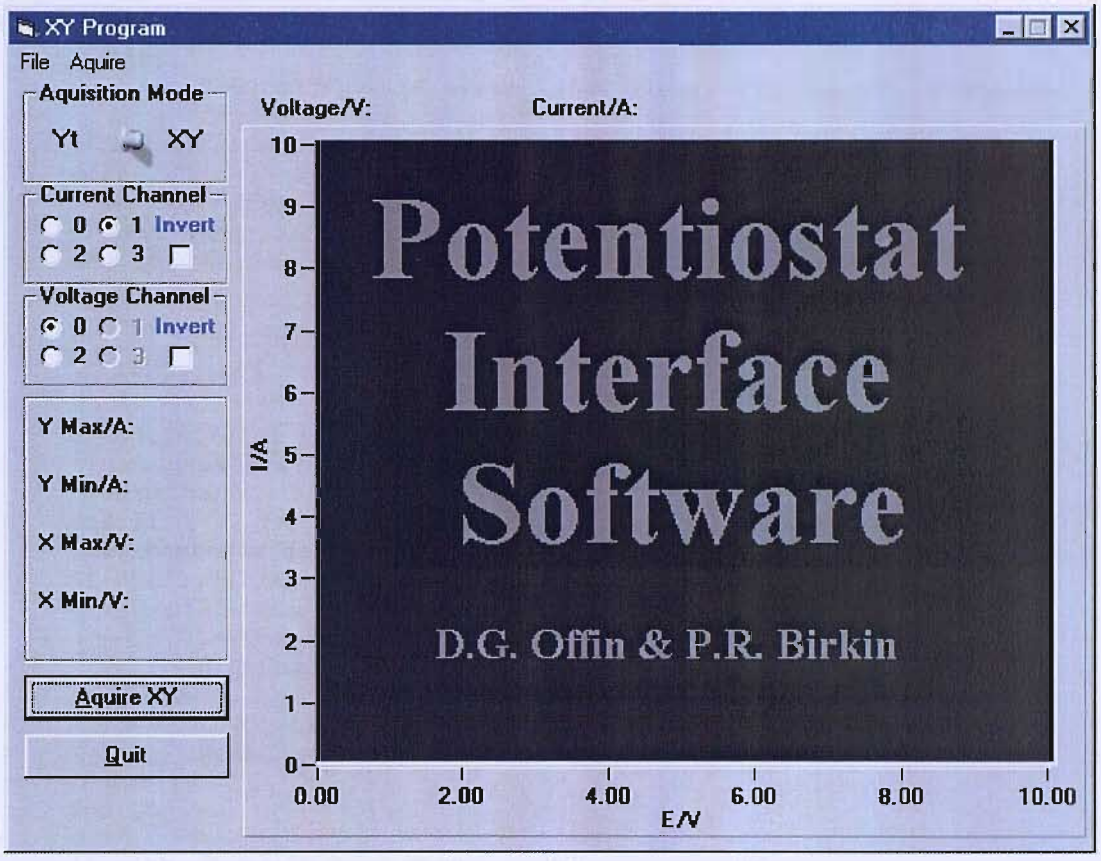


**Figure A.2** Screenshot of the user interface for the XY program.

#### Visual Basic code

```
Private Sub cmdStartXY_Click()

    'Clear title
    Shape1.Visible = False
    Label2.Visible = False
    Picture1.Visible = False
    FrmXY.Caption = "XY Program"

    'set aside memory to hold data
    MemHandle& = cbWinBufAlloc(NumPoints&)
    If MemHandle& = 0 Then Stop

    'clear variables and graph
    For N = 0 To 20000
```

```
    DataY(N) = Empty
    Datax(N) = Empty
Next N

CWGraphXY.ClearData

'get acquisition parameters and configure user interface
gai = InputBox("Enter Gain", "Enter Gain", gai)
If IsNumeric(gai) Then
   sweep = InputBox("Enter Sweep Rate (mV/s)", "Sweep Rate", sweep)
   If IsNumeric(sweep) Then
         File.Enabled = False
         Aquire.Enabled = False
         CWButton2.Enabled = False
         cmdStartXY.Visible = False
         cmdStopXY.Visible = True
         lblAquiring.Visible = True
   Else
         MsgBox "Invalid Sweep Rate. Please Try Again", vbCritical
         Exit Sub
   End If
Else
   MsgBox "Invalid Gain Setting. Please Try Again", vbCritical
   Exit Sub
End If


N = 0
countersave = 0

If optI0.Value = True Then
   LowChan% = 0
   HighChan% = 1
End If
'set channels for acquisition
If optI1.Value = True Then
   If optE0.Value = True Then
         LowChan% = 0
         HighChan% = 1
   Else
         LowChan% = 1
         HighChan% = 2
   End If
End If

If optI2.Value = True Then
   If optE1.Value = True Then
         LowChan% = 1
         HighChan% = 2
   Else
         LowChan% = 2
         HighChan% = 3
   End If
End If

If optI3.Value = True Then
   LowChan% = 2
   HighChan% = 3
End If

'set up ADC card for acquisition
CBCount& = NumPoints 'No. of samples averaged for each point
                     plotted
CBRate& = sweep * 200 'Acquisition rate
```

```
    If CBRate& < 1000 Then CBRate& = 1000 'Min acquisition rate = 1 kHz
    Options = CONVERTDATA 'convert data to 12-bit values
    Gain = BIP5VOLTS

    'start acquisition
    Do
      N = N + 1
Repeat:
      dummy% = DoEvents()'check to see if STOP has been clicked
      If StopAq = 1 Then
            Exit Sub
      End If


      Ulstat% = cbAInScan(BoardNum%, LowChan%, HighChan%, CBCount&,
      CBRate&, Gain, MemHandle&, Options)
      If Ulstat% <> 0 And Ulstat% <> 91 Then Stop

      'Transfer the data from the memory buffer set up by Windows to
      an array for use by Visual Basic
      Ulstat% = cbWinBufToArray(MemHandle&, ADData%(0), FirstPoint&,
      CBCount&)
      If Ulstat% <> 0 Then Stop

      'Convert data to Eng. units and transfer to variables
      X = -2
      TotChan0 = 0

      Do
            X = X + 2
            Ulstat% = cbToEngUnits(BoardNum%, Gain, ADData(X),
            EngUnits(X))
            If Ulstat% <> 0 Then Stop
            TotChan0 = TotChan0 + EngUnits(X)
      Loop Until X >= NumPoints - 2

      X = -1
      TotChan1 = 0

      Do
            X = X + 2
            Ulstat% = cbToEngUnits(BoardNum%, Gain, ADData(X),
            EngUnits(X))
            If Ulstat% <> 0 Then Stop
            TotChan1 = TotChan1 + EngUnits(X)
      Loop Until X >= NumPoints - 2

      AveChan0 = TotChan0 / (NumPoints / 2)
      AveChan1 = TotChan1 / (NumPoints / 2)


      'Check to see if potential has changed by 5 mV
      If Abs(AveChan1 - Datax(N - 1)) > 0.005 Then
            Datax(N) = AveChan1
            DataY(N) = AveChan0 / gai
      Else: GoTo Repeat
      End If

      If Check1.Value = 1 Then
            Datax(N) = Datax(N) * -1
      End If

      If Check2.Value = 1 Then
            DataY(N) = DataY(N) * -1
```

```
      End If

      'Plot data and display data values

      CWGraphXY.ChartXvsY Datax(N), DataY(N)

      lblShowVolts.Caption = Format$(Datax(N), "0.000")
      lblShowCurrent.Caption = Format(DataY(N), "0.00E-00")
      countersave = countersave + 1

   Loop Until N = 20000

End Sub
-----------------------------------------

Private Sub cmdStopXY_Click()

   StopAq = 1 'stop acquisition loop in cmdStartXY subroutine

   'configure user interface
   cmdStartXY.Visible = True
   lblAquiring.Visible = False
   File.Enabled = True
   Aquire.Enabled = True
   CWButton2.Enabled = True

   'find maximum and minimum values and display
   N = 0
   yma = DataY(1)
   ymi = DataY(1)
   xma = Datax(1)
   xmi = Datax(1)

   Do
      N = N + 1
      If DataY(N) > yma Then yma = DataY(N)
      If DataY(N) < ymi Then ymi = DataY(N)
      If Datax(N) > xma Then xma = Datax(N)
      If Datax(N) < xmi Then xmi = Datax(N)
   Loop Until N = countersave

   lblYmax.Caption = Format$(yma, "0.00E-00")
   lblYmin.Caption = Format$(ymi, "0.00E-00")

   lblXmax.Caption = Format$(xma, "0.000")
   lblXmin.Caption = Format$(xmi, "0.000")

End Sub
-----------------------------------------

Private Sub Open_Click()

   'configure common dialog control
   FrmXY.filebox.CancelError = True
   On Error GoTo ErrHandle
   FrmXY.filebox.FileName = "*.dat"
   FrmXY.filebox.InitDir = "C:\doug\data"
   FrmXY.filebox.Action = 1
   FrmXY.Caption = FrmXY.filebox.FileName
   Open FrmXY.filebox.FileName For Input As #4

   No = -1

   'write data from file to variables
```

```
    Do
       No = No + 1
       Input #4, E$
       Datax(No) = Val(E$)
       Input #4, i$
       DataY(No) = Val(i$)
    Loop Until EOF(4)
    Close #4

    'plot data
    CWGraphXY.ClearData
    For nop = 0 To No
       CWGraphXY.Plots.Item(noop).ChartXvsY Datax(nop), DataY(nop)
    Next

    'find maximum and minimum values and display
    N = 0
    yma = DataY(0)
    ymi = DataY(0)
    xma = Datax(0)
    xmi = Datax(0)

    Do
       N = N + 1
       If DataY(N) > yma Then yma = DataY(N)
       If DataY(N) < ymi Then ymi = DataY(N)
       If Datax(N) > xma Then xma = Datax(N)
       If Datax(N) < xmi Then xmi = Datax(N)
    Loop Until N = No

    lblYmax.Caption = Format$(yma, "0.00E-00")
    lblYmin.Caption = Format$(ymi, "0.00E-00")
    lblXmax.Caption = Format$(xma, "0.000")
    lblXmin.Caption = Format$(xmi, "0.000")

ErrHandle:     Exit Sub

End Sub
----------------------------------------

Private Sub Save_Click()

    'configure common dialog control
    FrmXY.filebox.CancelError = True
    On Error GoTo ErrHandle
    FrmXY.filebox.Flags = &H2&
    FrmXY.filebox.FileName = "*.dat"
    FrmXY.filebox.InitDir = "C:\doug\data"
    FrmXY.filebox.Action = 2
    FrmXY.Caption = FrmXY.filebox.FileName
    Open FrmXY.filebox.FileName For Output As #2

    'write data to file
    ns = 0
    Do
       ns = ns + 1
       Print #2, Datax(ns); ","; DataY(ns)
    Loop Until ns = countersave
    Close #2

ErrHandle:     Exit Sub

End Sub
```

### A.2.2 Yt program

Low time resolution current-time (Chapter 3) and potential-time (Chapter 6) data were recorded using the Yt program.

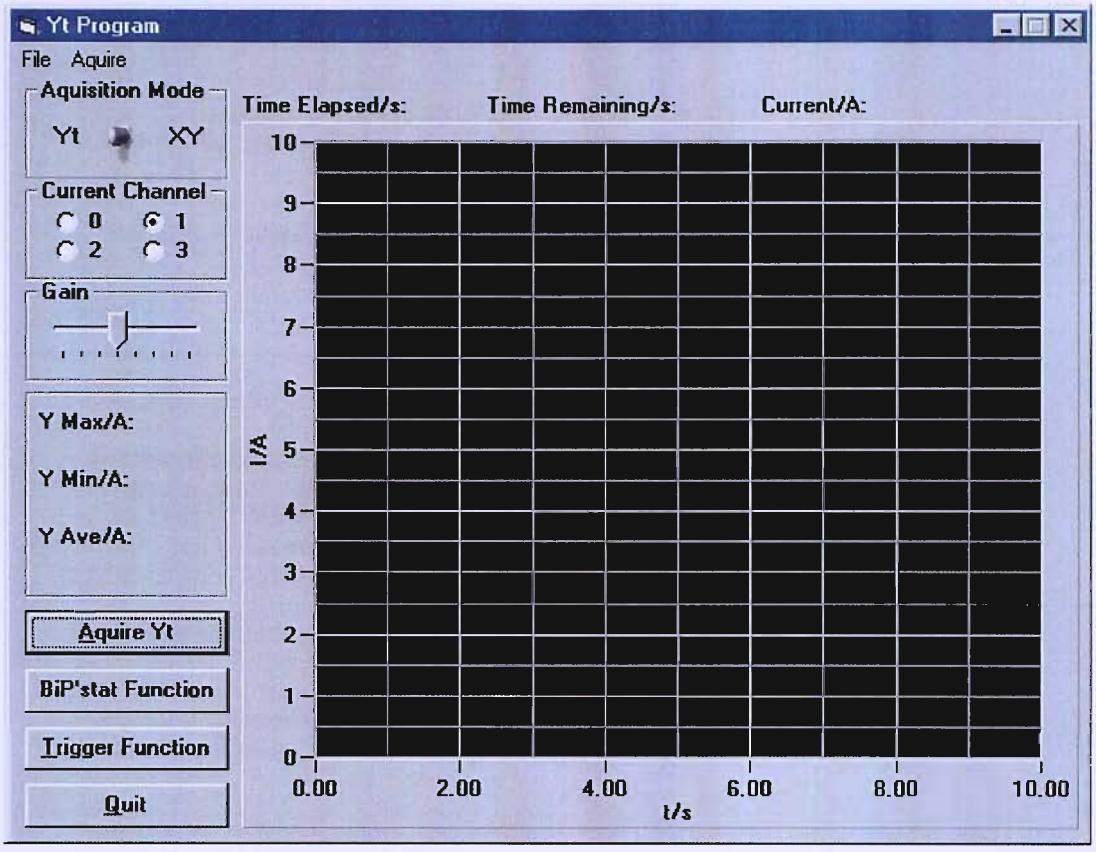


**Figure A.3** Screenshot of the user interface for the Yt program.

### Visual Basic code

```
Private Sub cmdStartYt_Click()

    'clear variables and graph
    For N = 0 To 20000
       DataY(N) = Empty
       Datax(N) = Empty
    Next N
    TotDataY = 0
    FrmYt.Caption = "Yt Program"
    CWGraphYt.ClearData

    'get acquisition parameters, configure interface and start timer
    DataXwin = InputBox("Enter aquisition time in seconds", "Aquisition
    Time", DataXwin)
    If DataXwin > 0 Then
       If IsNumeric(DataXwin) Then
             CWGraphYt.Plots.Item(1).XAxis.Maximum = DataXwin
             File.Enabled = False
             Aquire.Enabled = False
             CWButton1.Enabled = False
             cmdTrigger.Enabled = False
             CWNumEdit1.Enabled = False
             cmdStartYt.Visible = False
             tmrYt.Interval = DataXwin / (CWNumEdit1.Value / 1000)
```

```
            tmrYt.Interval = DataXwin / (CWNumEdit1.Value / 1000)
            counter = 0
            countersave = 0
            N = 0
            tim = 0
            tmrYt.Enabled = True
            tstart = Timer


      Else
            MsgBox "Invalid Aquisition Time. Please Try Again",
            vbCritical
      End If
   Else
      MsgBox "Invalid Aquisition Time. Please Try Again", vbCritical
   End If

End Sub
-----------------------------------------

Private Sub tmrYt_timer()

   'set acquisition channel
   If Option1.Value = True Then Chan% = 0
   If Option2.Value = True Then Chan% = 1
   If Option3.Value = True Then Chan% = 2
   If Option4.Value = True Then Chan% = 3

   N = (counter / tmrYt.Interval)
   Gain = BIP5VOLTS

   'acquire datapoint
   Ulstat% = cbAIn(BoardNum%, Chan%, Gain, DataValue%)
   If Ulstat% <> 0 Then Stop

   Ulstat% = cbToEngUnits(BoardNum%, Gain, DataValue%, EngUnits!)
   If Ulstat% <> 0 Then Stop

   'determine time since cmdStsartYt
   t = Timer
   tim = t - tstart

   If N = 0 Then tim = 0
      'display time elapsed, time remaining and data value
      timr = DataXwin - tim
      lblShowTimeLeft.Caption = Format(timr, "0.0")
      lblShowTime.Caption = Format(tim, "0.0")
      lblShowCurrent.Caption = Format(EngUnits! / 10 ^ Slider1.Value,
      "0.00E-00")
      'write time and data value to variables
      Datax(N) = tim
      DataY(N) = EngUnits! / 10 ^ Slider1.Value
      'plot data
      CWGraphYt.ChartXvsY Datax(N), DataY(N)

      If tim >= DataXwin Then
      tmrYt.Enabled = False
      cmdStartYt.Visible = True
      cmdStopYt_Click
   End If

   countersave = countersave + 1
   counter = counter + tmrYt.Interval
```

```
End Sub

-------------------------------------------

Private Sub cmdStopYt_Click()

    'stop timer and configure user interface
    tmrYt.Enabled = False
    cmdStartYt.Visible = True
    CWNumEdit1.Enabled = True
    File.Enabled = True
    Aquire.Enabled = True
    CWButton1.Enabled = True
    cmdTrigger.Enabled = True
    TotDataY = 0
    N = 0
    If countersave = 1 Then Exit Sub

    'find maximum, minimum and average values and display
    yma = DataY(1)
    ymi = DataY(1)
    Do
       N = N + 1
       If DataY(N) > yma Then yma = DataY(N)
       If DataY(N) < ymi Then ymi = DataY(N)
       TotDataY = TotDataY + DataY(N)
    Loop Until N = countersave - 1

    AveDataY = TotDataY / N
    lblYmax.Caption = Format$(yma, "0.00E-00")
    lblYmin.Caption = Format$(ymi, "0.00E-00")
    lblYAve.Caption = Format$(AveDataY, "0.00E-00")

End Sub
-------------------------------------------

Open and save routines are the same as in the XY program.
```

### A.2.3 Trigger program

A trigger program was written to enable the capture of individual current transient with high temporal resolution. This was used in Chapter 6 to record repassivation transients. It is different from the Yt program in two respects. First, a trigger criterion is set and data is only recorded what the condition is met. In this work, when the current exceeded the set value. Second, the data is collected and then plotted, rather than being displayed as it is collected (note the use of cbAInScan in place of cbAIn). This allows the data to be collected at very high rates (up to 20 MHz).

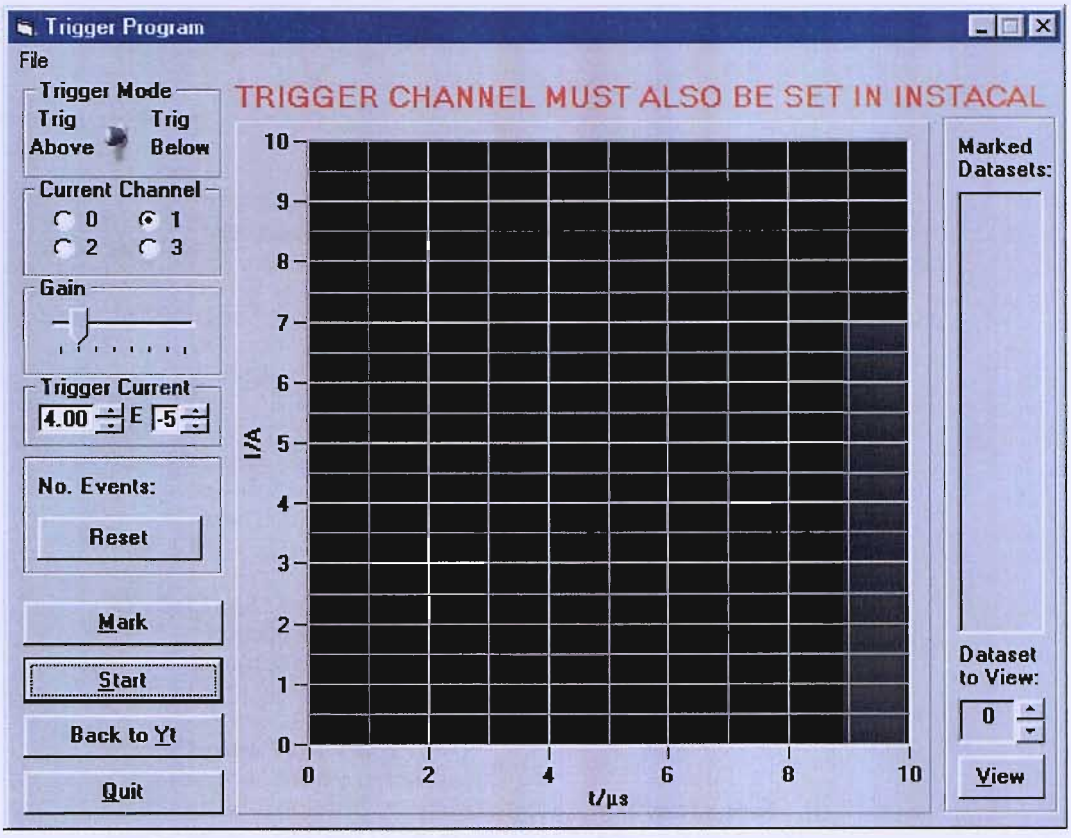


**Figure A.4** Screenshot of the user interface for the trigger program.

## Visual Basic code

```
Private Sub cmdStart_Click()

    FrmTrigger.Caption = "Trigger Program"
    StopAq = 0
    'set time for timeframe for each event and configure interface
    timeframe = InputBox("Enter event timeframe in microseconds (>50)",
    "Event Timeframe", 100)

    If timeframe >= 50 Then
       If IsNumeric(timeframe) Then
             cmdView.Enabled = False
             cmdBacktoYt.Enabled = False
             File.Enabled = False

             cmdStart.Visible = False
             cmdStop.Visible = True
       Else
             MsgBox "Invalid Timeframe. Please Try Again", vbCritical,
             "Error"
             Exit Sub
       End If
    Else
       MsgBox "Invalid Timeframe. Please Try Again", vbCritical,
       "Error"
       Exit Sub
    End If

    Do

       dummy% = DoEvents()
```

```
'set acquisition channel
  If StopAq = 1 Then
        Exit Sub
  End If

  If Option1.Value = True Then
        HighChan% = 0
        LowChan% = 0
  End If

  If Option2.Value = True Then
        HighChan% = 1
        LowChan% = 1
  End If

  If Option3.Value = True Then
        HighChan% = 2
        LowChan% = 2
  End If

  If Option4.Value = True Then
        HighChan% = 3
        LowChan% = 3
  End If

  'configure ADC card
  CBCount& = NumPoints&
  CBRate& = 1000000 * (NumPoints& / timeframe)
  Options = CONVERTDATA + EXTTRIGGER
  Gain = BIP5VOLTS

  'set trigger type and value
  If CWButton1.Value = False Then TrigType% = 0
  If CWButton1.Value = True Then TrigType% = 1
  gai = 10 ^ Slider1.Value
  TrigCurrent! = CWNumEdit1.Value * 10 ^ CWNumEdit2.Value
  TrigVoltage! = TrigCurrent! * gai

  Ulstat% = cbFromEngUnits(BoardNum%, Range%, TrigVoltage!,
  TrigValue%)

  Ulstat% = cbSetTrigger(BoardNum%, TrigType%, TrigValue%,
  TrigValue%)

  'acquire data
  Ulstat% = cbAInScan(BoardNum%, LowChan%, HighChan%, CBCount&,
  CBRate&, Gain, MemHandle&, Options)

  If Ulstat% <> 0 And Ulstat% <> 91 Then Stop

  'Transfer the data from the memory buffer set up by Windows to
  an array for use by Visual Basic

  Ulstat% = cbWinBufToArray(MemHandle&, ADData%(0), FirstPoint&,
  CBCount&)

  If Ulstat% <> 0 Then Stop

  counter = counter + 1
  datatoview = counter
  lblNoEvents.Caption = counter
  CWNumEdit3.Maximum = counter
```

```
      'convert data to Eng. units and write to variable
      For N = 0 To NumPoints - 1
            Ulstat% = cbToEngUnits(BoardNum%, Gain, ADData(N),
            EngUnits(N))
            If Ulstat% <> 0 Then Stop
            Data(counter, N) = EngUnits(N) / gai
      Next N

      'plot data
      CWGraph1.ClearData
      For np = 0 To NumPoints - 1
            If np = 0 Then time(np) = 0
            If np > 0 Then time(np) = time(np - 1) + (timeframe /
            NumPoints)
            CWGraph1.ChartXvsY time(np), Data(counter, np)
      Next np
   Loop Until counter = 1000

End Sub
-----------------------------------------

Private Sub cmdStop_Click()

   'interrupt loop in cmdStart subroutine
   StopAq = 1
   cmdStop.Visible = False
   cmdStart.Visible = True
   cmdView.Enabled = True
   cmdBacktoYt.Enabled = True
   File.Enabled = True

End Sub
-----------------------------------------

Private Sub cmdView_Click()

   datatoview = CWNumEdit3.Value
   'ensure datatoview is valid
   If datatoview > 0 Then
      If datatoview <= counter Then
            If IsNumeric(datatoview) Then
                  CWGraph1.ClearData
                  'plot data
                  For N = 0 To NumPoints - 1
                        If N = 0 Then time(N) = 0
                        If N > 0 Then time(N) = time(N - 1) +
                        (timeframe / NumPoints)
                        CWGraph1.ChartXvsY time(N), Data(datatoview,
                        N)
                  Next
            Else
                  MsgBox "Invalid Dataset. Please try again",
                  vbCritical, "Error"
            End If
      Else
            MsgBox "Invalid Dataset. Please try again", vbCritical,
            "Error"
      End If
   Else
      MsgBox "Invalid Dataset. Please try again", vbCritical, "Error"
   End If

End Sub
-----------------------------------------
```

```
Private Sub cmdReset_Click()

    List1.Clear
    counter = 0
    CWNumEdit3.Maximum = 0
    lblNoEvents.Caption = "0"
     s = -1

End Sub
----------------------------------------

Private Sub cmdMark_Click()

    s = s + 1
    Mark(s) = counter - 1
    List1.AddItem Mark(s)

End Sub
----------------------------------------

Private Sub SaveAll_Click()

    'configure common dialog control
    FrmTrigger.filebox.CancelError = True
    On Error GoTo ErrHandle
    FrmTrigger.filebox.Flags = &H2&
    FrmTrigger.filebox.FileName = "*.dat"
    FrmTrigger.filebox.InitDir = "C:\doug\data"
    FrmTrigger.filebox.Action = 2
    FrmTrigger.Caption = FrmTrigger.filebox.FileName
    Open FrmTrigger.filebox.FileName For Output As #7

    'write data to file
    For N = 0 To NumPoints - 1
       If N = 0 Then time(N) = 0
       If N > 0 Then time(N) = time(N - 1) + (timeframe / NumPoints)
    Next N

    For p = 0 To NumPoints - 1
       fileline$ = time(p)
       For q = 1 To counter
             fileline$ = fileline$ & "," & Data(q, p)
       Next q
       Print #7, fileline$
    Next p
   Close #7
ErrHandle:     Exit Sub

End Sub
```

## A.3 Fast acquisition software

Although the trigger program described in Section A.2.3 allows the detection of repassivation transients with high temporal resolution, each event is displayed after it is recorded. This delay means that not all the current transients that occur are captured and hence the trigger program was not suitable for counting transients (see Chapter 4). The Yt program described in Section A.2.2 lacks the temporal resolution to record current transients, as does the oscilloscope if

a long timeframe is required (the Tektronix TDS 22X series is limited to 2,500 datapoints). For these reasons, a program was written to record a large amount of data at high temporal resolution. The program records on two channels and also incorporates the function generator control program described in Section A.1. This allowed the ultrasound to be turned on, the data collected and ultrasound turned off by clicking one button.

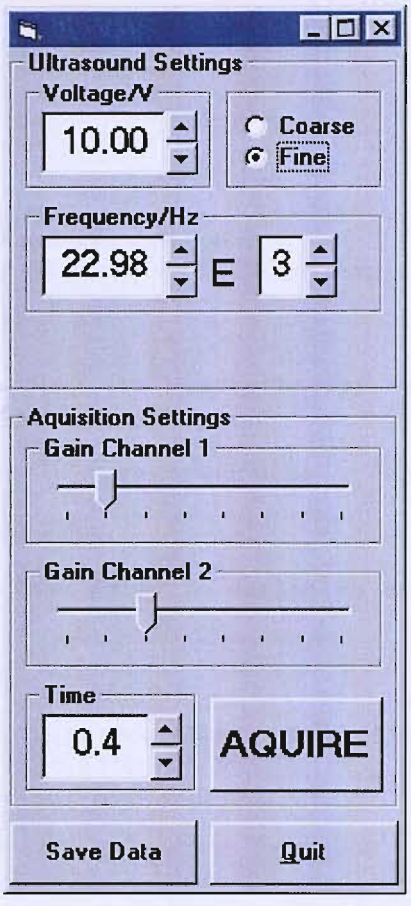


**Figure A.5** Screenshot of the user interface for the fast acquisition program.

### A.3.1 Visual Basic code

```
Private Sub cmdAquire_Click()

    'clear variables
    For N = 0 To 100000
       DataY1(N) = Empty
       DataY2(N) = Empty
       Datax(N) = Empty
    Next N

    'set acquisition parameters
    DataXwin = CWNumEdit2.Value
    LowChan% = 1
    HighChan% = 2
```

```
CBCount& = 100000              'total number of data points to collect
CBRate& = 100000 / DataXwin    'sampling rate
Options = CONVERTDATA          'return data as 12-bit values
Gain = BIP5VOLTS               ' set the gain


If CBRate& < 1000 Then CBRate& = 1000
If CBRate& > 20000000 Then
   MsgBox "Invalid Sampling Rate Required.", vbCritical + vbOKOnly,
   "Error"
   Exit Sub
End If

'Acquire data
cmdOutputOn_Click

Ulstat% = cbAInScan(BoardNum%, LowChan%, HighChan%, CBCount&,
CBRate&, Gain, MemHandle&, Options)
If Ulstat% <> 0 And Ulstat% <> 91 Then Stop

cmdOutputOff_Click

'Transfer the data from the memory buffer set up by Windows to an
array for use by Visual Basic

Ulstat% = cbWinBufToArray(MemHandle&, ADData%(0), FirstPoint&,
CBCount&)
If Ulstat% <> 0 Then Stop

'Transfer the data from array to variables and average
X = -2
TotChan0 = 0
Do
   X = X + 2
   Ulstat% = cbToEngUnits(BoardNum%, Gain, ADData(X), Chan0(X))
   If Ulstat% <> 0 Then Stop
   TotChan0 = TotChan0 + Chan0(X)
Loop Until X >= 49998

X = -1
TotChan1 = 0
Do
   X = X + 2
   Ulstat% = cbToEngUnits(BoardNum%, Gain, ADData(X), Chan1(X))
   If Ulstat% <> 0 Then Stop
   TotChan1 = TotChan1 + Chan1(X)
Loop Until X >= 49999

AveChan0 = TotChan0 / 50000
AveChan1 = TotChan1 / 50000

'convert to current and write time to variabe
For s = 0 To 49999
   DataY1(s) = Chan0(s) / 10 ^ Slider1.Value
   DataY2(s) = Chan1(s) / 10 ^ Slider2.Value
   If s = 0 Then
         Datax(s) = 0
   Else
         Datax(s) = Datax(s - 1) + (DataXwin / 50000)
   End If
Next s
```

---

cmdOutputOn and cmdOutputOff subroutines are given in Section A.1.1. The save subroutine is the same as XY program except there are two DataY(ns) ariables and the loop length is fixed; Loop Until ns = 49999.

## A.4 Peak finding program

In order to count the number of erosion transients recorded as a function of distance a peak finding program was written. The program can analyse two current traces in order to find peaks, sort in terms of peak height and display a histogram of the peak height distribution. The program reads from files with comma separated values in the format time, current1, current2 (as output by the fast data acquisition program described in Section A.3).

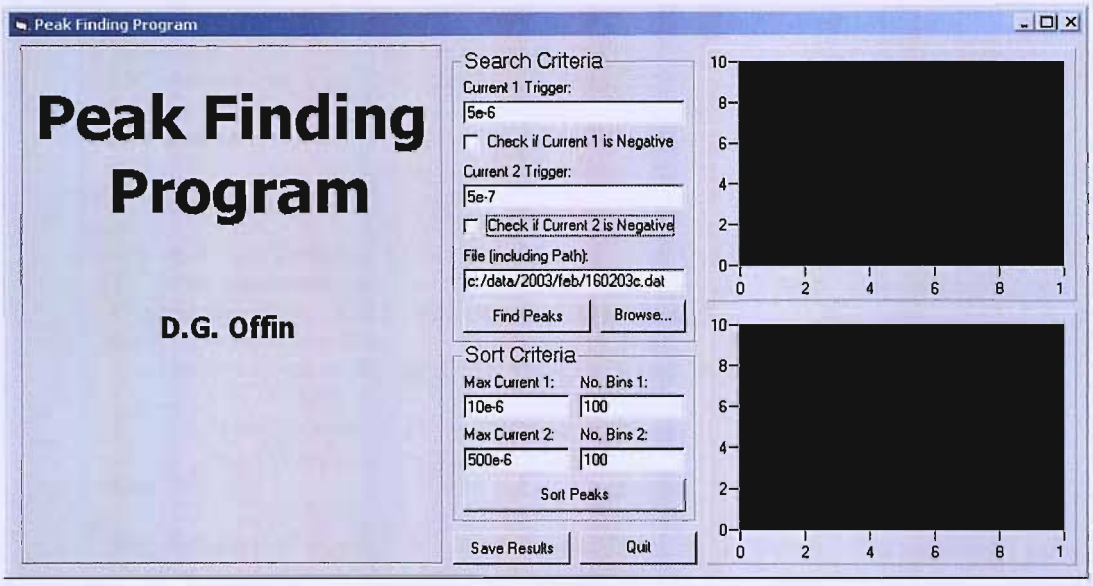


**Figure A.6** Screenshot of the user interface for the peak finding program.

### A.4.1 Visual Basic code

```
Private Sub cmdStart_Click()

    'Clear title
    Frame7.Visible = False
    Label11.Visible = False

    'open file
    FiletoOpen = txtFile.Text
    On Error GoTo DiskErrorHandle
    Open FiletoOpen For Input As #1

    'write file to variables
    no = -1

    Do
       no = no + 1
       Input #1, Tim$
```

```
    Input #1, Tim$
    Timearr(no) = Val(Tim$)
    Input #1, Current1$
    Currentarr1(no) = Val(Current1$)
    Input #1, Current2$
    Currentarr2(no) = Val(Current2$)
  Loop Until EOF(1)

  Close #1

  'Make negative currents positive
  For s = 0 To 250009
    If chkCurr1Neg.Value = 1 Then
      Currentarr1(s) = -Currentarr1(s)
    End If

    If chkCurr2Neg.Value = 1 Then
      Currentarr2(s) = -Currentarr2(s)
    End If
  Next s

  'set trigger current
  TrigCurrent1 = Val(txtcurr1trig.Text)
  TrigCurrent2 = Val(txtcurr2trig.Text)

  'find peaks
  z = 0
  zz = 0

  For x = 1 To 249995
    If Currentarr2(x) > Currentarr2(x - 1) And Currentarr2(x) >
    Currentarr2(x + 1) And Currentarr2(x + 1) > Currentarr2(x + 2)
    And Currentarr2(x) > Currentarr2(x + 3) And Currentarr2(x) >
    Currentarr2(x + 4) And Currentarr2(x) > TrigCurrent2 Then
          z = z + 1
          PeakCurrent2(z) = Currentarr2(x)
          PeakTime2(z) = Timearr(x)
    End If

    If Currentarr1(x) > Currentarr1(x - 1) And Currentarr1(x) >
    Currentarr1(x + 1) And Currentarr1(x) > Currentarr1(x + 2) And
    Currentarr1(x) > Currentarr1(x + 3) And Currentarr1(x) >
    Currentarr1(x + 4) And Currentarr1(x) > TrigCurrent1 Then
          zz = zz + 1
          PeakCurrent1(zz) = Currentarr1(x)
          PeakTime1(zz) = Timearr(x)
    End If
  Next x

  numpeaks2 = z
  numpeaks1 = zz

  'display peak times and currents in grid

  datatab.Cols = 2
  datatab.Rows = z + 1
  datatab.Col = 0
  datatab.Row = 0
  datatab.Text = "Time / s"
  datatab.Col = 1
  datatab.Row = 0
  datatab.Text = "Current / A"

  datatab2.Cols = 2
```

```
    datatab2.Rows = zz + 1
    datatab2.Col = 0
    datatab2.Row = 0
    datatab2.Text = "Time / s"
    datatab2.Col = 1
    datatab2.Row = 0
    datatab2.Text = "Current / A"

    For v = 1 To z
       datatab.Col = 0
       datatab.Row = v
       datatab.Text = Format(PeakTime2(v), "0.00E-00")
       datatab.Col = 1
       datatab.Row = v
       datatab.Text = Format(PeakCurrent2(v), "0.00E-00")
    Next v

    For w = 1 To zz
       datatab2.Col = 0
       datatab2.Row = w
       datatab2.Text = Format(PeakTime1(w), "0.00E-00")
       datatab2.Col = 1
       datatab2.Row = w
       datatab2.Text = Format(PeakCurrent1(w), "0.00E-00")
    Next w

    'show file name and number of peaks
    lblFilename.Caption = txtFile.Text
    lblNoPeaks1.Caption = numpeaks1
    lblNoPeaks2.Caption = numpeaks2

    'find miximum peak current and display
    maxpeakcurrent1 = PeakCurrent1(1)
    maxpeakcurrent2 = PeakCurrent2(1)

    For i = 1 To numpeaks1
       If PeakCurrent1(i) > maxpeakcurrent1 Then
         maxpeakcurrent1 = PeakCurrent1(i)
       End If
    Next i

    txtMaxCurrent1.Text = Format(maxpeakcurrent1, "0.00E-00")

    For j = 1 To numpeaks2
       If PeakCurrent2(j) > maxpeakcurrent2 Then
         maxpeakcurrent2 = PeakCurrent2(j)
       End If
    Next j

    txtMaxCurrent2.Text = Format(maxpeakcurrent2, "0.00E-00")

    Exit Sub

    DiskErrorHandle: MsgBox "Error-File not Found", vbExclamation +
    vbOKOnly

End Sub
----------------------------------------

Private Sub cmdSort_Click()

    'reset variables
    For n = 0 To 1000
       bin(n) = Empty
```

```
    bin2(n) = Empty
Next n

'get sort parameters
maxcurrent1 = Val(txtMaxCurrent1.Text)
maxcurrent2 = Val(txtMaxCurrent2.Text)
NoBins1 = Val(txtNoBins1.Text)
NoBins2 = Val(txtNoBins2.Text)
Binsize1 = maxpeakcurrent1 / NoBins1
Binsize2 = maxpeakcurrent2 / NoBins2

'sort peaks
For a = 1 To numpeaks1
   For b = 0 To NoBins1 - 1
         If PeakCurrent1(a) >= (b * Binsize1) And PeakCurrent1(a)
         <= (b + 1) * Binsize1 Then
               bin(b) = bin(b) + 1
         End If
   Next b
Next a

For c = 1 To numpeaks2
   For d = 0 To NoBins2 - 1
         If PeakCurrent2(c) >= (d * Binsize2) And PeakCurrent2(c)
         <= (d + 1) * Binsize2 Then
               bin2(d) = bin2(d) + 1
         End If
   Next d
Next c

'configure display grid
grdPeakSort.Rows = NoBins1 + 1
grdPeakSort.Col = 0
grdPeakSort.Row = 0
grdPeakSort.Text = "Current / A"
grdPeakSort.Col = 1
grdPeakSort.Row = 0
grdPeakSort.Text = "No. Peaks"

grdPeakSort2.Rows = NoBins2 + 1
grdPeakSort2.Col = 0
grdPeakSort2.Row = 0
grdPeakSort2.Text = "Current / A"
grdPeakSort2.Col = 1
grdPeakSort2.Row = 0
grdPeakSort2.Text = "No. Peaks"


'fill display grid
For e = 1 To NoBins2
   grdPeakSort2.Col = 0
   grdPeakSort2.Row = e
   grdPeakSort2.Text = Format((e) * Binsize2, "0.00E-00")
   grdPeakSort2.Col = 1
   grdPeakSort2.Row = e
   grdPeakSort2.Text = bin2(e - 1)
Next e

For f = 1 To NoBins1
   grdPeakSort.Col = 0
   grdPeakSort.Row = f
   grdPeakSort.Text = Format((f) * Binsize1, "0.00E-00")
   grdPeakSort.Col = 1
   grdPeakSort.Row = f
```

```
      grdPeakSort.Text = bin(f - 1)
    Next f

    cmdDisplay_Click

End Sub
---------------------------------------

Private Sub cmdDisplay_Click()

    CWGraph1.ClearData
    CWGraph2.ClearData

    If numpeaks2 <> 0 Then
      For l = 1 To NoBins2
        CWGraph1.ChartXvsY l * Binsize2, bin2(l - 1) * 100 / numpeaks2
      Next l
    End If

    If numpeaks1 <> 0 Then
      For m = 1 To NoBins1
        CWGraph2.ChartXvsY m * Binsize1, bin(m - 1) * 100 / numpeaks1
      Next m
    End If

End Sub
---------------------------------------

Private Sub cmdSave_Click()

    'configure common dialog box
    Filebox.CancelError = True
    On Error GoTo ErrHandle
    Filebox.Flags = cdlOFNOverwritePrompt
    Filebox.FileName = "*.dat"
    Filebox.InitDir = "C:\doug\data"
    Filebox.Action = 2
    Open Filebox.FileName For Output As #1

    If numpeaks1 > numpeaks2 Then
      maxpeaks = numpeaks1
      Else: maxpeaks = numpeaks2
    End If

    If NoBins1 > NoBins2 Then
      maxnobins = NoBins1
      Else: maxnobins = NoBins2
    End If

    If maxnobins > maxpeaks Then
      maxdata = maxnobins
      Else: maxdata = maxpeaks
    End If


    'write to file
    Print #1, "Dataset 1"; ","; ","; "Dataset 2"; ","; ","; ",";
    "Dataset 1"; ","; ","; "Dataset 2"
    Print #1, "Time/s"; ","; "Current/A"; ","; "Time/s"; ",";
    "Current/A"; ","; ","; "Current/A"; ","; "No. Peaks"; ",";
    "Current/A"; ","; "No. Peaks"

    For g = 1 To maxdata
```

```
    Close #1
    ErrHandle: Exit Sub

End Sub
----------------------------------------

Private Sub cmdBrowse_Click()

'configure common dialog box
    Filebox.CancelError = True
    On Error GoTo ErrHandle2
    Filebox.FileName = "*.*"
    Filebox.InitDir = "C:\doug\data"
    Filebox.Action = 1

    'put filename in textbox
    txtFile.Text = Filebox.FileName

    ErrHandle2: Exit Sub

End Sub
```

## A.5 Bubble simulation program

A bubble simulation program was written to solve the Rayleigh-Plesset equation using a four-order Runge Kutta method. This is effectively the program written in Turbo Pascal by Silva-Martinez [41] converted to Visual Basic and readers are directed to the original for full details of the methodology used.

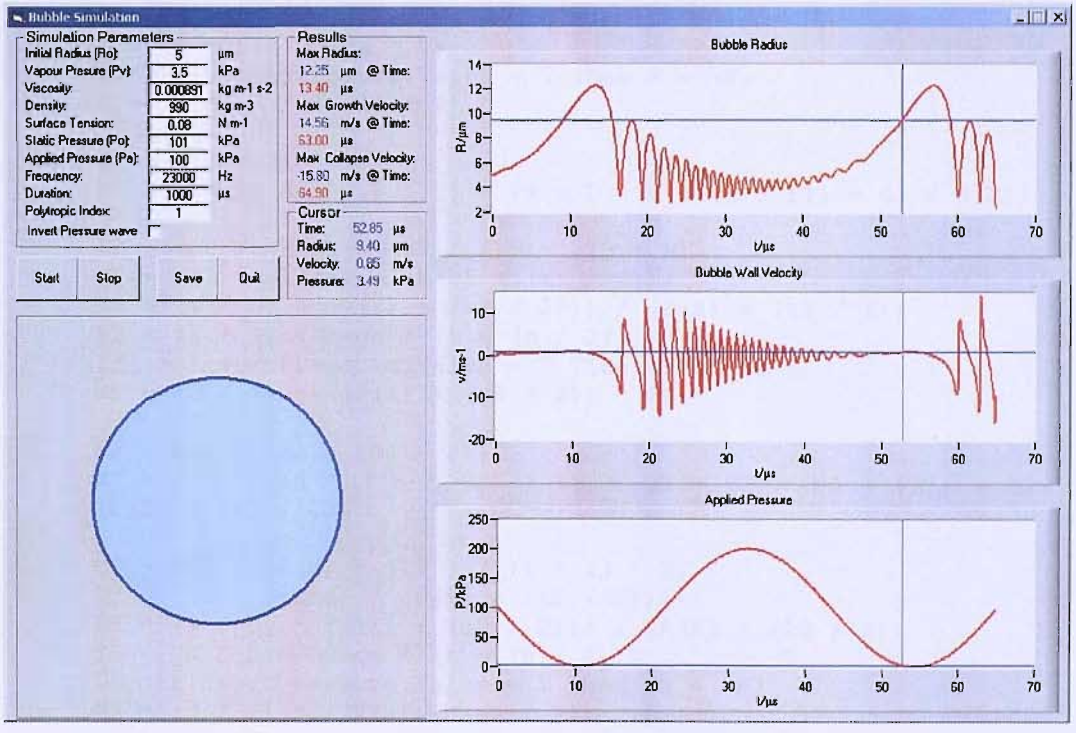


**Figure A.7** Screenshot of the user interface for the bubble simulation program.

## A.5.1 Visual Basic code

```
Private Sub cmdStart_Click()

    'clear form
    Timer1.Enabled = False
    GraphBubbleRadius.ClearData
    GraphPressure.ClearData
    GraphVelocity.ClearData
    StopGraph = 0
    shpBubble.Visible = False

    'write initial parameters to variables
    R0 = NumEditR0.Value * 0.000001
    P0 = NumEditP0.Value * 1000
    Pa = NumEditPa.Value * 1000
    Omega = NumEditOmega.Value * 2 * 3.141592654
    Tmax = NumEditTmax.Value * 0.000001
    Pv = NumEditPv.Value * 1000
    Nu = NumEditNu.Value
    Rho = NumEditRho.Value
    Sigma = NumEditSigma.Value
    h = Tmax / 10000
    K = NumEditPoly.Value
    t = 0
    X = 0
    R(0) = R0
    V(0) = 0
    A = 1 / Rho
    B = (P0 + ((2 * Sigma) / R0) - Pv)

    'Solve Rayliegh-Plesset equation
    Do
       C = (R0 / R(X)) ^ (3 * K)
       D = ((2 * Sigma) / R(X))
       E = (4 * Nu * V(X)) / R(X)
       F = Pa * Sin(Omega * t)
       If chkInvertPressure.Value = 1 Then F = -F
       G = (3 / 2) * (V(X) ^ 2)

       k1 = h * V(X)
       m1 = h * (((A * ((B * C) + Pv - D - E - P0 + F)) - G) / R(X))

       C2 = (R0 / (R(X) + (k1 / 2))) ^ (3 * K)
       D2 = ((2 * Sigma) / (R(X) + (k1 / 2)))
       E2 = (4 * Nu * (V(X) + (m1 / 2))) / (R(X) + (k1 / 2))
       F2 = Pa * Sin(Omega * (t + (h / 2)))
       If chkInvertPressure.Value = 1 Then F2 = -F2
       G2 = (3 / 2) * ((V(X) + (m1 / 2)) ^ 2)

       k2 = h * (V(X) + (m1 / 2))
       m2 = h * (((A * ((B * C2) + Pv - D2 - E2 - P0 + F2)) - G2) /
       (R(X) + (k1 / 2)))

       C3 = (R0 / (R(X) + (k2 / 2))) ^ (3 * K)
       D3 = ((2 * Sigma) / (R(X) + (k2 / 2)))
       E3 = (4 * Nu * (V(X) + (m2 / 2))) / (R(X) + (k2 / 2))
       F3 = Pa * Sin(Omega * (t + (h / 2)))
       If chkInvertPressure.Value = 1 Then F3 = -F3
       G3 = (3 / 2) * ((V(X) + (m2 / 2)) ^ 2)

       k3 = h * (V(X) + (m2 / 2))
       m3 = h * (((A * ((B * C3) + Pv - D3 - E3 - P0 + F3)) - G3) /
       (R(X) + (k2 / 2)))
```

```
    C4 = (R0 / (R(X) + (k3))) ^ (3 * K)
    D4 = ((2 * Sigma) / (R(X) + (k3)))
    E4 = (4 * Nu * (V(X) + (m3))) / (R(X) + (k3))
    F4 = Pa * Sin(Omega * (t + (h)))
    If chkInvertPressure.Value = 1 Then F4 = -F4
    G4 = (3 / 2) * ((V(X) + (m3)) ^ 2)

    k4 = h * (V(X) + m3)
    m4 = h * (((A * ((B * C4) + Pv - D4 - E4 - P0 + F4)) - G4) /
    (R(X) + (k3)))

    R(X + 1) = R(X) + ((1 / 6) * (k1 + (2 * k2) + (2 * k3) + k4))
    V(X + 1) = V(X) + ((1 / 6) * (m1 + (2 * m2) + (2 * m3) + m4))
    P(X) = P0 - F
    time(X) = t * 1000000#

    t = t + h
    X = X + 1
    On Error GoTo Finish
Loop Until X = 9999

Finish:

'calculate and display maximum and minimum values
VGrowMax = 0
VCollMax = 0
Rmin = R0
Rmax = 0

For y = 0 To X - 9
    If R(y) > Rmax Then
        Rmax = R(y)
        RmaxTime = time(y)
    End If
    If R(y) < Rmin Then
        Rmin = R(y)
    End If
    If V(y) > VGrowMax Then
        VGrowMax = V(y)
        VGrowMaxTime = time(y)
    End If
    If V(y) < VCollMax Then
        VCollMax = V(y)
        VCollMaxTime = time(y)
    End If
Next y

'display data in graphs and bubble animation
For y = 0 To X - 9
    Dummy = DoEvents()
    If StopGraph = 1 Then GoTo StopGraphing
    shpBubble.Visible = True
    shpBubble.Width = (4800 * (R(y) - Rmin)) / (Rmax - Rmin)
    shpBubble.Height = (4800 * (R(y) - Rmin)) / (Rmax - Rmin)
    shpBubble.Top = 2760 - (((4800 * (R(y) - Rmin)) / (Rmax - Rmin))
    / 2)
    shpBubble.Left = 2760 - (((4800 * (R(y) - Rmin)) / (Rmax -
    Rmin)) / 2)
    GraphBubbleRadius.ChartXvsY time(y), R(y) * 1000000
    GraphPressure.ChartXvsY time(y), P(y) / 1000
    GraphVelocity.ChartXvsY time(y), V(y)
Next y
```

```
    StopGraphing:

    lblMaxRadius.Caption = Format(Rmax * 1000000, "0.00")
    lblRadiusTime.Caption = Format(RmaxTime, "0.00")
    lblMaxGrowthVelocity.Caption = Format(VGrowMax, "0.00")
    lblMaxGrowthTime.Caption = Format(VGrowMaxTime, "0.00")
    lblMaxCollapseVelocity.Caption = Format(VCollMax, "0.00")
    lblMaxCollapseTime.Caption = Format(VCollMaxTime, "0.00")
    GraphBubbleRadius.Cursors.Item(1).XPosition = RmaxTime

    If X < 9999 And StopGraph = 0 Then MsgBox "Values out of range.
    Inertial collapse predicted.", vbInformation + vbOKOnly

    Timer1.Enabled = True

End Sub
-----------------------------------------

Private Sub Timer1_Timer()

    'display cursor position
    lblTime.Caption =
    Format(GraphBubbleRadius.Cursors.Item(1).XPosition, "0.00")
    lblRadius.Caption =
    Format(GraphBubbleRadius.Cursors.Item(1).YPosition, "0.00")
    GraphVelocity.Cursors.Item(1).XPosition =
    GraphBubbleRadius.Cursors.Item(1).XPosition
    lblVelocity.Caption =
    Format(GraphVelocity.Cursors.Item(1).YPosition, "0.00")
    GraphPressure.Cursors.Item(1).XPosition =
    GraphBubbleRadius.Cursors.Item(1).XPosition
    lblPressure.Caption =
    Format(GraphPressure.Cursors.Item(1).YPosition, "0.00")

    'change bubble animation to match cursor position
    shpBubble.Width = (4800 *
    (GraphBubbleRadius.Cursors.Item(1).YPosition / 1000000# - Rmin)) /
    (Rmax - Rmin)
    shpBubble.Height = (4800 *
    (GraphBubbleRadius.Cursors.Item(1).YPosition / 1000000# - Rmin)) /
    (Rmax - Rmin)
    shpBubble.Top = 2640 - (((4800 *
    (GraphBubbleRadius.Cursors.Item(1).YPosition / 1000000# - Rmin)) /
    (Rmax - Rmin)) / 2)
    shpBubble.Left = 2760 - (((4800 *
    (GraphBubbleRadius.Cursors.Item(1).YPosition / 1000000# - Rmin)) /
    (Rmax - Rmin)) / 2)

End Sub
-----------------------------------------

Private Sub cmdSave_Click()

    CommonDialog1.FileName = "*.dat"
    CommonDialog1.InitDir = "C:\doug\"
    CommonDialog1.Action = 2
    Open CommonDialog1.FileName For Output As #2

    ns = -1
    Do
      ns = ns + 1
      Print #2, time(ns); ","; R(ns) * 1000000; ","; V(ns); ","; P(ns)
      / 1000
    Loop Until ns = X
```

```
    Close #2

End Sub
-----------------------------------------

Private Sub Stop_Click()

    StopGraph = 1

End Sub
-----------------------------------------

Private Sub Quit_Click()

    End

End Sub
```

# Appendix B Publications

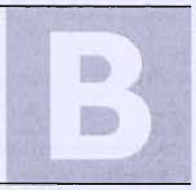

1. P. R. Birkin, D. G. Offin, P. F Joseph, T. G. Leighton, **Cavitation, shock waves and the invasive nature of sonoelectrochemistry,** *J. Phys. Chem. B,* **109**, 16997 (2005).

2. P. R. Birkin, D. G. Offin, T. G. Leighton, **The study of surface processes under electrochemical control in the presence of inertial cavitation,** *Wear,* **258**, 623 (2005).

3. P. R. Birkin, D. G. Offin, T. G. Leighton, **Experimental and theoretical characterisation of sonochemical cells. Part 2: cell disruptors (Ultrasonic horns) and cavity cluster collapse,** *Phys. Chem. Chem. Phys.,* **7**, 530 (2005).

4. P. R. Birkin, D. G. Offin, T. G. Leighton, **Electrochemical measurements of the effects of inertial acoustic cavitation by means of a novel dual microelectrode,** *Electrochem. Commun.,* **6**, 1174 (2004).

## References


1. W. B. McNamara, Y. T. Didenko, K. S. Suslick, *Nature,* **401**, 772 (1999).

2. E. B. Flint, K. S. Suslick, *Science,* **253**, 1397 (1991).

3. L. H. Thompson, L. K. Doraiswamy, *Ind. Eng. Chem. Res.,* **38**, 1215 (1999).

4. Y. G. Adewuyi, *Ind. Eng. Chem. Res.,* **40**, 4681 (2001).

5. K. A. J. Borthwick, W. T. Coakley, M. B. McDonnell, H. Nowotny, E. Benes, M. Groschl, *J. Microbiol. Methods,* **60**, 207 (2005).

6. E. K. Lee, R. J. Gallagher, A. M. Campbell, M. R. Prausnitz, *IEEE Trans. Biomed. Eng.,* **51**, 82 (2004).

7. M. Salisova, S. Toma, T. J. Mason, *Ultrason. Sonochem.,* **4**, 131 (1997).

8. M. Vinatoru, M. Toma, O. Radu, P. I. Filip, D. Lazurca, T. J. Mason, *Ultrason. Sonochem.,* **4**, 135 (1997).

9. P. Riesz, T. Kondo, C. M. Krishna, *Ultrasonics,* **28**, 295 (1990).

10. N. Serpone, R. Terzian, H. Hidaka, E. Pelizzetti, *J. Phys. Chem.,* **98**, 2634 (1994).

11. K. Inazu, Y. Nagata, Y. Maeda, *Chem. Lett.*, 57 (1993).

12. P. Kruus, R. C. Burk, M. H. Entezari, R. Otson, *Ultrason. Sonochem.,* **4**, 229 (1997).

13. T. J. Mason, A. Newman, J. P. Lorimer, J. Lindley, K. Hutt, *Ultrason. Sonochem.,* **3**, 53 (1996).

14. B. H. Han, P. Boudjouk, *Tetrahedron Lett.,* **22**, 2757 (1981).

15. A. G. Osborne, K. J. Glass, M. L. Staley, *Tetrahedron Lett.,* **30**, 3567 (1989).

16. D. H. Bremner, *Ultrason. Sonochem.,* **1**, S119 (1994).

17. T. J. Mason, *Chem. Soc. Rev.,* **26**, 443 (1997).

18. Y. Mastai, R. Polsky, Y. Koltypin, A. Gedanken, G. Hodes, *J. Am. Chem. Soc.,* **121**, 10047 (1999).

19. V. G. Pol, O. Palchik, A. Gedanken, I. Felner, *J. Phys. Chem. B,* **106**, 9737 (2002).

20. K. S. Suslick, G. J. Price, *Annu. Rev. Mater. Sci.,* **29**, 295 (1999).

21. J. J. Zhu, S. T. Aruna, Y. Koltypin, A. Gedanken, *Chem. Mat.,* **12**, 143 (2000).

22. J. R. Canselier, H. Delmas, A. M. Wilhelm, B. Abismail, *J. Dispersion Sci. Technol,* **23**, 333 (2002).

23. J. L. Hardcastle, R. G. Compton, *Electroanalysis,* **14**, 753 (2002).

24. R. S. Juang, K. H. Lin, *Colloid Surf. A-Physicochem. Eng. Asp.,* **238**, 43 (2004).

25. J. Kruusma, P. Tomcik, C. E. Banks, R. G. Compton, *Electroanalysis,* **16**, 852 (2004).

26. M. T. Timko, J. M. Diffendal, J. W. Tester, K. A. Smith, W. A. Peters, R. L. Danheiser, J. I. Steinfeld, *J. Phys. Chem. A,* **107**, 5503 (2003).

27. J. D. Wadhawan, F. Marken, R. G. Compton, *Pure Appl. Chem.,* **73**, 1947 (2001).

28. P. Cintas, J. L. Luche, *Green Chem.,* **1**, 115 (1999).

29. P. R. Birkin, T. G. Leighton, Y. E. Watson, J. F. Power, *Acoustics Bulletin,* **26**, 24 (2001).

30. T. G. Leighton, *The Acoustic Bubble,* Academic Press Limited, London (1994).

31. E. Neppiras, *A. Phys. Rep.,* **61**, 159 (1980).

32. A. J. Walton, G. T. Reynolds, *Adv. Phys.,* **33**, 565 (1984).

33. L. Rayleigh, *Phil. Mag.,* **34**, 94 (1917).

34. W. H. Besant, *Hydrostatics and Hydrodynamics,* Deighton Bell, Cambridge (1859).

35. M. S. Plesset, *J. App. Mech.,* **16**, 277 (1949).

36. E. A. Neppiras, B. E. Noltingk, *Proc. Phys. Soc. London,* **LXIV**, 1032 (1951).

37. B. E. Noltingk, E. A. Neppiras, *Proc. Phys. Soc. London,* **LXIII**, 674 (1950).

38. T. G. Leighton, *The Acoustic Bubble,* Academic Press Limited, London, §1.1.1b ii (1994).

39. H. Poritsky, *Proceedings of the First U.S National Congress on Applied Mechanics,* New York, 813-821 (1952).

40. M. J. Maron, R. J. Lopez, *Numerical Analysis: A Practical Approach,* Wadsworth, Belmont, CA. (1991).

41. S. Silva-Martinez, *Applications of ultrasound in electrochemistry,* PhD Thesis, University of Southampton (1997).

42. P. R. Birkin, J. F. Power, T. G. Leighton, *J. Chem. Soc., Chem. Commun.*, 2230 (2001).

43. P. R. Birkin, J. F. Power, T. G. Leighton, A. M. L. Vincotte, *Anal. Chem.*, **74**, 2584 (2002).

44. A. Weissler, *J. Am. Chem. Soc.,* **81**, 1077 (1959).

45. A. Weissler, H. W. Cooper, S. Snyder, *J. Am. Chem. Soc.,* **72**, 1769 (1950).

46. T. G. Leighton, *The Acoustic Bubble,* Academic Press Limited, London, §5.2 (1994).

47. T. G. Leighton, *The Acoustic Bubble,* Academic Press Limited, London, §5.4.1 (1994).

48. H. G. Flynn, *Physical Acoustics,* Academic Press, New York, 57-172 (1964).

49. H. G. Flynn, *J. Acoust. Soc. Am.,* **57**, 1379 (1975).

50. H. G. Flynn, *J. Acoust. Soc. Am.,* **58**, 1160 (1975).

51. W. L. Nyborg, *Ultrasound Med. Biol.,* **27**, 301 (2001).

52. R. E. Apfel, *J. Acoust. Soc. Am.,* **69**, 1624 (1981).

53. C. K. Holland, R. E. Apfel, *IEEE Trans.,* **36**, 204 (1989).

54. K. S. Suslick, D. A. Hammerton, R. E. Cline, *J. Am. Chem. Soc.,* **108**, 5641 (1986).

55. J. Šponer, *Ultrasonics,* **29**, 376 (1991).

56. W. J. Galloway, *J. Acoust. Soc. Am.,* **26**, 849 (1954).

57. M. Faraday, *Phil. Trans. Roy. Soc.*, **121**, 319 (1831).

58. C. Hullin, *Acustica,* **37**, 64 (1977).

59. A. Francescutto, R. Naberogoj, *Acustica,* **41**, 215 (1978).

60. P. R. Birkin, Y. E. Watson, T. G. Leighton, K. L. Smith, *Langmuir,* **18**, 2135 (2002).

61. D. G. Ramble, A. D. Phelps, T. G. Leighton, *Acustica,* **84**, 986 (1998).

62. F. Marken, R. P. Akkermans, R. G. Compton, *J. Electroanal. Chem,* **415**, 55 (1996).

63. S. A. Elder, *J. Acoust. Soc. Am.,* **31**, 54 (1958).

64. Y. Iwai, T. Okada, *Wear,* **133**, 233 (1989).

65. T. Okada, Y. Iwai, *Wear,* **133** (1989).

66. Y. Tomita, A. Shima, *J. Fluid. Mech.,* **169**, 535 (1986).

67. A. Philipp, W. Lauterborn, *J. Fluid. Mech.,* **361**, 75 (1998).

68. W. Lauterborn, H. Bolle, *J. Fluid. Mech.,* **72**, 391 (1975).

69. M. S. Plesset, R. B. Chapman, *J. Fluid. Mech.,* **47**, 283 (1971).

70. A. Properetti, *Ultrasonics,* **22**, 115 (1984).

71. I. Hansson, K. A. Mørch, *J. App. Phys.,* **51**, 4651 (1980).

72. I. Hansson, V. Kedrinskii, K. A. Mørch, *J. Phys. D: Appl. Phys.,* **15**, 1725 (1982).

73. P. R. Birkin, J. F. Power, M. E. Abdelsalam, T. G. Leighton, *Ultrason. Sonochem.,* **10**, 203 (2003).

74. A. J. Bard, *Anal. Chem.,* **35**, 1125 (1963).

75. W. L. Nyborg, M. I. L. Seegall, *Effects of acoustic microstreaming at electrodes,* Proceedings of the 3rd International Congress on Acoustics (1960).

76. W. E. Rowe, W. L. Nyborg, *J. Acoust. Soc. Am.*, **39**, 965 (1966).

77. H. Zhang, L. A. Coury, *Anal. Chem.*, **65**, 1552 (1993).

78. C. R. S. Hagan, L. A. Coury, *Anal. Chem.*, **66**, 399 (1994).

79. R. G. Compton, J. C. Eklund, F. Marken, T. O. Rebbitt, R. P. Akkermans, D. N. Waller, *Electrochimica Acta,* **42**, 2919 (1997).

80. J. Klima, C. Bernard, C. Degrand, *J. Electroanal. Chem.*, **367**, 297 (1994).

81. J. Klima, C. Bernard, C. Degrand, *J. Electroanal. Chem.*, **399**, 147 (1995).

82. R. G. Compton, J. C. Eklund, S. D. Page, T. J. Mason, D. J. Walton, *J. Appl. Electrochem.*, **26**, 1775 (1996).

83. F. Javier Del Campo, J. Melville, J. L. Hardcastle, R. G. Compton, *J. Phys. Chem. A,* **105**, 666 (2001).

84. J. L. Hardcastle, J. C. Ball, Q. Hong, F. Marken, R. G. Compton, S. D. Bull, S. G. Davies, *Ultrason. Sonochem.*, **7**, 7 (2000).

85. J. Reisse, H. Francois, J. Vandercammen, O. Fabre, A. Kirsh-de Mesmaeker, C. Maerschalk, J.-L. Delplancke, *Electrochimica Acta,* **39**, 37 (1994).

86. R. G. Compton, J. C. Eklund, D. N. Waller, F. Marken, *Electrochimica Acta,* **41**, 315 (1996).

87. J. C. Eklund, F. Marken, D. N. Waller, R. G. Compton, *Electrochimica Acta,* **41**, 1541 (1996).

88. F. Marken, R. P. Akkermans, R. G. Compton, *J. Electroanal. Chem.*, **415**, 55 (1996).

89. P. R. Birkin, S. Silva-Martinez, *J. Electroanal. Chem.*, **416**, 127 (1996).

90. P. R. Birkin, S. Silva-Martinez, *J. Chem. Soc., Chem. Commun.*, 1807 (1995).

91. E. Maisonhaute, P. C. White, R. G. Compton, *J. Phys. Chem. B,* **105**, 12087 (2001).

92. E. Maisonhaute, C. Prado, P. C. White, R. G. Compton, *Ultrason. Sonochem.*, **9**, 297 (2002).

93. E. Maisonhaute, B. A. Brooks, R. G. Compton, *J. Phys. Chem. B,* **106**, 3166 (2002).

94. S. A. Perusich, R. C. Alkire, *J. Electrochem. Soc.,* **138**, 708 (1991).

95. S. A. Perusich, R. C. Alkire, *J. Electrochem. Soc.,* **138**, 700 (1991).

96. R. G. Compton, J. C. Eklund, S. D. Page, G. H. W. Sanders, J. Booth, *J. Phys. Chem.,* **98**, 12410 (1994).

97. N. A. Madigan, C. R. S. Hagan, L. A. Coury, *J. Electrochem. Soc.,* **141**, L23 (1994).

98. P. R. Birkin, R. O'Conner, C.Rapple, S. Silva-Martinez, *J. Chem. Soc., Faraday Trans.,* **94**, 3365 (1998).

99. H. N. McMurray, B. P. Wilson, *J. Phys. Chem. A,* **103**, 3955 (1999).

100. V. Renaudin, N. Gondrexon, P. Boldo, C. Petrier, A. Bernis, Y. Gonthier, *Ultrason. Sonochem.,* **1**, S81 (1994).

101. P. R. Birkin, T. G. Leighton, J. F. Power, M. D. Simpson, A. M. L. Vinçotte, P. F. Joseph, *J. Phys. Chem. A,* **107**, 306 (2003).

102. T. Tuziuti, S. Hatanaka, K. Yasui, T. Kozuka, H. Mitome, *J. Chem. Phys.,* **116**, 6221 (2002).

103. S. Hatanaka, H. Mitome, K. Yasui, S. Hayashi, *J. Am. Chem. Soc.,* **124**, 10250 (2002).

104. H. Frenzel, H. Schultes, *Z. Phys. Chem.,* **27B**, 421 (1934).

105. M. P. Brenner, S. Hilgenfeldt, D. Lohse, *Rev. Mod. Phys.,* **74**, 425 (2002).

106. V. Griffing, *J. Chem. Phys.,* **20**, 939 (1952).

107. R. Lofstedt, B. P. Barber, S. J. Putterman, *Phys. Fluid. A,* **5** (1993).

108. B. P. Barber, S. J. Putterman, *Phys. Rev. Lett.,* **69**, 3839 (1992).

109. P. D. Jarman, *J. Acoust. Soc. Am.,* **32**, 1459 (1960).

110. T. Lepoint, D. De Pauw, F. Lepoint-Muille, M. Goldman, A. Goldman, *J. Acoust. Soc. Am.,* **101**, 2012 (1997).

111. Y. Frenkel, *Acta Phisiochemica,* **12**, 323 (1940).

112. M. P. Brenner, S. Hilgenfeldt, D. Lohse, *Rev. Mod. Phys,* **74**, 425 (2002).

113. J. R. Blake, *Phil. Trans. R. Soc. Lond. A*, 357 (1999).

114. J. D. N. Cheeke, *Can. J. Phys,* **75**, 77 (1997).

115. F. P. Ford, G. T. Burstein, T. P. Hoar, *J. Electrochem. Soc.,* **127**, 1325 (1980).

116. T. A. Alder, R. P. Waters, *Corros. Sci.,* **49**, 399 (1993).

117. G. T. Burstein, D. H. Davies, *J. Electrochem. Soc.,* **128**, 33 (1981).

118. G. T. Burstein, P. I. Marshall, *Corros. Sci.,* **23**, 125 (1983).

119. G. T. Burstein, R. C. Newman, *J. Electrochem. Soc.,* **128**, 2270 (1981).

120. D. Li, X. Mao, R. Zhu, *Corros. Sci.,* **49**, 877 (1993).

121. E.-A. Cho, C.-K. Kim, J.-S. Kim, H.-S. Kwon, *Electrochimica Acta,* **45**, 1933 (2000).

122. G. T. Burstein, R. J. Cinderey, *Corros. Sci.,* **32**, 1195 (1991).

123. G. T. Burstein, R. J. Cinderey, *Corros. Sci.,* **33**, 475 (1992).

124. R. J. Cinderey, G. T. Burstein, *Corros. Sci.,* **33**, 493 (1992).

125. R. J. Cinderey, G. T. Burstein, *Corros. Sci.,* **33**, 499 (1992).

126. G. T. Burstein, C. Lui, *Electrochimica Acta,* **39**, 873 (1994).

127. G. T. Burstein, K. Sasaki, *J. Electrochem. Soc.,* **148**, B282 (2001).

128. G. S. Frankel, B. M. Rush, C. V. Jahnes, C. E. Farrell, *J. Electrochem. Soc.,* **138**, 643 (1991).

129. G. S. Frankel, C. V. Jahnes, V. Brusic, A. J. Davenport, *J. Electrochem. Soc.,* **147**, 2290 (1995).

130. N. Cabrera, N. F. Mott, *Rep. Prog. Phys.,* **12**, 163 (1948/1949).

131. L. Young, *Can. J. Phys,* **37**, 276 (1959).

132. J. F. Dewald, *J. Electrochem. Soc.,* **102**, 1 (1955).

133. M. A. H. Lanyon, B. M. W. Trapnell, *Proc. Roy. Soc.*, **227A**, 387 (1954/1955).

134. N. Sato, M. Cohen, *J. Electrochem. Soc.*, **111**, 512 (1964).

135. D. D. Eley, P. R. Wilkinson, *Proc. R. Soc. Lond. A*, **227**, 387 (1960).

136. M. Green, *Prog. Semicond.*, **4**, 37 (1960).

137. J. T. Law, *J. Phys. Chem. Solid.*, **4**, 91 (1958).

138. C. AgraGutierroz, R. G. Compton, *Electroanalysis*, **10**, 204 (1998).

139. J. deDamborenea, J. M. Bastidas, A. J. Vazquez, *Electrochimica Acta*, **42**, 455 (1997).

140. T. B. Du, J. J. Chen, D. Z. Cao, *J. Mater. Sci.*, **36**, 3903 (2001).

141. V. Jovancicevic, S. Ramachandran, P. Prince, *Corrosion*, **55**, 449 (1999).

142. S. Sathiyanarayanan, C. Marikkannu, N. Palaniswamy, *Appl. Surf. Sci*, **241**, 477 (2005).

143. S. T. Selvi, V. Raman, N. Rajendran, *J. Appl. Electrochem.*, **33**, 1175 (2003).

144. E. Stupnisek-Lisac, A. Brnada, A. D. Mance, *Corros. Sci.*, **42**, 243 (2000).

145. A. Galal, N. F. Atta, M. H. S. Al-Hassan, *Mater. Chem. Phys.*, **89**, 38 (2005).

146. M. MetikosHukovic, R. Babic, Z. Grubac, S. Brinic, *J. Appl. Electrochem.*, **26**, 443 (1996).

147. M. A. Quraishi, J. Rawat, M. Ajmal, *Corrosion*, **54**, 996 (1998).

148. S. N. Raicheva, B. V. Aleksiev, E. I. Sokolova, *Corros. Sci.*, **34**, 343 (1993).

149. J. Uehara, K. Aramaki, *J. Electrochem. Soc.*, **138**, 3245 (1991).

150. A. Rauscher, G. Kutsan, Z. Lukacs, *Corros. Sci.*, **35**, 1425 (1993).

151. M. N. Desai, M. B. Desai, *Corros. Sci.*, **24**, 649 (1984).

152. M. J. Franklin, D. C. White, H. S. Isaacs, *Corros. Sci.*, **33**, 251 (1992).

153. K. Aramaki, *Corros. Sci.,* **44**, 2621 (2002).

154. B. D. Chambers, S. R. Taylor, M. W. Kendig, *Corrosion,* **61**, 480 (2005).

155. R. D. Armstrong, L. Peggs, A. Walsh, *J. Appl. Electrochem.,* **24**, 1244 (1994).

156. L. Dhouibi, E. Triki, M. Salta, P. Rodrigues, A. Raharinaivo, *Mater. Struct.,* **36**, 530 (2003).

157. A. G. Petersen, D. Klenerman, W. M. Hedges, *Corrosion,* **60**, 187 (2004).

158. A. G. Petersen, D. Klenerman, W. M. Hedges, M. L. Harris, *Corrosion,* **58**, 216 (2002).

159. P. N. Bartlett, *Biosensors a practical approach,* A. E. G. Cass, Ed, Oxford University Press, Oxford, 58-60 (1990).

160. G. Denuault, *Chemistry in Industry,* **18**, 678 (1996).

161. T. J. Mason, J. P. Lorimer, D. M. Bates, *Ultrasonics,* **30**, 40 (1992).

162. L. E. Kinsler, A. R. Frey, A. B. Coppens, J. V. Sanders, *Fundamentals of Acoustics,* John Wiley & Sons, Inc., New York (1982).

163. D. T. Blackstock, *Fundamentals of Physical Acoustics,* John Wiley & Sons, Inc., New York (2000).

164. B. Vyas, C. M. Preece, *J. App. Phys.,* **47**, 5133 (1976).

165. F. Burdin, N. A. Tsochatzidis, P. Guiraud, A. M. Wilhelm, H. Delmas, *Ultrason. Sonochem.,* **6**, 43 (1999).

166. F. E. Fox, R. Stanley, G. S. Larson, *J. Acoust. Soc. Am.,* **27**, 534 (1955).

167. T. G. Leighton, *Ultrason. Sonochem.,* **2**, S123 (1995).

168. M. W. Miller, C. C. Church, A. A. Brayman, M. S. Malcuit, R. W. Boyd, *Ultrasound Med. Biol.,* **15**, 67 (1988).

169. P. R. Birkin, J. F. Power, A. M. L. Vinçotte, T. G. Leighton, *Phys. Chem. Chem. Phys.,* **5**, 4170 (2003).

170. T. G. Leighton, *The Acoustic Bubble,* Academic Press Limited, London, §2.1.2 (1994).

171. M. Berthelot, *Ann. Chim. Phys,* **30**, 232 (1850).

172. J. L. Green, D. J. Durben, G. H. Wolf, C. A. Angell, *Science,* **249**, 649 (1990).

173. W. L. Nyborg, *Physical principles of ultrasound.* In *Ultrasound: its applications inmedicine and biology,* F. J. Fry, Ed, Elsevier, New York (1978).

174. L. Rayleigh, *Theory of Sound,* Macmillan, London, 2nd (1896).

175. K. Jochle, J. Debus, W. J. Lorenz, P. Huber, *Ultrasound Med. Bio.,* **22**, 329 (1996).

176. A. J. Coleman, M. J. Choi, J. E. Saunders, T. G. Leighton, *Ultrasound Med. Biol.,* **18**, 267 (1992).

177. R. O. Cleveland, O. A. Sapozhnikov, M. R. Bailey, L. A. Crum, *J. Acoust. Soc. Am.,* **107**, 1745 (2000).

178. R. G. Compton, J. C. Eklund, S. D. Page, T. O. Rebbitt, *J. Chem. Soc., Dalton Trans.*, 389 (1995).

179. J. P. Lorimer, B. Pollet, S. S. Phull, T. J. Mason, D.J.Walton, U. Geissler, *Electrochimica Acta,* **41**, 2737 (1996).

180. J. F. Power, *Electrochemical, Photographic, Luminescent and Acoustic Characterisation of Cavitation,* PhD Thesis, University of Southampton (2003).

181. P. R. Birkin, Y. E. Watson, T. G. Leighton, *J. Chem. Soc., Chem. Commun.*, 2650 (2001).

182. Y. E. Watson, P. R. Birkin, T. G. Leighton, *Ultrason. Sonochem.,* **10**, 65 (2003).

183. Y. E. Watson, *Electrochemical investigations of acoustically driven gas bubbles,* PhD Thesis, University of Southampton (2003).

184. P. Liljeroth, C. Johans, C. J. Slevin, B. M. Quinn, K. Kontturi, *Electrochem. Commun.,* **4**, 67 (2002).

185. P. I. Marshall, G. T. Burstein, *Corros. Sci.,* **23**, 1219 (1983).

186. G. T. Burstein, A.J.Davenport, *J. Electrochem. Soc.,* **136**, 936 (1989).

187. G. Lorang, M. D. C. Belo, A. M. P. Simoes, M. G. S. Ferreira, *J. Electrochem. Soc.,* **141**, 3347 (1994).

188. P. Schmuki, *J. Solid State Electrochem.,* **6**, 145 (2002).

189. C.-O. A. Olsson, D. Landolt, *Electrochimica Acta,* **48**, 1093 (2003).

190. C.-O. A. Olsson, D. Landolt, *J. Electrochem. Soc.,* **148**, B438 (2001).

191. M. Abdallah, *Mat. Chem. Phys.,* **82**, 786 (2003).

192. H. N. McMurray, D. A. Worsley, B. P. Wilson, *J. Chem. Soc., Chem. Commun.,* **8**, 887 (1998).